2016

Numerical & Experimental Evaluation of Encapsulated Phase Change Materials for Use in Thermal Energy Storage Applications

Laura D. Solomon
Lehigh University

Numerical & Experimental Evaluation of Encapsulated Phase Change Materials for Use in Thermal Energy Storage Applications

by

Laura Solomon

Presented to the Graduate and Research Committee

of Lehigh University

in Candidacy for the Degree of

Doctor of Philosophy

in

Mechanical Engineering

Lehigh University

(May 2016)

Approved and recommended for acceptance as a dissertation in partial fulfilment of the requirements for the degree of Doctor of Philosophy.

_____

Date

_____

Alparslan Oztekin

_____

Accepted Date

Committee Members:

_____

Alparslan Oztekin

_____

Sudhakar Neti

_____

Justin Jaworski

_____

Himanshu Jain

_____

Dileep Singh

Acknowledgments

I would like to thank my thesis advisors, Professors Alparslan Oztekin and Sudhakar Neti. They always provided useful advice throughout the duration of my research. Additionally, I would like to thank Charles McLaren for helping in the making of the calorimetry samples and, with Dmytro Savytskyy, for helping me with the SEM and XRD. I also wish to thank Ali Elmozughi for teaching me how to use FLUENT and for many thought-provoking conversations, as well as Nipun Goel with whom I have had the pleasure of sharing an office for the past four years.

I also want to thank my family for always believing in me and encouraging me to pursue my dreams and work hard in school. Additionally, I would like to thank my friends for all their support through the years, especially when times were rough Lastly, I need to thank my boyfriend Jimmy for his countless hours of proofreading

Table of Contents

Acknowledgments iv
Table of Contents v
List of Tables vii
List of Figures viii
ABSTRACT 1
CHAPTER I: INTRODUCTION 4
1.1 Thermal Energy Storage 5
1.2 Phase Change Materials 6
1.2.1 Encapsulated Phase Change Materials 9
1.3 Numerical Modeling of Phase Change Materials 12
1.4 Exergy Analysis 15
1.5 Current Objectives 17
CHAPTER II: NUMERICAL METHODS 20
2.1 Discretization Methods 20
2.2 Flow Solvers 23
2.3 Enthalpy Porosity Method 26
2.4 Volume of Fluid Method 28
2.5 Turbulence Modeling 30
2.5.1 Reynolds Averaged Navier-Stokes 31
2.5.2 k-ω SST Model 32
CHAPTER III: CALORIMETRY SYSTEM 35
3.1 Calorimeter System Design 35
3.2 Experimental Procedure 37
3.3 Energy Analysis 40
3.4 System Verification 45
3.5 Summary 46
CHAPTER IV: CALORIMETRY SIMULATIONS 48
4.1 Calorimetry Simulation Set Up 48
4.2 Internal Heat Transfer Results 50
4.3 External Heat Transfer Results 52
4.4 Conclusions 55
CHAPTER V: SPHERICAL EPCM CAPSULES 56
5.1 Mesh Independence 57
5.2 Melting of Spherical EPCM Capsules 58
5.3 Solidification of Spherical EPCM Capsules 64
5.4 Conclusions 69
CHAPTER VI: EFFECT OF INITIAL VOID LOCATION 71
6.1 Initial Random Void 73

6.2 Initial Central Void 75
6.3 Initial Upper Void 77
6.4 Case Comparison 80
6.5 Conclusions 82
CHAPTER VII: PILOT SCALE EPCM-BASED LATENT HEAT TES SYSTEM 85
7.1 System Description 85
7.2 HTF Results 88
7.3 EPCM Capsule Results 92
7.4 Comparison of Simulation with Experimental Results 101
7.5 Conclusions 102
CHAPTER VIII: EXERGY ANALYSIS OF EPCM-BASED TES SYSTEMS 105
8.1 System Description 105
8.2 Results 106
8.2.1 Charging Process 106
8.2.2 Discharging Process 125
8.3 Overall Cycle Efficiency 141
8.4 Conclusions 142
CHAPTER IX: USE OF METALLIC OXIDES AS PCMS FOR TES 145
9.1 Determination of a Suitable Metal Oxide for Use as a PCM 145
9.2 Testing of $Na_4B_2O_5$ Capsules 147
9.2.1 Design of $Na_4B_2O_5$ EPCM Capsules 148
9.2.2 Initial Calorimeter Testing 152
9.2.3 SEM Results 155
9.2.4 DSC Results 158
9.2.5 XRD Results 161
9.2.6 Revised Calorimeter Results 164
9.3 Conclusions 166
CHAPTER X: SUMMARY AND CONCLUSIONS 169
REFERENCES 175
VITA 182

List of Tables

Table 1. Model constants employed in the closure of the k-ω SST model 34

Table 2. Specifications of stainless steel calibration samples 44

Table 3. Thermal properties of stainless steel 304 [75]..... 44

Table 4. Results of verification testing..... 46

Table 5 Physical properties of air, stainless steel, calorimeter, aluminum and sodium chloride used in the calorimetry simulations..... 49

Table 6. Physical properties of $NaNO_3$, stainless steel, and air..... 57

Table 7. Temperature dependent properties of air, stainless steel, and $NaNO_3$ (all temperatures are in Kelvin) 86

Table 8. Properties of air, $NaNO_3$, $NaNO_2$, and KNO_3 used in exergy simulations .. 106

Table 9. Results of the charging and discharging process for the $NaNO_3$, $NaNO_2$, KNO_3, 2-PCM, 3-PCM, and sensible heat systems..... 142

Table 10. Physical properties of potential PCMS 147

Table 11. Final temperature of calorimeter for various capsule sizes..... 152

Table 12. Specifications of $Na_4B_2O_5$ EPCM samples..... 153

Table 13. Initial results of $Na_4B_2O_5$ calorimetry testing 153

Table 14. Sample 1 SEM EDS results..... 156

Table 15. Sample 2 SEM EDS results..... 157

Table 16. Updated results of $Na_4B_2O_5$ calorimetry testing with T_m= 641 °C 166

Table 17. Updated results of $Na_4B_2O_5$ calorimetry testing with T_m= 592 °C 166

List of Figures

Figure 1. Classification of phase change materials [3] (figure reproduced with permission) 8

Figure 2. Latent heat based heat storage capacity of various PCMs [12] (figure reproduced with permission) 8

Figure 3. Example computational domain for illustration purposes 21

Figure 4. Calorimeter system a schematic (right) and photograph (left) 36

Figure 5. Sample placed in carbon steel cylinder during heating process 38

Figure 6. Thermocouples used to measure sample temperature secured with copper wire 38

Figure 7. Calorimeter, air, and sample temperature over the course of an experiment 39

Figure 8. Temperature measurements during a typical calorimetry experiment [20] .. 40

Figure 9. Calibration results (R^2=0.97) [20] 45

Figure 10. Computational domain used for calorimetry simulations 50

Figure 11. Evolution of the solid–liquid interface in the NaCl capsule (a-d) and sectioned $MgCl_2$ sample [19] 51

Figure 12. Isotherms (a-e) and velocity magnitude (f-j) for the aluminum sample 3 cycle 3 simulation at various times 53

Figure 13. Experimental temperature, predicted volume averaged temperature, and theoretical equilibrium temperature for aluminum sample 3 cycle 3 54

Figure 14. The location of the liquid/solid interface with 20% void for various mesh sizes 58

Figure 15. Temperature, liquid fraction, velocity magnitude, and interface contours at 5 sec into melting (SteFo=0.0113) 60
Figure 16. Temperature, liquid fraction, velocity magnitude and interface contours at 15 sec into melting (SteFo=0.0339) 62
Figure 17. Temperature, liquid fraction, velocity magnitude and interface contours at 25 sec into melting (SteFo=0.0565) 63
Figure 18. Temperature, liquid fraction, velocity magnitude and interface contours at 5 sec into solidification (SteFo=0.0039) 65
Figure 19. Temperature, liquid fraction, velocity magnitude and interface contours at 60 sec into solidification (SteFo=0.0466) 67
Figure 20. Temperature, liquid fraction, velocity magnitude and interface contours at 240 sec into solidification (SteFo=0.1864) 68
Figure 21. The interfaces during (a-c) melting and (d-f) solidification at various times 69
Figure 22. Computational domain of EPCM capsule with various void locations 72
Figure 23. Heat transfer coefficient applied to EPCM capsule surface..... 72
Figure 24. Contours of the temperature, liquid fraction, volume fraction, & velocity magnitude for an EPCM capsule with an initially random void distribution at 90 sec (a-d), 185 sec (e-h) and 277 sec (i-l) into the melting process. 74
Figure 25. Contours of the temperature, liquid fraction, volume fraction, & velocity magnitude for an EPCM capsule with a void initially located at the center of the EPCM capsule at 74 sec (a-d), 147 sec (e-h) and 221 sec (i-m) into the melting process. 76

Figure 26. Contours of the temperature, liquid fraction, volume fraction, & velocity magnitude for an EPCM capsule with an initial void located at the top of the EPCM capsule at 180 sec (a-d), 260 sec (e-h) and 320 sec (i-l) into the melting process. 79

Figure 27. Schematic of test section [24](upper), 10 EPCM capsules with deflectors [24] (left), and computational domain (right) 87

Figure 28. Transient inlet temperature of the test section for both the experiment and simulation 88

Figure 29. Velocity magnitude in the XY (left) and YZ (right) symmetry planes at 4,000 sec (Re = 3285) 89

Figure 30. Isotherms in the HTF in the XY (upper) and YZ (lower) symmetry planes 91

Figure 31. Isotherms in the EPCM capsules in the XY (upper) and YZ (lower) symmetry planes 93

Figure 32. Velocity magnitude in the fifth and sixth EPCM capsules in the XY plane 95

Figure 33. Velocity magnitude in the fifth and sixth EPCM capsules in the YZ plane 96

Figure 34. Liquid fraction in the EPCM capsules in the XY (upper) and YZ (lower) symmetry planes 98

Figure 35. Void-PCM interface in the XY plane in the fifth and sixth EPCM capsules 99

Figure 36. Void-PCM interface in the fifth and sixth EPCM capsules in the YZ plane 100

Figure 37. Comparison between experimental and numerical results for the inlet, outlet, and tenth capsule temperature 102

Figure 38. Computational domain used for exergy evaluation 106

Figure 39. Velocity field after 5 sec (top), 100 sec (middle), and 40,400 sec (bottom). Re = 544 107

Figure 40. Outlet temperatures during the charging process for the $NaNO_3$ (solid), $NaNO_2$ (square), KNO_3 (circles), $NaNO_3/NaNO_2$ (dashed), $KNO_3/NaNO_3/NaNO_2$ (dash-dot) , and sensible heat (dot) systems 109

Figure 41. Isotherms at 10,400 sec for a) sensible heat only, b) NaNO3 (SteFo=0.47), c) $NaNO_2$ (SteFo=0.94), d) KNO_3 (SteFo=0.034), e) $NaNO_3$/NaNO2 (SteFo=0.75), f) $KNO_3/NaNO_3/NaNO_2$ (0.65) systems 110

Figure 42. Isotherms at 20,400 sec for a) sensible heat only, b) NaNO3 (SteFo=0.93), c) $NaNO_2$ (SteFo=1.85), d) KNO_3 (SteFo=0.066), e) $NaNO_3/NaNO_2$ (SteFo=1.48), f) $KNO_3/NaNO_3/NaNO_2$ (SteFo=1.27) systems 112

Figure 43. Isotherms at 30,400 sec for a) sensible heat only, b) NaNO3 (SteFo=1.38), c) $NaNO_2$ (SteFo=2.75), d) KNO_3 (SteFo=0.098), e) $NaNO_3/NaNO_2$ (SteFo=2.21), f) $KNO_3/NaNO_3/NaNO_2$ (SteFo=1.89) systems 113

Figure 44. Isotherms at 40,400 sec for a) sensible heat only, b) NaNO3 (SteFo=1.84), c) $NaNO_2$ (SteFo=3.66), d) KNO_3 (SteFo=0.13), e) $NaNO_3/NaNO_2$ (SteFo=2.93), f) $KNO_3/NaNO_3/NaNO_2$ (SteFo=2.52) systems 114

Figure 45. Liquid fraction at 10,400 sec for a) NaNO3 (SteFo=0.47), b) $NaNO_2$ (SteFo=0.94), c) KNO_3 (SteFo=0.034), d) $NaNO_3/NaNO_2$ (SteFo=0.75), e) $KNO_3/NaNO_3/NaNO_2$ (SteFo=0.65) systems 116

Figure 46. Liquid fraction at 20,400 sec for a) NaNO3 (SteFo=0.93), b) $NaNO_2$ (SteFo=1.85), c) KNO_3 (SteFo=0.066), d) $NaNO_3/NaNO_2$ (SteFo=1.48), e) $KNO_3/NaNO_3/NaNO_2$ (SteFo=1.27) systems 117

Figure 47. Liquid fraction at 30,400 sec for a) NaNO3 (SteFo=1.38), b) $NaNO_2$ (SteFo=2.75), c) KNO_3 (SteFo=0.098), d) $NaNO_3/NaNO_2$ (SteFo=2.21), e) $KNO_3/NaNO_3/NaNO_2$ (SteFo=1.89) systems 118

Figure 48. Liquid fraction at 40,400 sec for a) NaNO3 (SteFo=1.84), b) $NaNO_2$ (SteFo=3.66), c) KNO_3 (SteFo=0.13), d) $NaNO_3/NaNO_2$ (SteFo=2.93), e) $KNO_3/NaNO_3/NaNO_2$ (SteFo=2.52) systems 119

Figure 49. Temperature at the center of each EPCM capsule for the $KNO_3/NaNO_3/NaNO_2$ system 121

Figure 50. Energy stored in each EPCM capsule for the $KNO_3/NaNO_3/NaNO_2$ system 121

Figure 51. Energy stored in the $NaNO_3$ (solid), $NaNO_2$ (square), KNO_3 (circles), $NaNO_3/NaNO_2$ (dashed), $KNO_3/NaNO_3/NaNO_2$ (dash-dot), and sensible heat (dot) systems during the charging process 123

Figure 52. Exergy stored in the $NaNO_3$ (solid), $NaNO_2$ (square), KNO_3 (circles), $NaNO_3/NaNO_2$ (dashed), $KNO_3/NaNO_3/NaNO_2$ (dash-dot), and sensible heat (dot) systems during the charging process 123

Figure 53. Exergy efficiency of the charging process 125

Figure 54. Outlet temperatures during the discharging process for the $NaNO_3$ (solid), $NaNO_2$ (square), KNO_3 (circles), $NaNO_3/NaNO_2$ (dashed), $KNO_3/NaNO_3/NaNO_2$ (dash-dot), and sensible heat (dot) systems 126

Figure 55. Isotherms at 50,000 sec for a) sensible heat only, b) NaNO3 (SteFo=0.025), c) $NaNO_2$ (0.038), d) KNO_3 (0.71), e) $NaNO_3/NaNO_2$ (0.031), f) $KNO_3/NaNO_3/NaNO_2$ (0.25) systems (6800 sec into discharging) 127

Figure 56. Isotherms at 60,000 sec for a) sensible heat only, b) NaNO3 (SteFo=0.061), c) $NaNO_2$ (0.093), d) KNO_3 (1.75), e) $NaNO_3/NaNO_2$ (0.078), f) $KNO_3/NaNO_3/NaNO_2$ (0.63) systems (16,800 sec into discharging) 128

Figure 57. Isotherms at 70,000 sec for a) sensible heat only, b) NaNO3 (SteFo=0.098), c) $NaNO_2$ (0.15), d) KNO_3 (2.80), e) $NaNO_3/NaNO_2$ (0.12), f) $KNO_3/NaNO_3/NaNO_2$ (1.00) systems (26,800 sec into discharging) 130

Figure 58. Isotherms at 80,000 sec for a) sensible heat only, b) NaNO3 (SteFo=0.13), c) $NaNO_2$ (0.20), d) KNO_3 (3.84), e) $NaNO_3/NaNO_2$ (0.17), f) $KNO_3/NaNO_3/NaNO_2$ (1.37) systems (36,800 sec into discharging) 131

Figure 59. Liquid fraction at 50,000 sec for a) NaNO3 (SteFo=0.025), b) $NaNO_2$ (0.038), c) KNO_3 (0.71), d) $NaNO_3/NaNO_2$ (0.031), e) $KNO_3/NaNO_3/NaNO_2$ (0.25) systems (6800 sec into discharging) 132

Figure 60. Liquid fraction at 60,000 sec for a) NaNO3 (SteFo=0.061), c) $NaNO_2$ (0.093), d) KNO_3 (1.75), e) $NaNO_3/NaNO_2$ (0.078), f) $KNO_3/NaNO_3/NaNO_2$ (0.63) systems (16,800 sec into discharging) 133

Figure 61. Liquid fraction at 70,000 sec for a) NaNO3 (SteFo=0.098), c) $NaNO_2$ (0.15), d) KNO_3 (2.80), e) $NaNO_3/NaNO_2$ (0.12), f) $KNO_3/NaNO_3/NaNO_2$ (1.00) systems (26,800 sec into discharging) 135

Figure 62. Liquid fraction at 80,000 sec for a) NaNO3 (SteFo=0.13), c) $NaNO_2$ (0.20), d) KNO_3 (3.84), e) $NaNO_3/NaNO_2$ (0.17), f) $KNO_3/NaNO_3/NaNO_2$ (1.37) systems (36,800 sec into discharging) 136

Figure 63. Energy released in each EPCM capsule for the $KNO_3/NaNO_3/NaNO_2$ system 138

Figure 64. Energy released in the $NaNO_3$ (solid), $NaNO_2$ (square), KNO_3 (circles), $NaNO_3/NaNO_2$ (dashed), $KNO_3/NaNO_3/NaNO_2$ (dash-dot), and sensible heat (dot) systems during the discharging process 139

Figure 65. Exergy extracted in the $NaNO_3$ (solid), $NaNO_2$ (square), KNO_3 (circles), $NaNO_3/NaNO_2$ (dashed), $KNO_3/NaNO_3/NaNO_2$ (dash-dot), and sensible heat (dot) systems during the discharging process 139

Figure 66. Exergy efficiency of the discharging process 140

Figure 67. Na_2O-B_2O_3 phase diagram [97] 148

Figure 68. Schematic of EPCM capsule for analytical analysis 150

Figure 69. The temperature at the center of the EPCM capsule for a 25.4 mm by 50.8 mm (diameter by height), 25.4 mm by 76.2 mm, 50.8 mm by 50.8 mm, and 50.8 mm by 76.2 mm capsule size along with the critical cooling rate for $Na_4B_2O_5$ ... 151

Figure 70. EPCM sample during the filling process 153

Figure 71. Calorimeter & air temperature during sample 1 cycle 1 154

Figure 72. Sectioned $Na_4B_2O_5$ sample 1 (left) and sample 2 (right) 155

Figure 73. SEM photos of two locations in both sample 1 and sample 2. Scale bar for a-c are 5 microns while d is 1 micron 156

Figure 74. DSC of $Na_4B_2O_5$ Sample 1 159

Figure 75. DSC of $Na_4B_2O_5$ Sample 2 160

Figure 76. XRD of Middle of Sample 1 (upper) and $NaBO_2 \cdot 2H_2O$ ICDD Card No. 00-006-0122 (lower) 162

Figure 77. XRD of sample 2 (top), $NaBO_2$ (middle) ICDD Card No. 00-012-0492, and $Na_4B_2O_5$ ICDD Card No. 00-036-0878 163

ABSTRACT

A numerical heat transfer analysis of encapsulated phase change material (EPCM) capsules was conducted by employing the enthalpy-porosity and VOF methods simultaneously to capture the complex multi-phase heat transfer that occurs within the capsules. The results of the numerical methods employed were validated by comparing the final shape of the solid phase change material (PCM) predicted to that seen within sectioned experimental capsules. The validated methods were used to study the effect that an internal void space has on the heat transfer within an EPCM capsule. Its effect is immediately noticeable as the isotherms no longer form the concentric rings predicted by the unsteady diffusion equation since the void acts as an insulator reducing the conduction rate in the upper portion of the capsule. Additionally, the increased melting rate resulting from convection in the molten PCM further reshapes the solid-liquid interface. In contrast, the solidification process is conduction-dominated and limited by the thermal conductivity of the chosen PCM resulting in considerably longer solidification times.

The impact of an internal void on the overall heat transfer was further examined by considering three limiting cases of an upper void, central void, and random void distributions where the upper void is positioned opposite to the orientation of the gravitational vector. Since the PCM for the central void distribution is in direct contact with the entire capsule shell, it has the highest heat transfer rate during the initial melting stages leading to it having a melting time that is 22% and 39% faster than the random and upper void distributions. In an ideal world, one would like to keep the void located as close to the center of the capsule as possible. The

vastly different evolution of the solid-liquid interface for the three cases considered highlights the profound impact an internal void has on the temporal and spatial evolution of the solid-liquid interface.

The results for a single EPCM capsule were extended by evaluating the performance of a pilot-scale EPCM-based latent heat thermal energy storage (TES) system. The capsules sequentially showed the same evolution of the melting front within the capsules over the course of the charging process. The numerical results were compared to experimental recorded values for the temperature in the furthest downstream EPCM capsule. Agreement within 3% was seen during the initial solid sensible heating stages, however as the capsules began to melt the discrepancy increased due to a poor estimate for the values of the latent heat of fusion of $NaNO_3$. This resulted in a 8% faster predicted melting time. However, this has minimal effect on the overall energy storage of the system due to the large operational temperature range applied in the current experiment. 65% of the 22 MJ of energy release by the heat transfer fluid (HTF) was stored in the 17.7 kg of $NaNO_3$; 20% of this energy can be attributed to latent heat energy storage. Therefore, the system is able to store a large fraction of energy supplied by the HTF with a significant contribution from latent heat. Furthermore, if the operational temperature range were smaller the fraction of latent heat energy storage would have been significantly larger.

The second law analysis of an example TES system was conducted to determine the benefit of s system employing a multiple PCMs. As expected, the latent heat-based systems were able to store more energy and exergy with comparable efficiencies than systems that rely on sensible heat only. Furthermore, when the

overall cycle performance is examined, systems with multiple PCMs perform better than corresponding single PCM-based systems. While for the operating conditions and PCMs chosen the 2-PCM system was superior, great care is required during the design of an EPCM-based TES system as the difference between the melting point of the PCMs and the inlet temperatures during charging and discharging greatly affect the performance of the system.

Lastly, experimental evaluations of the use of metallic oxides as new novel PCMs were conducted. In particular, the eutectic compounds in the Na_2O-B_2O_3 system were investigated as they offer higher energy storage densities at melting temperatures comparable to the previously investigated nitrate and chloride salts. However, the material that was formed during the preparation of the samples was not a eutectic compound due to sodium evaporation and therefore did not melt congruently. Once the initial composition of the material was determined, the discrepancy between the theoretical and experimental energy storage were shown to be within the ±2% uncertainty of the calorimetry system. While these initial results are promising, further research is required before these metallic oxides can be integrated into EPCM-based latent heat TES systems as a superior alternative to the currently employed nitrate and chloride salts.

CHAPTER I: INTRODUCTION

Prior to the advent of coal-based power during the industrial revolution, all energy was produced via renewable means. The development of fossil fuel-based power generation rendered these renewable means of energy inefficient. For 200 years the cost and abundance of fossil fuels made the notion of using renewable energy uneconomical and therefore research focused on ways of improving the technology behind fossil fuel-based power. However, the world has come to the realization that fossil fuel resources are in fact limited, spurring a return to renewable power generation. Despite this revival, grid-scale electricity generation through renewable means is simply not cost-competitive with the currently operating fossil fuel power plants. Therefore, while the concept of using hydro, wind, and solar energies as means of power are not new ones, further research into improving their efficiency is required.

Of the various renewable resources, solar power is particularly attractive because while its intensity may vary it is available across the globe. There are two ways to generate electricity from solar radiation: either through the use of photovoltaic (PV) cells or at solar thermal power plants such as concentrating solar power (CSP) plants. PV cells directly convert the sun's rays into electricity by utilizing the photovoltaic effect of a material. At a CSP plant, the sun's rays are used to heat a thermal fluid that is then used to drive a power generation cycle such as the Brayton or Rankine cycle. Both of these approaches to electricity generation have to overcome the transient nature of solar radiation. This results in solar power plants having a low capacity factor (18%) when compared to fossil fuel plants (85%). The capacity factor

is a measure of the percentage of a plant's potential output that is actually output over a period of time.

One can improve the capacity factor of solar power plants if a means of energy storage was employed. Since electrical energy cannot be stored directly, excess electrical energy must be converted into either heat, mechanical, or chemical energy to be stored. This conversion results in energy losses not only during the storage process but also during energy retrieval, and reduces the effectiveness of the storage process and thus limits the amount of energy that can be retrieved. This is where solar thermal power has an advantage over most other forms of renewable energy; it has the ability to easily integrate storage in the means of thermal energy without costly conversation processes. This makes the use of CSP plants with thermal energy storage (TES) a highly attractive form of grid-scale electricity generation.

1.1 Thermal Energy Storage

TES is divided into three branches based on the principal behind the energy storage process. In sensible heat storage systems, energy is stored and released by raising and lowering the temperature of a material. The amount of energy stored depends on the heat capacity of the material and the temperature difference applied to the material. While sensible heat storage systems rely on large temperature differences, latent heat-based storage systems can store energy under nearly isothermal conditions by utilizing the vast quantities of energy required to induce a state change within a material. In a similar way, thermochemical energy storage systems use reversible endothermic/exothermic reactions to store and release energy. To reduce the cost of the storage system, a material with a high energy storage density should be

used. While thermochemical systems have the highest energy storage density of the three forms of TES, research into its usage is still in the early stages and uncertainties in the thermodynamic properties as well as reaction kinetics limit its usage.

Currently only sensible heat storage systems are used at operating CSP plants around the world. These systems use either a large volume of a solid material such as concrete, or a single- or two-tank molten salt-based storage system [1, 2]. These systems require an immense volume of material to store enough energy to efficiently operate the power plant for eight hours. For example, 28,500 tons of molten salt is required to operate the Andasol power plant in Spain for 7.5 hours. If a latent heat-based storage system was used instead, the amount of storage material could be greatly reduced yielding a lower system cost. This would result in a decrease in the levelized cost of electricity at CSP plants leading to them being not only cost-competitive with current fossil fuel-based plants but with other means of renewable energy as well.

1.2 Phase Change Materials

The main component of a latent heat-based TES system is the phase change material (PCM) that is used. Any material that undergoes a state change can potentially be used as a PCM for TES applications. Four different state or phase changes can occur: solid-solid, solid-liquid, liquid-gas, and solid-gas. During a solid-solid phase change the crystal structure of a material changes from one lattice configuration to another. While the small volumetric changes that occur during solid-solid phase changes make them ideal candidates for TES, the transitions are typically slow and have low transformation enthalpies relative to the other state changes. The

state change that is typically studied for TES applications is that of solid-liquid phase changes due to their relatively small volume changes and moderate enthalpy changes. Although liquid-gas transitions have high transformation energies, the large volume changes that occur and the complexity of storing the gaseous medium limit their use for TES applications. The last state transformation is when a solid material directly turns into a gas, such as dry ice. Solid-gas transitions have the same drawbacks as the use of liquid-gas transitions. Therefore the solid-liquid phase change is best suited for TES.

Whereas numerous materials exist that have melting temperatures in any desired temperature range, this alone does not make them a viable PCMs for TES applications. The material must also exhibit other desirable thermo-physical, kinetic, and chemical properties such as a high latent heat of fusion, small volume change, sufficient crystallization rate, and chemical stability, all while being abundant at low cost [3]. Generally, PCMs can be divided into three groups: organic, inorganic, and eutectic materials. A diagram of the classification of PCMs is shown in Figure 1. Extensive research has been conducted into potential materials for use in latent heat-based TES at temperatures below 120 °C that include paraffin waxes, fatty acids, and salt hydrates [4-9]. While these low temperature PCMs have numerous applications, materials with a melting point in excess of 300 °C are required for use at CSP plants [3]. Research into this high temperature area has primarily focused on the use of inorganic salts with some of the most notable materials being $NaNO_3$, KNO_3–$NaNO_3$ eutectics, and $MgCl_2$–NaCl eutectics [1, 3, 10, 11]. A comparison of the latent heat energy storage capacity of various PCMs is presented in Figure 2. Despite their

attractiveness all of these materials have the same drawback; a low thermal conductivity in the solid state [1].

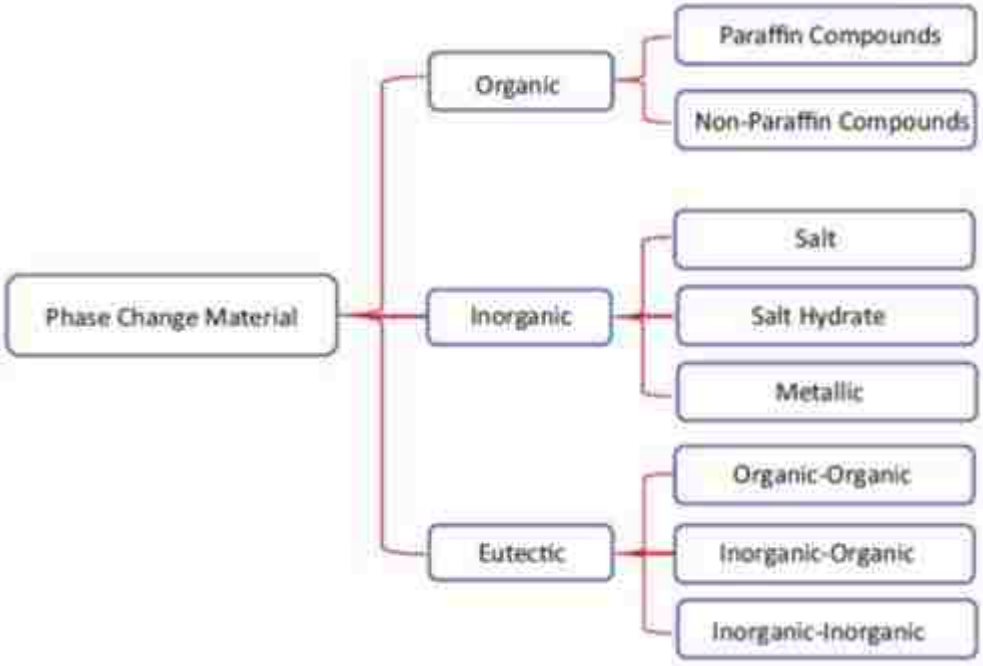

Figure 1. Classification of phase change materials [3] (figure reproduced with permission)

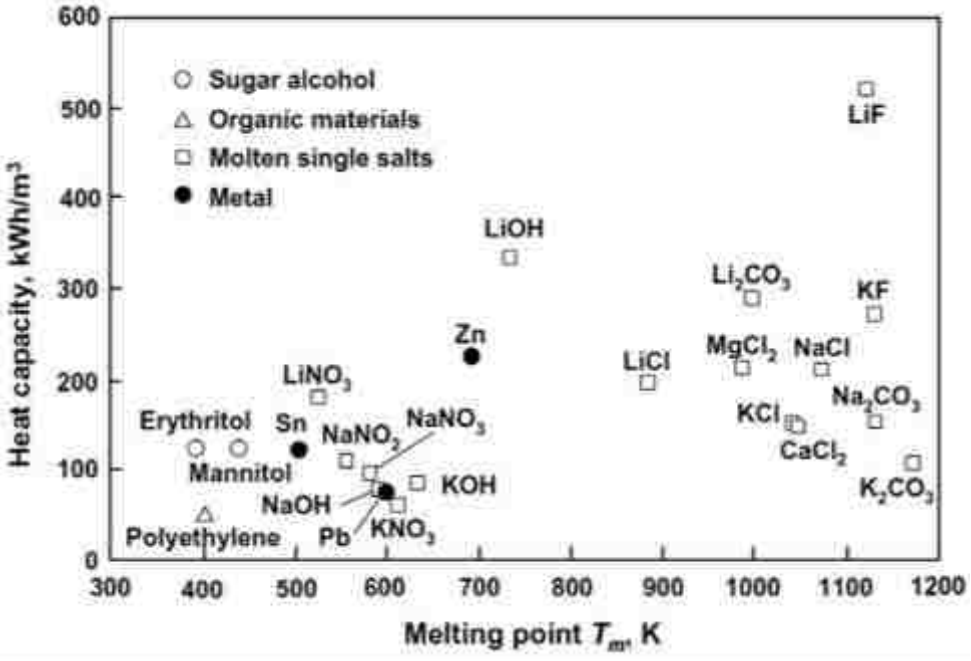

Figure 2. Latent heat based heat storage capacity of various PCMs [12] (figure reproduced with permission)

During the solidification process, the PCM has a tendency to stick to the heat exchanger surface. As time progresses, the solid layer increases in size, and due to the low thermal conductivity of the material it has a limiting effect on the heat transfer rate, prolonging the solidification process. Thus extensive research into different methods of improving the heat transfer within PCM-based systems has been conducted [13, 14]. These enhancements can be broken down into either material or system enhancements. Material enhancements are aimed at increasing the effective thermal conductivity of the base PCM by adding a secondary highly conductive material typically in the form of nanoparticles. System enhancements on the other hand increase the surface area of the heat exchanger to increase the heat transfer rate either usually by implementing fins or via encapsulation. While system enhancements may yield a more complex geometry, they do not experience the loss of energy storage capacity that occurs with material-based enhancements. Of particular interest is the use of encapsulated phase change material (EPCM) capsules.

1.2.1 Encapsulated Phase Change Materials

The encapsulation of PCMs into individual capsules improves the performance of the PCM since it results in a decrease in the charging/discharging time of the system due to the increase in the area over which heat transfer can occur [15, 16]. Nevertheless, the encapsulation of PCMs leads to its own unique difficulties that need to be overcome before it can be utilized efficiently and cost effectively at CSP plants as part of large scale TES. Careful consideration is required in the choice of a PCM and shell material pair as the two materials need to be chemically and metallurgically inert to prevent a loss of storage capacity from occurring over repeated thermal

cycling at elevated temperatures. Additionally, the shell material needs to withstand not only its own thermal stresses but the increase in internal pressure that results from the expansion of the PCM during melting [17]. Given the high temperatures experienced at CSP plants, metal encapsulation materials such as stainless steel, carbon steel, and nickel-based alloys are preferred [18]. To obtain the desired capsule characteristics, such as a high PCM to shell ratio and stability, there are two ways the PCMs can be encapsulated: by coating of a PCM pellet or filling a prefabricated shell with the desired PCM [11]. The disadvantage with the technique of coating PCM pellets is the ability to leave a sufficient void space such that the capsules do not rupture upon melting without the use of a sacrificial layer. This is not the same when prefabricated shells are used.

Research into both methods of encapsulation with various PCMs and shell materials have been conducted [2, 3, 18]. Zheng et al. [10] used conventional calorimetry to evaluate the performance of both sodium nitrate ($NaNO_3$) and a sodium chloride and magnesium chloride eutectic (NaCl-$MgCl_2$, 57 %*mol* NaCl) as PCMs that were encapsulated in carbon or stainless steel. They evaluated the storage capacity of the EPCM capsules over both short (~5 hours) and long term (~ 300 hours) cycling and the results indicated that the combination of the PCM and encapsulation material can be used for high temperature TES as no loss of storage capacity occurred [10]. As an increase in the operational temperature of a Rankine cycle increases its efficiency, a material that can store energy at higher temperatures is desirable. Zhao et al. [19] evaluated the performance of $MgCl_2$-stainless steel EPCM capsules. The capsules showed no deterioration of storage capacity after 480 hours of high temperature

exposure above 700 °C. Increasing the temperature even higher, NaCl-stainless steel EPCM capsules were evaluated and after 1,000 hours of exposure at 850 °C no degradation of the storage material could be detected [20-22].

While these results are promising, they were conducted on small (25.4 mm or 50.8 mm) laboratory-scale capsules. Zheng et al. [23] tested a pilot scale latent heat TES system that consisted of 10 cylindrical EPCM capsules with dimensions of 76.2 mm diameter and 254 mm long that were horizontally placed in a vertical test section. Hot air was forced over the capsules with a flow rate of 0.038 kg/s. They considered the use of $NaNO_3$, a NaCl-$MgCl_2$ eutectic, and a cascaded system of both NaCl-$MgCl_2$ and $NaNO_3$ [23, 24]. The system stored 211 kJ/kg of energy using $NaNO_3$ as the PCM over the temperature range of 250 to 386 °C and no reduction in storage capacity was seen after 40 hours of operation. When compared to a system that only had NaCl-$MgCl_2$ eutectic capsules, the cascaded system stored more energy after the first 30 min of operation, emphasizing the benefit of using multiple PCMs with varying melting temperatures. The results presented by Zheng et al. [23, 24] demonstrate the scalability of EPCM-based latent heat TES systems.

The results above were all conducted on prefabricated capsules that were filled with the desired amount of PCM and then sealed. While this process works for centimeter or larger capsules, it is difficult for sub-millimeter sized capsules. The advantage to smaller capsules is the reduction in discharging time as the characteristic length of the system is smaller; however these capsules tend to have smaller ratios of PCM to capsule shell which reduces the percentage of energy stored that is attributed to latent heat. These capsules are typically manufactured by coating PCM pellets first

with a sacrificial polymer layer to accommodate PCM expansion, and then depositing a thin layer of metal onto the capsules to prevent leakage. Alam et al. [25] presented a novel method of encapsulation that does not require this sacrificial layer by using a highly elastic polymer with a nickel coating. Using $NaNO_3$ as the PCM, these capsules were able to withstand 2,200 thermal cycles with no loss of storage capacity. Additionally, they tested a packed-bed system that held 770 capsules with a 2.7 cm diameter that survived 300 hours of testing without showing signs of mechanical or chemical deterioration [25].

While these results indicate that both nitrate- and chloride-based PCMs can be used for high temperature TES using EPCMs, they still have a low thermal conductivity in the solid phase that prolongs the solidification process. This led Zhao [21] and Solomon [20] to evaluate the use of metal-based PCMs by using zinc and aluminum. However, due to intermetallic reactions a loss of storage capacity occurred for both PCMs when encapsulated within a stainless steel shell. While this effect can be mitigated via the use of a protective paint, a non-metal based shell should be used. Despite the promising research that has been conducted, further research into new novel materials is required to further improve the technology of EPCM-based high temperature latent heat TES.

1.3 Numerical Modeling of Phase Change Materials

Various techniques have been employed to study heat transfer that involves a solid-liquid phase change. The progression of the solid-liquid interface can be tracked either directly or indirectly. The most popular method is the enthalpy-porosity method that was developed by Voller et al. [26] which indirectly tracks the location of the

solid-liquid interface using a parameter called the liquid fraction. The enthalpy-porosity method is also referred to as the volume tracking method [27]. Brent and Voller [28] conducted a fixed-grid solution of the coupled momentum and energy equations without resorting to variable transformations, and by utilizing a two-dimensional dynamic model they studied the influence of laminar natural convection on the melting process of gallium in rectangular cavities. Mackenzie and Robertson [29] solved the nonlinear enthalpy equation using a semi-implicit moving mesh discretization at each time step. Kholdadadi and Zhang [30] used an iterative finite-volume method to study the effect of buoyancy-driven convection on the constrained melting of PCMs within spherical containers by using primitive-dependent variables and Darcy's law to govern convection in a porous medium. Their results demonstrated the importance of the Prandtl number on the melting process at a fixed Rayleigh number and that natural convection in the molten PCM accelerates the melting process in comparison to pure diffusion models. Ismail et al. [31] characterized the solidification of various PCMs within cylindrical and spherical shells by examining the how different shell materials, capsule diameters, and surface temperatures affected the overall solidification process. Tan et al. [32] studied the effect of buoyancy-driven convection both experimentally and numerically by considering the constrained melting of n-octadecane inside a spherical glass shell.

Pinelli and Piva [33] incorporated the enthalpy-porosity method into Ansys FLUENT to investigate the use of n-octadecane in cylindrical capsules that were subject to a uniform exterior heat transfer coefficient. Assis et al. [34] conducted a parametric investigation of the melting of a paraffin wax PCM encapsulated within

spherical shells. Using the enthalpy-porosity method within FLUENT they were able to model a 15% void fraction, volumetric expansion of the PCM upon melting, and convection within the fluid media by simultaneously solving the conservation equations for the air void, solid PCM, and liquid PCM. Their model included a vent at the top of the capsule that expelled the air void as the PCM expanded. They validated their model using experimental results and were able to accurately capture the propagation of the solid-liquid interface [34]. Assis et al. [35] also conducted an analogous study on the solidification process within the same EPCM capsules.

Recently, Archibold et al. [36] extended the results of Assis et al. [34] to higher temperatures by employing $NaNO_3$ as the PCM. They obtained similar results and were able to capture the compression of the air void by considering a sealed capsule. The effects of radiative heat transfer within EPCM capsules was studied by Archibold et al. [37] by using NaCl as the PCM and their results indicate that radiative heat transfer increases the melting rate within the capsules. Bellan et al. [38] used an effective packed bed model to study the heat transfer that occurs in a bed of centimeter-sized spherical EPCM capsules and the effect of heat transfer fluid (HTF) flow rate, Stefan number, shell thickness, and shell material. Zhao et al. [39] compared the results of using both a front tracking and enthalpy-porosity method for the melting of $NaNO_3$ in both horizontally and vertically orientated cylindrical EPCM capsules and concluded that both models are able to accurately capture the propagation of the solid-liquid interface for both the melting and solidification processes.

While these numerical investigations lend insight into the complex heat transfer that occurs in latent heat based TES systems, they tend to make

simplifications that limit their accuracy such as neglecting convection in the molten PCM and the inclusion of an internal void space. The development of a model that incorporates all aspects of an EPCM-based latent heat TES system is required to further understand how these systems operate under real world conditions and can aid in the optimization of these systems to allow for cost-competitive electricity generation at CSP plants.

1.4 Exergy Analysis

While the energy efficiency of a TES system is an important factor in its performance and system cost, the exergy efficiency of the system needs to be considered as well since the purpose of TES systems is to store useful work and not just energy [40]. An energy analysis of latent heat-based TES systems does not reflect the quality of the energy that is stored or released and hence a second law analysis is required [41]. Exergy is the maximum useful work that can be produced by a system as it comes to equilibrium with the surroundings. Since the exergy efficiency (the ratio of exergy output to exergy input) of a system accounts for internal irreversibility, it is often lower when compared to the energy efficiency of the system [42-49].

El-Dessouky and Al-Juwayhel [50] studied the effect the HTF inlet temperature had on the exergy efficiency and showed that the maximum efficiency occurs when the smallest possible temperature difference between the initial PCM temperature and incoming HTF is used during charging. Ramayya and Ramesh [43] studied the effect of sensible heating and sub-cooling on the performance of a shell and tube-based latent heat system. Their results showed that sensible heating improves the efficiency of the melting process, the optimal melting temperature is higher for

systems that include sensible heating and sub-cooling, and that increasing the inlet HTF temperature during discharging increases the efficiency. Recently, Singh et al. [51] reported on the effect of varying inlet temperatures in the exergy performance of graphite foam impregnated with NaCl. They saw a similar trend and concluded that the optimal inlet temperature was 880 °C. In addition to the inlet temperature, the flow rate of the HTF is an important factor toward the performance of a latent heat-based TES system. An increase in the Reynolds (Re) number of a flow increases the required pumping power and the resulting pressure drop across the system leading to higher entropy generation and lower efficiency. However, Erek and Dincer [48] showed the opposite to be true possibly due to the smaller temperature drop seen in the HTF as it spends less time in the system as Re increases, although it should be noted that their analysis did not include the pumping power required in the exergy analysis.

While using multiple PCMs with varying melting temperatures has been shown to improve the energy efficiency of latent heat based TES systems [52-56], only a few investigations have also looked at the exergy efficiency of these systems as well [57-61]. As the HTF decreases in temperature along the streamwise direction in a single-PCM system, multi-PCM systems utilize PCMs with decreasing melting temperatures to improve the performance of the system. Watanabe and Kanzawa [57] showed that the rapid charging and discharging seen in multi-PCM systems leads to high charging, discharging, and overall exergy efficiencies. Domanski and Fellah [60] reported a 40% increase in overall efficiency for a two-PCM system over that of a single-PCM system. Gong and Mujumdar [61] reported similar results that showed a 74% increase for a three-PCM system due to the decrease in the charging and

discharging time of the system. Li et al. [62] studied the use of a two-PCM system for TES using finite-time thermodynamics and showed that an increase between 19-54% in efficiency is possible over that of a single-PCM system. Shabgard at el. [63] examined a cascaded latent heat storage system with gravity-assisted heat pipes and reported that the cascaded system recovered 10% more exergy over a 24 hour cycle compared to the best non-cascaded system considered. Recently, Mosaffa et al. [64] reported on the energy and exergy performance of a multi-PCM system for free cooling applications. Their study showed that higher exergy efficiency was achieved when using multiple PCMs and that decreasing the temperature difference between the HTF and PCM yielded an increase in efficiency with time. While these initial studies are a starting point, there are no reported studies on the exergy performance of EPCM-based latent heat TES systems for high temperature applications.

1.5 Current Objectives

The objective of this research has been two-fold; first to develop a numerical method that can be used to capture the complex multi-phase heat transfer that occurs within EPCM capsules in order to increase the accuracy of the model's ability to analyze the performance of EPCM capsules under real world conditions, and secondly to experimentally evaluate the use of metallic oxides as a new novel material for use as a PCM in high temperature TES applications.

The majority of the numerical investigations that have been conducted previously make assumptions that limit their accuracy. In particular it has been widely established that an internal void space is required within EPCM capsules to prevent rupturing, but it has mostly been ignored in part due to the added numerical

complexity. This causes the current numerical models to fail at accurately predicting the heat transfer within the EPCM capsules under real world operating conditions. This research aims to develop a numerical model that can incorporate not only this void space but also convection in the fluid media as well as volumetric expansion of the PCM upon melting. This model will then be used to study the impact of various void locations on the evolution of the solid-liquid interface within EPCM capsules as well as the performance of a pilot scale EPCM-based heat exchanger. Furthermore, the model can be used to optimize an EPCM-based latent heat TES system on both the energy and exergy performance of single- and multi-PCM systems.

Additionally, the previous experimental investigations into materials that can be used as high temperature PCMs have focused on the use of chloride- and nitrate-based salts. While these materials have yielded promising results, they have low thermal conductivities and are highly corrosive [11]. Metallic oxides offer a novel new choice of material to use as PCMs as they offer higher energy storage densities at comparable melting temperatures while being less reactive with metal-based encapsulation shells. Eutectic materials outside of the glass formation range in the Na_2O-B_2O_3 binary system are considered as potential PCMs for high temperature TES. Laboratory scale EPCM capsules are manufactured and their performance is evaluated by using an immersion calorimeter. As these materials exhibit the ability to form amorphous as well as crystalline materials, characterization of the PCM after thermal cycling is conducted via the use of x-ray diffraction, differential scanning calorimetry, and energy-dispersive x-ray spectroscopy. Successful competition of this

research would further advance the technology of high temperature latent heat-based TES for use at CSP plants leading to cost-competitive electricity generation.

CHAPTER II: NUMERICAL METHODS

Transient two- and three-dimensional simulations of the melting and solidification within EPCM capsules of various geometries and sizes were conducted by employing the appropriate combination of the enthalpy-porosity, volume of fluid (VOF), and turbulence models required for a desired system. The required set of governing equations was discretized in accordance with the finite-volume method and a pressured-based solver was employed within Ansys FLUENT.

2.1 Discretization Methods

The finite-volume method was used to convert the partial differential governing equations into a set of algebraic expressions that can be numerically evaluated. This technique consists of integrating the transport equations about each control volume (or cell) leading to a discrete equation that expresses the conservation law on a control volume basis. This discretization process can be illustrated by considering the unsteady conservation equation for the transport of a scalar quantity ϕ. To demonstrate, the integral form for an arbitrary control volume V is given in equation (1).

$$\int \frac{\partial \rho \phi}{\partial t} dV + \oint \rho \phi \vec{v} \cdot d\vec{A} = \oint \Gamma_\phi \nabla \phi \cdot d\vec{A} + \int_V S_\phi dV \quad \textbf{(1)}$$

where ρ is the density, $\vec{v}$ is the velocity vector, $\vec{A}$ is the surface area vector, Γ_ϕ is the diffusion coefficient, $\nabla\phi$ is the gradient of ϕ, and S_ϕ is a source term. An example control volume for illustration purposes is presented in Figure 3. When equation (1) is discretized it yields equation (2) for any given cell.

$$\frac{\partial \rho \phi}{\partial t} V + \sum_{f}^{N_{faces}} \rho_f \vec{v}_f \phi_f \cdot \vec{A}_f = \sum_{f}^{N_{faces}} \Gamma_\phi \nabla \phi_f \cdot \vec{A}_f + S_\phi V \quad \textbf{(2)}$$

where N_{faces} is the number of faces enclosing the cell, ϕ_f is the value of ϕ convected through face f, $\rho_f \vec{v}_f \cdot \vec{A}_f$ is the mass flux through the face, $\vec{A}_f$ is the area of the face *f*, $\nabla \phi_f$ is the gradient of ϕ at face f, and *V* is the cell volume. Equation (2) contains not only the unknown scalar ϕ at the center of the given cell but also the unknown values from the neighboring surrounding cells and typically this equation is non-linear in nature. Therefore a linearized form can be written as:

$$a_p \phi = \sum_{nb} a_{nb} \phi_{nb} + b \quad \textbf{(3)}$$

where the subscript *nb* refers to the neighbor cells and a_p and a_{nb} are the linearized coefficients for ϕ and ϕ_{nb}. Similar equations are written for each cell in the grid which results in a set of algebraic equations that can be solved with a Gauss-Seidel based linear equation solver.

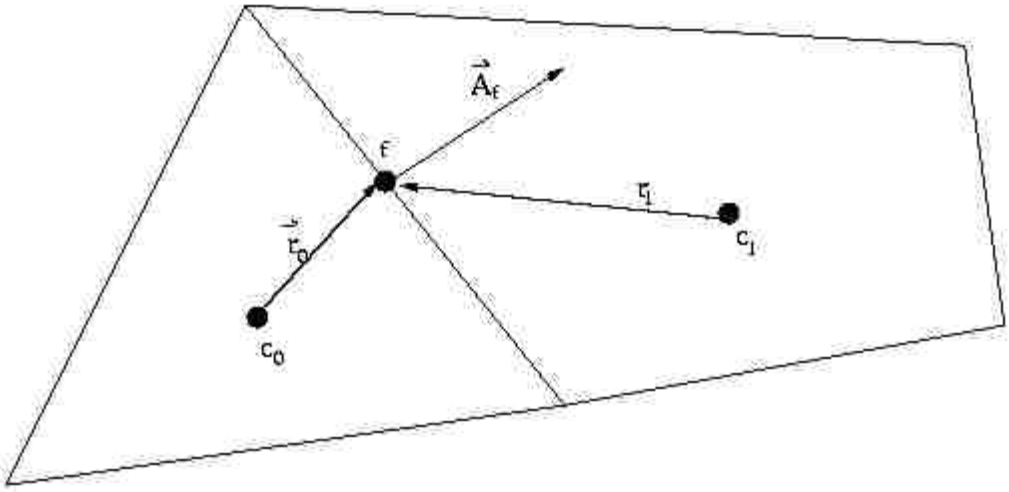

Figure 3. Example computational domain for illustration purposes

FLUENT stores the discrete values of the scalar quantity for the center of a cell; however face values are required for the convection term in equation (2) and therefore must be interpolated from the cell center values. This can be accomplished using an upwind scheme where the face value is derived from quantities in the cell upstream relative to the direction of the normal velocity v_n. Unless otherwise stated, a first-order upwind scheme is used for the spacial discretization of the numerical domain. Using this method, the face value of a cell is determined by assuming that the cell-center values of any field variable represent a cell-average value and therefore hold throughout the entire cell, thus the face values are identical to the cell quantities. Hence, for this scheme ϕ_f is set equal to the cell center value of ϕ for the upstream cell. It should be noted that the diffusion terms in equation (2) are central-differenced and therefore always have a second order accuracy independent of the spacial discretization scheme chosen.

Not only are gradients needed for constructing values of a scalar quantity at the cell faces, they are required for computing the diffusion terms and velocity derivative present in the governing equations. The Green-Gauss theorem is used to compute the gradient of the scalar quantities at the center of the cell via:

$$\left(\nabla\phi\right)_{c0} = \frac{1}{\nu}\sum_{f}\bar{\phi}_f \vec{A}_f \qquad \textbf{(4)}$$

The value of the face centroid ϕ_f is computed using the Green-Gauss cell-based method. For this method the face value in equation (4) is taken as the arithmetic mean of the values at the neighboring cell centers. For the example domain in Figure 3 it can be evaluated using the following equation:

$$\bar{\phi}_f = \frac{\phi_{c0} - \phi_{c1}}{2} \quad \textbf{(5)}$$

The only remaining term to be discretized in equation (2) is the time derivative, $\frac{\partial \rho \phi}{\partial t} V$. Temporal discretization requires the integration of every term in the differential equation by the time step Δt. For example, the temporal evolution of ϕ can be represented by equation (6) where the function $F(\phi)$ incorporates the spacial discretization. The temporal discretization is given by equation (7). The only question that remains is whether to evaluate $F(\phi)$ at the current time step n or the future time step $n+1$. Implicit time integration was used due to its independent stability with respect to the chosen time step. This method evaluates $F(\phi)$ at a future time and therefore the right hand side of equation (7) becomes $F(\phi^{n+1})$. Using an implicit technique, ϕ^{n+1} in any given cell is related to ϕ^{n+1} in the neighboring cells and hence cannot be solved for explicitly at the current time step n. Therefore equation (8) is solved iteratively at each time step until the solution is converged before preceding to the next time step.

$$\frac{\partial \phi}{\partial t} = F(\phi) \quad \textbf{(6)}$$

$$\frac{\phi^{n+1} - \phi^n}{\Delta t} = F(\phi) \quad \textbf{(7)}$$

$$\phi^{n+1} = \phi^n + \Delta t F(\phi^{n+1}) \quad \textbf{(8)}$$

2.2 Flow Solvers

FLUENT allows for the choice between density-based and pressure-based solvers. The only difference between these solvers is the linearization process used to

solve the discretized equations. However, since all of the numerical simulations conducted involve a phase change process, only pressure-based solvers can be used. These pressure-based solvers employ algorithms which belong to a general class of methods called the projection method in which the conservation of mass within the velocity field is achieved by solving a pressure equation [65]. A segregated algorithm is used in which the governing equations are solved sequentially within an iterative loop until convergence is obtained via the process outlined below:

1. Update fluid properties
2. Solve the momentum equations sequentially for *u*, *v*, and *w*
3. Solve the pressure correction (continuity) equation
4. Update face mass fluxes, pressure, and velocity field
5. Solve additional scalar equations (energy and turbulence)
6. Check for convergence

Since the discretized equations are solved in a decoupled manner, convergence is slower than if a coupled algorithm was used; however, the segregated algorithm is more memory-efficient.

For a pressure-based solver, the discretization scheme described above for a scalar transport equation is used to discretize the momentum equation yielding an equation for the *x*-momentum in the form:

$$a_p u = \sum_{nb} a_{nb} u_{nb} + \sum p_f A \cdot \hat{i} + S \qquad \textbf{(9)}$$

where a_p and a_{np} linearized coefficients, p_f is the pressure at the face of the cell, and S is a momentum source term. If the pressure field and mass fluxes were known a priori,

equation (9) could be solved in a similar manner as previously described. However, these are unknown and therefore a pressure interpolation scheme is required. The standard pressure interpolation scheme interpolates the pressure at the faces of a cell using the momentum equation coefficients [66]. For the example domain in Figure 3 this yields:

$$p_f = \frac{\frac{p_{c0}}{a_{p,c0}} + \frac{p_{c1}}{a_{p,c1}}}{\frac{1}{a_{p,c0}} + \frac{1}{a_{p,c1}}} \quad \textbf{(10)}$$

where p_{c0} and p_{c1} are the cell center pressures and $a_{p,c0}$ and $a_{p,c1}$ are the momentum coefficients for the cell center. The above procedure works well provided the pressure variation between cell centers is smooth. When the stand pressure interpolation scheme fails, the pressure staggering option (PRESTO!) scheme can be used. This scheme uses the discrete continuity balance for a staggered control volume to compute the face pressure in a similar manner to the staggered-grid schemes used for structured meshes [67].

Due to the way the continuity and momentum equations are discretized for a pressure-based solver, the pressure and velocity field become coupled. The semi implicit method for pressure linked equations (SIMPLE) algorithm uses a relationship between the velocity and pressure corrections to enforce mass conservation and obtain the pressure field. Alternatively, the pressure-implicit with splitting of operators (PISO) pressure-velocity coupling scheme can be used. It is based on a higher degree approximation of the relation between the corrections for the pressure and velocity field. It incorporates neighbor corrections that increase the stability of the solution

when larger time steps are used. Both the SIMPLE and PISO pressure-velocity coupling schemes were used in the numerical evaluations conducted.

2.3 Enthalpy Porosity Method

In order to model a phase change process, the standard energy conservation equation needs to be modified to include the latent energy released during the phase change. There are two ways to numerically track the evolution of the melting front within a computational domain: either explicitly or indirectly. The most common method is that of the enthalpy-porosity method developed by Voller et al. [26] which indirectly tracks the progression of the solid-liquid interface using a parameter called the liquid fraction, γ. In regards to the enthalpy-porosity method the computational domain is broken down into a solid region, a liquid region, and a mushy zone based on the value of the liquid fraction within a given cell. The liquid fraction is defined as:

$$\gamma = \begin{cases} 0 & T < T_{solidus} \\ \dfrac{T - T_{solidus}}{T_{liquidus} - T_{solidus}} & T_{solidus} < T < T_{liquidus} \\ 1 & T > T_{liquidus} \end{cases} \quad \textbf{(11)}$$

where $T_{solidus}$ and $T_{liquidus}$ are the solidus and liquidus temperatures, respectively, of the material. The difference between the solidus and liquidus temperature defines the size of the mushy zone; for a congruently melting material they are equal. A value of $\gamma = 0$ corresponds to a solid region while a value of $\gamma = 1$ defines a liquid region and a value of $0 < \gamma < 1$ represents the mushy zone. The mushy zone is treated as a "pseudo" porous material by placing a source term in the momentum equation that dampens the velocity to zero as the liquid fraction decreases. Applying the liquid fraction to the

momentum and energy conservation equations for laminar flow yields the following set of governing equations:

$$\frac{\partial}{\partial t}(\rho)+\frac{\partial}{\partial x_i}(\rho u_i)=0 \quad \textbf{(12)}$$

$$\frac{\partial}{\partial t}(\rho u_i)+\frac{\partial}{\partial x_i}(\rho u_j u_i)=\mu\left(\frac{\partial^2 u_i}{\partial x_j \partial x_j}\right)-\frac{\partial p}{\partial x_i}+\rho g_i+\frac{c(1-\gamma)^2}{\gamma^3+\varepsilon}u_i \quad \textbf{(13)}$$

$$H=h_{sref}+\int_{T_{ref}}^{T} c_p dT+\gamma L \quad \textbf{(14)}$$

$$\frac{\partial}{\partial t}(\rho H)+\frac{\partial}{\partial x_i}(\rho u_i H)=\frac{\partial}{\partial x_i}\left(k\frac{\partial T}{\partial x_i}\right) \quad \textbf{(15)}$$

where i ranges from 1 to 3, u_i is the velocity vector, ρ is the density, μ is the viscosity, p is the pressure, g_i is the gravitational acceleration vector, H is the total enthalpy (sensible + latent), k is the thermal conductivity, T is the temperature, h_{sref} is the sensible reference enthalpy, T_{ref} is the reference temperature, c_p is the specific heat capacity, and L is the latent heat of fusion. The last term in equation (13) is the source term added to model the mushy zone. The model constant c corresponds to the amplitude of the damping effect where higher values yield quicker reductions in the velocity. For the numerical investigations carried out, this constant was set to a value of 5×10^6 kg/m^{3}s. Lastly ε is a small computational constant taken to be 0.001 that prevents a singularity when γ=0. Using the finite volume method described above, these equations are discretized and solved iteratively at each node until a convergence of 10^{-3} is reached for the continuity and momentum equations and 10^{-6} for the energy equation.

2.4 Volume of Fluid Method

In order to study the compression of an internal void space resulting from the volumetric expansion of the PCM upon melting, the above set of governing equations for a solid-liquid phase change must be extended to multiple phases. While FLUENT offers three multiphase models only the volume of fluid (VOF) model can be used in conjunction with the enthalpy-porosity based melting and solidification model. The VOF model can be used to model domains that consist of two or more immiscible fluids. The model tracks the volume fraction of each fluid present in the domain and then solves a single momentum and energy equation over the entire domain using volume weighted properties [68-70].

The volume fraction of the n^{th} fluid, α_n, is used to determine the fraction of the n^{th} fluid present within a given cell. When α_n equals zero the given cell is empty of the n^{th} fluid. Similarly, when α_n is 1 the cell is full of the n^{th} fluid. If a cell contains the interface been the n^{th} fluid and one or more other fluids, α_n is between 0 and 1. Tracking on the interface between the fluids or phases is accomplished by solving a modified continuity equation for the volume fraction of n-1 secondary phases, thus replacing equation (12) with

$$\frac{\partial}{\partial t}\left(\alpha_n \rho_n\right) + \frac{\partial}{\partial x_i}\left(\alpha_n \rho_n u_i\right) = 0 \qquad \textbf{(16)}$$

The volume fraction of the primary phase is calculated based on the principal that within a given cell the sum of the volume fraction must be equal to 1 as seen in equation (17). After the volume fraction of each phase is known throughout the entire domain, volume weighted properties are calculated. An example of how these volume-

weighted properties are calculated is given in equation (18) for density. As the energy equation is also shared among the phases, the enthalpy (H) and temperature (T) are taken to be mass-averaged variables given by equation (19). The enthalpy of each phase (H_n) is calculated based on the specific and latent heat of that phase and the shared temperature.

$$\sum_{n=1}^{n} \alpha_n = 1 \tag{17}$$

$$\rho = \sum \alpha_n \rho_n \tag{18}$$

$$H = \frac{\sum_{n=1}^{n} \alpha_n \rho_n H_n}{\sum_{n=1}^{n} \alpha_n \rho_n} \tag{19}$$

Using these weighted properties, equations (13) - (15) are iteratively solved to capture a solid-liquid phase change within a multiphase domain. It should be noted that while these equations are written for laminar flow, the process is the same when a turbulence model is used. A single set of governing transport equations are solved over the entire domain and the turbulence variables, such as the turbulence kinetic energy and specific dissipation rate, are shared by all the phases present.

The governing equations are discretized in the manner described above and both implicit and explicit schemes were used in the calculation of the volume fraction in the various simulations conducted. The first order upwind scheme was used to calculate the face fluxes when implicit VOF was employed. When explicit VOF was used the face fluxes are calculated using either interface reconstruction or finite volume discretization schemes. For the interface reconstruction method the geometric reconstruction approach was employed. When this method is used the standard

interpolation schemes are used in a completely filled cell whereas for cells that contain the interface, the interface is represented using a piecewise-linear approach [68]. When the viscosity between two fluids in the domain is high, the compressive interface capturing scheme for arbitrary meshes (CICSAM) method can be used to ensure convergence. The CICSAM method is a finite volume-based high resolution differencing scheme based on the work of Ubbink [69]. Lastly, for explicit time-dependent VOF calculations, equation (16) is solved using an explicit time-marching scheme where FLUENT automatically refines the time step based on the maximum Courant Number.

2.5 Turbulence Modeling

When the flow around a cylinder is turbulent, the heat transfer coefficient around the capsule is increased, thus turbulence is beneficial in TES systems; however it adds an added level of complexity to the numerical simulations. Reynolds (Re) number is used to determine whether a flow is in the laminar or turbulence regime. Re based on the diameter of the cylindrical EPCM capsules is defined as:

$$\mathrm{Re} = \frac{\rho v D}{\mu} \tag{20}$$

where, ρ is the density of the HTF, v is the superficial velocity, D is the diameter of the capsule, and μ is the viscosity of the HTF. Flow past a cylinder can be considered in transition when Re is greater than 100. For the flow conditions seen at CSP plants it is likely that this will be the case and therefore a turbulence model must be employed.

The choice of a turbulence model depends on the physics of the problem, the level of accuracy required, available computational resources, and the time required to complete a simulation. The difficulty with modeling turbulence is that it occurs over a wide range of length and time scales which increases the computational demand. While a direct numerical simulation (DNS) can be used to fully resolve all of the turbulent length scales and directly solve the Navier-Stokes equations, the computational demand required scales with the cube of Re. Large eddy simulations (LES) reduce the time and length scales that are solved by utilizing low-pass filtering of the Navier-Stokes equations. Therefore by filtering out the smallest time and length scales LES models reduce the computational cost at the expense of some degree of accuracy. The oldest turbulence modeling method is using the Reynolds-averaged Navier-Stokes (RANS) equations. RANS models are able to capture the entire range of turbulent length scales by governing the transport of the average flow quantities. The RANS-based models have the lowest computational requirement and are widely used in engineering applications.

2.5.1 Reynolds Averaged Navier-Stokes

Due to its low computational demand and wide use, a RANS-based turbulence model was chosen. RANS-based models use Reynolds averaging to decompose the instantaneous variables into their time-averaged and fluctuating components. For example the velocity vector u can be defined as the sum of the mean velocity $\bar{u}$ and the fluctuating velocity u', equation (21).

$$u_i = \bar{u}_i + u_i' \tag{21}$$

The same process can be used for the scalar properties like pressure or energy. Therefore the time averaged continuity and momentum equations are written as:

$$\frac{\partial \rho}{\partial t} + \frac{\partial}{\partial x_i}\left(\rho \bar{u}_i\right) = 0 \tag{22}$$

$$\frac{\partial}{\partial t}\left(\rho \bar{u}_i\right) + \frac{\partial}{\partial x_i}\left(\rho \bar{u}_i \bar{u}_j\right) = -\frac{\partial \bar{p}}{\partial x_i} + \frac{\partial}{\partial x_j}\left[\mu\left(\frac{\partial \bar{u}_i}{\partial x_j} + \frac{\partial \bar{u}_j}{\partial x_i} - \frac{2}{3}\delta_{ij}\frac{\partial \bar{u}_i}{\partial x_i}\right)\right] + \frac{\partial}{\partial x_j}\left(-\rho\overline{u_i' u_j'}\right) \tag{23}$$

The above equations have the general form of the instantaneous Navier-Stokes equations only with time averaged variables and additional terms that represent the effects of turbulence; mainly the Reynolds stresses, $-\rho\overline{u_i' u_j'}$, which must be modeled in order to close the problem [71].

2.5.2 k-ω SST Model

In order to close the RANS equations the Reynolds stresses need to be modeled. The Boussinesq hypothesis relates the Reynolds stresses to the mean velocity gradients such that [72]:

$$-\rho\overline{u_i' u_j'} = \tau_{ij} = \mu_t\left(\frac{\partial \bar{u}_i}{\partial x_j} + \frac{\partial \bar{u}_j}{\partial x_i}\right) - \frac{2}{3}\left(\rho k + \mu_t \frac{\partial \bar{u}_k}{\partial x_k}\right)\delta_{ij} \tag{24}$$

where μ_t is the turbulent viscosity and k is the turbulent kinetic energy. The k-ω shear-stress transport (SST) model closes the problem by relating the turbulent viscosity to the turbulence kinetic energy (k) and specific dissipation rate (ω) and solving transport equations for both k and ω.

The major differences between the k-ω and k-ω SST models are a gradual change from the standard k-ω model in the inner region of the boundary layer to a high-Re k-ε model in the outer part and a modified turbulence viscosity formulation to

account for the transport effects of the principal turbulent shear stress. Developed by Menter [73] the *k-ω* SST model blends the accuracy of the *k-ω* model in near-wall regions with the free-stream independence of the *k-ε* model in the far field. The turbulent kinetic energy and specific dissipation rate transport equations are listed in equation (25) and (26) respectively and the turbulent viscosity is defined in equation (27)

$$\frac{\partial}{\partial t}(\rho k)+\frac{\partial}{\partial x_j}\left(\rho k\bar{u}_j\right)=\tau_{ij}\frac{\partial \bar{u}_i}{\partial x_j}+\frac{\partial}{\partial x_j}\left[\left(\mu+\sigma_k\mu_t\right)\frac{\partial k}{\partial x_j}\right]-\rho\beta^* k\omega \tag{25}$$

$$\frac{\partial}{\partial t}(\rho\omega)+\frac{\partial}{\partial x_j}\left(\rho\omega\bar{u}_j\right)=\frac{\partial}{\partial x_j}\left[\left(\mu+\sigma_\omega\mu_t\right)\frac{\partial \omega}{\partial x_j}\right]+\frac{\gamma\rho}{\mu_t}\left(\tau_{ij}\frac{\partial \bar{u}_i}{\partial x_j}\right)-\beta\rho\omega^2+2\left(1-F_1\right)\frac{\rho\sigma_{\omega 2}}{\omega}\frac{\partial k}{\partial x_j}\frac{\partial \omega}{\partial x_j} \tag{26}$$

$$\mu_t=\frac{\rho a_1 k}{max\left(a_1\omega,\Omega F_2\right)} \tag{27}$$

where Ω is the vorticity magnitude (equation (34)) and σ_k, β^*, σ_ω, β, and a_1 are closure constants. Unlike in the standard *k-ω* model, the constants in the *k-ω* SST model are a blend of the *k-ω* and *k-ε* model constants as defined in equation (28) for a constant ϕ. Additional functions are defined in equations (29) to (33) and the model constants are listed in Table 1. The first-order upwind discretization method outlined previously is used to discretize and iteratively solve the turbulence model equations in conjunction with the enthalpy-porosity and VOF methods to solve for both the internal and external heat transfer in an EPCM based latent heat TES system.

$$\phi=F_1\phi_1+\left(1-F_1\right)\phi_2 \tag{28}$$

$$F_1=tanh\left(arg_1^4\right) \tag{29}$$

$$arg_1=min\left[max\left(\frac{\sqrt{k}}{\beta^*\omega d},\frac{500\nu}{d^2\omega}\right),\frac{4\rho\sigma_{\omega 2}k}{CD_{k\omega}d^2}\right] \tag{30}$$

$$CD_{k\omega}=max\left(2\rho\sigma_{\varpi 2}\frac{1}{\omega}\frac{\partial k}{\partial x_j}\frac{\partial \omega}{\partial x_j},10^{-20}\right) \tag{31}$$

$$F_2 = tanh\left(arg_2^2\right) \tag{32}$$

$$arg_2 = max\left(2\frac{\sqrt{k}}{\beta^*\omega d}, \frac{500\nu}{d^2\omega}\right) \tag{33}$$

$$\Omega = \sqrt{2W_{ij}W_{ij}} \tag{34}$$

$$W_{ij} = \frac{1}{2}\left(\frac{\partial \overline{u}_i}{\partial x_j} + \frac{\partial \overline{u}_j}{\partial x_i}\right) \tag{35}$$

Table 1. Model constants employed in the closure of the k-ω SST model

$\gamma_1 = \frac{\beta_1}{\beta^*}\frac{\sigma_{\omega 1}\kappa^2}{\sqrt{\beta^*}}$		$\gamma_2 = \frac{\beta_2}{\beta^*}\frac{\sigma_{\omega 2}\kappa^2}{\sqrt{\beta^*}}$
$\sigma_{k1} = 0.85$	$\sigma_{\omega 1} = 0.5$	$\beta_1 = 0.075$
$\sigma_{k2} = 1.0$	$\sigma_{\omega 2} = 0.856$	$\beta_2 = 0.0828$
$\beta^* = 0.09$	$\kappa = 0.41$	$a_1 = 0.31$

CHAPTER III: CALORIMETRY SYSTEM

In an effort to push TES applications to higher temperatures, additional research into candidate high temperature melting PCMs is required. While it is possible to evaluate the thermal properties of a material using differential scanning calorimetry (DSC) or differential thermal analysis (DTA), these methods do not allow for the study of the compatibility of the PCM with the encapsulation material. Therefore, in an effort to evaluate the performance of the entire EPCM capsule, a specially designed immersion calorimeter was constructed, calibrated, and used for all testing required of the candidate PCMs [10, 20, 21, 24].

3.1 Calorimeter System Design

The calorimetry system that was used consists of a cylindrical metal container with a diameter of 21 cm and a height of 24 cm. The container holds approximately 4.5 kg of silicone oil. In an effort to reduce heat loss from the system to the surroundings, the metal container was insulated using 4 mm polymer foam. To further isolate the system from its surrounds, the insulated container was housed within two 5 mm thick foam board lidded guard boxes. The interior guard box is 30 cm high by 28 cm wide and the exterior guard box is 36 cm high by 36 cm wide. A schematic of the calorimetry system is shown in Figure 4.

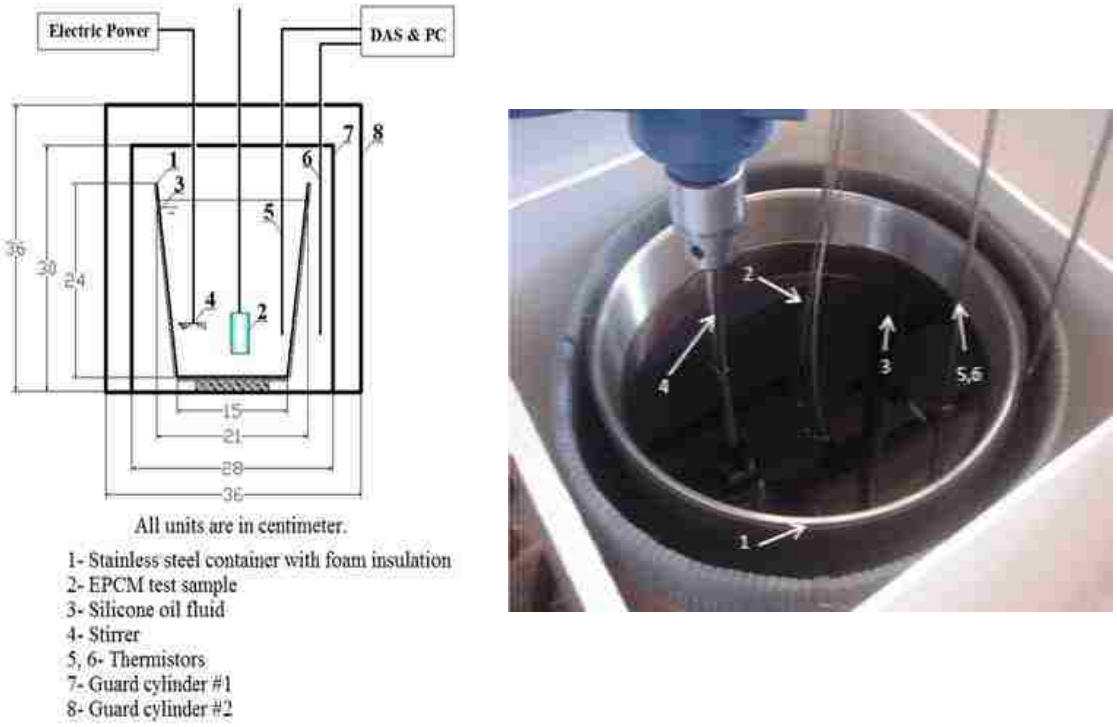

Figure 4. Calorimeter system a schematic (right) and photograph (left)

The mass of silicone oil in the system allows for a suitable temperature increase that ensures the enthalpy transferred to the system from the hot EPCM samples can be measured accurately. If the temperature increase is too small the temperature measurements will not be as accurate, but if the change is too large problems can arise such as the generation of bubbles that result in inaccuracies. It was determined that a mass of approximately 4.5 kg would be sufficient to yield desirable results [10, 21, 24]. Dynalene 600 was chosen as the silicone oil for use due to its relatively high flash point (315 °C), its low vapor pressure (333 Pa), and its favorable thermal conductivity (0.156 W/mK) [74]. The thermal conductivity helps to ensure a uniform temperature distribution within the system whereas the low vapor pressure

reduces energy loss caused by nucleation of the silicone oil when the hot sample is submerged.

In order to ensure there was a uniform temperature distribution within the calorimeter system, an electric mixer was used throughout the duration of the experiment. The temperature of the calorimeter is taken to be the temperature of the silicone oil and was measured using a thermistor. In order to determine the amount of heat lost from the system, the ambient air temperature was measured between the metal container and the first guard box. As laboratory conditions and final sample temperature differ with each experiment, the heat loss from the system varies and was therefore calculated for each individual experiment. In order to suspend the EPCM sample in the calorimeter and avoid heat loss through conduction to the container, a wire rod was welded to the top of each sample.

3.2 Experimental Procedure

Prior to each experiment, the mass of the silicone oil was measured as losses occur when the sample is removed at the conclusion of the experiment. These losses are on the order of a few grams. Additionally, the samples were weighed to ensure that leakage of the PCM had not occurred during the experiment. To begin the experiment, the samples were heated from room temperature to approximately 50 degrees above the material's melting temperature, and then held at that temperature for 2 hours to ensure a uniform temperature within the sample and complete melting of the PCM. In an effort to promote uniform heat transfer, the sample was either covered with an insulating fiber mat or placed within a carbon steel cylinder, Figure 5. The temperature

of the sample was measured during the heating process by securing three thermocouples around the sample using copper wire, as seen in Figure 6.

Figure 5. Sample placed in carbon steel cylinder during heating process

Figure 6. Thermocouples used to measure sample temperature secured with copper wire

After being held at the desired temperature, the charged sample is quickly submerged into the calorimeter in an effort to reduce heat loss. Once the sample is submerged, the lids are placed on the guard boxes and any remaining gaps are sealed using additional pieces of foam board and weights. An example of the temperatures recorded during the length of an experiment are shown in Figure 7. While the

temperature of the calorimeter and air are measured over the entire experiment, the temperature of the sample is only recorded during the heating phase. A typical heating phase has a duration of approximately 3 hours, whereas the cooling phase is completed after 2 hours. In Figure 7, after 9,000 sec the sample was submerged in the calorimeter, at which point its temperature began to increase.

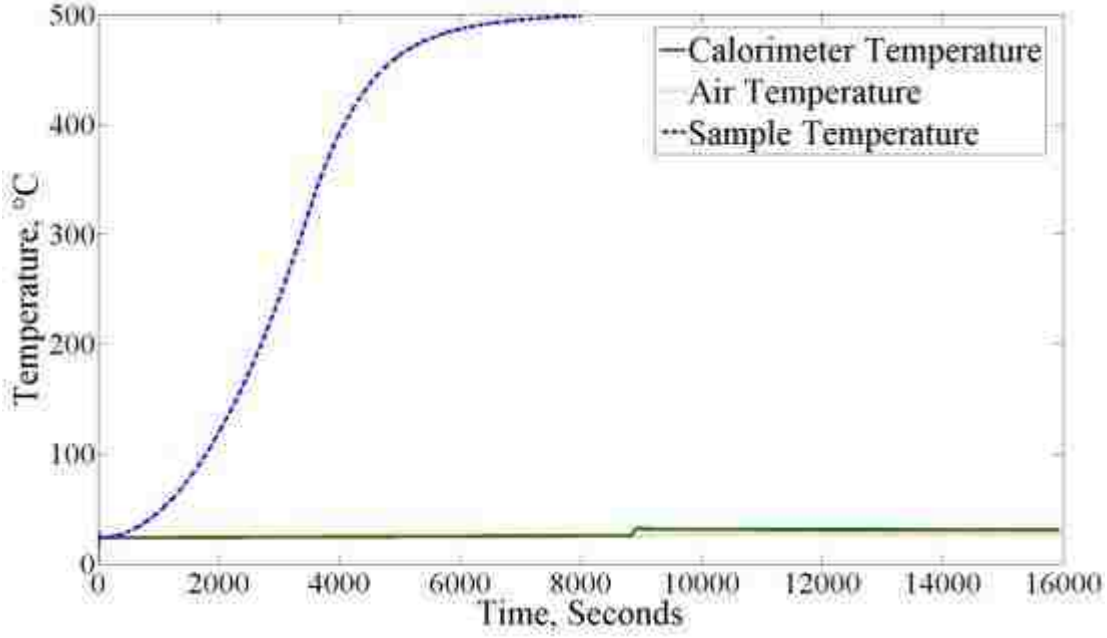

Figure 7. Calorimeter, air, and sample temperature over the course of an experiment

The increase in temperature of the calorimeter system is more readily seen in Figure 8. As soon as the sample is submerged in the calorimeter, it begins to transfer its stored thermal energy, increasing the system's temperature. After a period of time the sample and calorimeter will have reached equilibrium. This is called the equilibrium time, t_e. The time it takes the system to reach equilibrium is dependent on the sample size, the material being tested, the final temperature of the sample, and the initial temperature of the calorimeter. In an effort to ensure that the sample and calorimeter have reached equilibrium, only the last 3,000 sec of the cooling process

are used. Once equilibrium has been reached, the temperature of the sample and calorimeter decreases slowly due to heat lost to the environment. The rate at which heat is lost from the system is related to the rate of the temperature decrease. Therefore, the amount of heat lost from the system can be calculated and the theoretical equilibrium temperature can be determined. Using this zero loss equilibrium temperature and the initial calorimeter temperature, the amount of energy transferred to the system from the sample is calculated. This value is then compared to the theoretical energy stored in the sample during heating based on the material's properties.

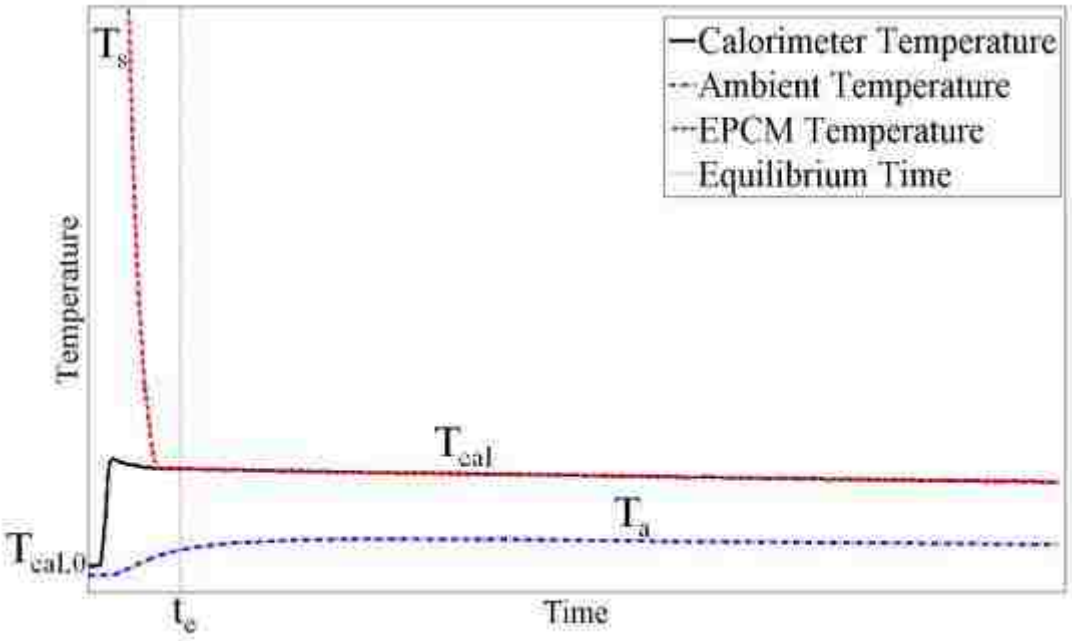

Figure 8. Temperature measurements during a typical calorimetry experiment [20]

3.3 Energy Analysis

The temperature data recorded during each experiment was input into MATLAB in order to calculate the heat loss and equilibrium temperature, as well as the energy transferred to the calorimeter, the energy stored in the sample, and the

discrepancy between them [20, 21, 24]. The equations governing the conservation of energy for the calorimetry system are:

$$\dot{Q}_{net} = \left[m_{cal} c_{p,cal} \frac{dT_{cal}}{dt} + m_{PCM} c_{p,PCM} \frac{dT_{cal}}{dt} + m_{cap} c_{p,cap} \frac{dT_{cal}}{dt} \right]_{after\_t_e} = -hA(T_{cal} - T_a) + \dot{Q}_{mixer} \quad \textbf{(36)}$$

$$Q_{loss} = \int_{t_0}^{t} \dot{Q}_{net}\, dt = \int_{t_0}^{t} [-hA(T_{cal} - T_a) + \dot{Q}_{mixer}]dt \quad \textbf{(37)}$$

$$Q_{EPCM,EXP} = Q_{cal} - Q_{loss} \quad \textbf{(38)}$$

$$Q_{cal} = m_{cal} c_{p,cal} \left(T_{cal} - T_{cal,0} \right) \quad \textbf{(39)}$$

$$Q_{EPCM,theo} = Q_{cap} + Q_{PCM} \quad \textbf{(40)}$$

$$Q_{cap} = m_{cap} \int_{T_{cal}}^{T_{s,0}} c_{p,cap} dT \quad \textbf{(41)}$$

$$Q_{PCM} = m_{pcm} c_p^l (T_{s,0} - T_m) + m_{pcm} L + m_{pcm} c_p^s (T_m - T_{cal}) \quad \textbf{(42)}$$

where m_{cal} is the mass of calorimeter; $c_{p,cal}$ is the effective heat capacity of the calorimeter; T_{cal} is the temperature of the calorimeter; $T_{cal,0}$ is the initial calorimeter temperature; m_{cap} is the mass of the capsule; $c_{p,cap}$ is the heat capacity of the capsule; m_{PCM} is the mass of the PCM; $c_{p,PCM}^s$ is the solid heat capacity of the PCM; $c_{p,PCM}^l$ is the liquid heat capacity of the PCM; L is the latent heat of the PCM; $T_{s,0}$ is the initial sample temperature; T_a is the air temperature; and T_m is the melting temperature of the PCM.

In order to calculate both the theoretical energy stored by the EPCM sample (Q_{EPCM_theo}) and the energy transferred to the calorimetry system (Q_{EPCM_EXP}), the theoretical equilibrium temperature of the system (calorimeter and cooled sample) is required. However, in order to find the theoretical equilibrium temperature, the heat lost (Q_{loss}) from the system during the experiment is needed. Due to variations in

experimental conditions, the heat loss must be calculated for each experiment individually. This is accomplished by using the rate at which the temperature of the system decreased over the last 3,000 sec of the experiments.

However, the rate at which heat is lost from the calorimeter requires a transient heat transfer analysis. While there are several ways to solve a transient heat transfer problem, the simplest is the method of lumped capacitance. Lumped capacitance assumes that the temperature difference inside the substance is negligible. This can be expected in our system due the moderate thermal conductivity of the silicone oil and the presence of the electric mixer. A uniform temperature distribution within the system is verified using several thermal couples placed at various heights and radii during a cooling period [20, 21, 24]. Therefore, the temperature of the calorimeter at any time after the equilibrium time is represented by the following equation:

$$T_{cal} = (T_{cal,0} - T_a)\exp\left[\frac{-hA}{m_{so}c_p}t\right] + T_{cal,0} = a_1 \exp\left[\frac{-a_2}{m_{so}c_p}t\right] + a_3 \quad \textbf{(43)}$$

where $T_{cal,0}$ is the initial calorimeter temperature, T_a is the air temperature, h is the heat transfer coefficient, A is the surface area of the calorimeter, m_{so} is the mass of the silicone oil, c_p is the effective heat capacity of the system, and t is the time at which the temperature is desired. While some of the constants in equation (43) are unknown, they can be determined by curve fitting the recorded temperature of the calorimeter over the course of the experiment. Then, by differentiating the equation found for temperature, the total heat loss rate in the system, including the now-cooled EPCM sample, is determined by using the following equation:

$$\dot{Q}_{net} = (m_{PCM} c^{s}_{p,PCM} + m_{cap} c_{p,cap} + m_{cal} c_{p,cal}) \times \left[\left(\frac{-a_2}{mc_p} \right) \left(a_1 \exp\left(\frac{-a_2}{mc_p} \right) * t \right) \right] \quad \textbf{(44)}$$

Additionally, as seen in equation (37), $\dot{Q}_{net}$ is also equal to the rate of heat lost from the system to the surroundings through convection plus the heat input to the calorimeter by the mixer. By plotting the heat rate determined from equation (44) versus the difference in temperature between the calorimeter and the surrounding air, the two unknown coefficients in equation (37), hA and $\dot{Q}_{mixer}$, are determined. Knowing these coefficients, the cumulative heat loss from the calorimeter (Q_{loss}) at any time is calculated by integrating $\dot{Q}_{net}$ from the initial time the sample was submerged in the system, t_0, to any subsequent time t later.

After the heat loss has been determined, the theoretical equilibrium temperature of the system at any time after the equilibrium time can be determined using equation (45).

$$T_{theo} = \frac{\left(m_{cal} c_{p,cal} + m_{PCM} c^{s}_{p,PCM} + m_{cap} c_{p,cap} \right) \times T + Q_{loss}}{\left(m_{cal} c_{p,cal} + m_{PCM} c^{s}_{p,PCM} + m_{cap} c_{p,cap} \right)} \quad \textbf{(45)}$$

The temperature T in the above equation is calculated by using equation (43). The theoretical temperature was then used as T_{cal} in equations (38) - (42) to calculate the theoretical and experimental enthalpies.

In addition to the heat loss, the effective heat capacity of the calorimeter is required. The heat capacity of the calorimetry system cannot simply be taken as that of the silicone oil alone because it only accounts for 83% of the mass of the system. The other 17% is made up of the metal container (0.6kg), the foam insulation (0.242kg),

and the mixer blade (0.0966kg). These three components each have their own heat capacity and contribute to the calorimeter's storage ability.

Therefore, the heat capacity of the calorimeter system was determined via calibration using two solid standard stainless steel 304 samples that were heated to various temperatures. The dimensions and masses of these samples are listed in Table 2. Stainless steel 304 was chosen because of its well-documented thermal properties and high melting point, thus allowing for the samples to store only sensible heat over a wide range of temperatures. The thermal properties of stainless steel are listed in Table 3 [75]. Due to the variation of the specific heat over the applied temperature range, integration was applied to calculate the energy stored in the stainless steel samples. The results of the calibration tests, depicted in Figure 9, were well represented by the following equation, in the operational range of 25-60 $^{\circ}$C

$$c_{p,cal} = 2.5297 \times T_{cal} + 1312.6 \quad \textbf{(46)}$$

where $c_{p,\,cal}$ is the effective heat capacity of the entire calorimeter system in J/kg K and T_{cal} is the calorimeter temperature in $^{\circ}$C.

Table 2. Specifications of stainless steel calibration samples

	Mass of Sample (g)	Size (Diameter × Height)
Sample 1	834.3	3.81 cm × 10.16 cm
Sample 2	185.1	2.53 cm × 4.64 cm

Table 3. Thermal properties of stainless steel 304 [75]

Melting Point ($^{\circ}$C)	Heat Capacity (J/kg K)						
1397	300 K	400 K	600 K	800 K	1000 K	1200 K	1500K
	477	515	557	582	611	640	682

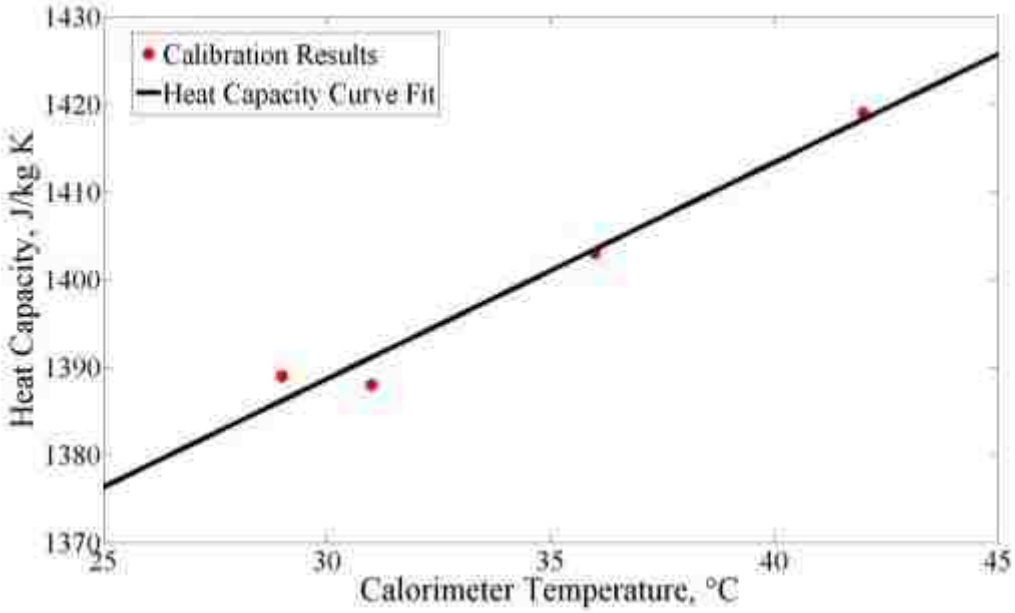

Figure 9. Calibration results (R^2=0.97) [20]

3.4 System Verification

After calibration of the effective heat capacity of the system was completed, the overall performance of the calorimeter was determined by performing several verification tests. The calorimeter's ability to accurately measure sensible heat and latent heat was determined by calculating the energy stored in the two stainless steel samples used for calibration and an aluminum sample that contained 42.45 g of aluminum by using the experimental procedure describe above. The discrepancy between the theoretical and experimental enthalpies was calculated using the following equation;

$$\%Discrepancy = \frac{Q_{EPCM,theo} - Q_{EPCM,\exp}}{Q_{EPCM,theo}} \times 100 \quad \textbf{(47)}$$

A positive discrepancy indicates that less energy was transferred to the calorimeter than predicted based on material properties. Conversely, a negative discrepancy means that more energy was transferred to the calorimeter than theoretically stored in the

sample. Due to inaccuracies in the measurements of temperature both positive and negative discrepancies can occur.

The results of the verification tests for both sensible and latent heat storage are tabulated in Table 4. It can be seen that the energy balance between the theoretical and experimental energy storage was satisfied with less than ±2% discrepancy, lending confidence to both the experimental method and calorimetry measurements used to determine the performance of candidate PCMs.

Table 4. Results of verification testing

Sample	Charged Temperature	Theoretical Equilibrium Temperature	Theoretical Energy Stored	Measured Energy Stored	Discrepancy
Stainless Steel #1	256 °C	37.7 °C	94.1 kJ	94.7 kJ	-0.64 %
Stainless Steel #1	390 °C	46.1 °C	153.0 kJ	152.6 kJ	0.26 %
Stainless Steel #2	480 °C	31.7 °C	44.8 kJ	44.5 kJ	0.70 %
Stainless Steel #1	555 °C	56.7 °C	228.0 kJ	227.4 kJ	0.26 %
Aluminum #1	720 °C	32.2 °C	76.1 kJ	74.6 kJ	1.9 %
Aluminum #1	700 °C	33.0 °C	74.7 kJ	76.0 kJ	-1.7 %

3.5 Summary

A conventional immersion calorimeter was specially designed for use in the testing of candidate PCMs for use in high temperature TES at CSP plants. The designed system consisted of an insulated container of approximately 4.5 kg of silicone oil that was further insulated using foam board boxes. The effective heat

capacity of the calorimeter was determined through calibration by using standard stainless steel samples in the temperature range of 25-60 $^{\circ}$C. The results of calibration showed that 90% of the effective heat capacity of the system was from the silicone oil.

Additionally, using the stainless steel samples and an aluminum EPCM sample, the accuracy of the calorimeter measurements for both sensible heat and latent heat was evaluated by performing an energy balance analysis between the theoretical storage capability of each sample and the experimentally measured value. Additional details on the use of aluminum as a PCM were presented by Zhao [21] and Solomon [20]. From the results of the verification tests, it was determined that the overall accuracy of the designed calorimeter was ±2%. These results make not only the calorimeter's ability to measure the thermal energy stored in an EPCM sample credible but also the experimental method used.

CHAPTER IV: CALORIMETRY SIMULATIONS

In an effort to validate the use of the enthalpy-porosity and VOF methods' ability to accurately capture the heat transfer within EPCM capsules, simulations of the laboratory-scale calorimetry experiments were conducted.

4.1 Calorimetry Simulation Set Up

Two-dimensional axisymmetric numerical simulations were conducted to gain a greater understanding of the heat transfer that occurs both within the EPCM capsules and in the calorimeter. A schematic of the experimental setup is presented in Figure 4 and the computational domain considered is shown in Figure 10. A detailed description of the calorimetry system is presented in section 3.1. The main component of the system is the 4.5 kg of Dynalene 600 silicone oil. The temperature of the calorimeter was measured throughout the entire experiment using thermistors, and in order to ensure a uniform temperature distribution within the system an electric mixer was used. The EPCM capsules used for the laboratory scale testing have a diameter of 2.54 cm and a height of 5.08 cm with a 1.5875 mm thick stainless steel capsules shell. A 20-30% approximate void space was left within the capsules to allow for the thermal expansion of the PCM upon melting and ensure the capsules do not rupture.

Two sodium chloride (NaCl) and thee aluminum (Al) EPCM capsules were experimentally tested to evaluate their performance as PCMs for use in high temperature TES applications. The experimental results were reported by Solomon [20] and Zhao [21] and showed that while NaCl showed no deterioration of storage capacity after prolonged thermal cycling, the Al capsules showed a significant loss of storage capacity. The simulations were conducted using the experimental data from

the third cycle for the third Al sample and for the second cycle for the first NaCl sample after 1,000 hours of high temperature exposure. The relevant thermal properties used in the simulations are listed in Table 5.

Table 5 Physical properties of air, stainless steel, calorimeter, aluminum and sodium chloride used in the calorimetry simulations

Air		**Aluminum**	
Specific Heat Capacity (J/kg °C)	1,006 [75]	Density (kg/m^3)	$2855.8 - 0.5126T \quad 300 < T < 973$ $2614.8 - 0.0265T \quad 973 < T < 1200$ [76]
Thermal Conductivity (W/m K)	0.0242 [75]	Solid Specific Heat Capacity (J/kg °C)	903 [77]
Viscosity (kg/m s)	1.79×10-5 [75]	Liquid Specific Heat Capacity (J/kg °C)	1177 [77]
Stainless Steel 304		Viscosity (kg/m s)	0.0012 [76]
Density (kg/m^3)	7,900 [75]	Thermal Conductivity (W/m K)	237 [76]
Specific Heat Capacity (J/kg °C)	477	Latent Heat (kJ/kg)	397.3 [77]
Thermal Conductivity (W/m K)	14.7 [75]	**Sodium Chloride**	
Calorimeter		Density (kg/m^3)	2137.9 – 0.5418×T [78]
Density (kg/m^3)	1252.6 – 0.9983×T [74]	Solid Specific Heat Capacity (J/kg °C)	931 [78]
Specific Heat Capacity (J/kg °C)	2.47×T + 640.13 [10, 19]	Liquid Specific Heat Capacity (J/kg °C)	1215 [78]
Viscosity (kg/m s)	0.0486	Thermal Conductivity (W/m K)	0.5
Thermal Conductivity (W/m K)	0.147	Viscosity (kg/m s)	0.001008 [78]
		Latent Heat (kJ/kg)	430 [78]

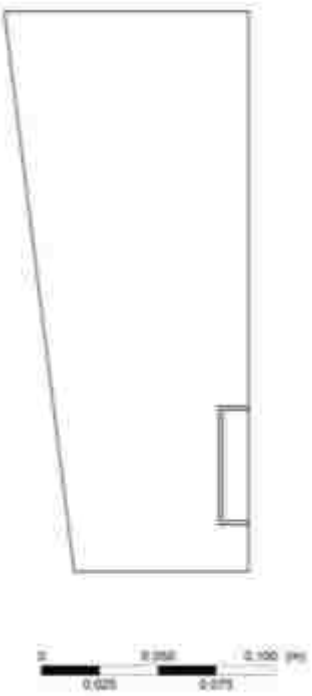

Figure 10. Computational domain used for calorimetry simulations

4.2 Internal Heat Transfer Results

When the hot EPCM samples are submerged within the calorimeter they begin to transfer their stored energy to the silicone oil and the PCM begins to rapidly solidify. The PCM begins to solidify along the side and bottom of the capsule, Figure 11a. Since the solidification process is conduction-dominated, the solid-liquid interface slowly propagates radially inwards and the ever-increasing solid layer has a limiting effect on the heat transfer within the capsule, Figure 11b. As the PCM cools it contracts however the solidified PCM sticks to the capsule surface at the expanded height; therefore as the air void expands it forms a "V"-shaped depression in the center of the capsule, Figure 11c and d. The upward increase in the solid seen in Figure 11 is a byproduct of the way the density of the PCM is modeled and it flattens over the course of the simulation.

A photograph of a sectioned magnesium chloride ($MgCl_2$) sample [19] after experimentation is shown in Figure 11e. There is a strong visual agreement in the final shape of the solid PCM from both the simulation and experimental capsule. The bottom of the dip is 1.4 cm above the bottom of the capsule compared to 1.7 cm in the experimental capsule. The thickness of the solid layer at the top of the dip is 0.6 cm in both cases. Ideally, a comparison would be made using the NaCl capsules but regretfully a photo of the sectioned capsule was not taken. However, NaCl and $MgCl_2$ have similar thermal conductivities (~5 W/mK) and thermal expansion coefficients (~3×10^{-4}/K), therefore a similar dip would form within both EPCM capsules. It takes 165 sec for the NaCl capsule to solidify completely. A similar evolution of the solid-liquid interface is seen within the aluminum capsule and it has a total solidification time of 35 sec due to its vastly higher thermal conductivity compared to that of NaCl.

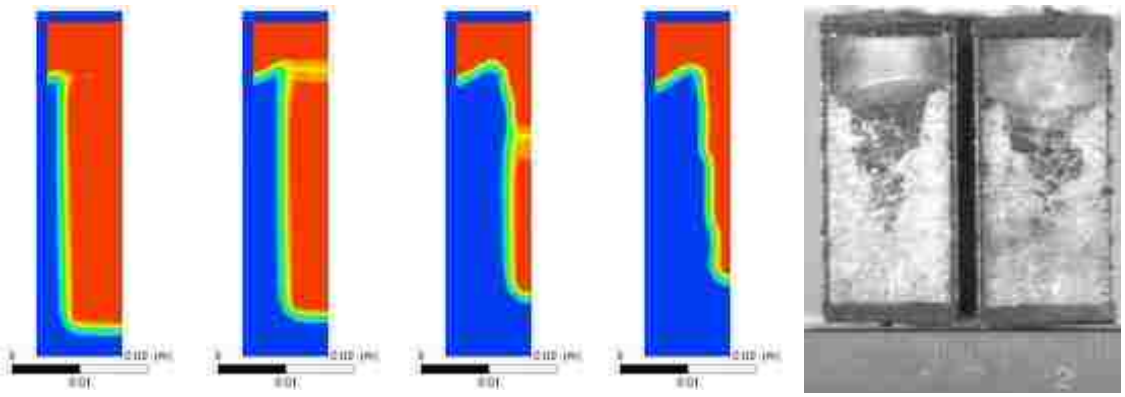

a) Liquid Fraction @ 30 sec (SteFo=0.078) | b) Liquid Fraction @ 60 sec (SteFo=0.155) | c) Liquid Fraction @ 120 sec (SteFo=0.310) | d) Liquid Fraction @ 200 sec (SteFo=0.517) | e) Sectioned $MgCl_2$ Capsule [19]

Figure 11. Evolution of the solid–liquid interface in the NaCl capsule (a-d) and sectioned $MgCl_2$ sample [19]

4.3 External Heat Transfer Results

Once the EPCM sample is immersed in the calorimeter, there is a rapid increase in the temperature of the system before the system slowly approaches equilibrium. After the EPCM capsule is submerged in the system, a large thermal gradient forms in the silicone oil directly above the EPCM sample, Figure 12a. This results in the formation of a large vortex above the sample due to convection in the oil, Figure 12f. There are also two small vortices forming in the air gap at the top of the system as the air is heated as well as a vortex around the outside of the EPCM capsule. As the sample continues to cool, a thermal gradient has formed within the silicone oil, Figure 12b. Additionally, the strength of the vortex above the EPCM sample is decreasing as after 300 sec the EPCM sample has released the majority of its stored energy, Figure 12g. After 1800 sec the EPCM sample has transferred all of its stored energy to the calorimeter and now has the same temperature as the surrounding silicone oil, Figure 12c. From this point forward, the temperature gradient within the system slowly decreases towards equilibrium, Figure 12d and e. Furthermore, there is no convection present in the system after the sample has given up all of its stored energy except for two weak recirculating vortices present in the air gap near the edge of the system, Figure 12h-j. A similar temperature evolution is seen within the calorimeter system for the NaCl simulation and therefore the results are not pictured here.

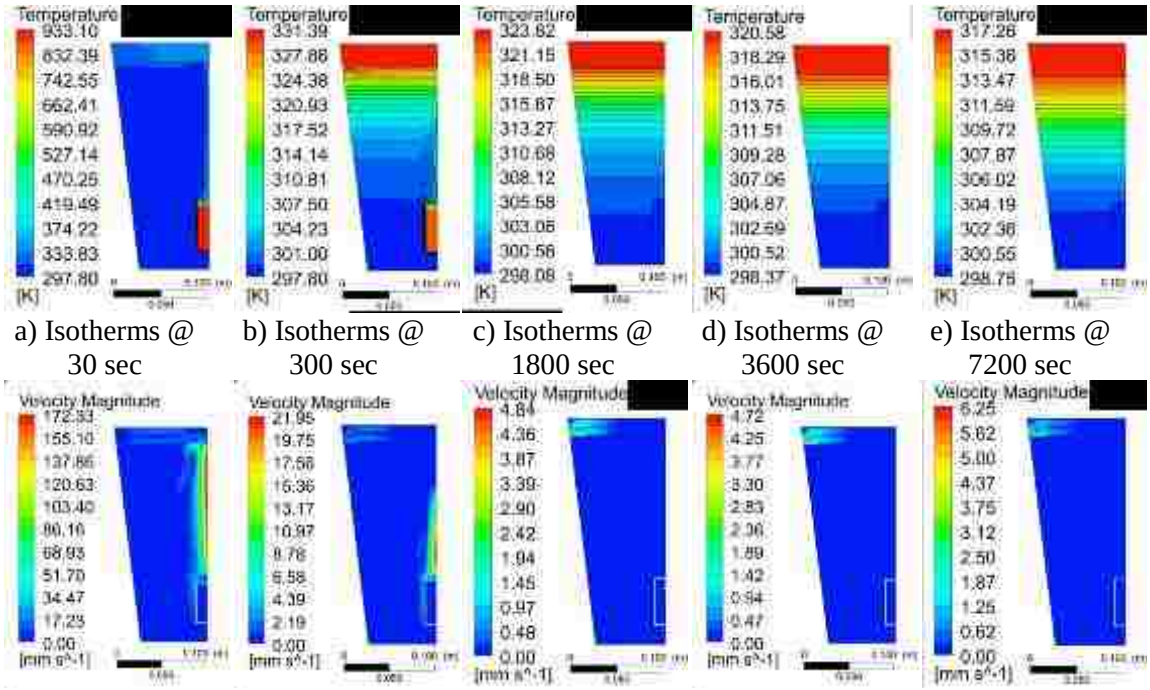

a) Isotherms @ 30 sec | b) Isotherms @ 300 sec | c) Isotherms @ 1800 sec | d) Isotherms @ 3600 sec | e) Isotherms @ 7200 sec

f) Velocity @ 30 sec | g)Velocity @ 300 s | h) Velocity @ 1800 s | i) Velocity @ 3600 s | j) Velocity @ 7200 s

Figure 12. Isotherms (a-e) and velocity magnitude (f-j) for the aluminum sample 3 cycle 3 simulation at various times

An electric mixer is used during the duration of the experiments to ensure there is a uniform temperature present throughout the entire calorimeter system; however due to the added computational demand it was neglected leading the simulations to predict a large temperature gradient within the system. Therefore, in order to compare the predicted temperatures with the experimentally recorded values, a volume-weighted average temperature is calculated at various discrete time steps. The results are shown in Figure 13 along with the raw experimental data. Good agreement is obtained during the initial rapid temperature increase. After 200 sec however, the experimental temperature begins to decrease due to heat lost to the environment. After the heat loss has been accounted for, the experimental equilibrium temperature that the sample and calorimeter would have reached under ideal conditions is calculated. For

the third cycle of the third aluminum sample experiment the theoretical equilibrium temperature was 308 K, shown by the dashed red line in Figure 13. The simulations predicted a value of 307 K which is a less than 1% difference from the experimental value, shown by the green dash-dot line in Figure 13. Good agreement is also seen between the experimental and predicted equilibrium temperature for the NaCl case with values of 307 K and 308 K respectively.

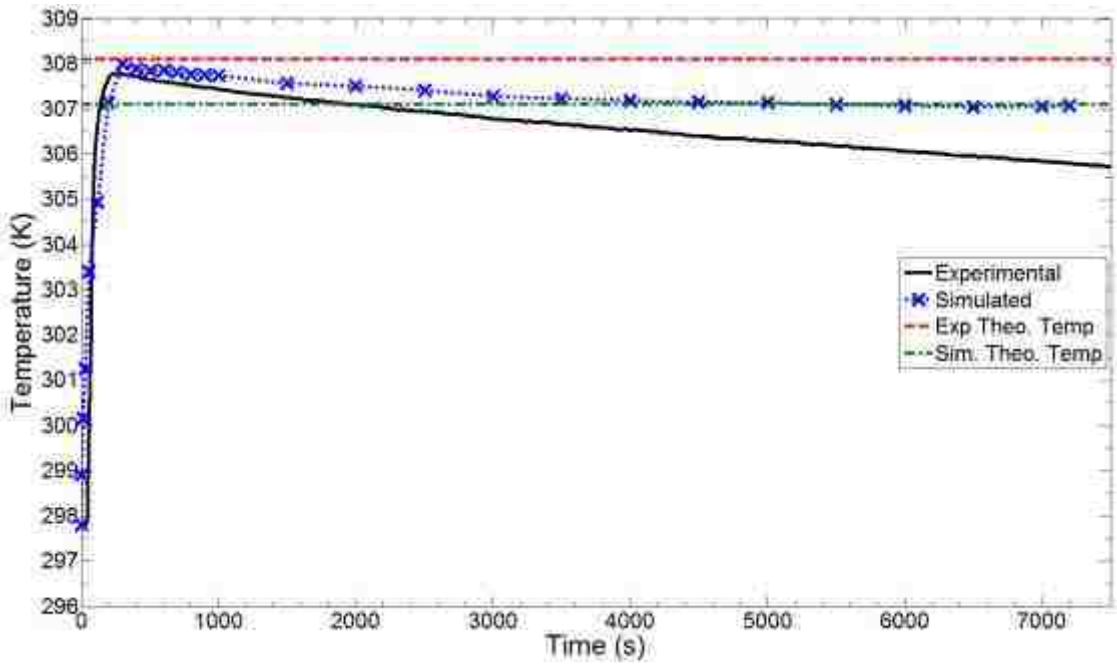

Figure 13. Experimental temperature, predicted volume averaged temperature, and theoretical equilibrium temperature for aluminum sample 3 cycle 3

The agreement between the experimental and predicted temperatures along with the final shape of the solid-liquid interface demonstrate that the numerical methods employed are capable of accurately capturing the complex multiphase heat transfer that occurs both within the EPCM capsules and the calorimetry system. A combination of the enthalpy-porosity and VOF methods have been used to study the characteristics of high temperature PCMs in literature [36, 39, 79, 80]; however the

method was validated for low temperature PCMs only. The results presented here extend the validation of the methods used to higher temperatures and lend further credence to the experimental methods used.

4.4 Conclusions

A numerical model of the calorimetry system used to experimentally evaluate the energy storage capability of potential PCMs for high temperature TES was developed. This model lends insight into the complex heat transfer that occurs during the conducted experiments. The impact of the thermal conductivity of a PCM is emphasized by the vastly shorter solidification time for the Al capsule compared to the NaCl. The final shape of the solid NaCl predicted by the simulation matched that seen in a sectioned $MgCl_2$ capsule, demonstrating the ability of the model to capture the contraction of the PCM upon solidification and expansion of the void space within the capsule. Additionally, the difference between the experimental and predicted equilibrium temperatures was under 1% and good agreement was seen during the initial temperature increase of the system. Therefore the model is also accurately capturing the heat transfer in the calorimeter in addition to the heat transfer within the EPCM capsule. Thus the enthalpy-porosity and VOF methods can be used simultaneously to further investigate the behavior of EPCM capsules used for high temperature TES applications.

CHAPTER V: SPHERICAL EPCM CAPSULES

To examine the effect that an internal void has on the heat transfer within an EPCM capsule, a three-dimensional simulation of a 22 mm diameter sphere with a 1 mm thick shell was conducted using $NaNO_3$ as the PCM and stainless steel as the encapsulation material. Air is considered as the void material and is modeled as an ideal gas. The thermal properties of $NaNO_3$, air, and stainless steel are listed in Table 6. The melting point of $NaNO_3$ is 308 °C. The properties of $NaNO_3$ at the desired temperatures are not precisely known as there is a wide range reported in literature [81]; therefore the properties used were determined experimentally by Zheng et al. [10]. The size of the internal void is dependent on the coefficient of thermal expansion of the PCM which for $NaNO_3$ is 4.0×10^{-4} 1/K. Therefore, an air void of approximately 20% is considered at the top of the capsules. A constant temperature boundary condition was applied to the surface of the capsule. For the melting process the capsules had an initial temperature of 523 K and the surface temperature was set to 750 K. The temperatures are reversed for the solidification process. The enthalpy-porosity and VOF methods were employed simultaneously to solve for the heat transfer within the capsule while considering convection in the fluid media and expansion of the PCM upon melting.

Table 6. Physical properties of $NaNO_3$, stainless steel, and air

	Density (kg/m^3)	Thermal conductivity (W/m·K)	Specific Heat (J/kg·K)	Viscosity (kg/m.s)	Latent Heat (kJ/kg)
Solid $NaNO_3$	2,260[81]	0.5 [78]	1,588 [10]	---	162.5 [10]
Liquid $NaNO_3$	1,900 [78]	0.5 [78]	1,650 [10]	2.85×10^{-3} [78]	
Stainless Steel	7900 [75]	14.9[75]	477 [10]	---	---
Air	Ideal Gas	0.0242 [75]	1,006 [75]	1.79×10^{-5} [75]	---

5.1 Mesh Independence

The use of the enthalpy-porosity and VOF methods, described in Chapter II, to capture the complex heat transfer within EPCM capsules has been previously validated in literature [34-36, 79] using experimental results and in Chapter IV. Both mesh independence and time step independence were tested for a 25.4 mm capsule with a 773 K constant surface temperature and 523 K initial capsule temperature. Mesh refinement was tested by using three meshes with a decreasing nominal cell size that resulted in meshes with 2290, 4276, and 8736 uniformly distributed nodes. The results are presented in Figure 14 where blue is the remaining solid region and red is the molten PCM. The overall shape of the remaining solid is the same in all three cases with the only difference being the refinement of the mushy zone. Furthermore, the total melting time for all three cases was the same; 49.5 sec (SteFo=0.05) using a time step of 0.02 sec. The Stefan and Fourier numbers are defined in equations (48) and (49) respectively in the next section. Using a mesh with 4276 nodes, the time step independence was tested using time steps of 0.01, 0.02, and 0.03 sec. The results showed insignificant differences and thus a time step of 0.01 sec was chosen to carry

out the calculations. A similar process was carried out for the spherical EPCM capsule and a tetrahedral mesh with a max cell size of 6×10^{-4} m was chosen yielding a total of 15,376 nodes.

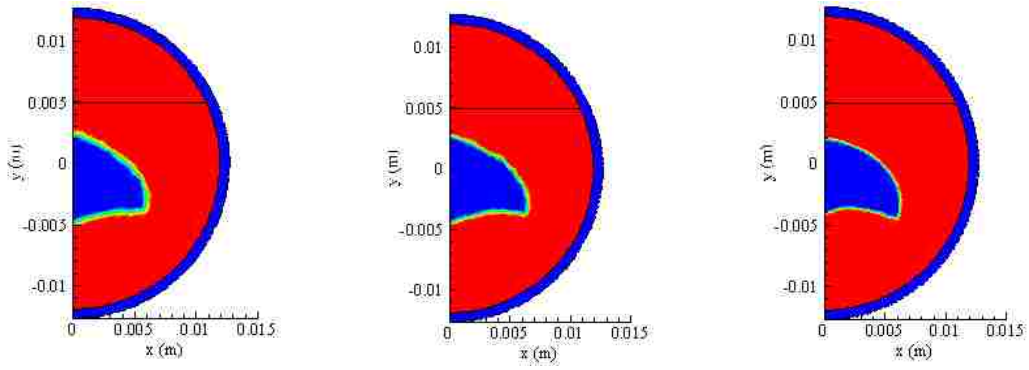

a) 2290 nodes b) 4276 nodes c) 8736 nodes

Figure 14. The location of the liquid/solid interface with 20% void for various mesh sizes

5.2 Melting of Spherical EPCM Capsules

Due to symmetry about the Y-axis, the heat transfer in the XY and YZ planes are identical and therefore, only the results for the XY plane are shown. However, the presence of the void at the top of the capsule removes the symmetry about the X-axis that would result from a uniformly heated capsule. The isotherms, velocity magnitude, liquid fraction, and specific heat capacity 5 sec into the melting process are shown in Figure 15. The specific heat capacity is used to depict the evolution of both the solid-liquid interface and the void-PCM interface as a constant value was used for both the solid and liquid $NaNO_3$ phases as well as for the air. The results have been non-dimensionalized with respect to the product of Stefan (Ste) number and Fourier (Fo) number. Ste is the ratio of sensible heat to latent heat, equation (48). For melting, the liquid heat capacity is used and ΔT is the difference between the surface temperature

and the melting point of $NaNO_3$ (581 K). Therefore, Ste has a constant value of 1.72 during melting. Fo is the ratio of diffusive transport to the energy storage rate of a material, equation (49). Based on the properties of $NaNO_3$, Fo equals 0.001318*t*, where *t* is time.

$$Ste = \frac{c_p \Delta T}{L} \tag{48}$$

$$Fo = \frac{kt}{\rho c_p r^2} \tag{49}$$

The impact of the void is immediately noticeable as the isotherms in the XY and ZX planes are different. In the ZX plane, they take on the circular concentric rings predicted by the solution of the unsteady diffusion equation. In the XY plane however, the air acts as an insulator reducing the heat transfer in the upper part of the capsule leading to the isotherms being "U"-shaped in the PCM, Figure 15a. At this early stage, the natural convection in the molten PCM is minimal as only a small fraction of the PCM has melted; however two recirculating vortices have formed in the air void, Figure 15b. In the ZX plane, the solid-liquid interface is always circular in shape and propagates radially inward whereas in the XY plane it is "U"-shaped as it is truncated at the void-PCM interface, Figure 15d. Here and throughout blue denotes a solid region and red a liquid region. The solid-liquid and void-PCM interface are shown in Figure 15c where blue is the stainless steel shell, green is the air void, orange is solid $NaNO_3$, and red is molten $NaNO_3$. As the PCM melts it expands and slowly compresses the void as it now occupies approximately 13% of the capsule's volume.

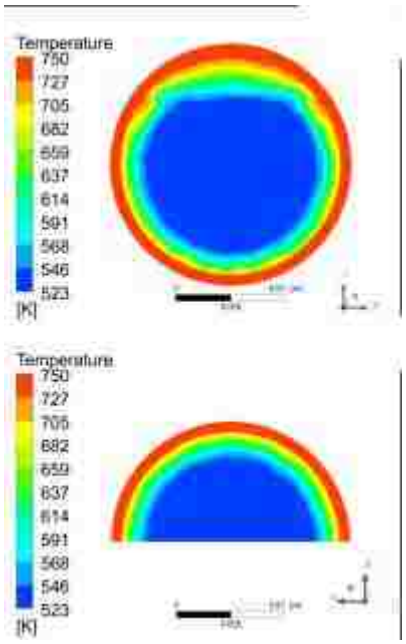

(a) Temperature on XY (upper) & ZX (lower) Planes @ 5 sec
SteFo=0.0113

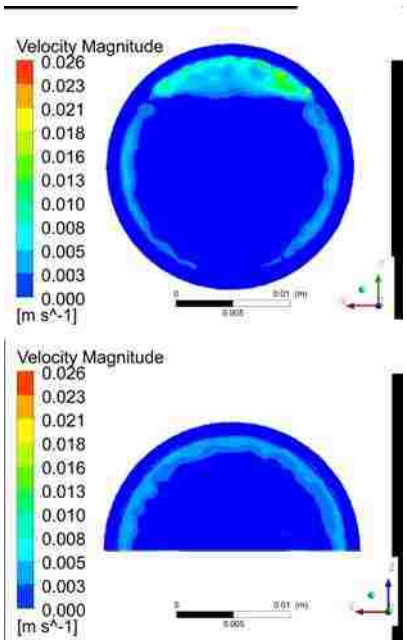

(b) Velocity Magnitude on XY (upper) & ZX (lower) Planes @ 5 sec
SteFo=0.0113

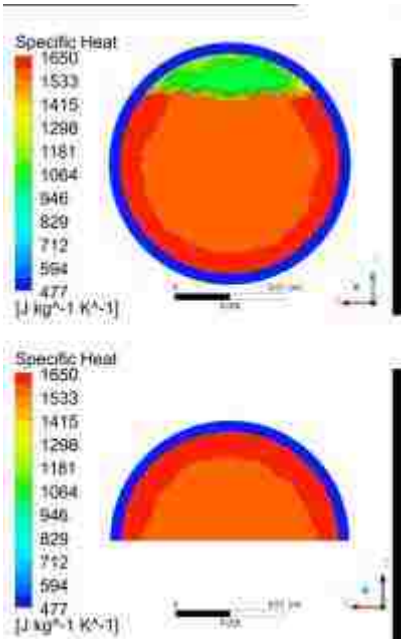

(c) Interfaces on XY (upper) & ZX (lower) Planes @ 5 sec
SteFo=0.0113

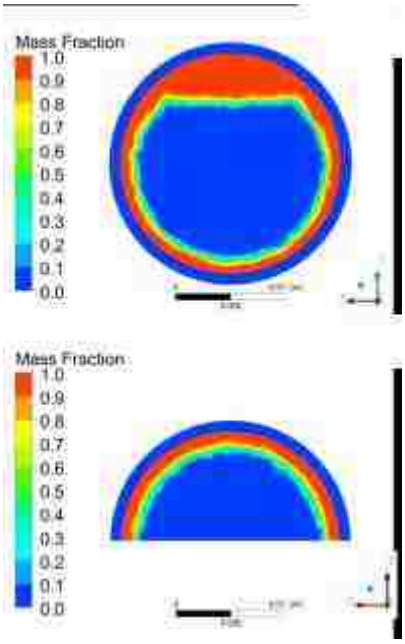

(d) Liquid Faction on XY (upper) & ZX (lower) Planes @ 5 sec
SteFo=0.0113

Figure 15. Temperature, liquid fraction, velocity magnitude, and interface contours at 5 sec into melting (SteFo=0.0113)

As melting progresses, natural convection occurs within the molten PCM and enhances the heat transfer rate. This leads to the isotherms in the XY plane being reshaped from a “U”-shape into a teardrop shape within the remaining solid PCM whereas in the molten PCM the temperature has begun to stratify, Figure 16a. In addition to the recirculating vortices in the air void, two vortices have formed within the molten PCM: one along the capsule edge where the molten PCM is heated and rises and the other along the remaining solid PCM where it is cooled and sinks, Figure 16b. The recirculating vortices result in a faster melting rate along the air-PCM interface than in the bottom of the capsule despite the poor conductance of heat through the air. As the PCM melts, it continues to compress the air void further at the top of the capsule as it is now only 8% of the capsule volume, Figure 16c. The presence of convection within the molten PCM has also changed the shape of the solid-liquid interface into a teardrop shape in the XY plane, Figure 16d. In the ZX plane there is still a uniform heat transfer rate and thus the isotherms and solid-liquid interface remain circular as they propagate radially inward. Vortices have also formed along the capsule edge and the remaining solid PCM; however these vortices are of a lower magnitude as the ZX plane is perpendicular to the gravitational force vector minimizing the effects of natural convection.

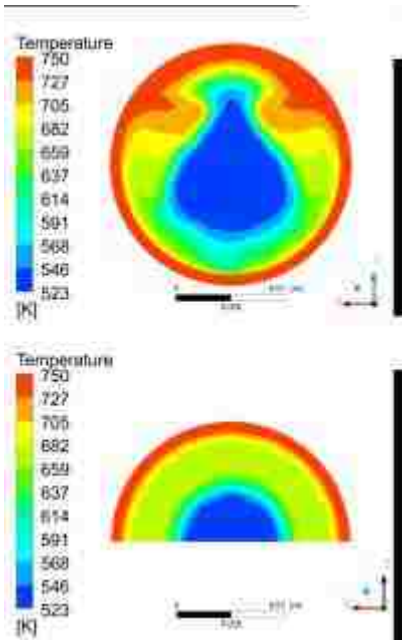

(a) Temperature on XY (upper) & ZX (lower) Planes @ 15 sec
SteFo=0.0339

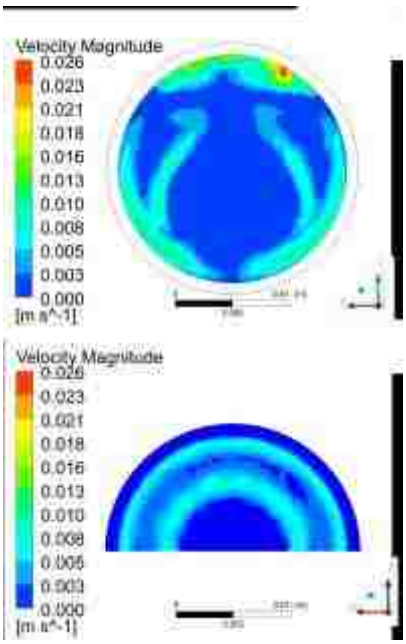

(b) Velocity Magnitude on XY (upper) & ZX (lower) Planes @ 15 sec
SteFo=0.0339

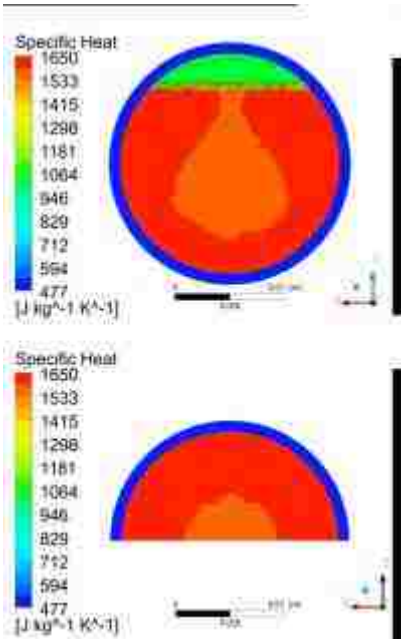

(c) Interfaces on XY (upper) & ZX (lower) Planes @ 15 sec
SteFo=0.0339

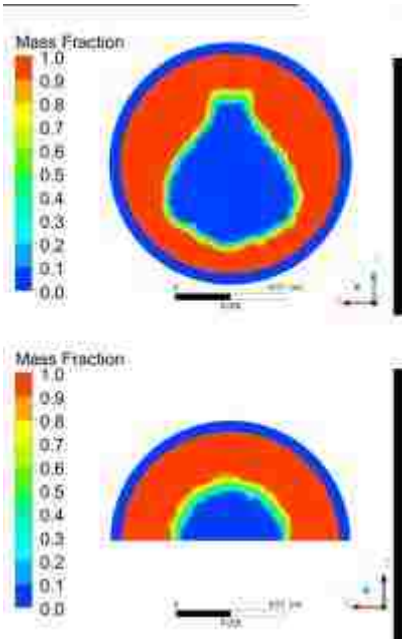

(d) Liquid Faction on XY (upper) & ZX (lower) Planes @ 15 sec
SteFo=0.0339

Figure 16. Temperature, liquid fraction, velocity magnitude and interface contours at 15 sec into melting (SteFo=0.0339)

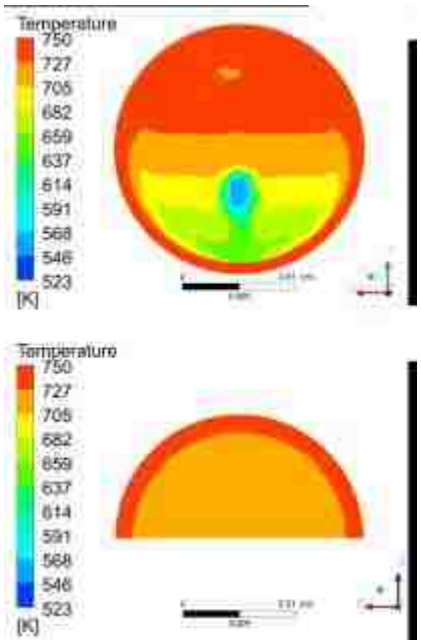

(a) Temperature on XY (upper) & ZX (lower) Planes @ 25 sec SteFo=0.0565

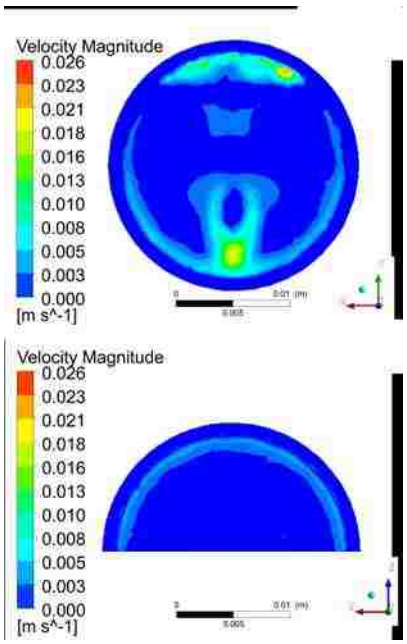

(b) Velocity Magnitude on XY (upper) & ZX (lower) Planes @ 25 sec SteFo=0.0565

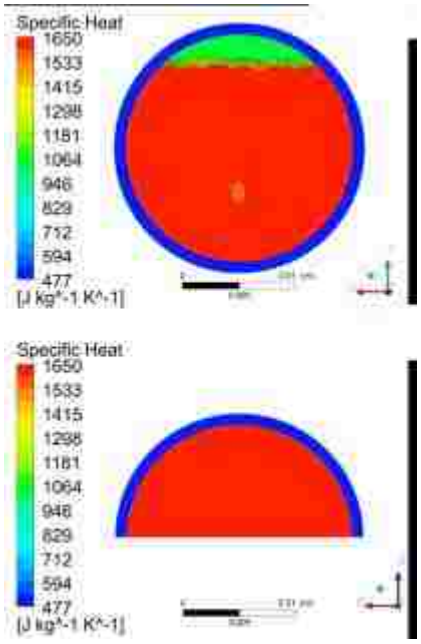

(c) Interfaces on XY (upper) & ZX (lower) Planes @ 25 sec SteFo=0.0565

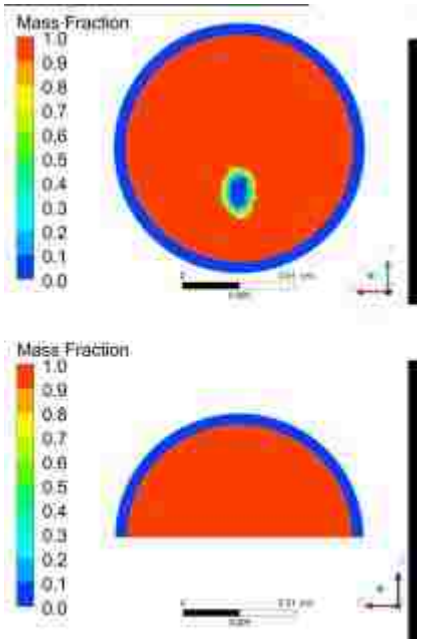

(d) Liquid Faction on XY (upper) & ZX (lower) Planes @ 25 sec SteFo=0.0565

Figure 17. Temperature, liquid fraction, velocity magnitude and interface contours at 25 sec into melting (SteFo=0.0565)

As the melting process nears completion the temperature within the capsule is stratified in the XY plane and uniform in the ZX plane, Figure 17a. The vortices in the air void remain as well as those along the capsule edge and the remaining solid. As the remaining solid is close to the bottom of the capsule, a recirculating vortex has formed in the molten PCM in between the capsule edge and the remaining solid, Figure 17b. A higher heat transfer rate in the ZX plane results in a slightly faster melting time compared to that of the XY plane where a small oval-shaped solid remains, Figure 17d. The remaining solid PCM is also off center due to the insulating effect of the air void. The air void has been compressed to half its original size and now occupies only 6% of the total capsule volume, Figure 17c. It takes a total of 30 sec for the capsule to melt completely. The evolution of both the solid-liquid interface and void-PCM interface over both the melting and solidification process is presented in Figure 21.

5.3 Solidification of Spherical EPCM Capsules

Upon completion of the melting process, the capsule was allowed to heat to a uniform temperature of 750 K before the solidification process was initiated by switching the surface temperature to 523 K. After the surface temperature is switched, the temperature within the molten PCM decreases rapidly resulting in a linear temperature distribution in the XY plane and a nominal temperature of 650 K in the ZX plane, Figure 18a. During this initial period, a recirculating vortex forms along the capsule edge but it is much weaker than that seen during the melting phase, Figure 18b. The PCM begins to solidify along the bottom of the capsule and the solid gradually grows up the capsule sides, Figure 18d.

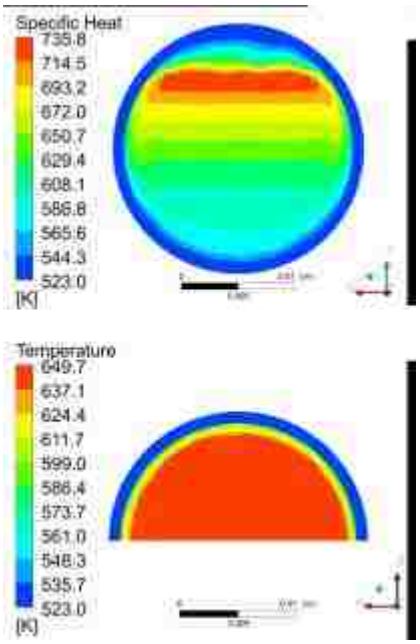

(a) Temperature on XY (upper) & ZX (lower) Planes @ 5 sec
SteFo=0.0039

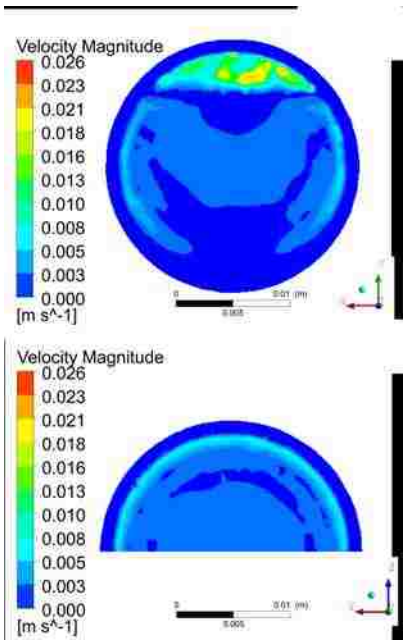

(b) Velocity Magnitude on XY (upper) & ZX (lower) Planes @ 5 sec
SteFo=0.0039

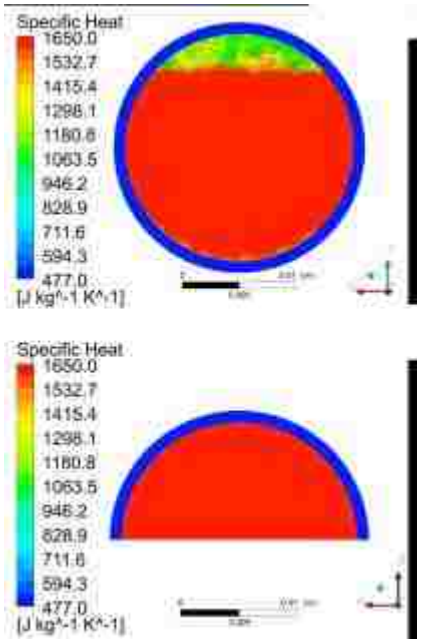

(c) Interfaces on XY (upper) & ZX (lower) Planes @ 5 sec
SteFo=0.0039

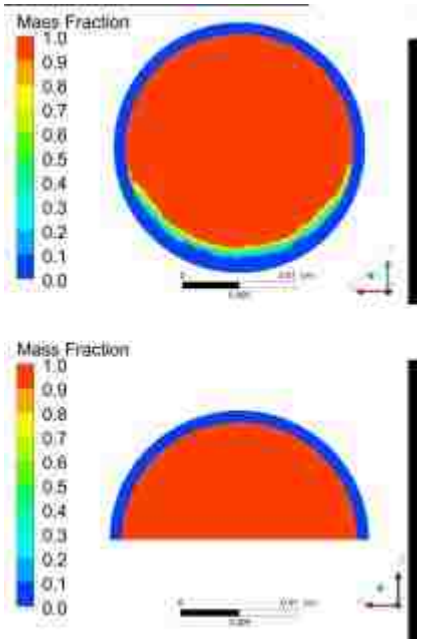

(d) Liquid Faction on XY (upper) & ZX (lower) Planes @ 5 sec
SteFo=0.0039

Figure 18. Temperature, liquid fraction, velocity magnitude and interface contours at 5 sec into solidification (SteFo=0.0039)

One minute after the surface temperature has been changed the solid PCM has decreased to the melting temperature (581 K). The results are again non-dimensionalized using the product of Ste and Fo numbers, however this time the solid specific heat capacity is used leading to a constant Ste of 0.567 and a Fo number of 0.00137*t*. Much like during the initial stages of the melting process, the isotherms in the XY plane are "U"-shaped whereas they are circular in the ZX plane, Figure 19a. The only convection present in the capsule are the two vortices in the air void as the remaining molten PCM is a uniform temperature, Figure 19b. This results in the solidification process being conduction-dominated. In the ZX plane the solid-liquid interface is again circular in shape and it slowly propagates radially inward. In the XY plane however, the presence of the void results in a "U" shaped interface, Figure 19d. As the PCM solidifies it contracts which allows the compressed air void to expand slowly and now occupies 10% of the capsule, Figure 19c.

As the PCM continues to solidify, the increasing solid region asymptotically decreases the heat transfer rate which results in an increase in the total solidification time. The air void has greatly reduced the amount of heat that is transferred from the shell to the PCM leading to the PCM solidifying from the bottom up, Figure 20d. As was seen during the melting process, the heat transfer rate is greater in the ZX plane than the XY plane resulting in a faster solidification time. Upon complete solidification the air void has fully expanded back to its original size, Figure 20c. The total solidification time is 300 sec. Again, the evolution of both the solid-liquid and air-PCM interface are presented in Figure 21 for both the melting and solidification.

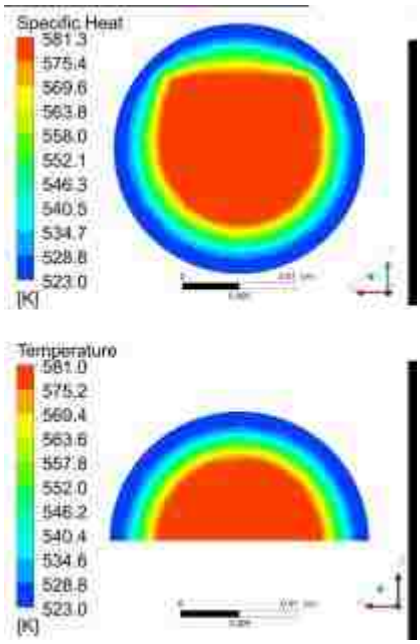

(a) Temperature on XY (upper) & ZX (lower) Planes @ 60 sec
SteFo=0.0466

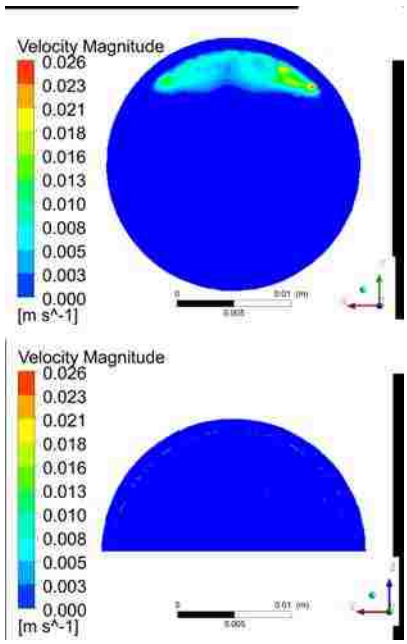

(b) Velocity Magnitude on XY (upper) & ZX (lower) Planes @ 60 sec
SteFo=0.0466

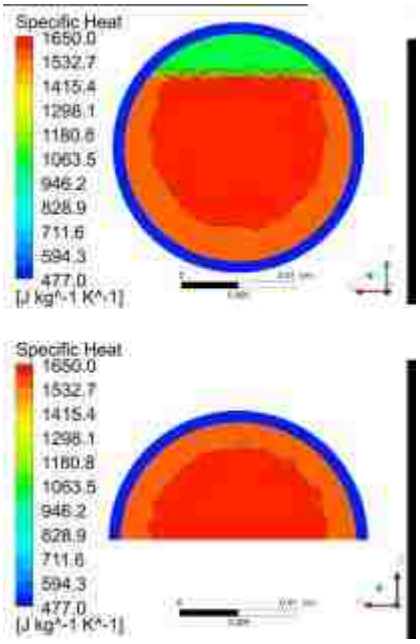

(c) Interfaces on XY (upper) & ZX (lower) Planes @ 60 sec
SteFo=0.0466

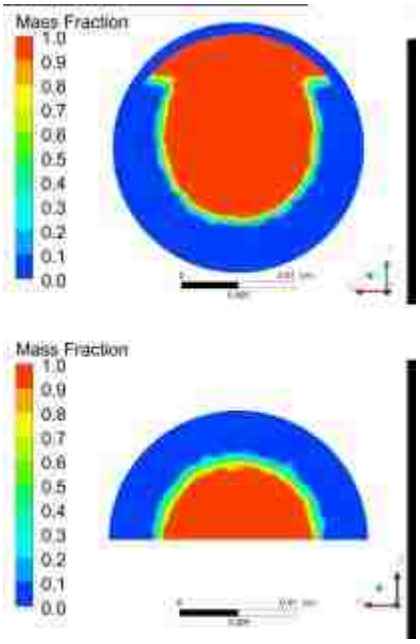

(d) Liquid Faction on XY (upper) & ZX (lower) Planes @ 60 sec
SteFo=0.0466

Figure 19. Temperature, liquid fraction, velocity magnitude and interface contours at 60 sec into solidification (SteFo=0.0466)

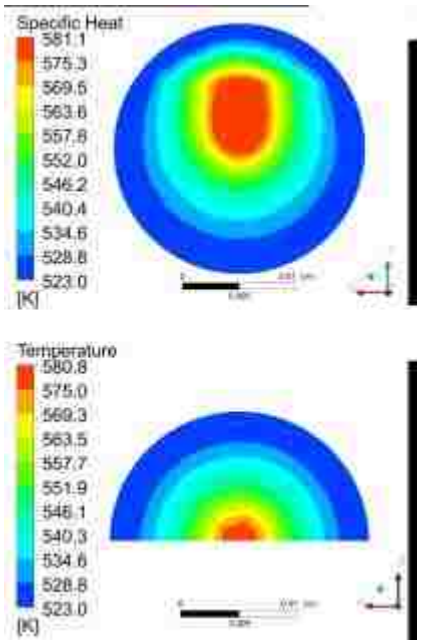

(a) Temperature on XY (upper) & ZX (lower) Planes @ 240 sec SteFo=0.1864

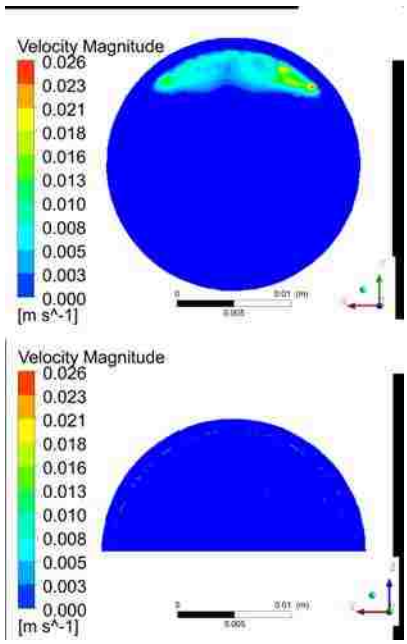

(b) Velocity Magnitude on XY (upper) & ZX (lower) Planes @ 240 sec SteFo=0.1864

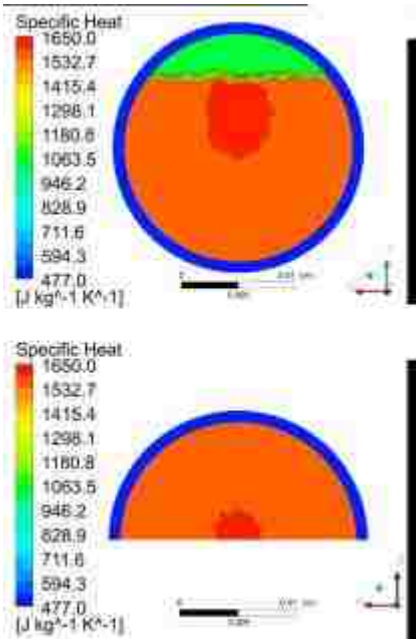

(c) Interfaces on XY (upper) & ZX (lower) Planes @ 240 sec SteFo=0.1864

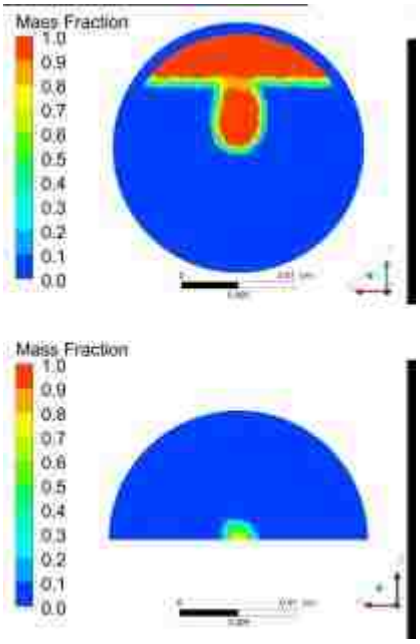

(d) Liquid Faction on XY (upper) & ZX (lower) Planes @ 240 sec SteFo=0.1864

Figure 20. Temperature, liquid fraction, velocity magnitude and interface contours at 240 sec into solidification (SteFo=0.1864)

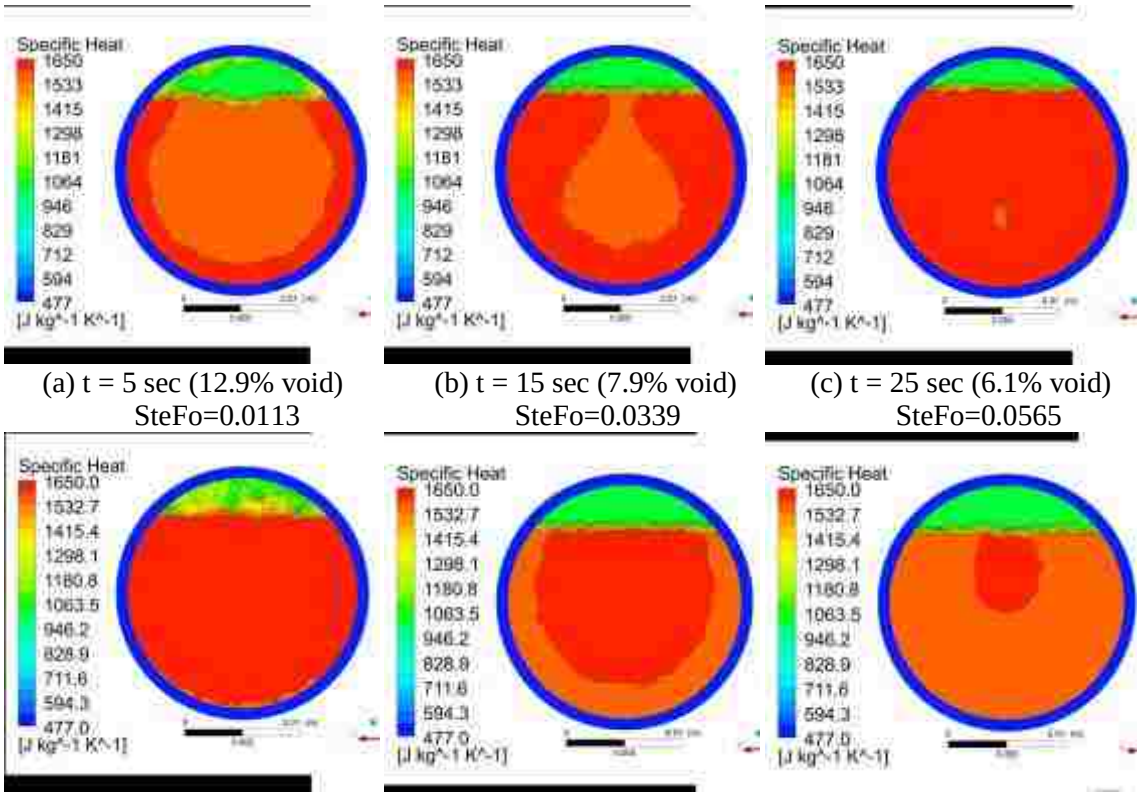

(a) t = 5 sec (12.9% void) SteFo=0.0113

(b) t = 15 sec (7.9% void) SteFo=0.0339

(c) t = 25 sec (6.1% void) SteFo=0.0565

(d) t = 5 sec (6.7% void) SteFo=0.0039

(e) t = 60 sec (9.9% void) SteFo=0.0466

(f) t = 240 sec (11.4% void) SteFo=0.1864

Figure 21. The interfaces during (a-c) melting and (d-f) solidification at various times

5.4 Conclusions

The effect of an internal void and natural convection on the heat transfer that occurs within EPCM capsules is numerically investigated using a three-dimensional model of a 22 mm diameter spherical capsule with a constant surface temperature and using $NaNO_3$ as the PCM. The presence of a void at the top of the capsule removes the symmetry about the X-axis that is usually present for a uniformly heated sphere. This leads to the solid-liquid interface behaving differently in the XY and ZX planes. In the ZX plane, the isotherms form concentric circular rings as per the solution of the unsteady diffusion equation; thus the solid-liquid interface is always circular in shape and propagates radially inward. In the XY plane, the solid-liquid interface is "U"-

shaped during the conduction-dominated phase of the heat transfer during melting due to the insulating effect of the void. As convection becomes the dominant mode of heat transfer, it increases the heat transfer rate along the air-PCM interface resulting in a teardrop-shaped remaining solid. The overall melting process is also slightly faster in the ZX plane. As the PCM melts it expands and compresses the void from an initial 15% to 6% when melting is completed, over a 50% reduction in size.

Unlike the melting process, solidification is conduction-dominated and is therefore limited by the thermal conductivity of the solid PCM. The ever-increasing solid asymptotically decreases the heat transfer rate prolonging the solidification process. For the considered case, complete solidification takes 300 sec which is 10 times longer than the melting process. It should be noted that the difference between the melting point of the PCM and the capsule wall is 100 K smaller during solidification than it was during melting resulting in a smaller Ste. The resulting slower heat transfer rate coupled with the lack of natural convection in the liquid PCM contribute to the increased solidification time. At the end of solidification, the void expanded back to its original volume fraction as the PCM contracted.

These results highlight the impact that both natural convection and an internal void have on the heat transfer and therefore evolution of the solid-liquid interface within EPCM capsules. Accurate predictions of the performance of an EPCM-based TES system cannot be made unless a model that captures the resulting complex multi-phase heat transfer caused by these effects is used.

CHAPTER VI: EFFECT OF INITIAL VOID LOCATION

The way an EPCM capsule is manufactured can result in different initial void locations. To study the effect of the initial void location on the heat transfer that occurs within EPCM capsules, three initial void locations (a central void, random void, and upper void) were considered. The computational domain is presented in Figure 22 for a 25.4 mm diameter cylindrical EPCM capsule horizontally orientated in a cross-flow with the HTF. A convective boundary condition was applied that corresponds to a turbulent exterior flow and the heat transfer coefficient based on the local Nusselt number [82, 83] is shown in Figure 23. $NaNO_3$ was considered as the PCM and stainless steel was used for the encapsulation material. The thermal properties of both materials are listed in Table 6; additionally the melting temperature of $NaNO_3$ is 308 °C. To model convection in the molten PCM, the following expression was used for the density of $NaNO_3$ in the liquid phase:

$$\rho_l = 2341.56 - 0.76T \quad \textbf{(50)}$$

To accommodate the thermal expansion of $NaNO_3$ (β = 4.0×10^{-4} 1/K) upon melting, an air void of approximately 20% was considered. The density of air was modeled in accordance with the ideal gas law and the heat capacity, thermal conductivity, and viscosity used are listed in Table 6. A free stream temperature of 500 °C was used for the HTF with an initial capsule temperature of 25 °C. A triangular mesh with 8442 nodes and an element size of 1×10^{-4} m was used. Using the methods described previously, the enthalpy-porosity and VOF models were used to track the evolution of the solid-liquid and air-PCM interfaces.

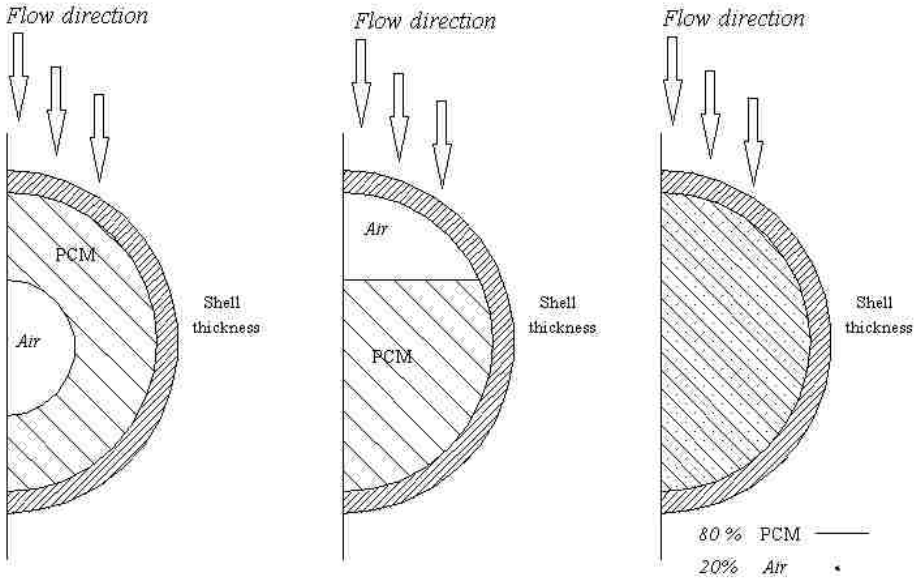

Figure 22. Computational domain of EPCM capsule with various void locations

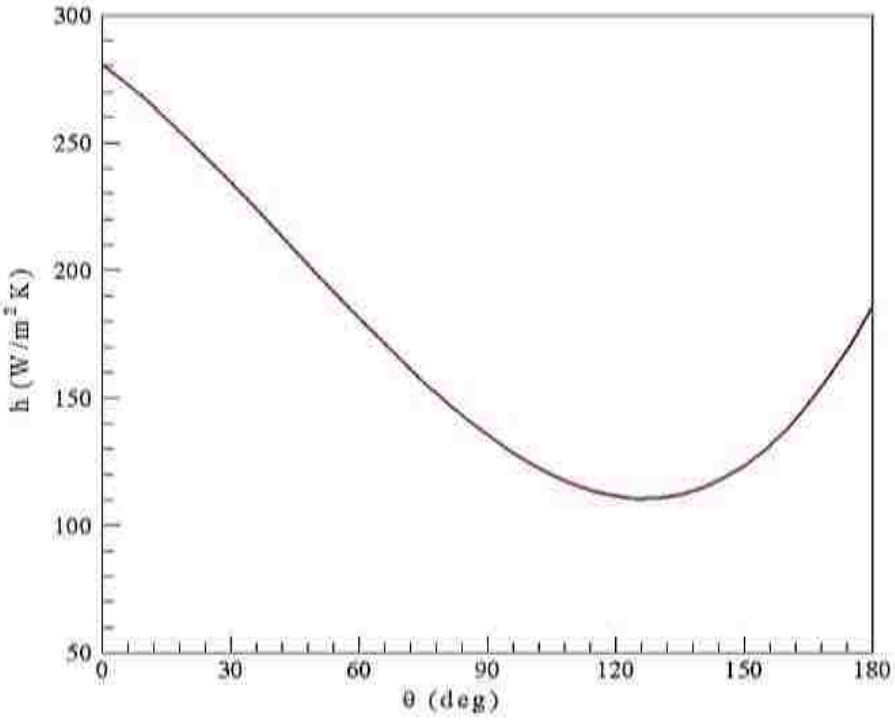

Figure 23. Heat transfer coefficient applied to EPCM capsule surface

6.1 Initial Random Void

Compression of a powder PCM into a pellet offers control over the void fraction by varying the force applied. This results in an initial uniform distribution of air throughout the entire PCM. The given HTF arrangement results in the heat transfer coefficient being highest at the top of the capsule, thus the PCM begins melting along the capsule shell in the upper portion of the capsule. The isotherms, liquid fraction, volume fraction, and velocity magnitude at 90 sec into the melting process are presented in Figure 24a-20d. The results have also been non-dimensionalized using the product of the Ste and Fo numbers. The isotherms within the capsule are initially concentric due to the uniform thermal conductivity within the PCM, Figure 24a. The liquid fraction is depicted in Figure 24b. As the PCM melts, the air diffuses to the top of the capsule due to the difference in their respective densities, and an air void begins to form at the top of the capsule, Figure 24c. Here blue is air and red is the $NaNO_3$ PCM. The initial solid PCM is yellow which corresponds to the initial 20% void fraction. Natural convection in the molten PCM is enhanced due to the separation of the air and $NaNO_3$, increasing the melting rate along the forming void-PCM interface.

As melting progresses, convective effects within the molten PCM coupled with the insulating effect of the forming air void have reshaped the initially concentric isotherms into more of a teardrop shape, Figure 24e. This results in the solid-liquid interface taking on a teardrop shape as well as it propagates radially inward, Figure 24f. The air and $NaNO_3$ have continued to separate as the PCM melts leading to the formation of a distinct air void at the top of the capsule, Figure 24g. Two recirculating vortices have formed within the molten PCM, one along the capsule edge where the

molten PCM is heated and rises and the other along the remaining solid PCM where the molten PCM cools and sinks, Figure 24h.

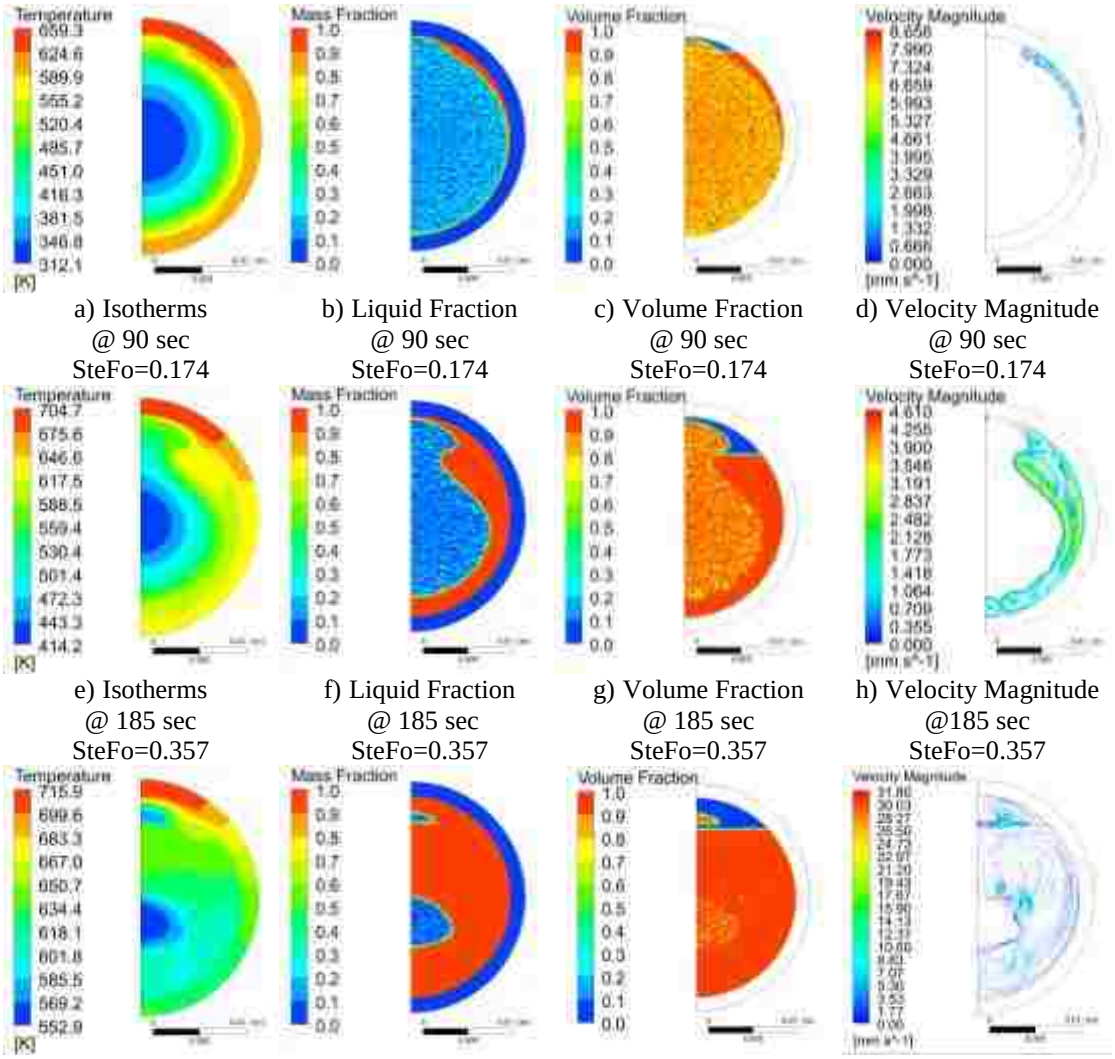

a) Isotherms @ 90 sec SteFo=0.174 | b) Liquid Fraction @ 90 sec SteFo=0.174 | c) Volume Fraction @ 90 sec SteFo=0.174 | d) Velocity Magnitude @ 90 sec SteFo=0.174

e) Isotherms @ 185 sec SteFo=0.357 | f) Liquid Fraction @ 185 sec SteFo=0.357 | g) Volume Fraction @ 185 sec SteFo=0.357 | h) Velocity Magnitude @185 sec SteFo=0.357

i) Isotherms @ 277 sec SteFo=0.534 | j) Liquid Fraction @ 277 sec SteFo=0.534 | k) Volume Fraction @ 277 sec SteFo=0.534 | l) Velocity Magnitude @ 277 sec SteFo=0.534

Figure 24. Contours of the temperature, liquid fraction, volume fraction, & velocity magnitude for an EPCM capsule with an initially random void distribution at 90 sec (a-d), 185 sec (e-h) and 277 sec (i-l) into the melting process.

The convection induced due to the separation of the air and $NaNO_3$ phases is so intense that it results in the remaining solid PCM splitting into two regions. The temperature within the capsule has become stratified within the molten PCM with

minor deviations resulting from the presence of the remaining solid PCM, Figure 24i. Convection in the molten PCM increased the melting rate in the upper portion of the capsules despite the insulating effect of the air void resulting in an oval-shaped solid PCM, Figure 24j. The small remaining solid PCM at the top of the capsule melts from the bottom up and as the air and $NaNO_3$ separate it results in an area of high velocity that is an order of magnitude larger than previously seen during the melting process, Figure 24l. It takes 308 sec for the 20% random void capsule to melt completely, and as one would expect the air diffused to the top of the capsule as the PCM melted due to the difference in their respective densities.

6.2 Initial Central Void

If a solid PCM is used to fill the capsule shell, the center can be drilled out to leave sufficient void space within the capsule; therefore an initial central void location was considered. Since the PCM is in direct contact with the capsule shell it has the highest heat transfer rate at the start of melting. Furthermore, the uniform thermal conductivity in the PCM results in concentric circular isotherms per the solution to the unsteady diffusion equation for pure diffusional heat transfer, Figure 25a. Much like in the case of a random void distribution, the PCM beings to melt along the upper portion of the capsule shell, Figure 25b. As the air is completely encased within the solid PCM, it cannot diffuse until the PCM melts along the air-PCM interface, however recirculating vortices can be seen within the air void, Figure 25c and d.

As time progresses, convection in the molten PCM has increased the heat transfer rate in the upper portion of the capsule, causing the solid-liquid interface to flatten, Figure 25f. The isotherms have remained primarily circular with a

stratification forming in the molten PCM in the upper portion of the capsule, Figure 25e. As the PCM has yet to melt along the air-$NaNO_3$ interface, the air is still trapped at the center of the capsule. The two recirculating vortices have again formed along the capsule shell and solid PCM, Figure 25h.

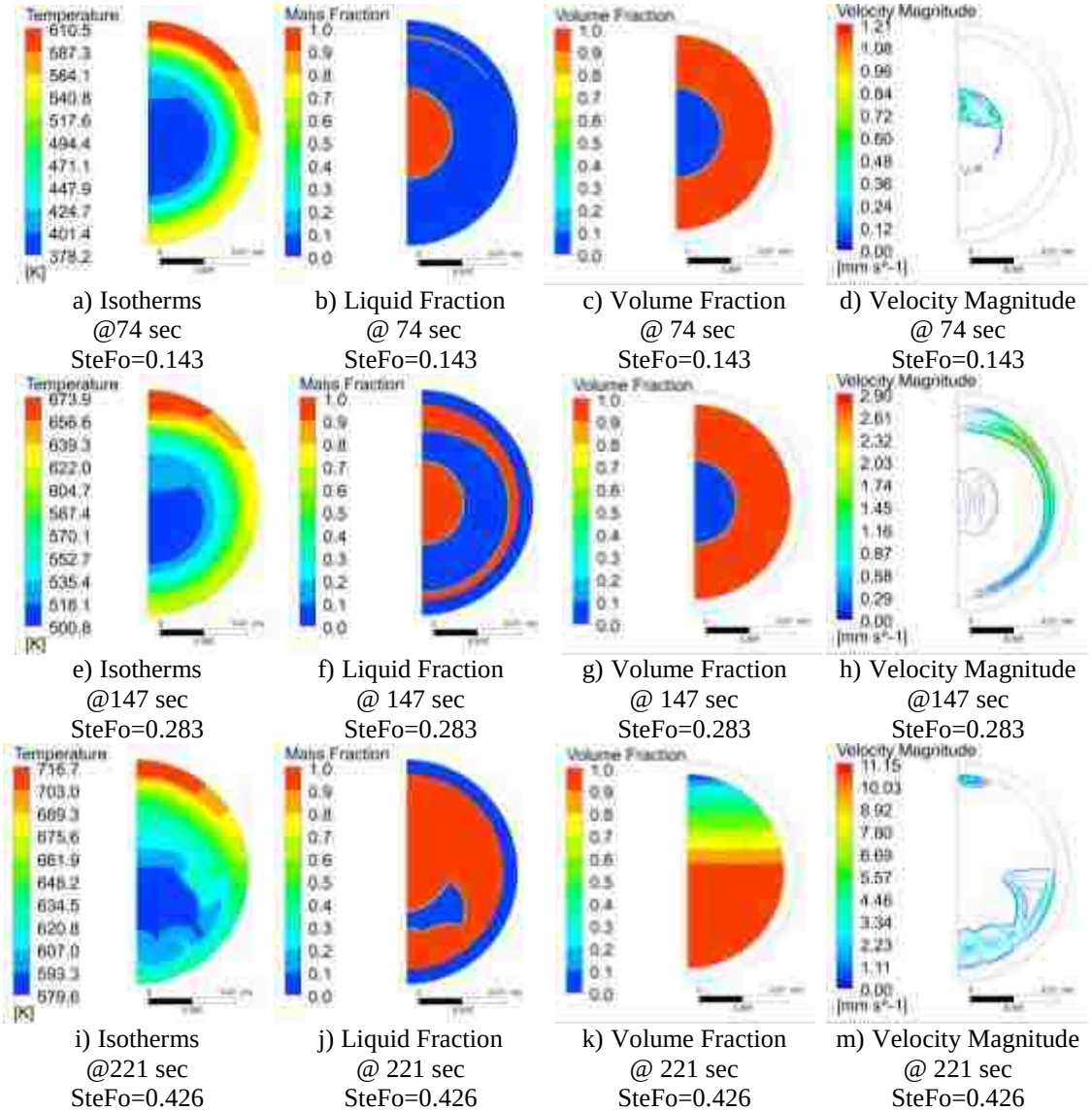

Figure 25. Contours of the temperature, liquid fraction, volume fraction, & velocity magnitude for an EPCM capsule with a void initially located at the center of the EPCM capsule at 74 sec (a-d), 147 sec (e-h) and 221 sec (i-m) into the melting process.

As soon as the PCM melts along the air interface, the air begins to diffuse rapidly due to pressure buildup and results in an erratic velocity field. However, after this initial period, there is little to no convection present in the upper half of the capsule due to the lack of a temperature gradient to drive natural convection, Figure 25k. The only convection present within the capsule during the late stages of melting is the vortices along the capsule shell and remaining solid PCM that were seen previously; additionally two smaller vortices have formed in the bottom of the capsule, Figure 25m. The isotherms within the capsule have been distorted as a result of convection with a stratification of temperature present in the molten PCM, Figure 25i. The remaining solid PCM is "C"-shaped and as the diffused air lowers the effective thermal conductivity in the upper portion of the capsules, the remaining solid melts primarily from the bottom up, Figure 25j.

It takes 252 sec for the central void capsule to melt completely. At the completion of melting, less than 10% of the air has fully diffused to the top of the capsule. If the capsule is solidified shortly after the melting process has completed, the air does not have time to diffuse fully from the molten salt. After several additional melting and solidification cycles the fraction of air at the top of the capsule increased minimally. However, if the capsule is allowed to reach a uniform temperature of 773 K before solidification begins, 95% of the air is able to diffuse fully before the initial solidification process.

6.3 Initial Upper Void

Due to gravitational effects, it is likely that the air would diffuse to the top of the EPCM capsule and for a horizontally orientated cylindrical capsule would result in

the upper void distribution. This initial void location could be manufactured by filling the EPCM capsules with the desired mass of molten PCM and then cooling the capsules horizontally or by machining a solid PCM into the desired shape. The effect of the void space at the top of the capsule is immediately seen as the isotherms within the capsule are no longer circular but are "U"-shaped, Figure 26a. The air acts as an insulator reducing the heat transfer rate in the upper half of the capsule and as the capsules are heated from the top it retards the initial heating of the capsule, therefore it takes longer for the PCM to begin melting. When melting finally starts, it begins along the capsule shell at the air-PCM interface, Figure 26b. As the PCM melts it expands and compresses the air void, Figure 26c. In addition to convection within the air, two recirculating vortices have formed along the capsule edge and solid PCM, Figure 26d. These vortices increase the heat transfer along the air-$NaNO_3$ interface increasing the melting rate despite the poor conductive heat transfer from the air to the PCM.

The effect of the increase in heat transfer from convection in the molten PCM is more evident later into the melting process as the PCM has melted across the entire air-PCM interface despite poor the conductive heat transfer. The isotherms have been reshaped into a teardrop shape, Figure 26e. The solid-liquid interface is also teardrop shaped, however vortices that have begun to form in the bottom of the capsule have accelerated the melting process leading to two circular indents, Figure 26f. The initial 20% air void has been further compressed as the PCM continues to expand upon melting, Figure 26g. The two vortices along the capsule edge and solid PCM have increased in intensity, Figure 26h.

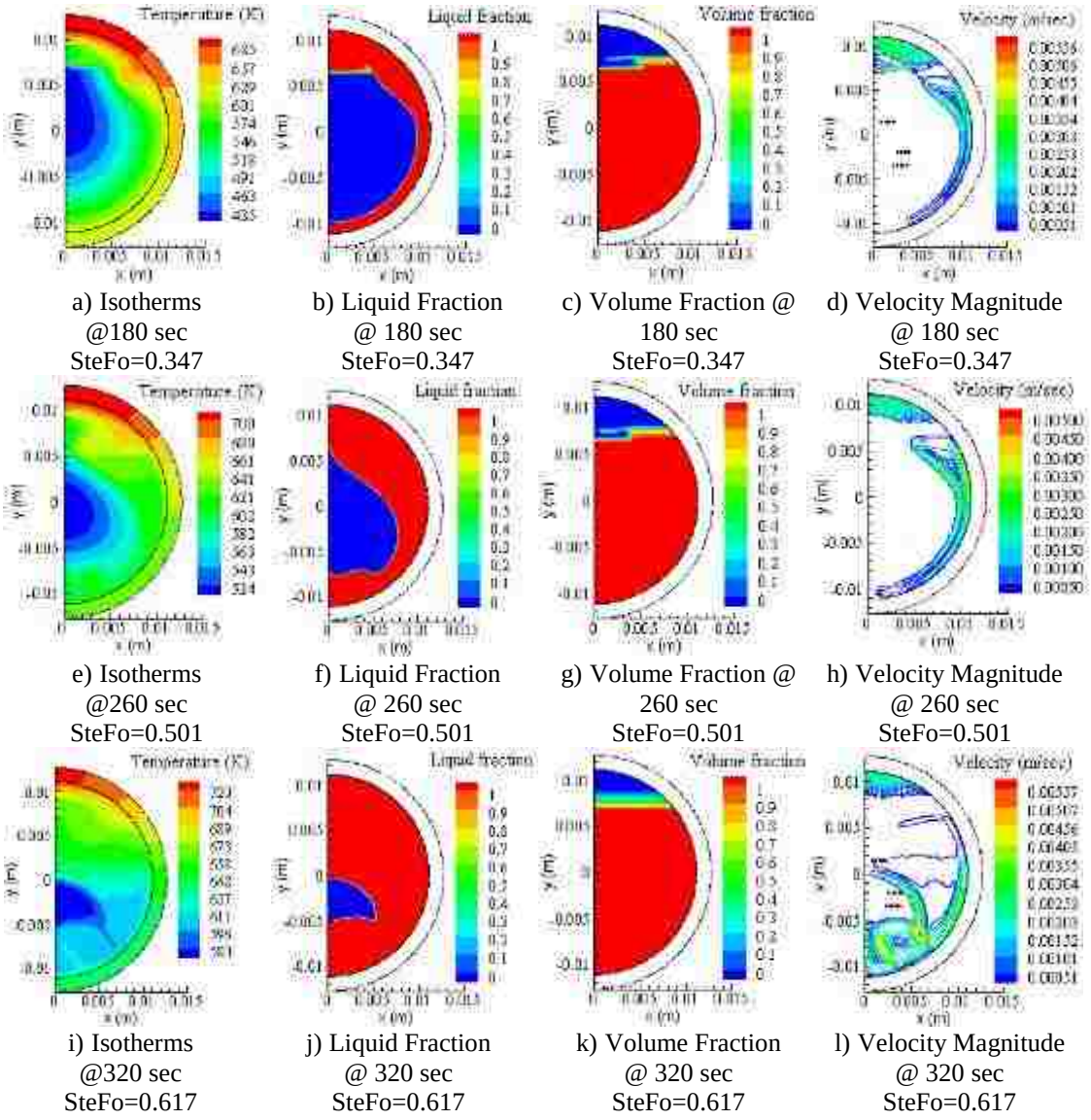

a) Isotherms @180 sec SteFo=0.347 | b) Liquid Fraction @ 180 sec SteFo=0.347 | c) Volume Fraction @ 180 sec SteFo=0.347 | d) Velocity Magnitude @ 180 sec SteFo=0.347

e) Isotherms @260 sec SteFo=0.501 | f) Liquid Fraction @ 260 sec SteFo=0.501 | g) Volume Fraction @ 260 sec SteFo=0.501 | h) Velocity Magnitude @ 260 sec SteFo=0.501

i) Isotherms @320 sec SteFo=0.617 | j) Liquid Fraction @ 320 sec SteFo=0.617 | k) Volume Fraction @ 320 sec SteFo=0.617 | l) Velocity Magnitude @ 320 sec SteFo=0.617

Figure 26. Contours of the temperature, liquid fraction, volume fraction, & velocity magnitude for an EPCM capsule with an initial void located at the top of the EPCM capsule at 180 sec (a-d), 260 sec (e-h) and 320 sec (i-l) into the melting process.

As the melting process nears completion, the temperature distribution within the molten salt has begun to stratify, Figure 26i. Convection in the molten PCM has continued to increase the melting rate in the upper portion of the capsule and additionally, a large vortex has formed at the bottom of the capsule leading to a

crescent-shaped remaining solid, Figure 26j. The void space has been compressed to approximately 50% of its original size due to the expansion of the PCM, Figure 26k. The vortices at the bottom of the capsule have joined together to form one large vortex that is accelerating the melting of the bottom of the solid PCM; additionally the two recirculating vortices along the capsule edge and remaining solid remain, Figure 26l. It takes 350 sec for the capsule to melt completely, which is the longest melting time of the three cases considered.

6.4 Case Comparison

The ideal void location would be for it always to be located at or near the center of the capsule as to avoid the low thermal conductivity of air. For the initial central void location, the entire PCM is in contact with the capsule shell, and since the capsules are heated from the top it has the highest initial heat transfer rate. During the initial stages of the melting process, conduction is the dominant mode of heat transfer and thus the isotherms and therefore solid-liquid interface are circular in shape. As convection begins to dominate the heat transfer the increase in heat transfer flattens the isotherms and solid-liquid interface in the top of the capsule. The air remains trapped at the center of the capsule until the PCM melts along the air-PCM interface. Once this occurs there is an initially rapid expansion of the air into the molten salt. However, after this initial period the diffusion process is slow as there is no strong thermal gradient to drive the process. The presence of air within the molten salt reduces the effective thermal conductivity in the upper half of the capsule leading to a reduction in the heat transfer rate. Therefore the remaining solid PCM melts from the bottom up. Upon completion of the melting process less than 10% of the air is able to

fully diffuse to the top of the capsule with a minimal increase seen after multiple thermal cycles. It takes a total of 252 sec for the central void capsule to melt.

A common method of making EPCM capsules involves the use of a compressed powder PCM. This method allows for control over the void fraction by varying the pressure applied and results in a uniform distribution of air throughout the entire PCM. Like in the case of a central void, the PCM is in contact with the entire capsule shell; however the presence of air in the PCM results in a lower effective thermal conductivity. This leads to a slower heat transfer rate during the initial conduction period. When the capsule begins to melt, the air and $NaNO_3$ phases start to separate leading to an increase in the natural convection within the molten PCM. Unlike in the central void case with the random void distribution, the diffusion of the air and $NaNO_3$ occurs slowly as the PCM melts instead of all at once. This allows for complete diffusion to have occurred by the end of the melting process. The formation of the air void at the top of the capsule during melting has an insulating effect on the top of the capsule. Despite the resulting poor conductive heat transfer, convection in the molten PCM accelerates the melting process along the void-PCM interface. It takes 308 sec for the random void capsule to melt which is 22% slower than the central void case due to the reduction in the effective thermal conductivity resulting from the presence of air throughout the PCM and the insulating effect of the void that forms at the top of the capsule.

Due to gravitational effects, one would expect that upon the completion of melting the air will diffuse to the top of the capsule creating a void that is always located at the top of the capsule. The effect of a void located at the top of the capsule

on the heat transfer within the capsule is immediately evident as the air acts as an insulator and retards the heat flux into the PCM during the initial conduction-dominated stage. Therefore it takes the upper void capsule the longest amount of time to start melting and when it finally does so it beings at the air-PCM interface along the capsule shell. Until significant melting occurs, the majority of the heat received by the PCM is from the sides and bottom of the capsule. However, once the PCM melts across the entirety of the air-PCM interface convection in the molten salt increases the heat transfer rate in the upper portion of the capsule. This leads to the remaining solid PCM melting primarily from the top down. The upper void capsule exhibits the highest level of convection in the bottom of the capsule during the late stages of melting. The upper void case had the longest melting time of 350 sec which is 39% slower than the central void and 14% slower than the random void distribution. These results emphasize the impact that the location of the internal void has on the heat transfer that occurs within an EPCM capsule.

6.5 Conclusions

Despite the fact that an internal void space is necessary within an EPCM capsule to mitigate the rise in internal pressure, its effect on the heat transfer that occurs within the capsules has mostly been ignored in the various numerical evaluations conducted. To investigate the impact of the void location, three limiting cases of void placement were examined. A heat transfer analysis of the melting within 25.4 mm diameter stainless steel-$NaNO_3$ EPCM capsules was conducted that included an initial 20% void faction and convection within the fluid media. The simulations were conducted by simultaneously employing the VOF and enthalpy-porosity methods

to accurately capture the multiphase heat transfer within the capsule. The initial temperature of the capsule was set to 25 °C since the void distributions are only feasible during the initial charging of the capsule due to diffusion of the air within the capsule. A turbulent convective boundary condition with a liquid HTF was applied with a freestream temperature of 500 °C.

Although the cases of an initial central or random void are not repeatable upon cycling of the EPCM capsule, the results highlight the impact the location of the void has on the overall heat transfer. The capsule with the central void has the shortest melting time for the initial melting of the capsules. It was 22% and 39% faster than the random void and upper void capsules, respectively. Since pure PCM is in direct contact with the EPCM shell until the air can diffuse, it has the highest rate of heat transfer into the PCM of the three cases presented specifically during the initial conduction-dominated phase.

The random void distribution presents a middle ground between the central and upper voids. Like the central void the PCM is in direct contact with the capsule shell. However the presence of air throughout the PCM lowers the effective thermal conductivity which results in a slower conductive heat transfer rate. As the PCM melts, the air and $NaNO_3$ phases separate which increases the strength of the natural convection which occurs within the molten PCM. The random void melts 22% slower than the central void and 12% faster than the upper void capsule. The upper void has the longest melting time as the void has an insulating effect and reduces the conductive heat transfer in the top of the capsules where the heat transfer coefficient is the highest.

While under the influence of gravity, one would expect the air to diffuse to the top of the capsule. However, the behavior of the void is not only dependent on the operating conditions of the EPCM capsule but on the PCM that is used as well. Thus, depending on the design of the TES storage system the initial location of the void can impact the performance of the system for numerous cycles. Ideally, one would like for the void always to be located at or near the center of the EPCM capsule as to limit its negative effects on the overall charging time. These results emphasize the impact an internal void has on the overall heat transfer within EPCM capsules. Additionally, the initial location of the void has a profound effect on both the spatial and temporal evolution of the solid-liquid interface. In order to evaluate the performance of EPCM capsules under realistic operating conditions, a numerical model that accounts for all aspects of the internal (natural convection and an internal void) and external (convective boundary condition) heat transfer must be considered.

CHAPTER VII: PILOT SCALE EPCM-BASED LATENT HEAT TES SYSTEM

A heat transfer analysis of a pilot scale EPCM-based latent heat TES system that was designed and tested by Zheng at al. [23] was conducted. Unlike in previous investigations, the heat transfer within the EPCM capsules as well as the exterior flow is modeled simultaneously to capture the full behavior of the system.

7.1 System Description

The designed test section has a height of 111.8 cm, a width of 26 cm, and a depth of 9.3 cm. The walls of the test section are stainless steel 304 with a thickness of 3.175 mm. The EPCM capsules are 7.62 cm in diameter with a length of 25.4 cm. A schematic of the system and the computational domain considered are presented in Figure 27. A three-dimensional model of one-quarter of the test section was used as the computational domain. To reduce the computational requirements, the 15 cm of insulation was neglected and the thickness of the test section wall was doubled to account for the sensible heat stored in both the walls and insulation over the course of the experiment. Additionally, heat lost from the test section to the surrounding was ignored and a perfectly insulated boundary condition applied.

The 10 EPCM capsules are horizontally oriented and vertically stacked within the test section. In order to match the experimental flow rate of 0.038 kg/s, a mass flux boundary condition of 1.6 kg/m^2s was applied at the inlet of the numerical model. The temperature of the entering HTF is shown in Figure 28, where it increases from room temperature to 440 °C. The initial temperature of the system was 22 °C. $NaNO_3$ was used as the PCM, stainless steel was used for the capsule shell, and air was used as the HTF. The thermal properties used are listed in Table 7. Each capsule was filled with

1.77 kg of $NaNO_3$, therefore a 26% void is considered within each capsule. The turbulent flow in the test section was modeled using the *k-ω* SST model and the enthalpy-porosity and VOF methods were used to capture the heat transfer within the EPCM capsules. The cut cell meshing technique in Ansys was employed with a max face size of 6.4×10^{-3} m resulting in 4.3 million quadrilateral elements with 5.3 million nodes.

Table 7. Temperature dependent properties of air, stainless steel, and $NaNO_3$ (all temperatures are in Kelvin)

Air	
Density (kg/m^3)	$-5.74\times10^{-9}T^3+1.20\times10^{-5}T^2-9.13\times10^{-3}T+2.98$ [75]
Specific Heat Capacity (J/kg K)	$3\times10^{-5}T^2-1.34\times10^{-2}T+1006.5$ [75]
Thermal Conductivity (W/m K)	$2.201\times10^{-8}T^2+6.31\times10^{-5}T+4.79\times10^{-3}$ [75]
Viscosity (kg/m s)	$4\times10^{-8}T+7.98\times10^{-6}$ [75]
Stainless Steel 304	
Density (kg/m^3)	7,900 [75]
Specific Heat Capacity (J/kg K)	$-0.0002T^2+0.4101T+376.44$ [75]
Thermal Conductivity (W/m K)	15 [75]
$NaNO_3$	
Density (kg/m^3)	$2341.56-0.76T$ [78]
Solid Specific Heat Capacity (J/kg K)	1,588 [10]
Liquid Specific Heat Capacity (J/kg K)	1,650 [10]
Solid Thermal Conductivity (W/m K)	0.55 [84]
Liquid Thermal Conductivity (W/m K)	0.68 [85]
Latent Heat (kJ/kg)	162.5 [10]

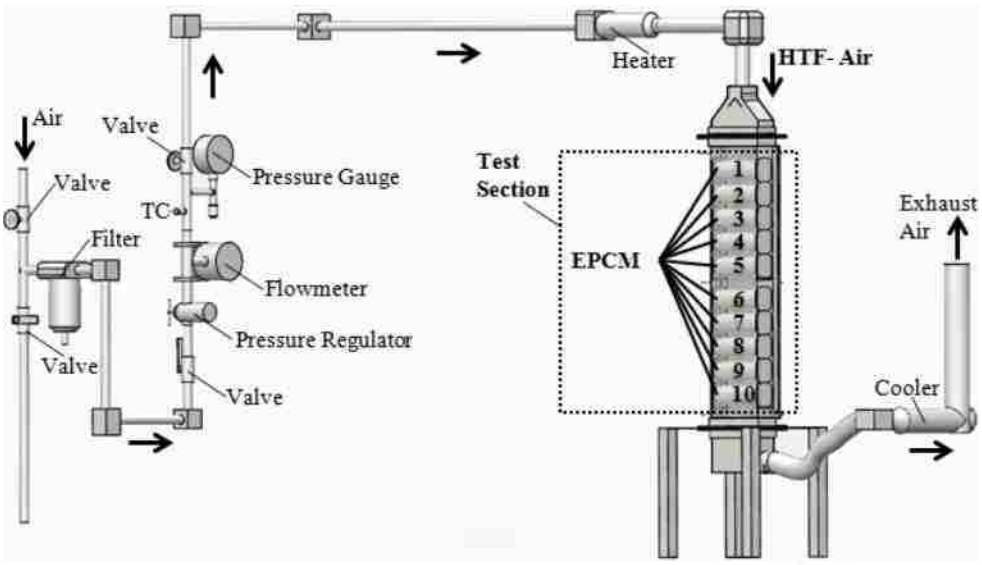

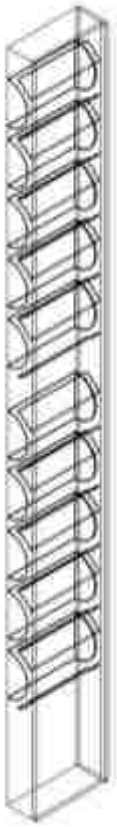

Figure 27. Schematic of test section [24](upper), 10 EPCM capsules with deflectors [24] (left), and computational domain (right)

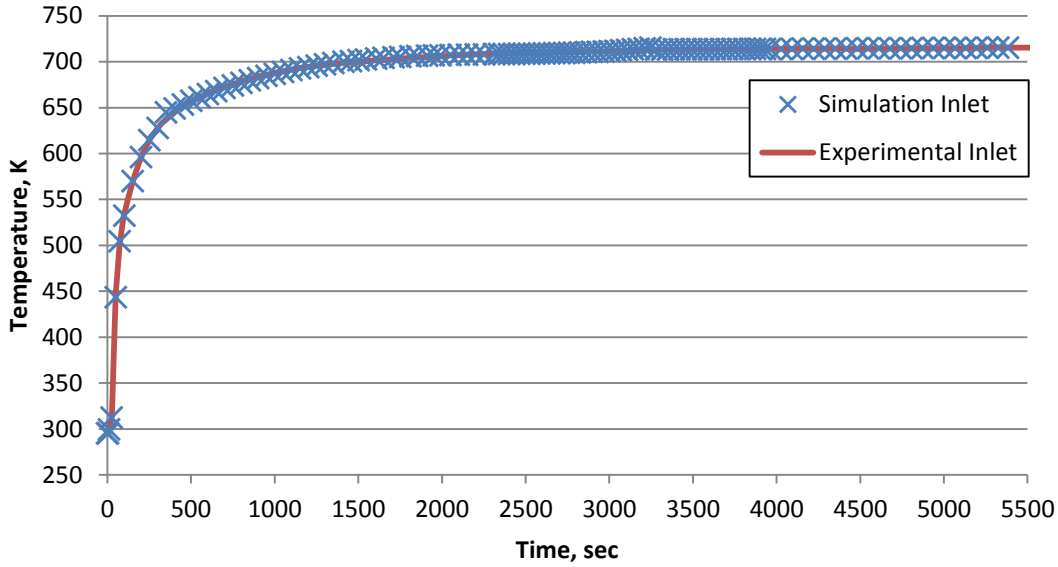

Figure 28. Transient inlet temperature of the test section for both the experiment and simulation

7.2 HTF Results

The chosen mass flow rate results in a superficial inlet velocity of 3.2 m/s and a Re of 3285 based on capsule diameter; thus the flow within the test section is turbulent. To prevent the large wakes that occur behind a cylinder when it is placed in a turbulent flow, metal deflectors are employed. These deflectors direct the HTF around the capsules minimizing the wake region as seen in Figure 29. The highest velocity occurs 90 degrees down from the top of the capsule with a velocity magnitude 6 times that of the inlet velocity, Figure 29. A stagnation point occurs at the top and bottom of the capsules. A small fraction of the HTF is able to bypass the capsules into the gap between the deflectors and the test section wall. This fluid expands and forms a weak recirculating vortex between the deflectors. A larger vortex forms between the fifth and sixth capsules where there is a larger space between the capsules. However, as the bulk of the HTF is still directed onto the sixth capsule and a large wake is

prevented, the deflections are performing as intended. A similar vortex was seen at the bottom of the test section after the tenth capsule. Additionally, two counter-circulating vortices form between each capsule near the colder test section wall.

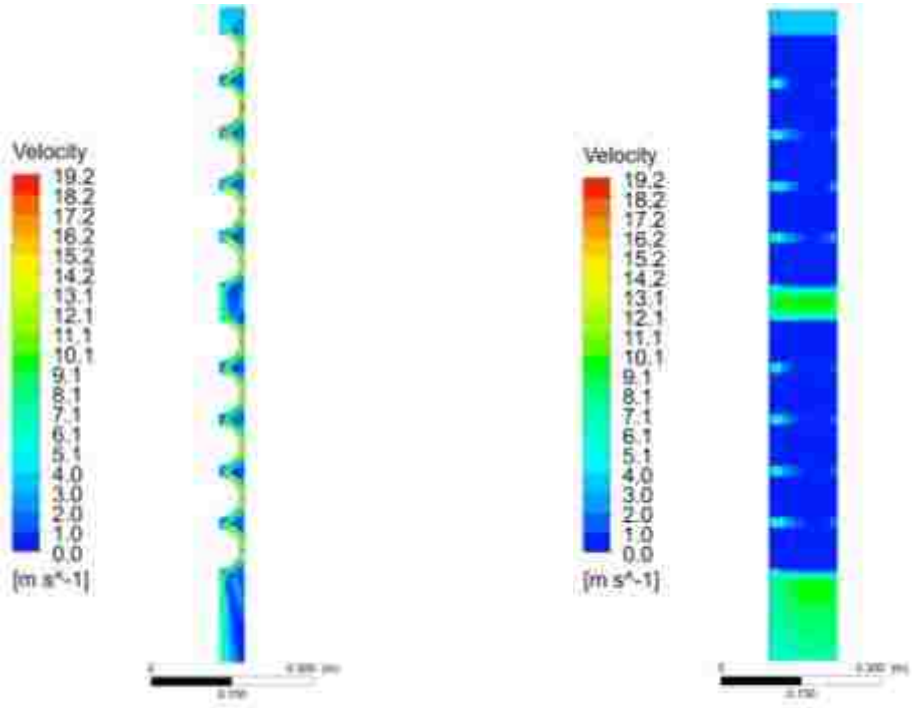

Figure 29. Velocity magnitude in the XY (left) and YZ (right) symmetry planes at 4,000 sec (Re = 3285)

The hot HTF enters the test section where it is directed around the EPCM capsules by the deflectors. As the HTF begins to transfer its energy to the cold EPCM capsules a large temperature drop over the length of the test section occurs, Figure 30a. Although the HTF enters with a uniform temperature distribution across the width of the test section, there is a diagonal temperature gradient in the HTF from the bottom corner upwards towards the middle of the EPCM capsules, Figure 30b. As the charging process continues and the capsules begin to melt, the temperature drop experienced by the HTF decreases, Figure 30c. The temperature gradient in the HTF

around the capsules has decreased particularly in the upper portion of the test section, Figure 30d. Additionally, there is a linear temperature distribution forming in the outlet region due to the velocity distribution resulting from the use of the deflectors as the warm HTF is directed towards the center of the system.

Midway through the charging process, there is now only an approximate 100 degree temperature drop in the HTF as all the capsules have begun to melt, Figure 30e. There is also now a near-uniform temperature distribution around the first five capsules with a decrease in the gradient around the last five capsules in addition to a decrease in the gradient at the outlet of the system, Figure 30f. After 3000 sec, the first three capsules are completely melted resulting in the inlet portion of the test section having a uniform temperature close to that of the inlet temperature, Figure 30g. There is now only a small gradient remaining in the last five capsules, Figure 30h. Near the end of the charging process only the last three capsules are not completely melted leading to the entire top half of the system having the same temperature as the inlet, Figure 30i. A small temperature gradient is still present around the last three capsules as they continue to store energy, Figure 30j. Furthermore, the temperature change across the width of the outlet has decreased significantly.

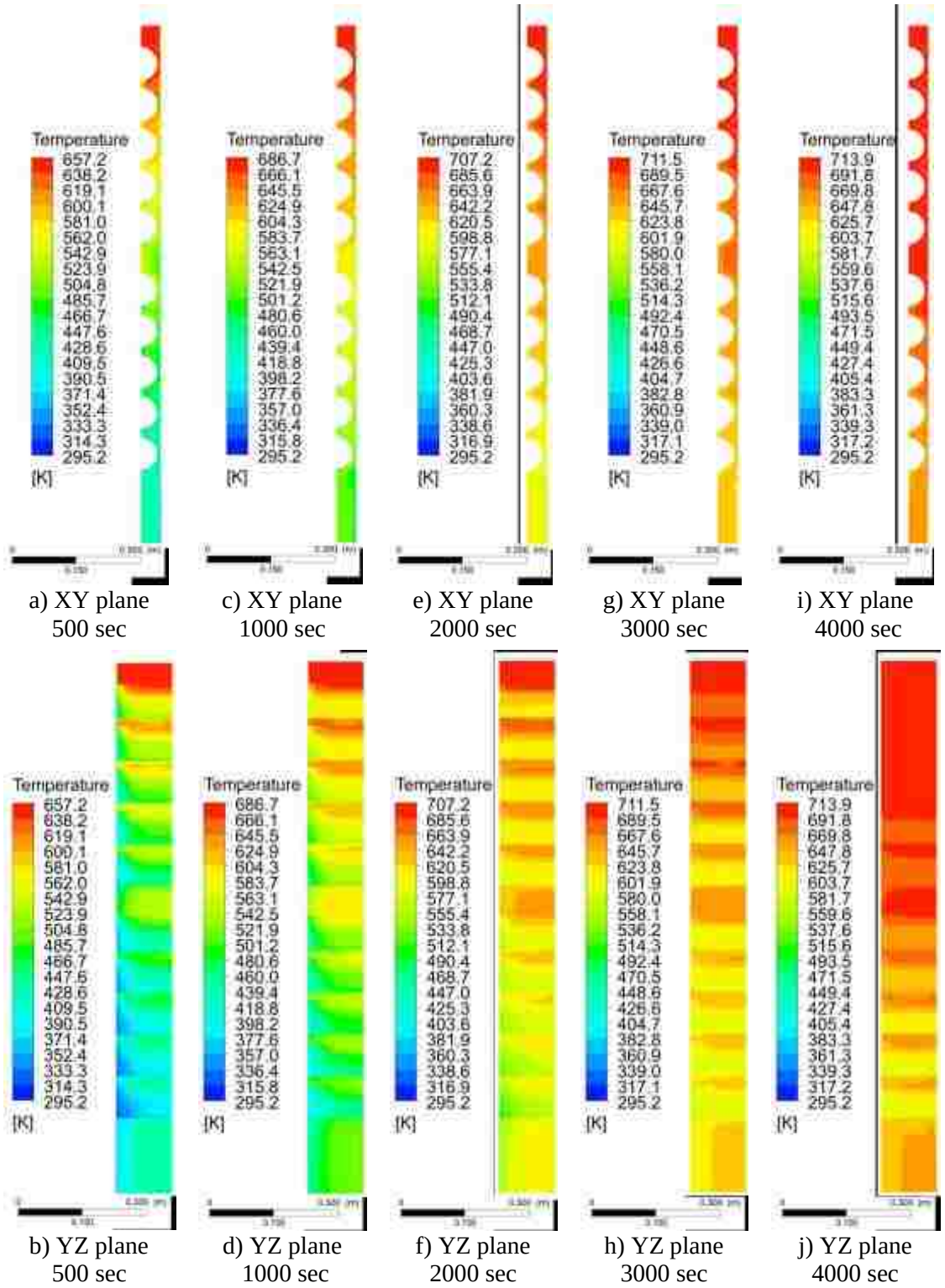

a) XY plane 500 sec | c) XY plane 1000 sec | e) XY plane 2000 sec | g) XY plane 3000 sec | i) XY plane 4000 sec

b) YZ plane 500 sec | d) YZ plane 1000 sec | f) YZ plane 2000 sec | h) YZ plane 3000 sec | j) YZ plane 4000 sec

Figure 30. Isotherms in the HTF in the XY (upper) and YZ (lower) symmetry planes

7.3 EPCM Capsule Results

The use of the deflectors promotes a near uniform heat transfer coefficient around the 10 EPCM capsules, but the presence of the void at the top of the capsule reduces the heat transfer rate in the upper portion of the capsules. This results in the XY plane isotherms being “U”-shaped instead of circular as seen during the initial conduction-dominated sensible heating phase, Figure 31a. In the YZ plane there is a nearly symmetric temperature variation about the center of the capsules with a higher temperature variation in the upper portion of the capsule due to the presence of the air void; additionally the warmer capsule end leads to “L”-shaped isotherms in the solid PCM, Figure 31b. As the PCM melts, convection in the molten PCM accelerates the heat transfer rate in the upper portion of the EPCM capsule causing the isotherms first to become vertical and then angle inward as seen in the first five capsules, Figure 31c. The isotherms remain “U”-shaped in the bottom five capsules as there has not been a significant amount of melting to allow for convection to take effect. In a similar manner, convection has increased the heat transfer near the capsule end rounding the isotherms inward in the first and second capsules whereas the isotherms remain unchanged in the bottom capsules, Figure 31d.

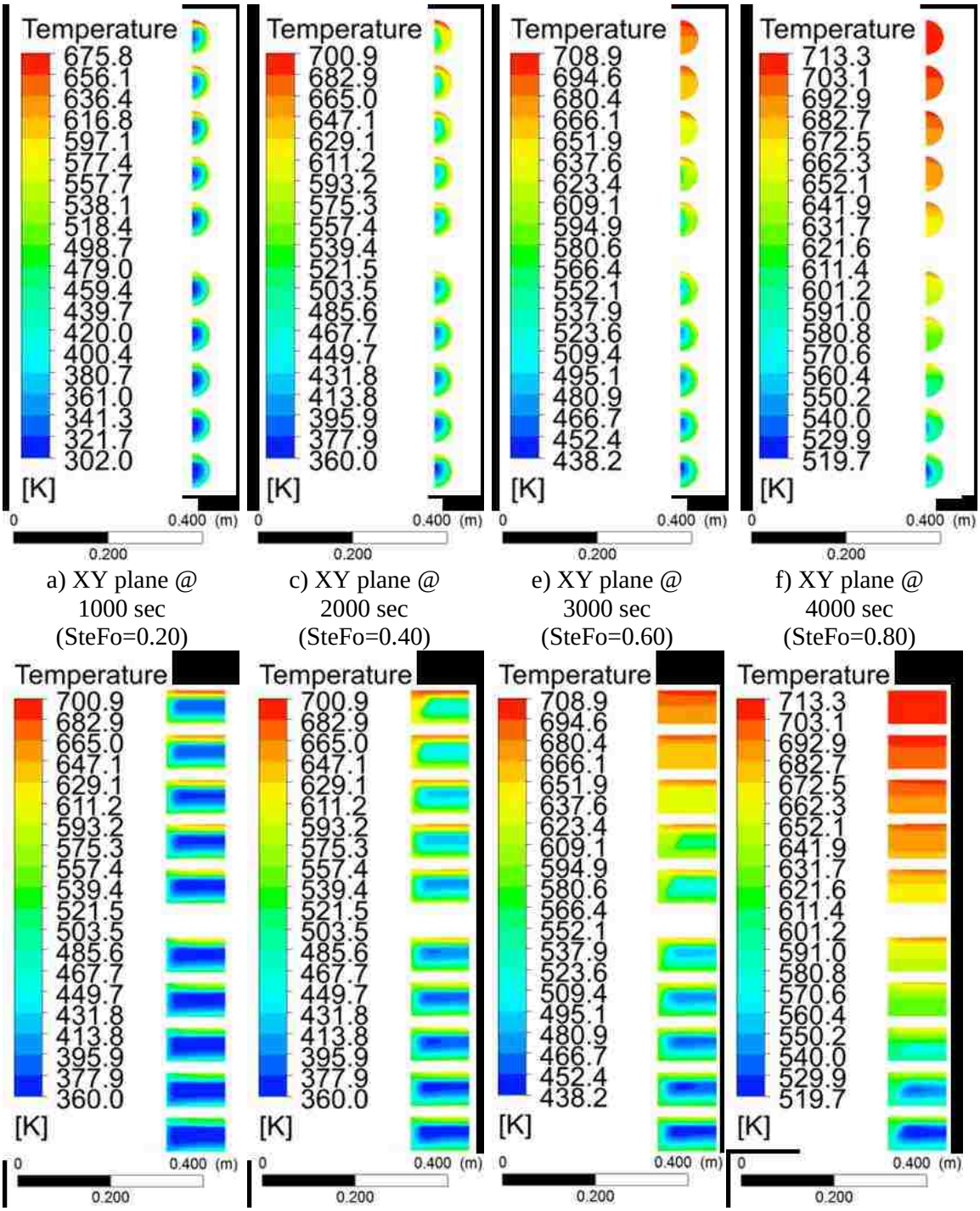

a) XY plane @ 1000 sec (SteFo=0.20)

c) XY plane @ 2000 sec (SteFo=0.40)

e) XY plane @ 3000 sec (SteFo=0.60)

f) XY plane @ 4000 sec (SteFo=0.80)

b) YZ plane @ 1000 sec (SteFo=0.20)

d) YZ plane @ 2000 sec (SteFo=0.40)

f) YZ plane @ 3000 sec (SteFo=0.60)

h) YZ plane @ 4000 sec (SteFo=0.80)

Figure 31. Isotherms in the EPCM capsules in the XY (upper) and YZ (lower) symmetry planes

After 3000 sec the first, second, and third capsules are completely melted and therefore the isotherms have become stratified within the capsules in both the XY and YZ planes. Convection in the fourth, fifth, and sixth capsules has started to accelerate the heat transfer in the upper half of the capsules and near the capsule edge in a similar manner seen previously in the first three capsules, Figure 31e and f. The isotherms in the bottom capsules have remained "U"- and "L"-shaped in the XY and YZ planes respectively as those capsules are still in the conduction-dominated sensible heating phase of the charging process. This shape can be seen clearer by examining the liquid fraction. As the charging process nears completion, all but the last three capsules are completely melted; therefore the isotherms in the first eight capsules have become stratified. The same increase in the heat transfer rate from convection has occurred in the ninth and tenth capsules reshaping the isotherms in the same manner as the in the eight previous capsules as they melted, Figure 31g and h. As with the results in the previous chapters, the results presented for the heat transfer within the EPCM capsules have been non-dimensionalized using the product of the Ste and Fo number.

All ten EPCM capsules exhibit very similar evolution in the velocity field over the course of the charging process, therefore only the results for the fifth and sixth capsules are shown in Figure 32 for the XY plane and Figure 33 for the YZ plane. Prior to the PCM melting the only convection present in the EPCM capsules are the two recirculating vortices present in the air void in the XY plane, Figure 32a, and the vortex in the YZ plane near the capsule edge, Figure 33a. After 2000 sec the fifth and sixth capsules have just begun to melt and therefore there is insufficient molten PCM for convective cells to form, Figure 32b. After 2500 sec however, two vortices have

formed in the molten PCM, one along the capsule shell and the other along the colder solid PCM in the XY plane, Figure 32c. As there is a larger fraction of molten PCM in the fifth capsule than the sixth, the vortices in the fifth capsule are stronger. In the YZ plane, a vortex has begun to form along the edge of the fifth EPCM capsule, Figure 33b.

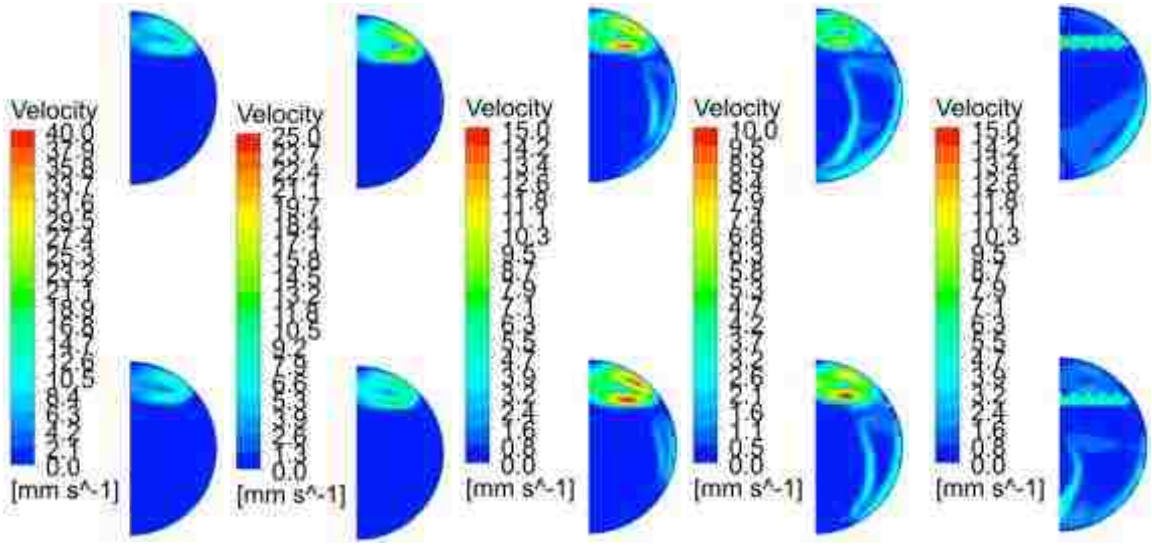

1000 sec (SteFo=0.20) | 2000 sec (SteFo=0.40) | 2500 sec (SteFo=0.50) | 3000 sec (SteFo=0.60) | 3500 sec (SteFo=0.70)

Figure 32. Velocity magnitude in the fifth and sixth EPCM capsules in the XY plane

By 3000 sec a significant portion of the PCM has melted in both capsules and the two vortices along the capsule shell and the remaining solid PCM have intensified, Figure 32d. The vortex at the end of the fifth capsule has spilt in two with one vortex remaining along the hotter capsule end cap and the other around the remaining solid PCM. Additionally, small recirculating vortices have formed in the bottom of the fifth EPCM capsule, accelerating melting, Figure 33c. Furthermore, the vortices at the end of the capsule have begun to form in the sixth capsule as it melts. After the fifth capsule has completely melted, a small vortex remains along the bottom capsule edge

in addition to several small vortices that are present at the PCM-void interface and the PCM is at a lower temperature compared to the air void. In the sixth capsule, the two previously seen vortices remain as well as the same small vortices forming along the PCM-void interface, Figure 32e. While there is minimal velocity in the fifth capsules in the YZ plane, in the sixth capsule however, the vortices along the capsule end have intensified as the PCM melts and small vortices have begun forming in the bottom of the capsule, Figure 33d. In both capsules the convection present at the PCM-void interface is seen along the entire length of the capsule.

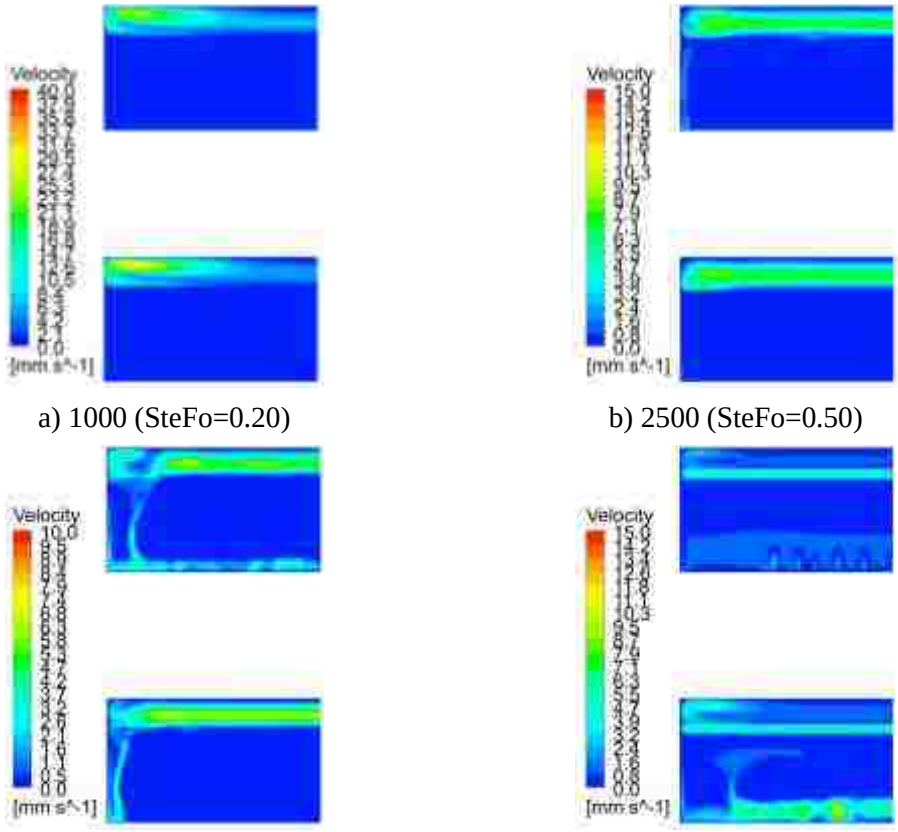

a) 1000 (SteFo=0.20)

b) 2500 (SteFo=0.50)

c) 3000 (SteFo=0.60)

d) 3500 (SteFo=0.70)

Figure 33. Velocity magnitude in the fifth and sixth EPCM capsules in the YZ plane

The first EPCM capsule begins to melt at 750 sec and by 1000 sec the first three capsules have begun to melt. The PCM begins to melt along the capsule edge at the PCM-air interface, Figure 34a and b. As the charging process continues, melting has started in all capsules. In the first three capsules, convection in the molten PCM has accelerated the melting rate in the upper portion of the capsule causing the solid-liquid interface to slant inward, Figure 34c. In the fourth and fifth capsules the solid-liquid interface is "U"-shaped like the isotherms. In the YZ plane, melting starts at the capsule end and due to convection the solid-liquid interface becomes curved as the melting front propagates towards the center of the capsule, Figure 34d.

After 3000 sec the first three capsules are entirely melted. A small oval-shaped solid remains near the bottom of the fourth capsule as convection in the molten PCM accelerated melting in the upper portion of the capsule. The solid-liquid interface in the bottom five capsules evolves in the same manner as previously seen in the upper capsules where convective effects have accelerated melting in the upper half of the capsule angling the solid-liquid interface inward, Figure 34e. Additionally convection in the molten PCM has accelerated melting along the capsule bottom and near the capsule end, Figure 34f. As the charging process nears completion, only the last three capsules remain un-melted. In the eighth capsule a small circular solid region remains near the bottom of the capsule in the XY plane and in the YZ plane the remaining solid is an oblong oval due to the effects of convection, Figure 34h. The solid-liquid interface in the last two capsules exhibits the same characteristics that were seen in the previous eight capsules.

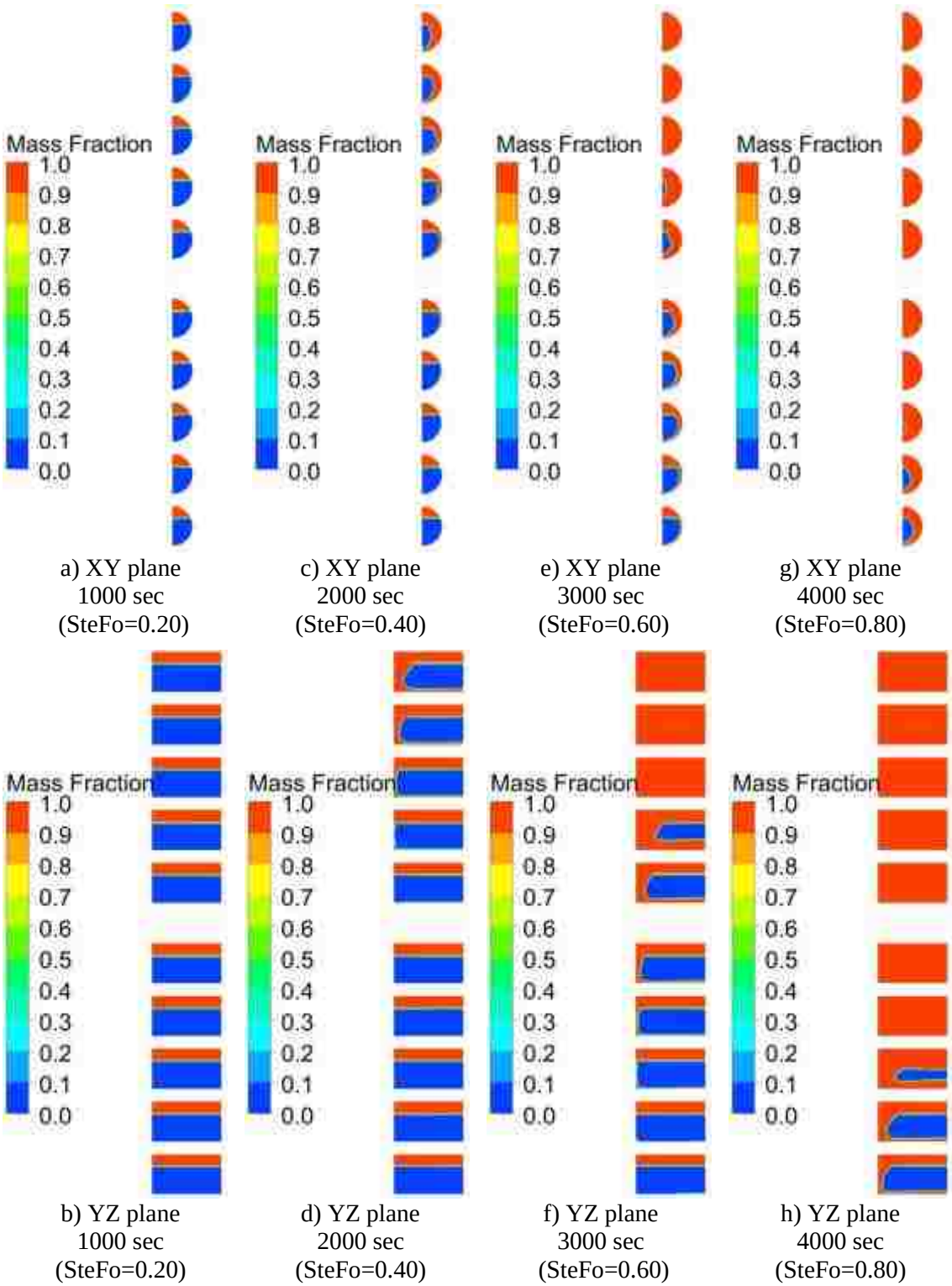

a) XY plane 1000 sec (SteFo=0.20)

c) XY plane 2000 sec (SteFo=0.40)

e) XY plane 3000 sec (SteFo=0.60)

g) XY plane 4000 sec (SteFo=0.80)

b) YZ plane 1000 sec (SteFo=0.20)

d) YZ plane 2000 sec (SteFo=0.40)

f) YZ plane 3000 sec (SteFo=0.60)

h) YZ plane 4000 sec (SteFo=0.80)

Figure 34. Liquid fraction in the EPCM capsules in the XY (upper) and YZ (lower) symmetry planes

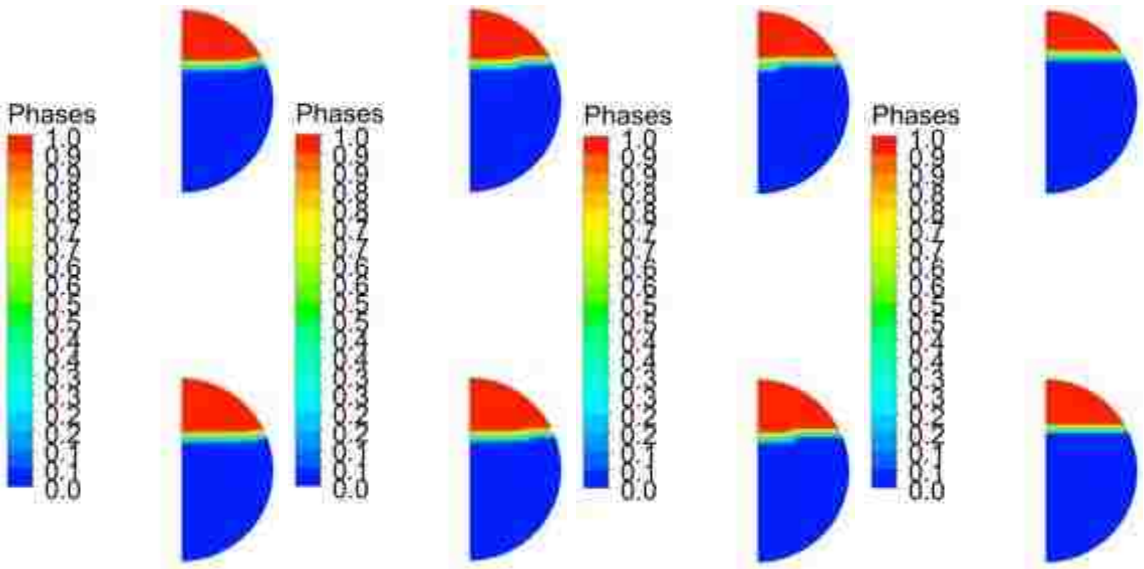

a) 2000 sec (SteFo=0.40) b) 2500 sec (SteFo=0.50) c) 3000 sec (SteFo=0.60) d) 3500 sec (SteFo=0.70)

Figure 35. Void-PCM interface in the XY plane in the fifth and sixth EPCM capsules

The 10 EPCM capsules consecutively experience the same evolution in the melting front; therefore the results for the expansion of the PCM upon melting are examined only for the fifth and sixth capsules. When the PCM first begins to melt it expands into the air void causing the edge of the PCM-air interface to push upwards, Figure 35a. The void now occupies 22% of the fifth capsule whereas it occupies 23% in the sixth capsule as a greater portion of the PCM has melted in the fifth capsule. At this point in time, the PCM has yet to melt near the capsule end and therefore the PCM-void interface remains completely flat, Figure 36a. As the PCM continues to melt it further compresses the void to 21.6% and 22% in the fifth and sixth capsule respectively, Figure 35b. After 2500 sec the PCM has begun to melt near the capsule ends pushing the PCM-void interface upwards at the end of the capsule, Figure 36b. The fifth capsule is about halfway melted after 3000 sec which has compressed the void to 20.6% whereas the void occupies 21.6% in the sixth capsule, Figure 35c and

Figure 36c. Once the PCM is fully melted in both capsules the void has been compressed to nearly 30% of its original size and now occupies 19% of the capsule volumes, Figure 35d & Figure 36d.

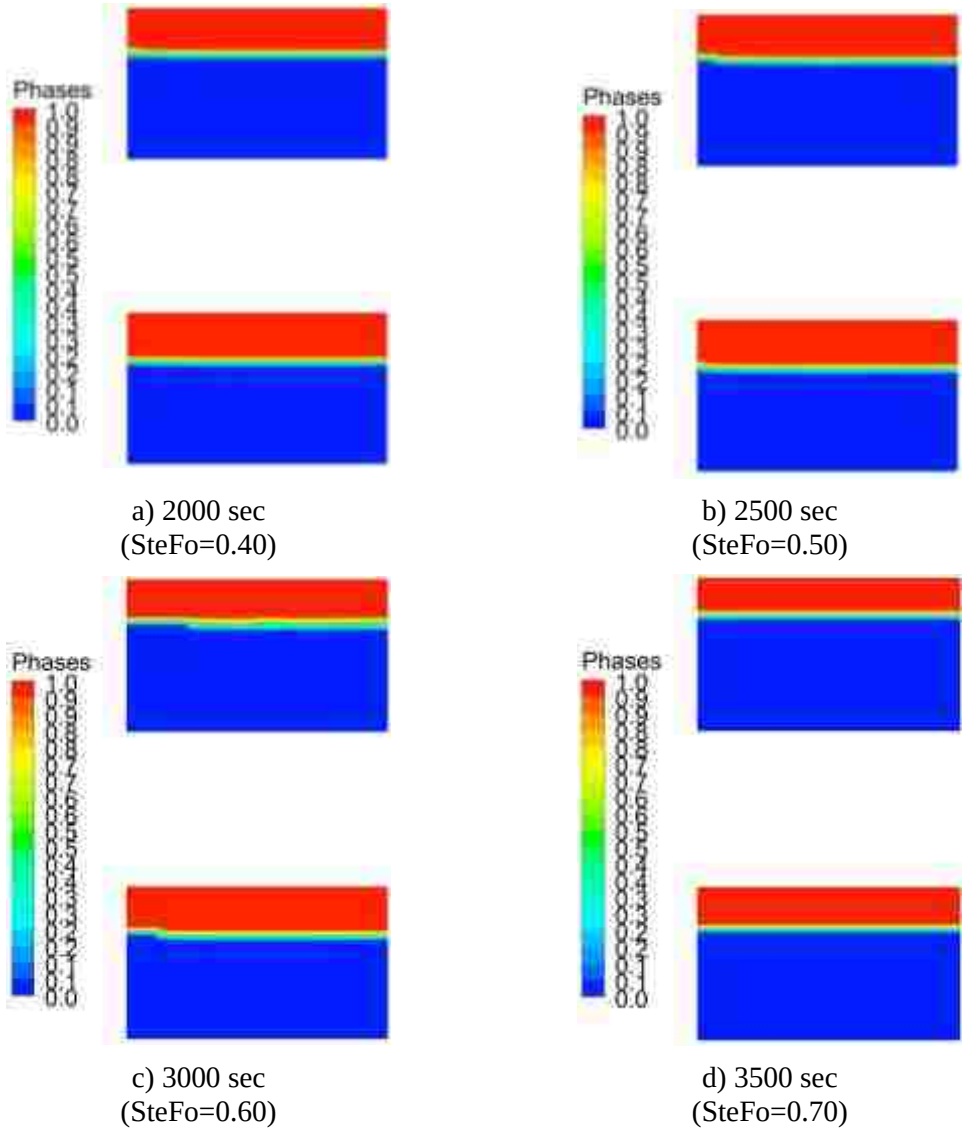

Figure 36. Void-PCM interface in the fifth and sixth EPCM capsules in the YZ plane

7.4 Comparison of Simulation with Experimental Results

A comparison of the experimental and predicted temperatures at the inlet and outlet of the test section as well as 6 mm above the bottom of the tenth capsule are presented in Figure 37. During the first 2000 sec the difference between the predicted and experimental results for the temperature in the tenth capsule was less than 3%. After the tenth capsule starts to melt the simulation begins to predict a higher temperature than the experimental results. A similar trend is seen with the outlet temperature of the system. Additionally, the simulation predicts a total melting time of 4612 sec which is 7.6% faster than the 4992 sec melting time indicated by the experiments. After the capsules are fully melted both the experiments and simulations show the same rate of temperature increase within the capsules offset by the difference in melting time. Given the good agreement during the solid sensible heating phase the likely cause of the faster predicted melting time is the use of an incorrect value for the latent heat of $NaNO_3$. Bauer et al. [81] reported that the average value is 172 kJ/kg which is 8% higher than the 162.5 kJ/kg that was used during the numerical analysis.

A total of 22 MJ of energy was lost by the HTF over the course of the charging process. The EPCM capsules stored a total of 17.5 MJ which accounts for 79.5% of the energy lost by the HTF. The remaining 20.5% goes into sensibly heating the test section walls and deflectors. The total energy stored in the capsules is 4.9% less than the 18.4 MJ reported by Zheng et al. [23]; however it is within their estimated calculation error. Of the energy stored by the capsules, 3.3 MJ is stored in the stainless steel capsule shell and 14.2 MJ is stored in the 17.7 kg of $NaNO_3$ which accounts for 81.1% of the total energy stored by the capsules. This is 13.6% higher than the 12.5

MJ reported by Zheng et al. [23] which is likely caused by the way Zheng et al. calculated the total energy storage as they only measured the temperature of the tenth capsule and therefore had to estimate the temperature distribution within the test section based on the inlet and outlet temperatures. Furthermore, of the 142 MJ of energy stored in the $NaNO_3$, 20.3% is attributed to the latent heat of fusion.

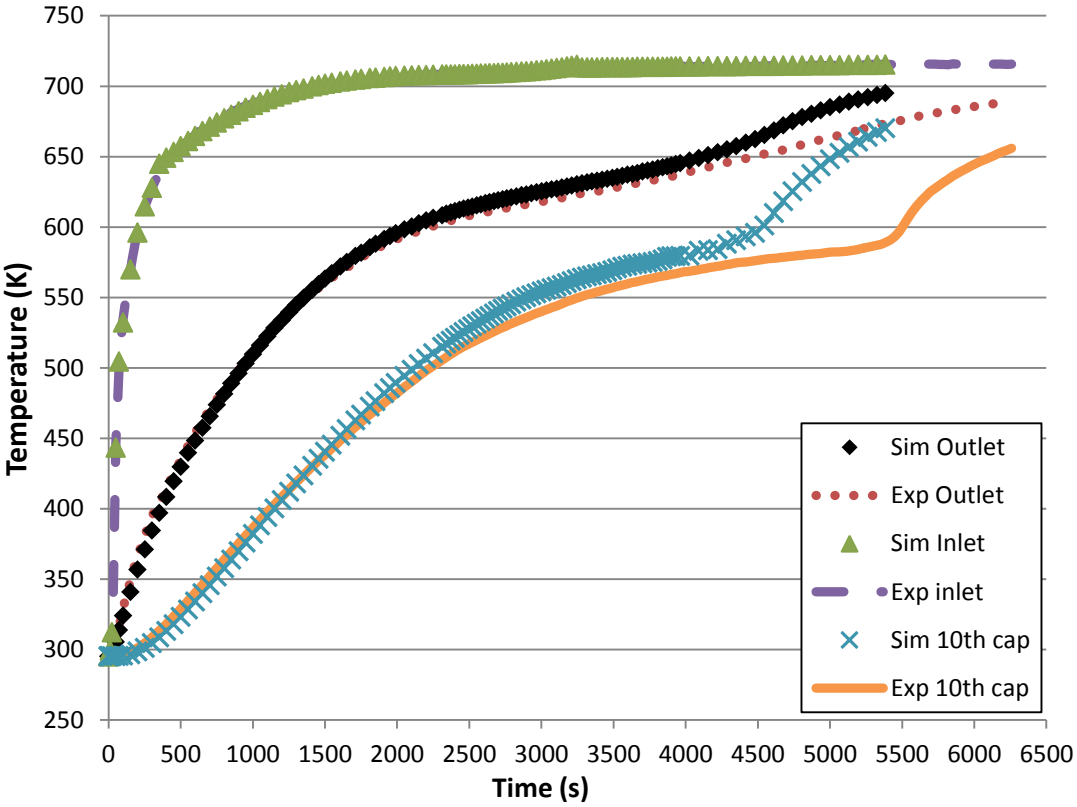

Figure 37. Comparison between experimental and numerical results for the inlet, outlet, and tenth capsule temperature

7.5 Conclusions

A numerical analysis of a pilot scale EPCM-based latent heat TES system was conducted. In order to improve the heat transfer around the capsules and avoid the large wake that is present with cross flow around cylindrical capsules, metal deflectors are employed. Despite the uniform heat transfer around the capsules promoted by the

deflectors the presence of the void at the top of the capsule reduces the heat transfer rate in the upper half of the capsule. This leads to the isotherms being “U”-shaped in the solid PCM while conduction is the dominant mode of heat transfer. Once the PCM begins to melt, natural convection in the molten PCM increases the heat transfer rate accelerating melting along the PCM-void interface. This causes the isotherms, and in turn the solid-liquid interface, to slant inward in the upper portion of the capsule. While the capsules initially begin melting along the capsule edge in the center of the channel, the increased heat transfer from the capsule end to the PCM results in the solid-liquid interface propagating from the ends towards the center of the capsule. In addition to the vortices that are present in the air void, two recirculating vortices form in the molten PCM, one along the capsule edge and the other around the remaining solid PCM, both in the XY and YZ planes. The 10 EPCM capsules consecutively experience the same evolution in the solid-liquid interface and therefore show the same expansion of the PCM and compression of the void from an initial 26% to 19% when the PCM is fully melted.

Good agreement is seen between the predicted and measured temperature of the tenth capsule and test section outlet during the sensible heating phase of the charging process. However, the simulation predicted a total melting time that was 8% faster than indicated by the experimental results. The good agreement obtained during the sensible heating phase indicates that an incorrect value of the latent heat of fusion was used during the simulation. Indeed the value established previously via calorimetry experiments is 8% lower than the average value reported in literature. After melting has completed and the PCM begins to super heat both the predicted and

measured temperatures show the same rate of temperature increase just offset in time by the early completion of melting. It should be noted that the value of latent heat used only slightly under predicts the total energy stored due to the large fraction of sensible heat stored by the system.

A total of 17.5 MJ of energy was stored in the 10 EPCM capsules which accounts for 80% of the energy given up by the HTF. The remaining energy goes into sensibly heating the test section walls and the metal deflectors. Of the total energy stored in the EPCM capsules 14.2 MJ is stored in the 17.7 kg of $NaNO_3$ and 3.3 MJ is stored in the stainless steel capsule shells. Additionally, 20% of the energy stored by the PCM is attributed to the latent heat of fusion of $NaNO_3$. Therefore the system is able to store a large fraction of energy supplied by the HTF where a significant portion is from latent heat. Furthermore, if the system was to consist of either a greater number of capsules, larger capsules, or a smaller operating range was applied then the fraction of energy stored via latent heat would be increased. These results demonstrate the scalability of an EPCM-based latent heat TES system for use at CSP plants.

CHAPTER VIII: EXERGY ANALYSIS OF EPCM-BASED TES SYSTEMS

The purpose of a TES system is just not to store energy but to store useful work, therefore performing a first law analysis of the system does not give a true indication of its overall performance and thus a second law analysis is required. The quality of the energy stored is a measure of the useful work that can be produced from the system as it reaches equilibrium with the surroundings, i.e. exergy. A first and second law analysis of an example EPCM-based TES system was conducted to investigate the benefit of using a multi-PCM system as well as to identify key aspects of the system's performance.

8.1 System Description

A two-dimensional simulation on the cross section of a system that consists of 72 76.2 mm diameter EPCM capsules was conducted. The computational domain is presented in Figure 38. A perfectly insulated boundary condition was applied to the exterior wall and therefore irreversibilities associated with heat loss are neglected. A 20% void space was considered within each capsule; however the effect of natural convection in the molten PCM was neglected. The turbulent flow around the capsules was modeled using the *k-ω SST* model and the phase change within the capsules was captured using the enthalpy-porosity method. Air was used as the HTF with an inlet mass flux of 0.2607 kg/m^{2}s. The initial temperature of the system was set to 551 K for the start of the charging cycle. The capsules were then heated for a 12 hour duration where the inlet temperature of the HTF was a constant 611 K. At the end of the charging process, the direction of the HTF was reversed and it now enters the system from the bottom with a temperature of 551 K. The capsules are then allowed to cool

for 12 hours. Six systems are considered: a pure sensible heat system, all $NaNO_3$, all $NaNO_2$, all KNO_3, a 2 PCM system ($NaNO_3$/$NaNO_2$), and a 3 PCM system (KNO_3/$NaNO_3$/$NaNO_2$). The thermal properties used are listed in Table 8.

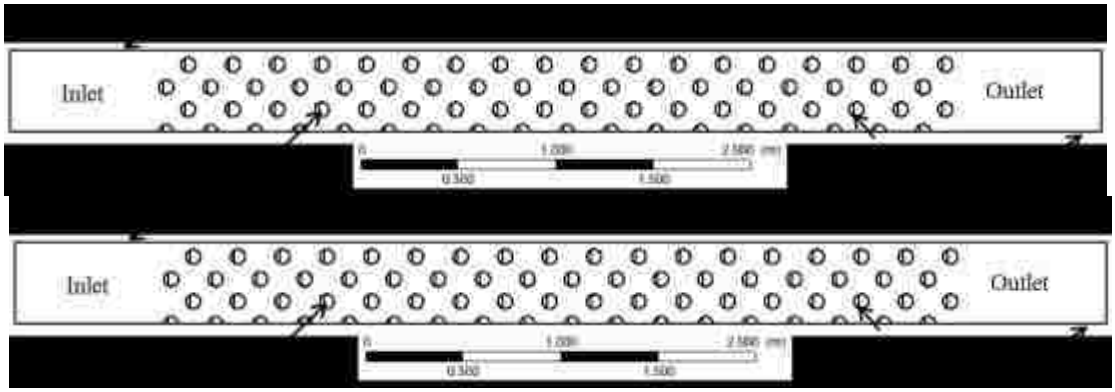

Figure 38. Computational domain used for exergy evaluation

Table 8. Properties of air, $NaNO_3$, $NaNO_2$, and KNO_3 used in exergy simulations

	$NaNO_3$	$NaNO_2$	KNO_3	Air
Density (kg/m^3) [78]	1900 [78]	1812 [86]	1870 [86]	0.5214 [75]
Viscosity (Ns/m^2)	0.00285 [78]	0.002666 [86]	0.002367 [86]	3.65×10^{-5} [75]
Thermal Conductivity (W/mK)	0.550/0.680 [85]	0.665/0.765 [86]	0.481/0.878 [86]	0.0242 [75]
Solid Heat Capacity(kJ/kg)	1.588 [23]	1.733 [86]	1.240 [86]	---
Liquid Heat Capacity(kJ/kg)	1.650 [23]	2.553 [86]	1.341 [86]	1006.4 [75]
Latent Heat (kJ/kg)	162.5 [23]	180.12 [86]	99.73 [86]	---

8.2 Results

8.2.1 Charging Process

The HTF enters the system with a velocity of 0.5 m/s which results in a Re of 544 for the system based on the diameter of the capsule. After an initial transient period, approximately 10 sec, the velocity field reaches steady state conditions and remains unchanged over the remainder of the charging process, Figure 39. The

staggered arrangement of the capsules reduces the wake that forms behind the cylinders as it effectively directs the HTF onto the next row of capsules promoting a uniform heat transfers coefficient around the capsules. A stagnation point forms at the top of the first row of capsules. Additionally, large wakes form behind the last row of capsules. Since the first column of EPCM capsules is next to the wall of the system, there is a slight increase in the velocity magnitude of the HTF between the capsules are the wall compared to the rest of the system. The maximum velocity is 2.8 times the inlet velocity and occurs 90 degrees down from the top of the EPCM capsules.

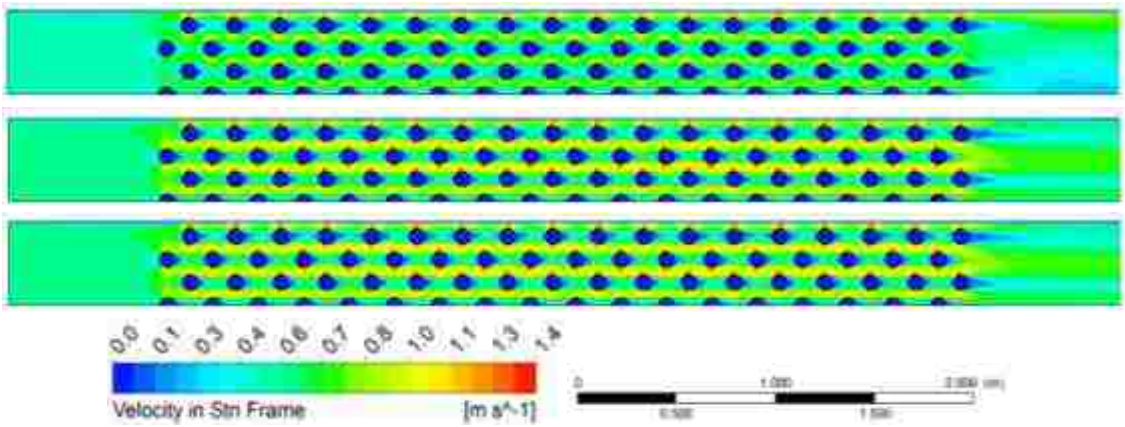

Figure 39. Velocity field after 5 sec (top), 100 sec (middle), and 40,400 sec (bottom). Re = 544

The outlet temperatures for the six systems over the entire charging process are shown in Figure 40. For a system that includes only sensible heating, the outlet temperature asymptotically approaches the inlet temperature over the course of the charging process. For systems that involve a phase change, one would expect the outlet temperature to increase until the melting point is reached at which time the outlet of the system remains relatively constant until the entire system has melted at which time the outlet temperature again begins to increase asymptotically to the inlet

temperature. This behavior was seen for the $NaNO_3$ system. The outlet temperature of the KNO_3 system however behaves in a manner similar to the sensible heat system since the melting point of the PCM (610 K) is extremely close to the inlet temperature. The $NaNO_2$ system on the other hand has the largest difference between the inlet temperature and the melting point as it is only 555 K. This leads to a larger slope in the outlet temperature during the melting process than seen in the $NaNO_3$ case due to the higher heat transfer rate. The 2-PCM system presents a middle ground between the $NaNO_3$ and $NaNO_2$ systems as it has a higher outlet temperature than the $NaNO_2$ system and a higher slope than the $NaNO_3$ system indicating that more energy was being stored at a quicker rate. The 3-PCM system has the most consistent energy storage rate over the course of the charging process and the two inflection points indicate when the $NaNO_2$ and $NaNO_3$ capsules have completed melting. A third point would be seen for the KNO_3 capsules if a higher inlet temperature was used that would allow the capsules to superheat.

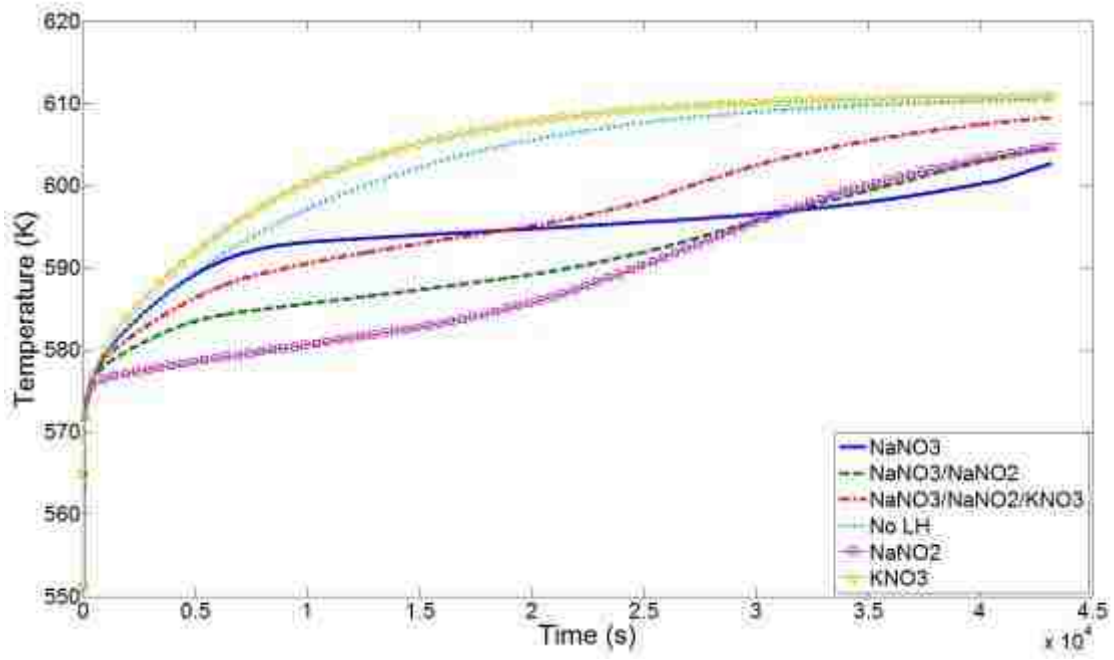

Figure 40. Outlet temperatures during the charging process for the $NaNO_3$ (solid), $NaNO_2$ (square), KNO_3 (circles), $NaNO_3/NaNO_2$ (dashed), $KNO_3/NaNO_3/NaNO_2$ (dash-dot) , and sensible heat (dot) systems

While the evolution of the outlet temperature lends insight into the behavior of the system, a greater understanding can be gained by looking at the temperature evolution of the entire system. The temperature contours for all six systems after 10,400 sec are shown in Figure 41. The sensible heat only and KNO_3 systems have the smallest temperature drop in the HTF fluid across the system with a row-wise linear distribution in the temperature of the EPCM capsules, Figure 41a and d. In the $NaNO_3$ system, a larger temperature difference in the HTF was seen and the capsules are at a uniform temperature of 581 K, Figure 41b. An even greater temperature drop was present in the $NaNO_2$ system and while the EPCM capsules are at a nominal temperature of 555 K, the capsules in the top half of the system show a radial temperature gradient as the molten PCM begins to superheat, Figure 41c. A similar temperature drop was seen in the HTF for the 2- and 3-PCM systems as in the $NaNO_2$

system. For the 2-PCM case, the first 36 capsules are at the 581 K and the bottom 36 capsules are at 555 K which represents the melting point of the respective PCMs, Figure 41e. Additionally a radial temperature gradient forms in the bottom capsules as seen in the $NaNO_2$ system. In the 3-PCM case while the $NaNO_3$ (middle) and $NaNO_3$ (bottom) capsules show a temperature distribution akin to the 2-PCM system, the KNO_3 capsules in the top of the system have a decreasing row-wise nominal temperature as the capsules are sensibly heated to the 610 K melting point, Figure 41e.

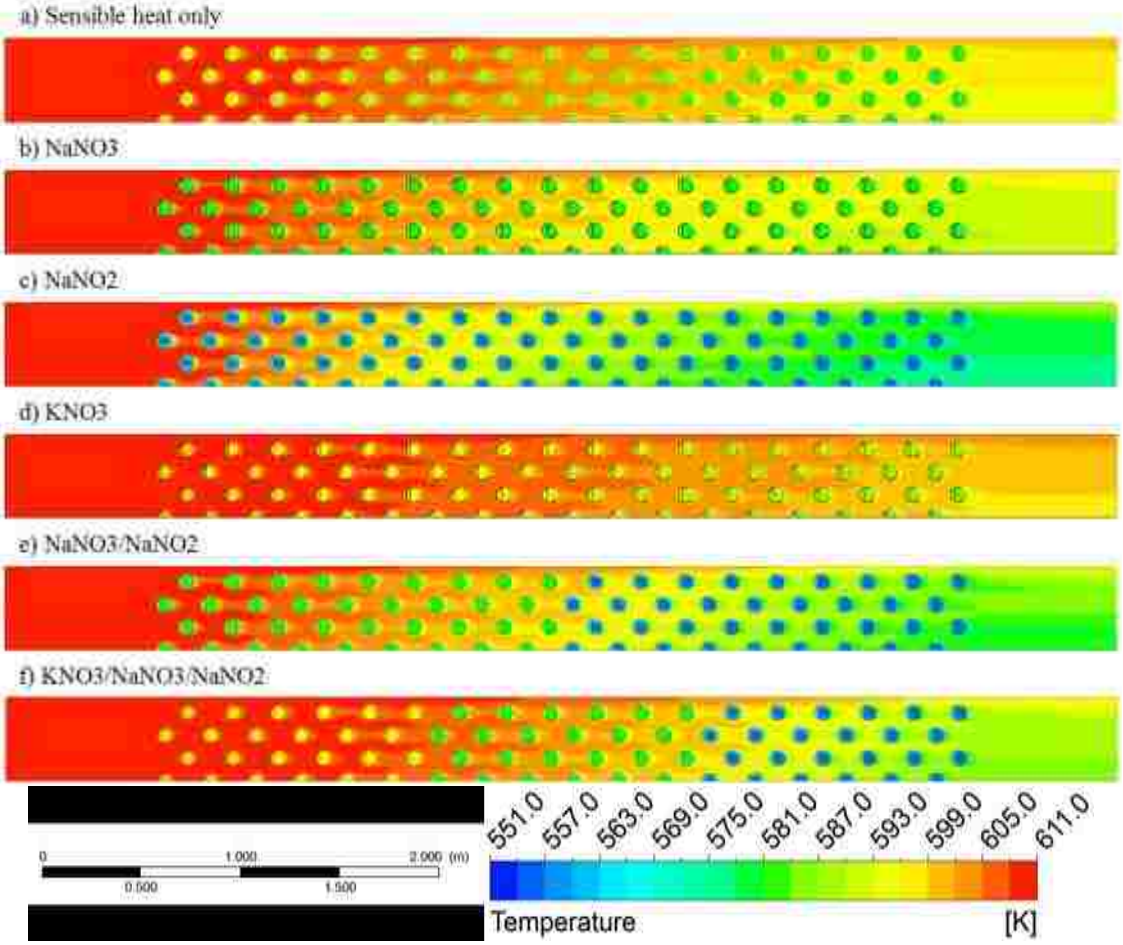

Figure 41. Isotherms at 10,400 sec for a) sensible heat only, b) NaNO3 (SteFo=0.47), c) $NaNO_2$ (SteFo=0.94), d) KNO_3 (SteFo=0.034), e) $NaNO_3$/NaNO2 (SteFo=0.75), f) KNO_3/$NaNO_3$/$NaNO_2$ (0.65) systems

The results presented have been non-dimensionalized in the same manner as in previous chapters using a product of Ste and Fo number where an average value of Ste and Fo numbers are used for the multi-PCM cases.

After 20,400 sec the temperature drop in the HTF of the sensible heat system has greatly reduced, Figure 42a. A greater reduction was seen in the KNO_3 system for both the HTF and EPCM capsules, Figure 42d. A marginal change was seen in the thermal gradient in the HTF for the $NaNO_3$ system as the capsules are still melting, Figure 42b. A similar decrease in the temperature drop within the HTF fluid was seen for the $NaNO_2$ system, however as the capsules in the top of the system have finished melting there is now a row-wise temperature distribution in the capsules and the radial thermal gradient in the bottom capsules has increased, Figure 42c. The temperature drop for the 2-PCM system is between the $NaNO_3$ and $NaNO_2$ cases and while the $NaNO_3$ capsules remain at 581 K, the $NaNO_2$ capsules show the same radial distribution seen in the $NaNO_2$ case, Figure 42e. For the 3-PCM case, the KNO_3 capsules have a row-wise decreasing capsule temperature, the $NaNO_3$ capsules are at 581 K, and the $NaNO_2$ capsules have a radial gradient similar to the 2-PCM case, Figure 42f.

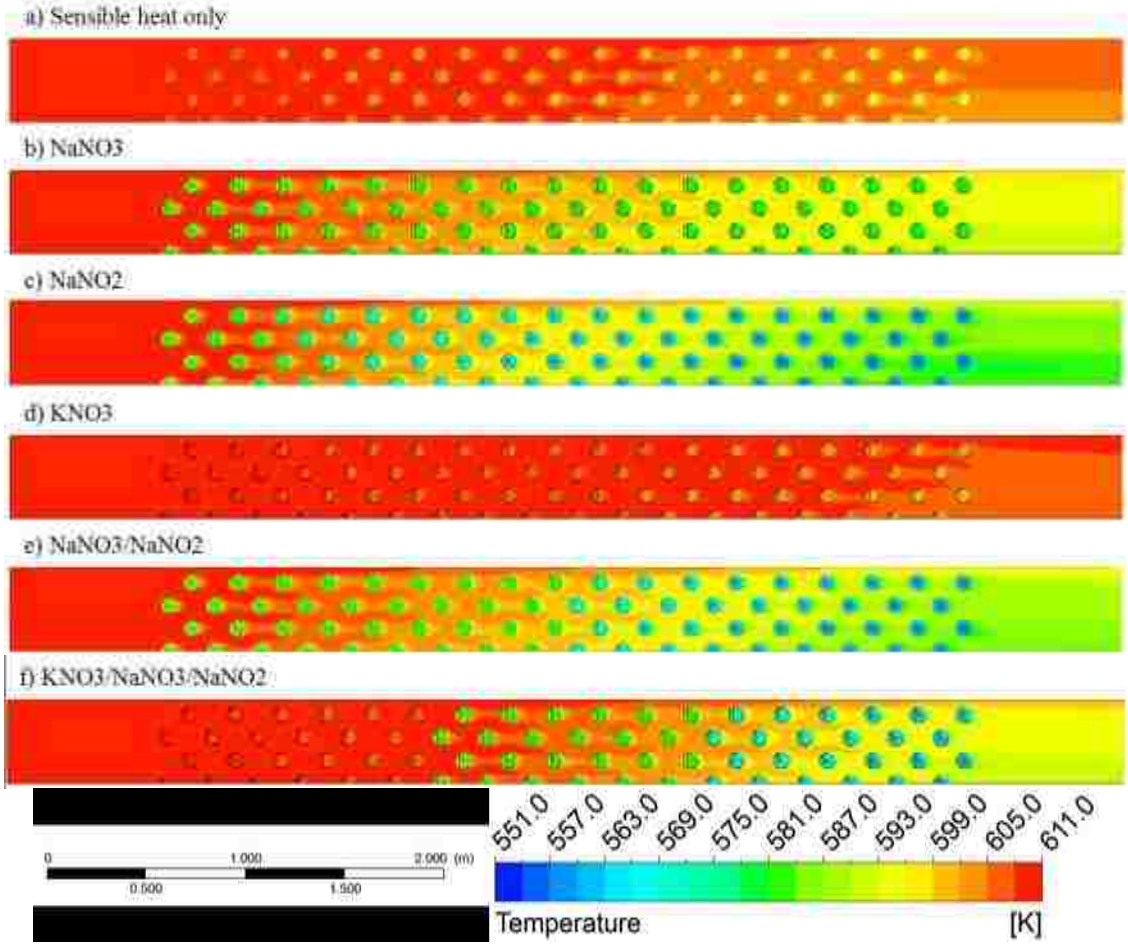

Figure 42. Isotherms at 20,400 sec for a) sensible heat only, b) NaNO3 (SteFo=0.93), c) $NaNO_2$ (SteFo=1.85), d) KNO_3 (SteFo=0.066), e) $NaNO_3/NaNO_2$ (SteFo=1.48), f) $KNO_3/NaNO_3/NaNO_2$ (SteFo=1.27) systems

By 30,400 sec the entire KNO_3 system has reached a near uniform temperature distribution and the EPCM capsules have started melting, Figure 43d. The temperature drop in the sensible heat system has further decreased and now only has a slightly greater temperature drop than the KNO_3 system, Figure 43a. The majority of the capsules in the $NaNO_3$ system are still melting and therefore remain at 581 K; however the first few capsules have completely melted and have begun to superheat yielding a higher capsule temperature, Figure 43b. At this point all of the $NaNO_2$ capsules have finished melting and therefore a row-wise linear temperature

distribution has formed in the capsules, Figure 43c. Although only half of the $NaNO_3$ capsules in the 2-PCM case have melted, a similar temperature distribution was seen within the EPCM capsules as seen in the $NaNO_2$ system, Figure 43e. The temperature drop of the HTF in the $NaNO_3$, $NaNO_2$, and 2-PCM systems are nearly identical. A smaller drop in temperature was seen for the 3-PCM case. Additionally, while the KNO_3 capsules are at a uniform temperature and have just begun melting, the $NaNO_2$ and $NaNO_3$ capsules have finished melting resulting in a row-wise thermal gradient, Figure 43f.

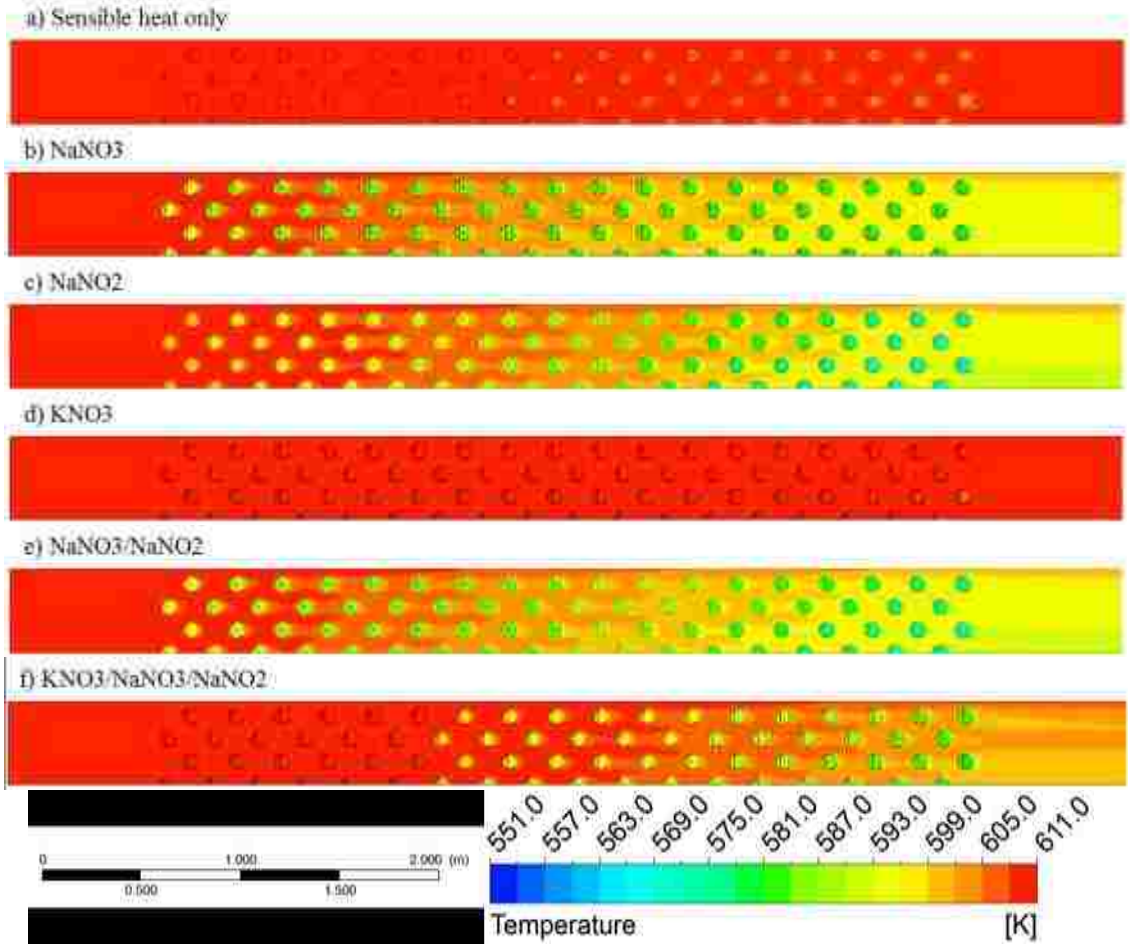

Figure 43. Isotherms at 30,400 sec for a) sensible heat only, b) NaNO3 (SteFo=1.38), c) $NaNO_2$ (SteFo=2.75), d) KNO_3 (SteFo=0.098), e) $NaNO_3$/$NaNO_2$ (SteFo=2.21), f) KNO_3/$NaNO_3$/$NaNO_2$ (SteFo=1.89) systems

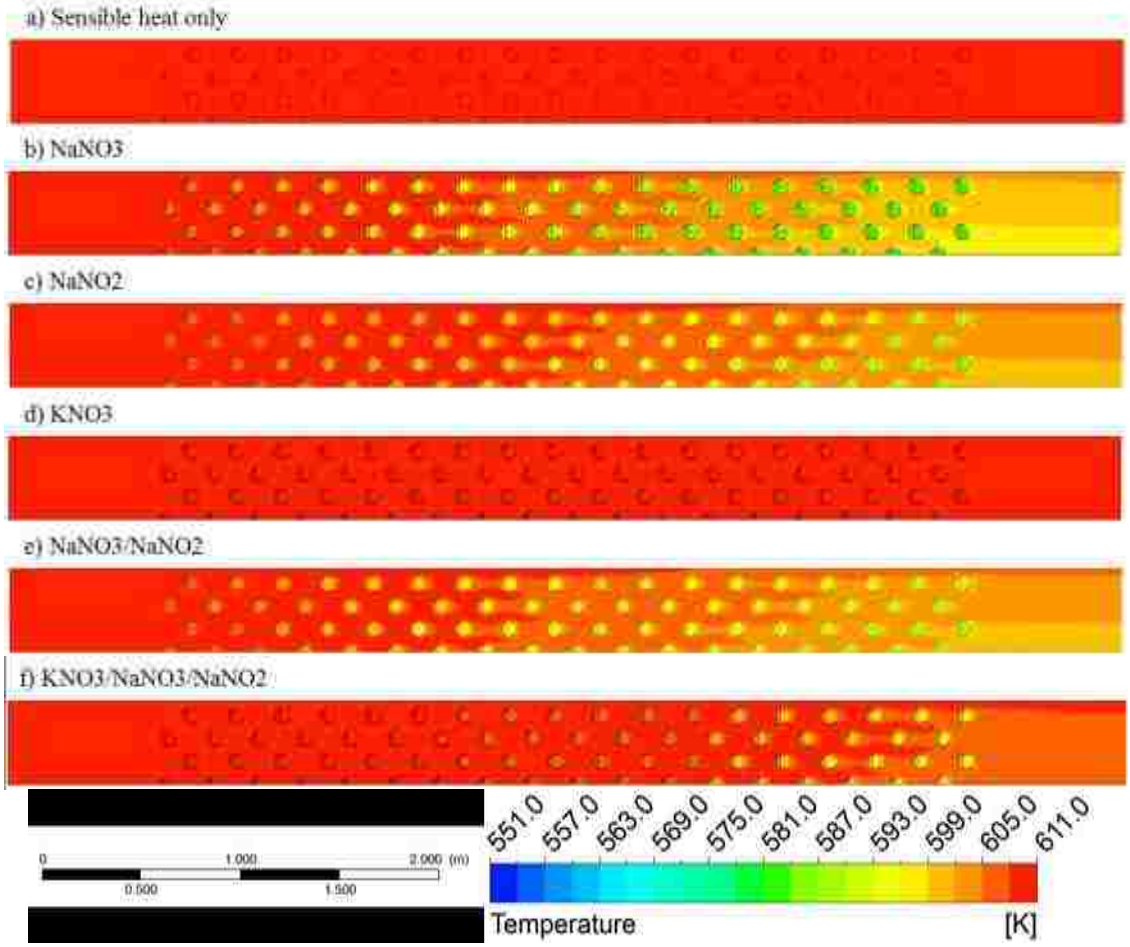

Figure 44. Isotherms at 40,400 sec for a) sensible heat only, b) NaNO3 (SteFo=1.84), c) $NaNO_2$ (SteFo=3.66), d) KNO_3 (SteFo=0.13), e) $NaNO_3/NaNO_2$ (SteFo=2.93), f) $KNO_3/NaNO_3/NaNO_2$ (SteFo=2.52) systems

As the charging process nears completion, the systems are approaching a uniform temperature distribution. There is now no temperature drop in either the sensible heat or KNO_3 systems, Figure 44a and d respectively. The largest temperature in the HTF was seen in the $NaNO_3$ case as the EPCM capsules have still not fully melted, Figure 44b. However, a row-wise temperature distribution has formed in the capsules. This row-wise distribution has decreased in the $NaNO_2$ system, Figure 44c. Again the 2-PCM system resembles the average of the $NaNO_2$ and $NaNO_3$ systems

while the temperature gradient was larger than the $NaNO_2$ case it was smaller than the $NaNO_3$ system and it has completely melted, Figure 44e. While being larger than the pure KNO_3 system, the temperature drop of the 3-PCM system was significantly smaller than the 2-PCM system, Figure 44f. Additionally, as the system is also entirely melted, the row-wise thermal gradient continues to decreases towards a uniform 611 K value.

While the staggered arrangement of the EPCM capsules promotes a near uniform heat transfer coefficient around the capsules, the void space at the top of the capsules acts as an insulator and reduces the rate of heat transfer in the upper half of the capsules. Furthermore since convection within the fluid media was neglected, the solid-liquid interface is "U"-shaped throughout the entire melting process as it propagates radially inward. Note that in the liquid fraction contours blue is solid and red is liquid. There is also a void space at the top of the capsule that always remains liquid. After 10,400 sec the first 36 capsules in the $NaNO_3$ system have begun melting, Figure 45a; whereas in the $NaNO_2$ system all of the capsules have started melting with the first 24 capsules being approximately half melted, Figure 45b. The capsules in the KNO_3 system however have yet to start melting as they have not reached the 610 K melting point, Figure 45c. In the 2-PCM system a similar melt fraction was seen within the $NaNO_2$ capsules as in the middle of the $NaNO_2$ system while the $NaNO_3$ capsules have just begun melting, Figure 45d. The $NaNO_3$ and $NaNO_2$ capsules in the 3-PCM system have a lower melt fraction than those in the 2-PCM system and the KNO_3 capsules have yet to begin melting, Figure 45e.

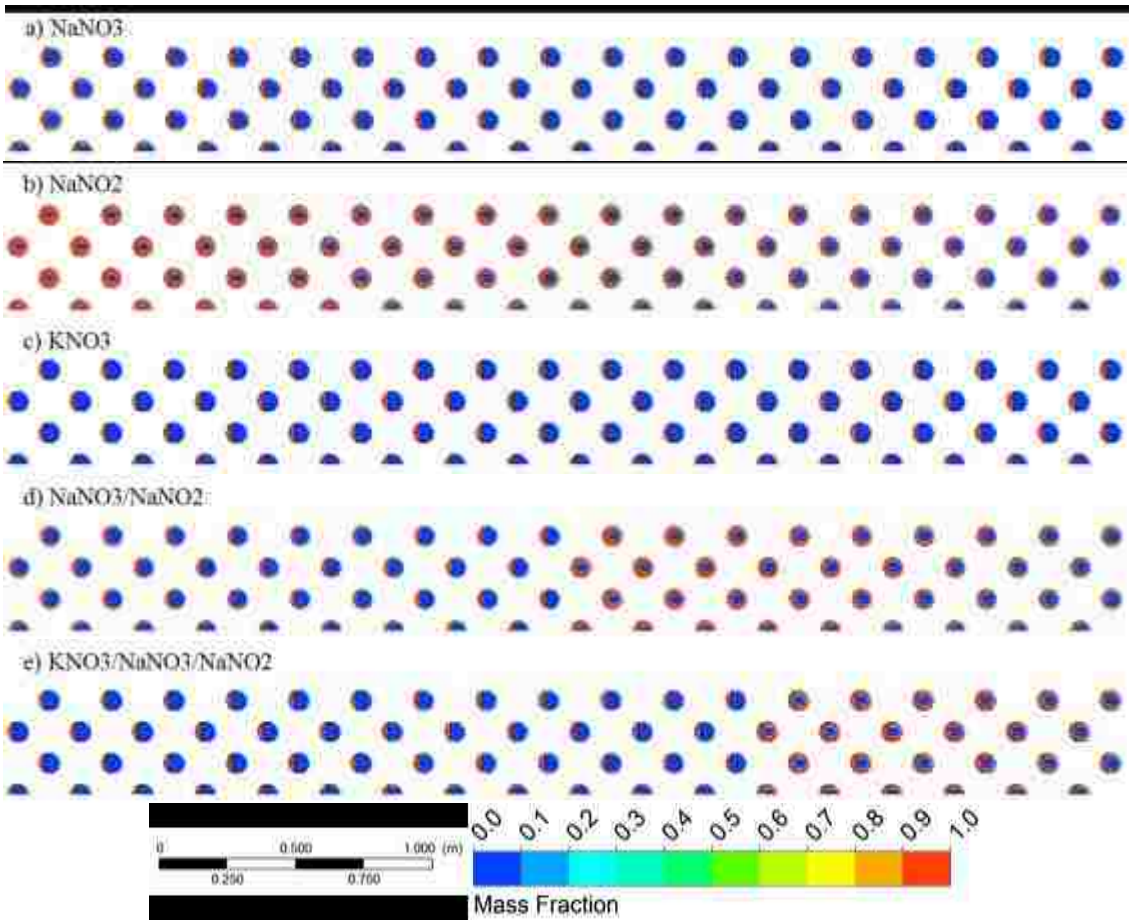

Figure 45. Liquid fraction at 10,400 sec for a) NaNO3 (SteFo=0.47), b) $NaNO_2$ (SteFo=0.94), c) KNO_3 (SteFo=0.034), d) $NaNO_3/NaNO_2$ (SteFo=0.75), e) $KNO_3/NaNO_3/NaNO_2$ (SteFo=0.65) systems

As the charging process continues, the melt fraction within the $NaNO_3$ system has increased as all the capsules have now started melting and the first 24 capsules are halfway melted, Figure 46a. In the $NaNO_2$ system the top half of the system is completely melted and the bottom capsules are over halfway melted, Figure 46b. The capsules in the KNO_3 system have still yet to begin melting, Figure 46c. The fraction of molten PCM in the $NaNO_3$ in the 2-PCM system has increased and there is only a small solid portion remaining in the $NaNO_2$ capsules, Figure 46d. As with the all KNO_3 system, the KNO_3 capsules in the 3-PCM system have yet to start melting whereas the $NaNO_3$ capsules are now nearly halfway melted and half the $NaNO_2$

capsules are completely melted with the remaining capsules being nearly melted, Figure 46e.

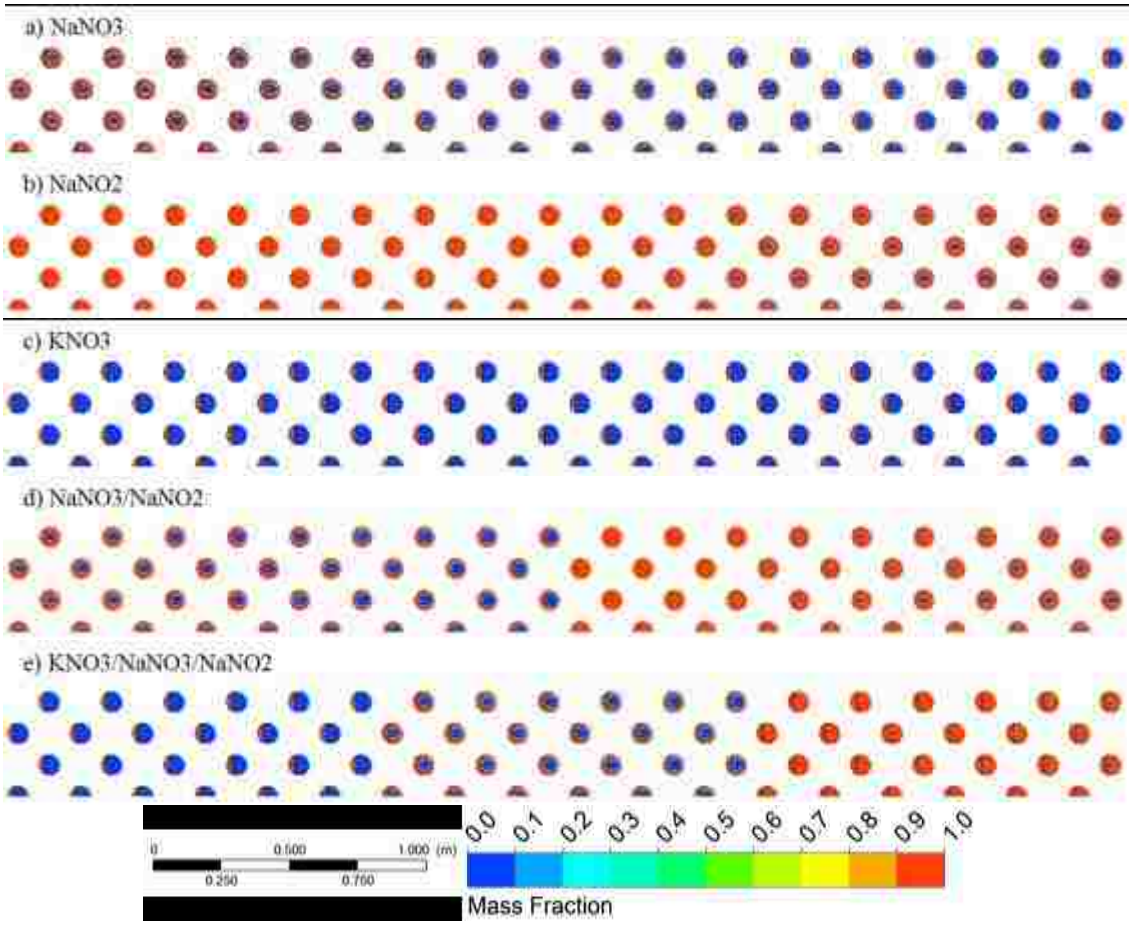

Figure 46. Liquid fraction at 20,400 sec for a) NaNO3 (SteFo=0.93), b) $NaNO_2$ (SteFo=1.85), c) KNO_3 (SteFo=0.066), d) $NaNO_3/NaNO_2$ (SteFo=1.48), e) $KNO_3/NaNO_3/NaNO_2$ (SteFo=1.27) systems

By 30,400 sec all of the capsules in the $NaNO_2$ system are completely melted, whereas the capsules in the top of the KNO_3 system have just begun to melt, Figure 47b and c respectively. Note the lines present in the fully melted capsules are the PCM-void interfaces. While partial melting was observed throughout the capsules in the other systems as they fully melt from the top of the system to bottom, the capsules in the KNO_3 system melt sequentially without displaying partial melting in the lower

capsules. The fraction of molten PCM in the $NaNO_3$ system has continued to increase where first 24 capsules are nearly completely melted, the middle 24 are approximately halfway melted, and the bottom 24 are a quarter melted, Figure 47a. For the 2-PCM system, a similar liquid fraction was seen in the $NaNO_3$ capsules as seen in the $NaNO_3$ system while the $NaNO_2$ capsules are completely melted, Figure 47d. The KNO_3 capsules in the 3-PCM system have finally begun melting in the same sequential manner as the KNO_3 system where only one diagonal row shows signs of melting at a time. Additionally, the $NaNO_3$ and $NaNO_2$ capsules have completely melted by this time, Figure 47.

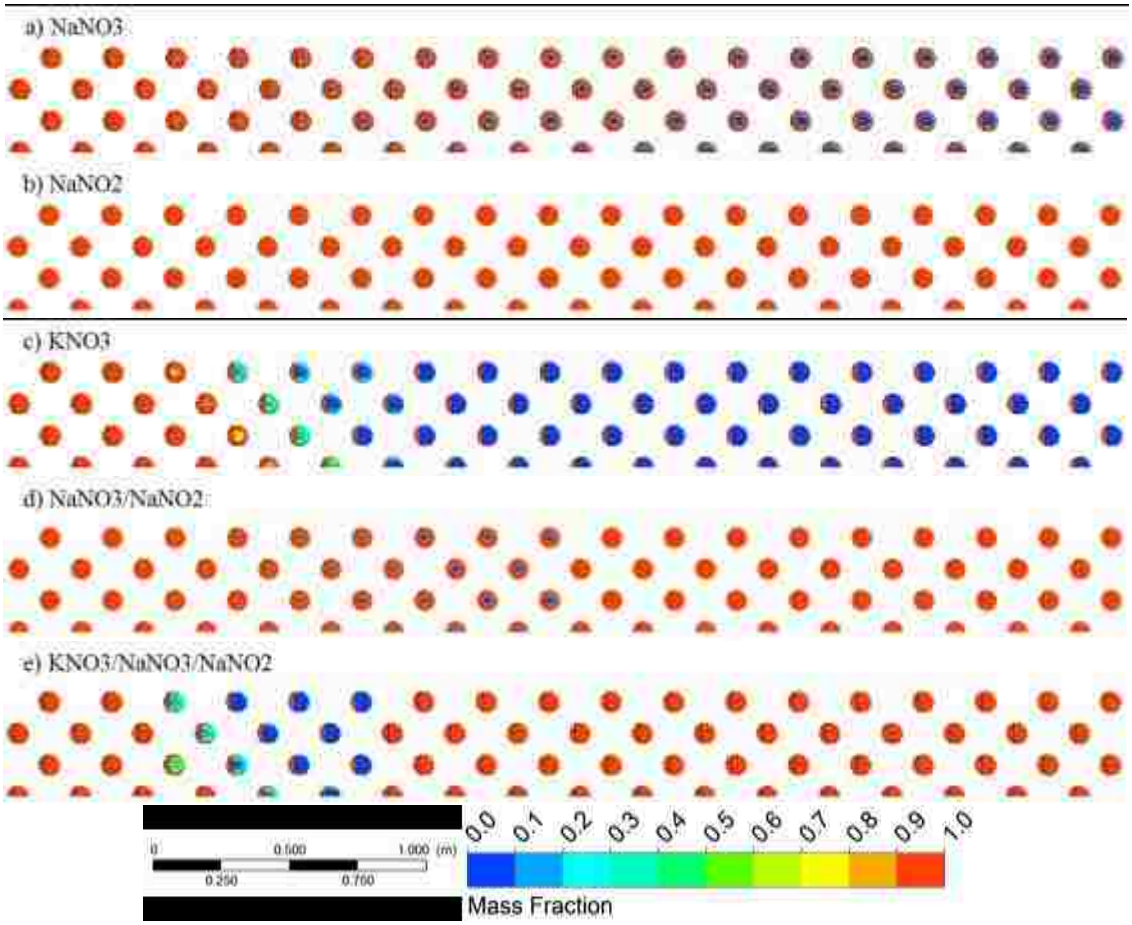

Figure 47. Liquid fraction at 30,400 sec for a) NaNO3 (SteFo=1.38), b) $NaNO_2$ (SteFo=2.75), c) KNO_3 (SteFo=0.098), d) $NaNO_3/NaNO_2$ (SteFo=2.21), e) $KNO_3/NaNO_3/NaNO_2$ (SteFo=1.89) systems

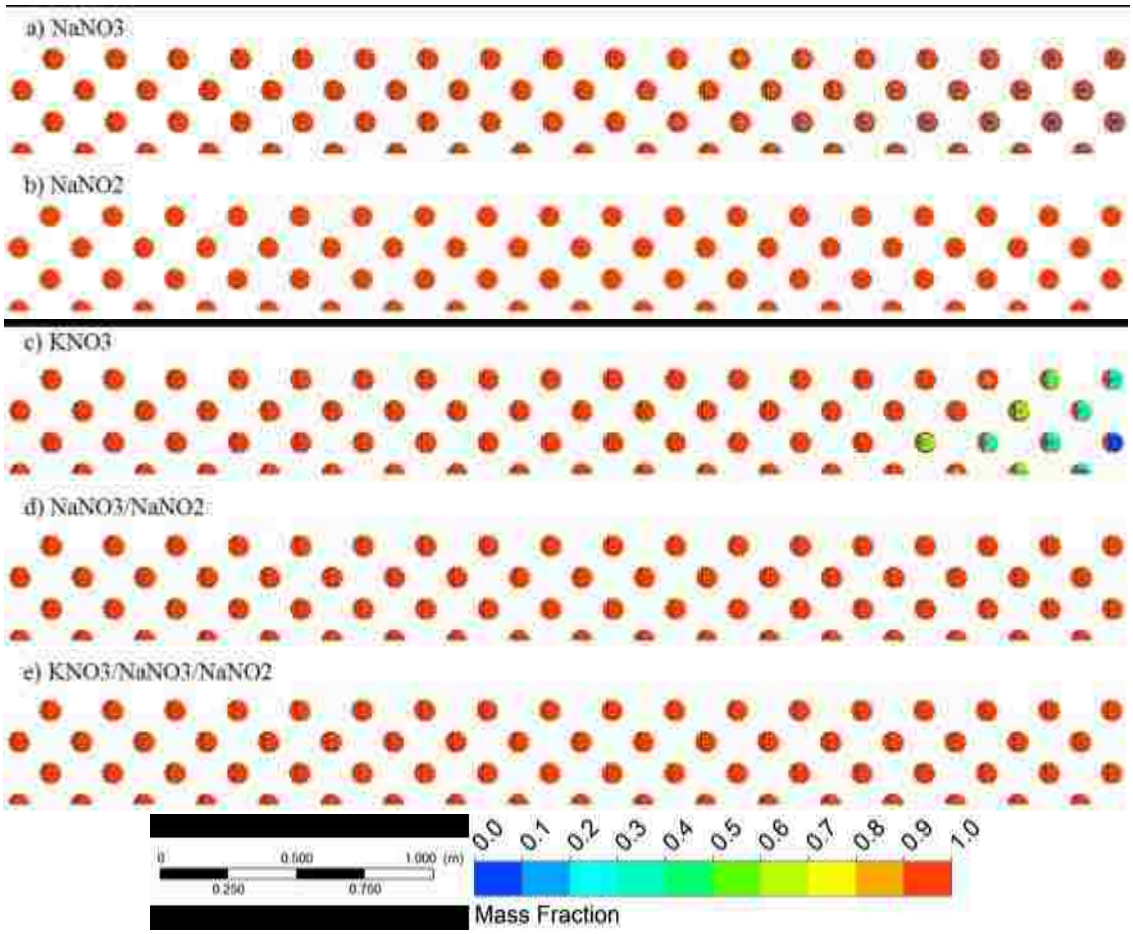

Figure 48. Liquid fraction at 40,400 sec for a) NaNO3 (SteFo=1.84), b) $NaNO_2$ (SteFo=3.66), c) KNO_3 (SteFo=0.13), d) $NaNO_3/NaNO_2$ (SteFo=2.93), e) $KNO_3/NaNO_3/NaNO_2$ (SteFo=2.52) systems

As the charging process nears completion, the first 48 $NaNO_3$ capsules have melted completely and the remaining capsules are over halfway melted, Figure 48a. Despite the prolonged onset of the melting in the KNO_3 system, only the last 12 capsules remain un-melted at this point in time, Figure 48c. The 2-PCM and 3-PCM systems have completely melted with melting times of 36,245 sec and 35,050 sec respectively. The $NaNO_2$ system had the shortest melting time of 30,411 sec which can be attributed to the large temperature difference between the inlet temperature and the melting point of the system. The $NaNO_3$ system melts in 41,100 sec whereas the

KNO_3 system barely completes melting by the end of the charging process (43,200 sec). With the exception of the $NaNO_2$ system, the multi-PCM system decreases the total melting time of the system.

A uniform temperature distribution within the EPCM capsules was assumed to simplify the energy and exergy calculations. The temperature at the center of all 72 capsules for the 3-PCM system is presented Figure 49. The energy and exergy stored in the PCM for each capsule in the system was individually calculated using the following equations and the temperature at the capsule center [41]:

$$Q_{stored} = \begin{cases} m_i c_{pi}^{s}\left(T - 551\right) & if \quad T < T_{mi} \\ m_i c_{pi}^{s}\left(T_{mi} - 551\right) + m_i L_i & if \quad T = T_{mi} \\ m_i c_{pi}^{s}\left(T_{mi} - 551\right) + m_i L_i + m_i c_{pi}^{l}\left(T - T_{mi}\right) & if \quad T > T_{mi} \end{cases} \tag{51}$$

$$Ex_{stored} = \begin{cases} m_i c_{pi}^{s}\left[\left(T - 551\right) - T_o \, ln\left(\frac{T}{551}\right)\right] & if \quad T < T_{mi} \\ m_i c_{pi}^{s}\left[\left(T_{mi} - 551\right) - T_o \, ln\left(\frac{T_{mi}}{551}\right)\right] + m_i L_i\left[1 - \left(\frac{T_o}{T}\right)\right] & if \quad T = T_{mi} \\ m_i c_{pi}^{s}\left[\left(T_{mi} - 551\right) - T_o \, ln\left(\frac{T_{mi}}{551}\right)\right] + m_i L_i\left[1 - \left(\frac{T_o}{T_{mi}}\right)\right] & if \quad T > T_{mi} \\ \quad + m_i c_{pi}^{l}\left[\left(T - T_{mi}\right) - T_o \, ln\left(\frac{T}{T_{mi}}\right)\right] & \end{cases} \tag{52}$$

where the subscript *i* is used to denote the properties of one of the three PCMs used. The energy stored in the capsules for the 3-PCM case as a function of time is shown in Figure 52. Since the energy calculation uses the capsule center temperautre, there is a jump in the energy storage when the melting point is reached followed by a period of time during which the energy remains constant as the melting front propigates inward.

Once the melting front has passed the energy stored in the capsules begins to increase as the capsules superheat.

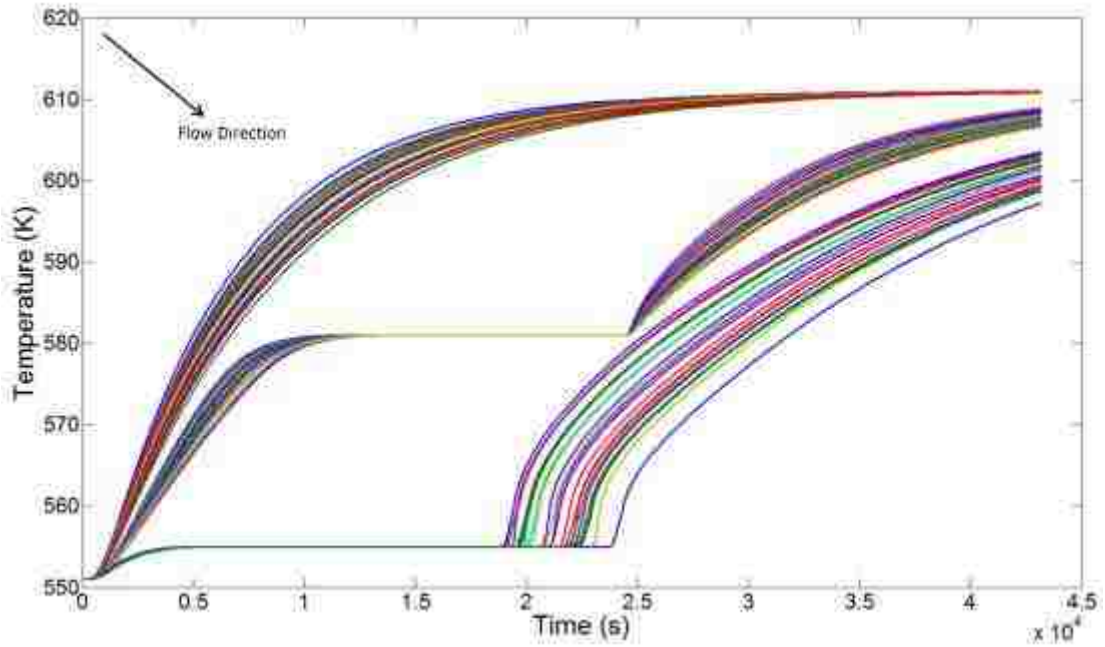

Figure 49. Temperature at the center of each EPCM capsule for the $KNO_3/NaNO_3/NaNO_2$ system

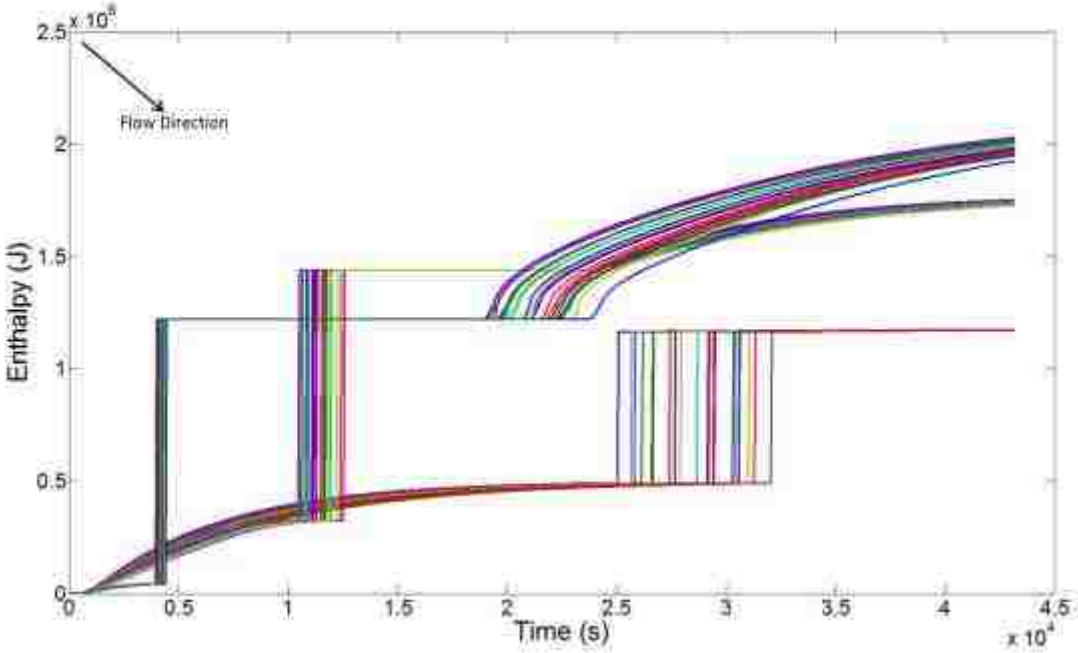

Figure 50. Energy stored in each EPCM capsule for the $KNO_3/NaNO_3/NaNO_2$ system

The individual energy stored by the EPCM capsules was summed to determine the total energy stored in the system as a function of time. The total exergy stored was calculated in the same way. The total energy and exergy stored in the six systems considered are presented in Figure 51 and Figure 52. For the 3-PCM case, the first jump in energy storage occurs at 3,750 sec when the $NaNO_2$ capsules begin to melt. From this point until 10,000 sec the increase in energy storage is from the sensible heating of the $NaNO_3$ and KNO_3 capsules. At 10,000 sec the $NaNO_3$ capsules begin to melt resulting in the second jump in energy storage. The energy storage rate then levels off as the only increase is from the sensible heating of the KNO_3 capsules. At 20,000 sec the $NaNO_2$ capsules sequentially complete melting leading to an increase in stored energy from liquid superheating. The $NaNO_3$ capsules complete melting at the same time that the first KNO_3 capsule begins melting at 25,000 sec; however as the KNO_3 capsules melt sequentially the increase in energy storage occurs over a greater period of time. A similar trend was seen in the energy storage of the other systems. The $NaNO_2$ system stores the most energy (142 MJ) whereas the KNO_3 system stores the least (84.4 MJ) due to a lack of liquid superheating and its lower value of latent heat. Additionally, as the systems all store energy at roughly the same temperature, the exergy stored by the PCMs follows the same trend as the energy storage. Again the $NaNO_2$ system has the highest exergy content at the end of the charging process while the KNO_3 system has the lowest.

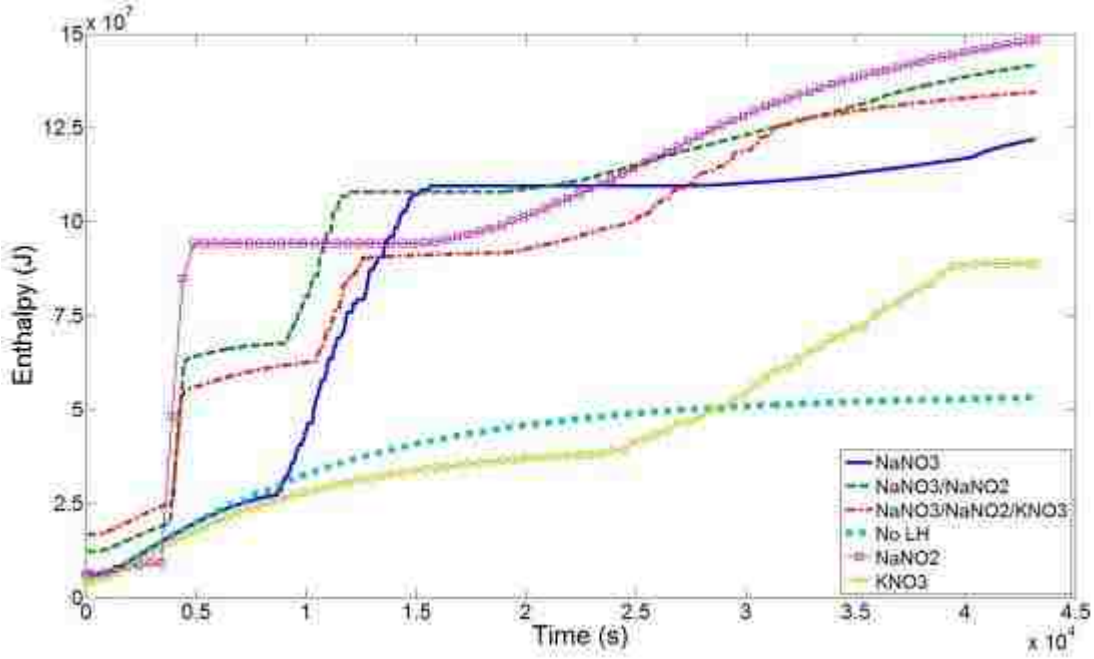

Figure 51. Energy stored in the $NaNO_3$ (solid), $NaNO_2$ (square), KNO_3 (circles), $NaNO_3/NaNO_2$ (dashed), $KNO_3/NaNO_3/NaNO_2$ (dash-dot), and sensible heat (dot) systems during the charging process

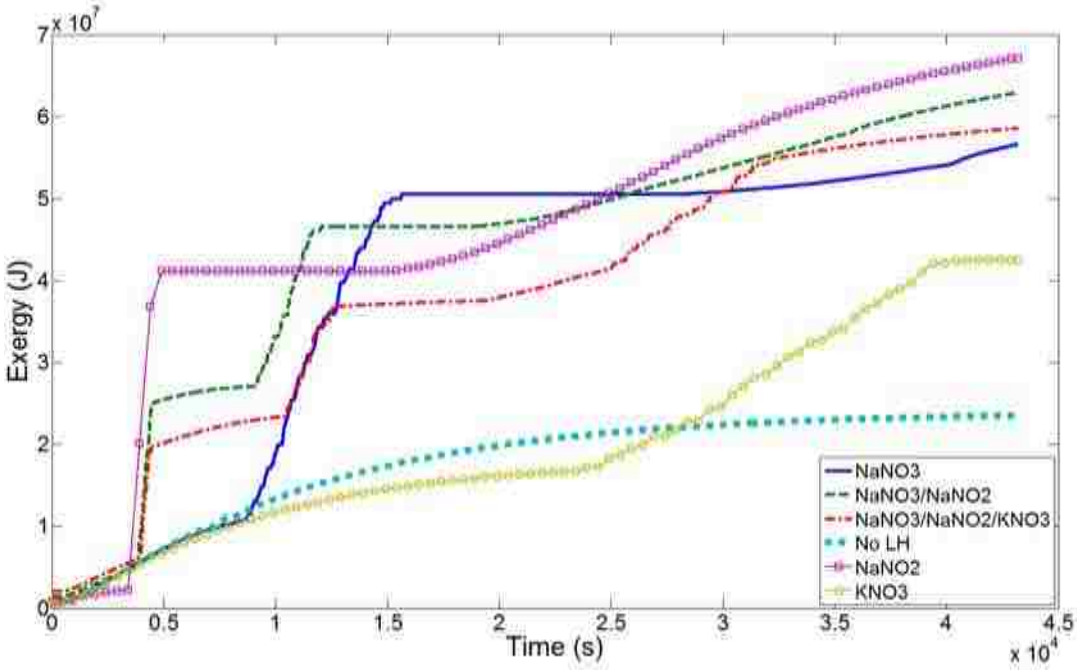

Figure 52. Exergy stored in the $NaNO_3$ (solid), $NaNO_2$ (square), KNO_3 (circles), $NaNO_3/NaNO_2$ (dashed), $KNO_3/NaNO_3/NaNO_2$ (dash-dot), and sensible heat (dot) systems during the charging process

The efficiency of the charging process is defined as the rate of exergy stored in the PCM divided by the exergy rate possessed by the HTF before contact with the PCM [41]. The exergy possessed by the HTF is given by equation (53) and neglects the input power required to pump the HTF through the system. Using this definition the exergy stored is compared to the maximum possible exergy that is being supplied.

$$\dot{E}x_{inout} = \dot{m}_{HTF} c_{p,HTF} \left[\left(T_{HTF,in} - T_o \right) - T_o \, ln\left(\frac{T_{HTF,in}}{T_o} \right) \right] \quad \textbf{(53)}$$

$$\eta_{char} = \frac{\dot{E}x_{stroed}}{\dot{E}x_{input}} \quad \textbf{(54)}$$

The charging efficiency for the six systems considered is presented in Figure 53. The large amounts of energy and therefore exergy stored when the PCM melts results in a spike in the efficiency. Since the $NaNO_2$ system has a large temperature difference between the inlet temperature and melting point and the highest latent heat value, it has a higher energy and therefore exergy storage rate when the capsules melt. This leads to the $NaNO_2$ system having the highest charging efficiency of 38%. The high latent heat of $NaNO_2$ also allows the 2-PCM system to have a higher efficiency than the 3-PCM system due to the higher number of $NaNO_2$ capsules in the system. The efficiency of the sensible heat system increases during the initial heating stages but then decreases over the remainder of the charging process as the exergy storage rate decreases as the system slowly approaches the inlet temperature. The KNO_3 system behaves in a similar manner to the sensible heat system except there is an increase in the efficiency when the capsules finally begin to melt at 25,000 sec. Additionally, as the capsules melt sequentially the increase occurs at a slower rate than in the other

systems. The low value of latent heat and small temperature difference make the KNO_3 system have the worst performance of the latent heat-based systems.

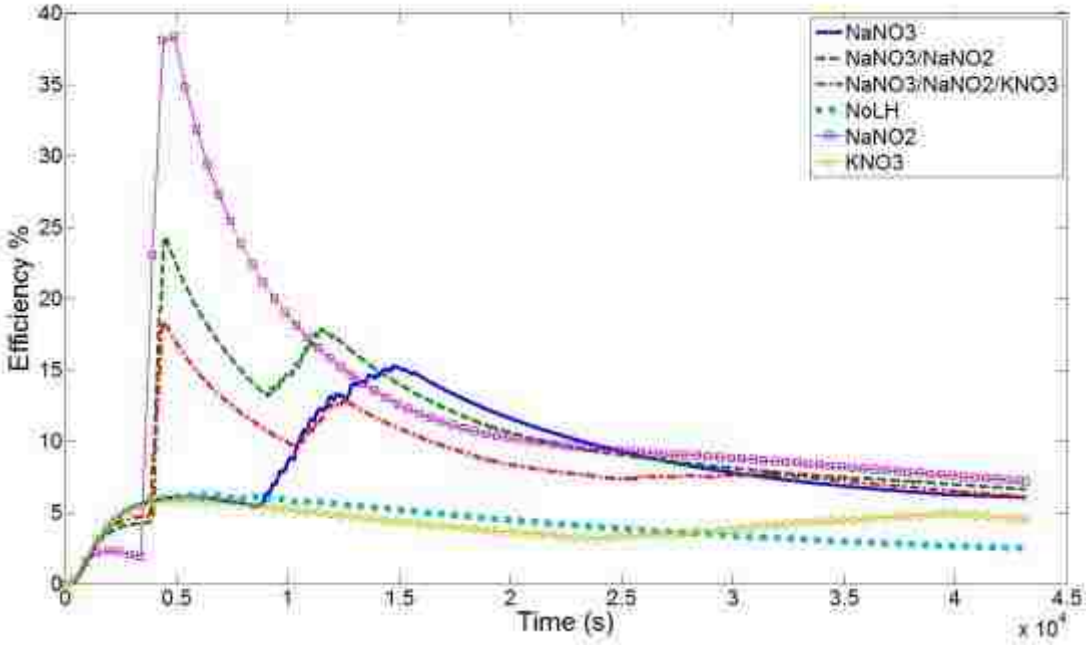

Figure 53. Exergy efficiency of the charging process

8.2.2 Discharging Process

At the conclusion of the charging process, the direction and temperature of the HTF was reversed and now enters the system from the bottom at 551 K, Figure 38 bottom. After the initial transient period, the velocity field reaches steady state conditions and resembles the mirror image of the velocity field seen during charging in Figure 39. The evolution of the outlet temperature during the discharging process for the systems considered is presented in Figure 54. Similar to the charging process, the outlet temperature of the sensible heat system asymptotically decreases towards the 551 K inlet temperature. The outlet of the $NaNO_3$ system also behaves in a similar way to that of the charging process where now it decreases to the melting point of

$NaNO_3$ and then slowly decreases until all of the capsules have completely melted at which time it then begins to decrease asymptotically to the inlet temperature.

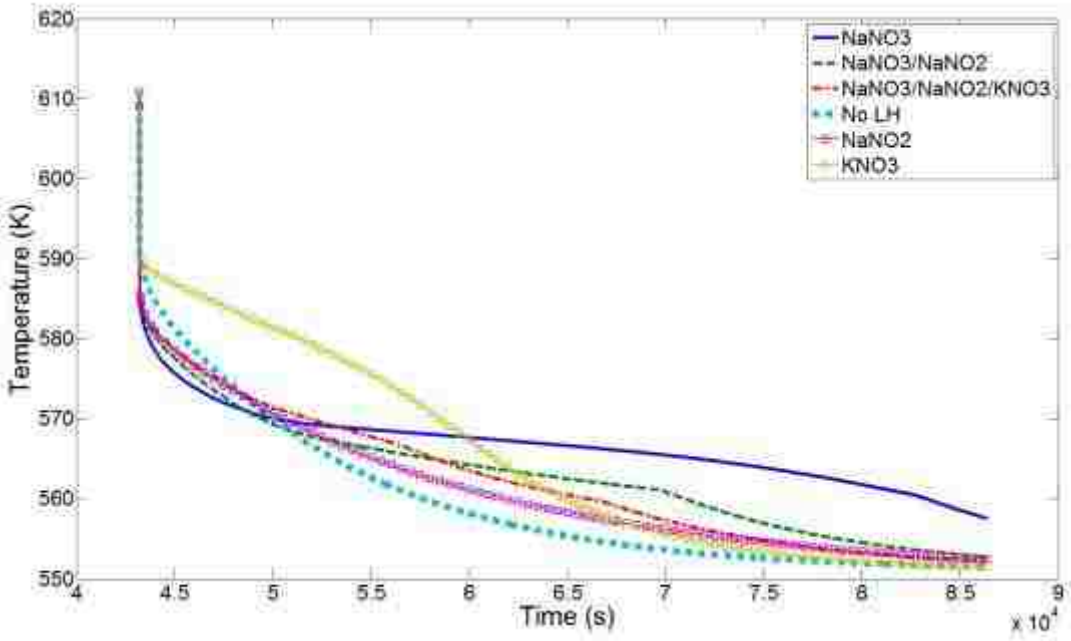

Figure 54. Outlet temperatures during the discharging process for the $NaNO_3$ (solid), $NaNO_2$ (square), KNO_3 (circles), $NaNO_3/NaNO_2$ (dashed), $KNO_3/NaNO_3/NaNO_2$ (dash-dot), and sensible heat (dot) systems

The biggest differences are seen in the $NaNO_2$ and KNO_3 systems as their roles have been reversed as now the $NaNO_2$ system has the smallest temperature difference between the inlet temperature and melting point causing the outlet temperature to behave in the same manner as the sensible heat only system. The large temperature difference seen in the KNO_3 system leads to a high-energy retrieval rate and a larger slope during the solidification process than seen in the $NaNO_3$ case before the outlet temperature decreases rapidly after the capsules have solidified. The 3-PCM system has the same consistent energy release rate during discharging as seen during the charging process. Furthermore, the 2-PCM system was again in the middle of the pure $NaNO_3$ and $NaNO_2$ systems with a higher temperature than the $NaNO_2$ case and larger

slope than the $NaNO_3$ system. The inflection point at 70,000 sec denotes the point at which the $NaNO_3$ capsules have solidified completely.

At the start of the discharging process, there was a rapid drop in the temperature of the EPCM capsules in the sensible heat, $NaNO_3$, $NaNO_2$, and 2-PCM systems. The temperature increase of the HTF across these systems was nearly identical, Figure 55a-c and e. The EPCM capsules in the bottom half of the $NaNO_3$ system are now at 581 K and have begun to solidify, Figure 55b. Similarly the $NaNO_3$

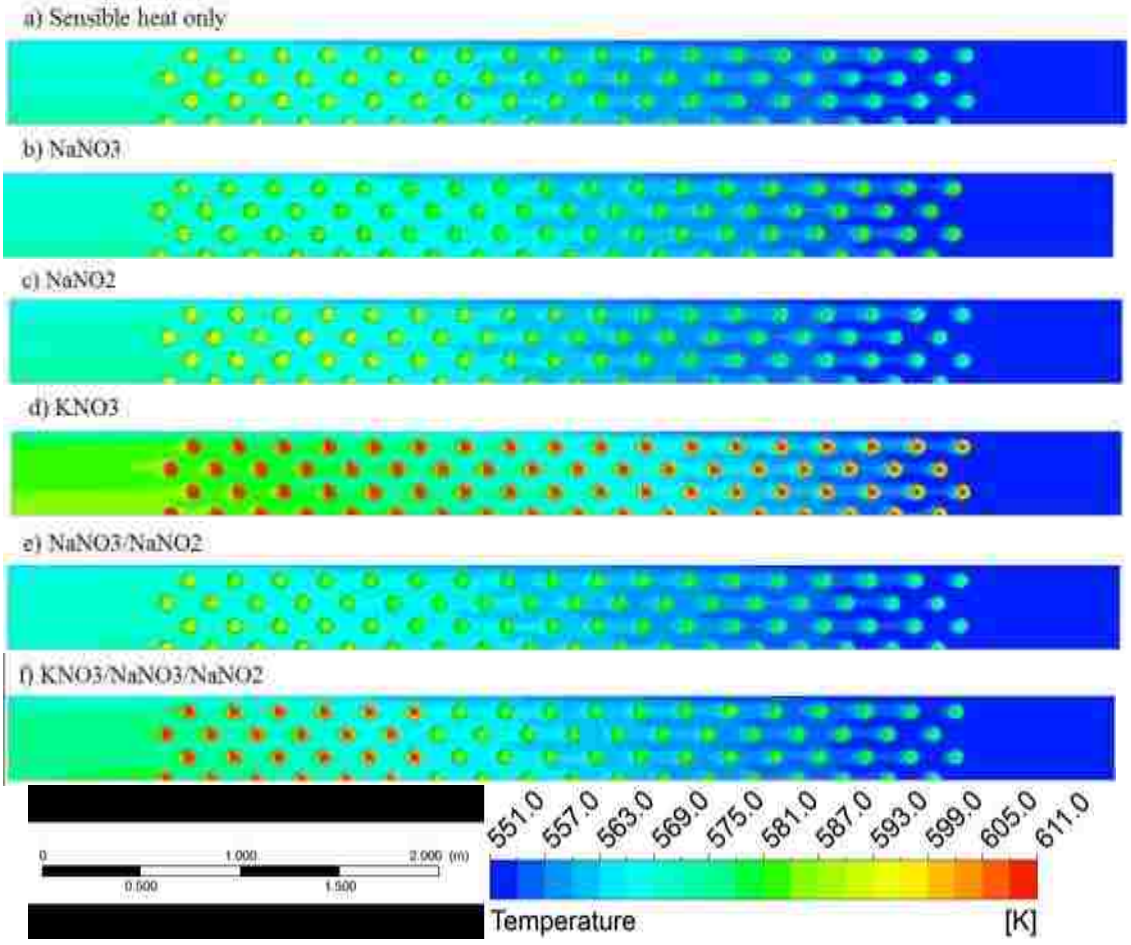

Figure 55. Isotherms at 50,000 sec for a) sensible heat only, b) NaNO3 (SteFo=0.025), c) $NaNO_2$ (0.038), d) KNO_3 (0.71), e) $NaNO_3/NaNO_2$ (0.031), f) $KNO_3/NaNO_3/NaNO_2$ (0.25) systems (6800 sec into discharging)

capsules in the 2-PCM case have started to solidify as well, Figure 55e. The temperature increase in the HTF for the KNO_3 system was higher as all of the capsules have begun to solidify, Figure 55d. In the 3-PCM case the increase in the temperature of the HTF was higher than the 2-PCM case although it is still lower than the KNO_3 system, Figure 55f. Additionally, a radial thermal gradient forms in the solidified KNO_3 capsules in both the KNO_3 and 3-PCM systems.

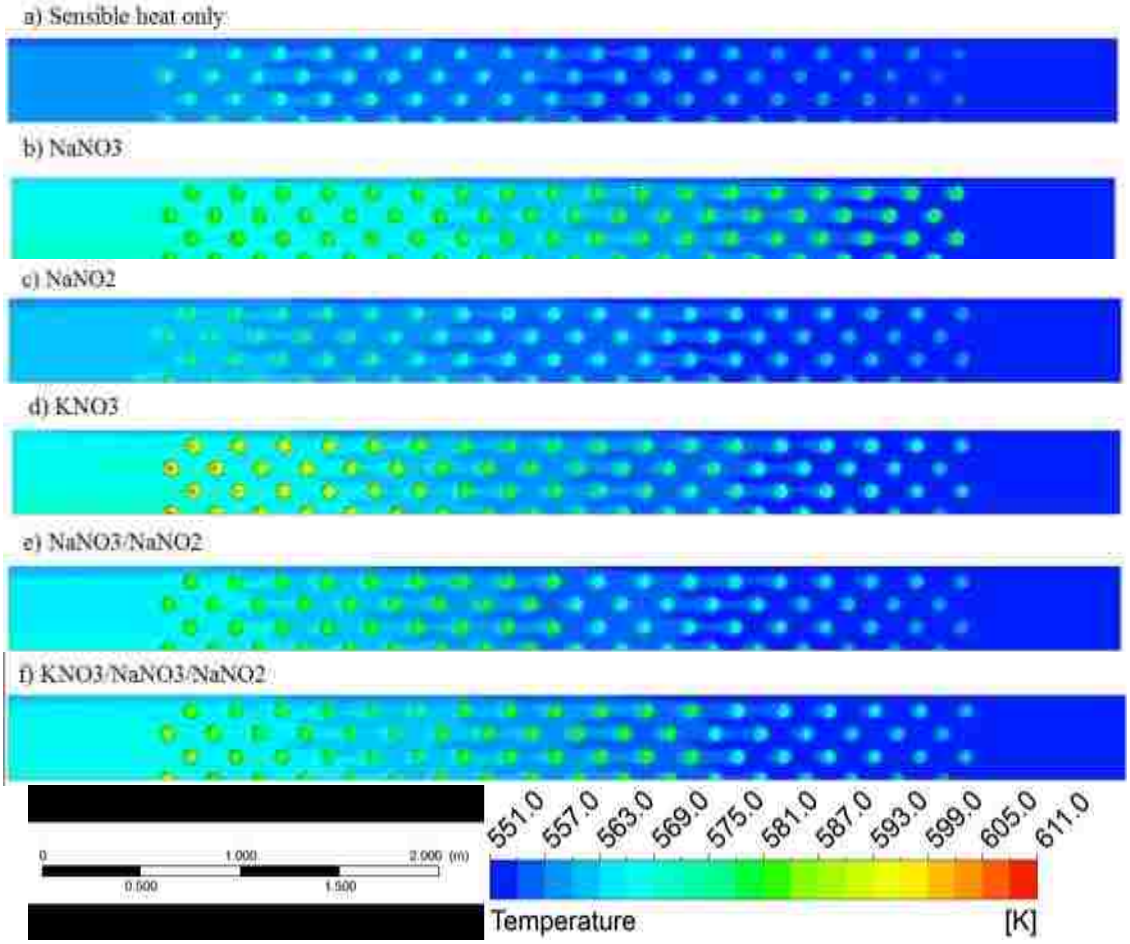

Figure 56. Isotherms at 60,000 sec for a) sensible heat only, b) NaNO3 (SteFo=0.061), c) $NaNO_2$ (0.093), d) KNO_3 (1.75), e) $NaNO_3/NaNO_2$ (0.078), f) $KNO_3/NaNO_3/NaNO_2$ (0.63) systems (16,800 sec into discharging)

As the discharging process continues the temperature increase in the HTF has decreased in all of the systems where the largest decrease was seen in the sensible heat system, Figure 56a. A slightly larger temperature increase was seen in the $NaNO_2$ system, Figure 56c, while a minimal change in the temperature distribution of the $NaNO_3$ has occurred as the EPCM capsules continue to solidify, Figure 56b. The KNO_3 capsules have finished solidifying leading to a row-wise increasing capsule temperature from the bottom to the top of the system while the capsules in the top rows still have a radial temperature gradient, Figure 56d. The 2-PCM system has a slightly smaller temperature increase within the HTF than the $NaNO_3$ case, Figure 56e. The $NaNO_3$ capsules are at the 581 K melting point while there is a row-wise temperature gradient in the $NaNO_2$ capsules. A similar temperature increase was seen in the 3-PCM case where there is a row-wise distribution in the $NaNO_2$ and KNO_3 capsules, and the $NaNO_3$ capsules are still at 581 K, Figure 56f.

26,800 sec into the discharging process there is no longer a temperature increase in the HTF for the sensible heat system; however a row-wise distribution still remains in the EPCM capsules, Figure 57a. The largest increase in the HTF temperature was seen with the $NaNO_3$ system as the capsules are still releasing energy as they solidify, Figure 57b. A slight temperature increase remains in the HTF for the $NaNO_2$ and KNO_3 systems, Figure 57c and d respectively. While both systems have a row-wise thermal gradient in the EPCM capsules, the capsules in the KNO_3 system are completely solidified whereas the $NaNO_2$ capsules have just begun to melt. The second largest temperature increase was seen in the 2-PCM system where the $NaNO_3$ capsules are at 581 K and the row-wise gradient in the $NaNO_2$ capsules has decreased,

Figure 57e. There was a slightly smaller temperature increase in the 3-PCM system and as all of the capsules have solidified, there is a row-wise temperature distribution in the three sets of PCMs, Figure 57f.

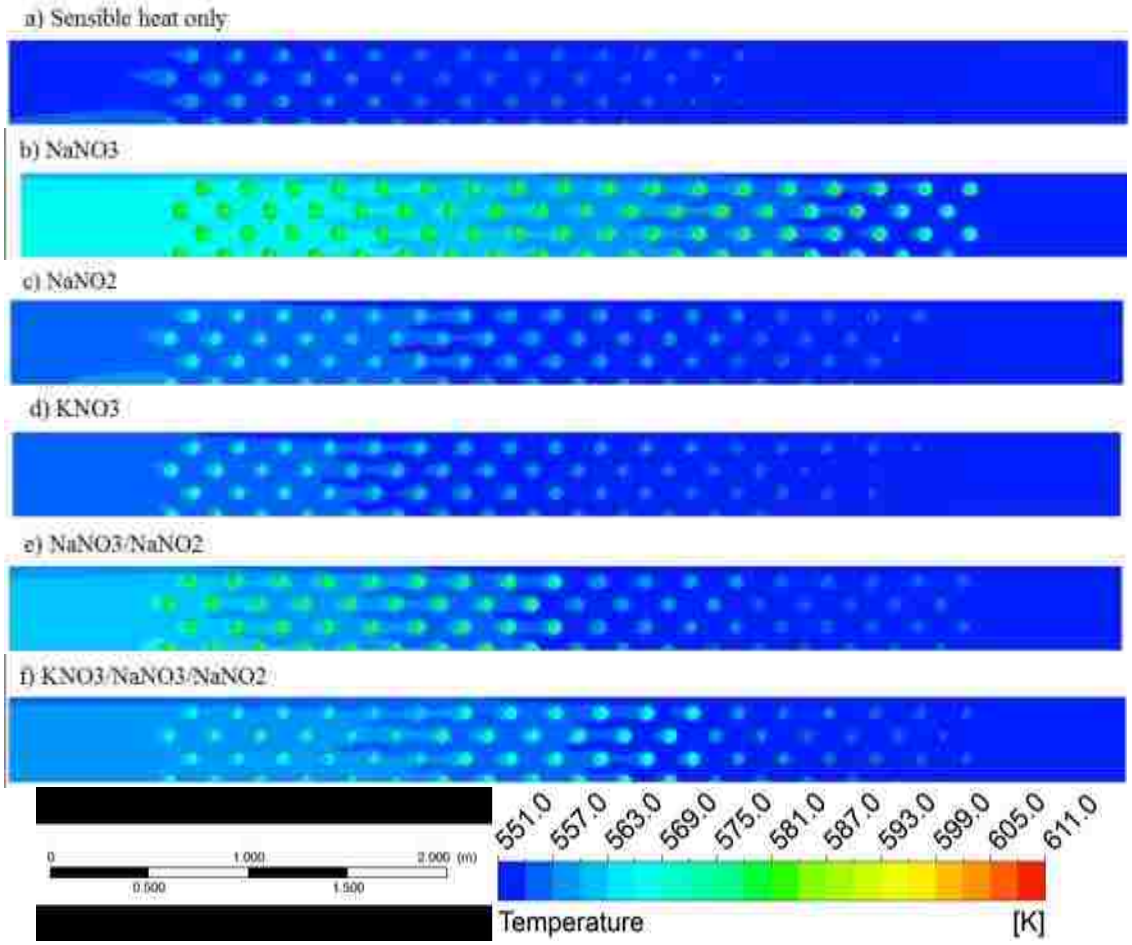

Figure 57. Isotherms at 70,000 sec for a) sensible heat only, b) NaNO3 (SteFo=0.098), c) $NaNO_2$ (0.15), d) KNO_3 (2.80), e) $NaNO_3/NaNO_2$ (0.12), f) $KNO_3/NaNO_3/NaNO_2$ (1.00) systems (26,800 sec into discharging)

As the discharging process nears completion the temperature distribution in the EPCM capsules of the sensible heat system has decreased to the point where the entire system is now at a near uniform temperature, Figure 58a. Despite having decreased, the temperature increase in the $NaNO_3$ system was still the largest as the capsules in the top of the system are still solidifying, Figure 58b. At this point there was no

temperature increase in the HTF in the $NaNO_2$ system, however as with capsules in the $NaNO_3$ system there was still a row-wise thermal gradient as the capsules continue to melt, Figure 58c. The temperature increase in the KNO_3 system has decreased to the point where it has only a slightly larger temperature variation in the EPCM capsules than in the sensible heat system, Figure 58d. A similar trend was seen in the 2- and 3-PCM cases as well, Figure 58 e and f.

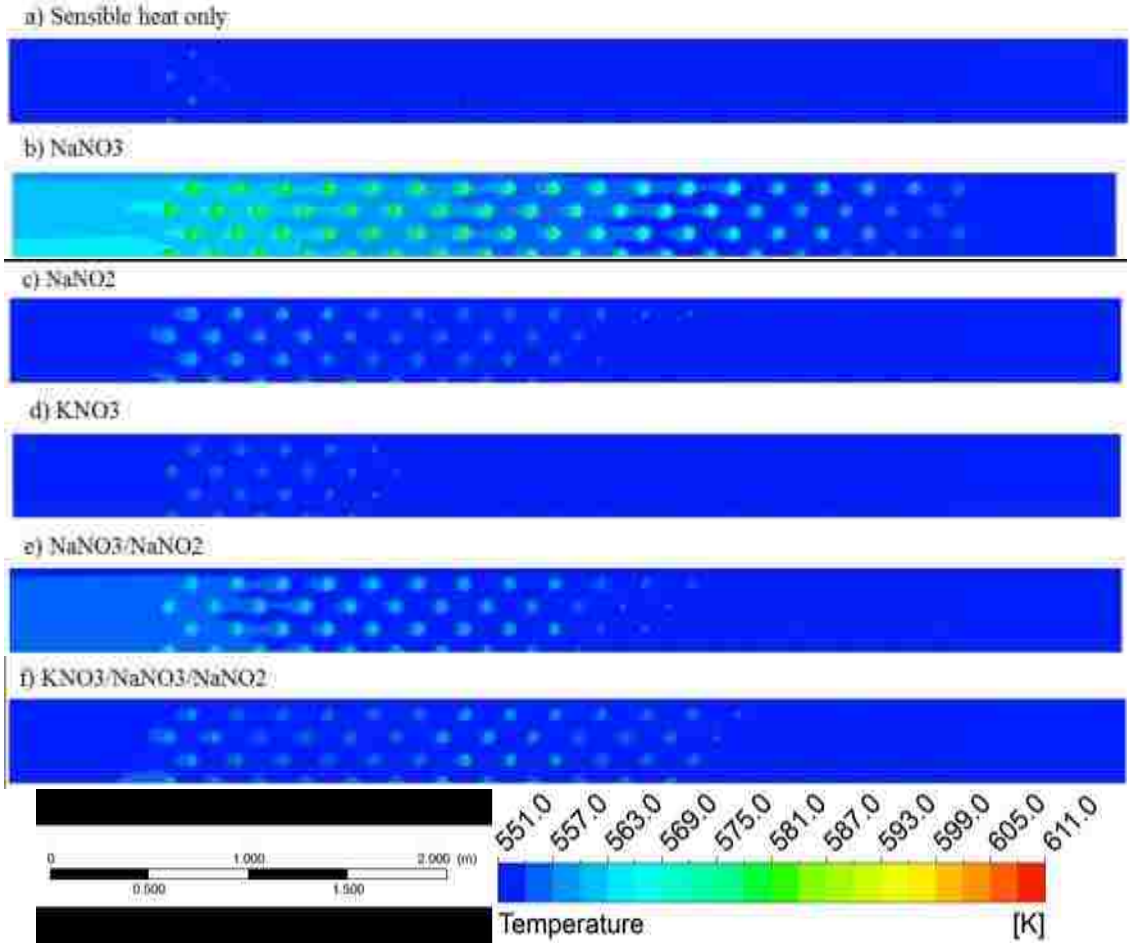

Figure 58. Isotherms at 80,000 sec for a) sensible heat only, b) NaNO3 (SteFo=0.13), c) $NaNO_2$ (0.20), d) KNO_3 (3.84), e) $NaNO_3/NaNO_2$ (0.17), f) $KNO_3/NaNO_3/NaNO_2$ (1.37) systems (36,800 sec into discharging)

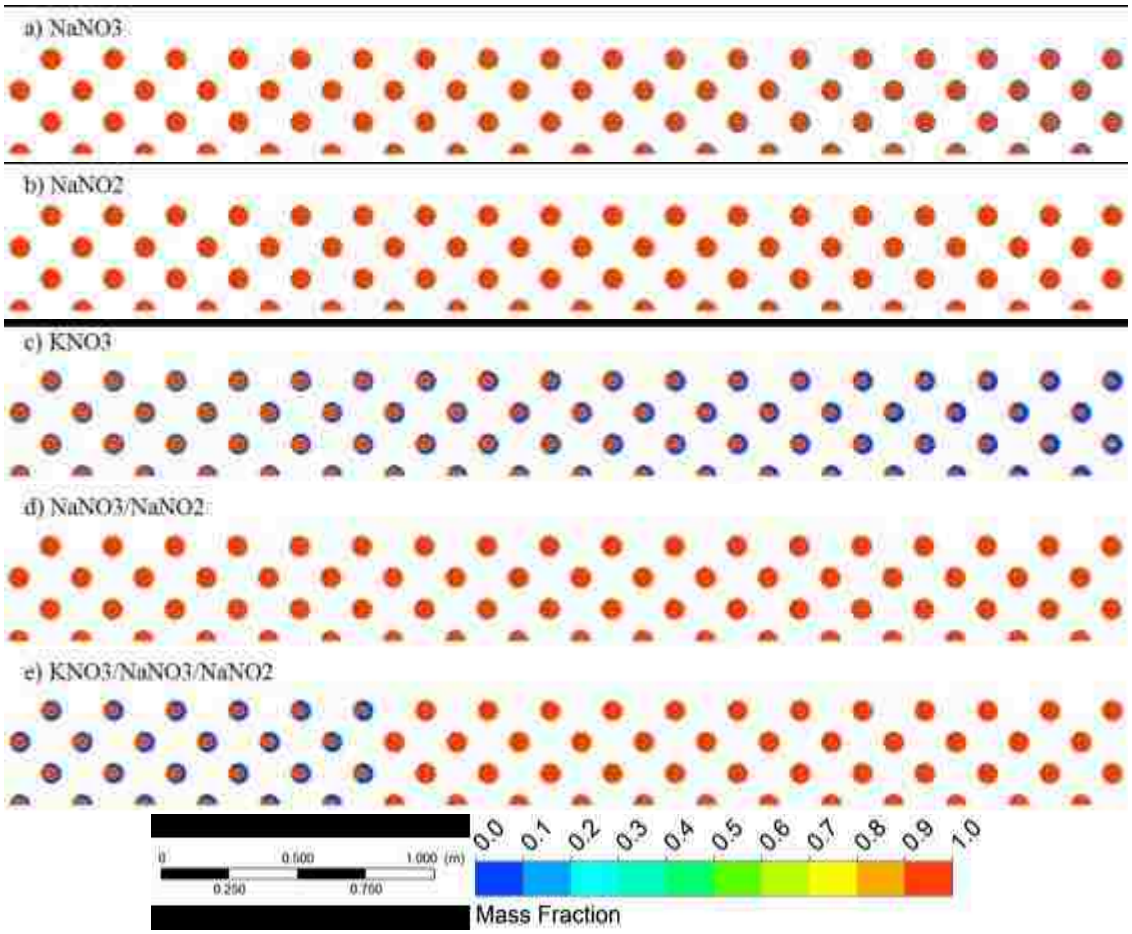

Figure 59. Liquid fraction at 50,000 sec for a) NaNO3 (SteFo=0.025), b) $NaNO_2$ (0.038), c) KNO_3 (0.71), d) $NaNO_3/NaNO_2$ (0.031), e) $KNO_3/NaNO_3/NaNO_2$ (0.25) systems (6800 sec into discharging)

The solid-liquid interface is "U"-shaped throughout the solidification process and although convection in the molten PCM is neglected, previous results have shown that the solidification process is conduction-dominated and therefore the shape of the solid-liquid interface is unaffected. Additionally, since the HTF enters the system from the bottom, solidification begins along the bottom edge of the capsules and then propagates radially inward. The capsules in the $NaNO_3$ system begin to solidify almost immediately after the discharging process begins, Figure 59a. The capsules in the $NaNO_2$ system have not yet cooled to the 555 K melting point and therefore have not

started to solidify, Figure 59b. In the KNO_3 case however, all of the capsules are partially solidified where the capsules in the bottom of the system are approximately halfway solidified, Figure 59c. There was a thin solid layer in the bottom of the last $NaNO_3$ capsules in the 2-PCM system whereas the $NaNO_2$ capsules are still completely molten, Figure 59d. For the 3-PCM system, the KNO_3 capsules are halfway solidified, there was a thin solid layer at the bottom of the $NaNO_3$ capsules, and the $NaNO_2$ capsules have yet to melt, Figure 59e.

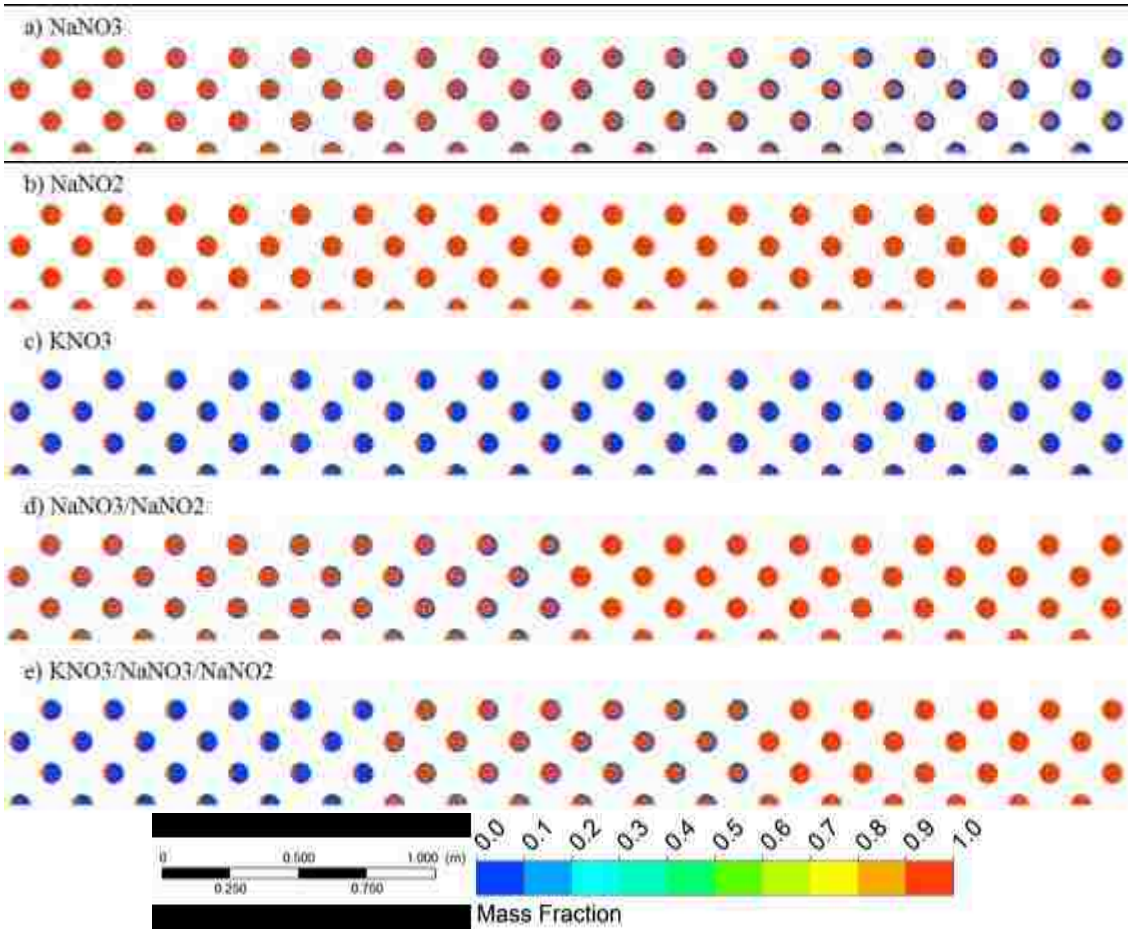

Figure 60. Liquid fraction at 60,000 sec for a) NaNO3 (SteFo=0.061), c) $NaNO_2$ (0.093), d) KNO_3 (1.75), e) $NaNO_3/NaNO_2$ (0.078), f) $KNO_3/NaNO_3/NaNO_2$ (0.63) systems (16,800 sec into discharging)

As the discharging process continues, the solid fraction in the $NaNO_3$ capsules increases where the last 24 capsules are now halfway solidified, Figure 60a. While the $NaNO_2$ system has still yet to start solidifying, the capsules in the KNO_3 system are completely solid, Figure 60b and c. Likewise, the $NaNO_3$ capsules in the 2-PCM system are still completely molten while the solid fraction in the $NaNO_3$ capsules has increased, Figure 60d. The same trend was observed in the 3-PCM case where the KNO_3 capsules have finished solidifying, the fraction of solid in the $NaNO_3$ capsules has increased, and the $NaNO_2$ capsules remain completely melted, Figure 60e.

After 26,800 sec the solid fraction in the $NaNO_3$ has continued to increase and now the last 24 capsules are completely solid and the middle capsules are approximately 50% solidified, and the first 24 are only 25% solidified, Figure 61a. The capsules in the $NaNO_2$ system have just begun to solidify and due to the small temperature difference between the melting point and inlet temperature the capsules solidify row by row like seen with the KNO_3 system during the melting process, Figure 61b. The $NaNO_3$ capsules in the 2-PCM system have almost completed solidified while the $NaNO_2$ capsules have just started solidification, Figure 61d. The KNO_3 and $NaNO_3$ capsules in the 3-PCM system have finished solidifying while the $NaNO_2$ capsules have finally started to solidify, Figure 61e.

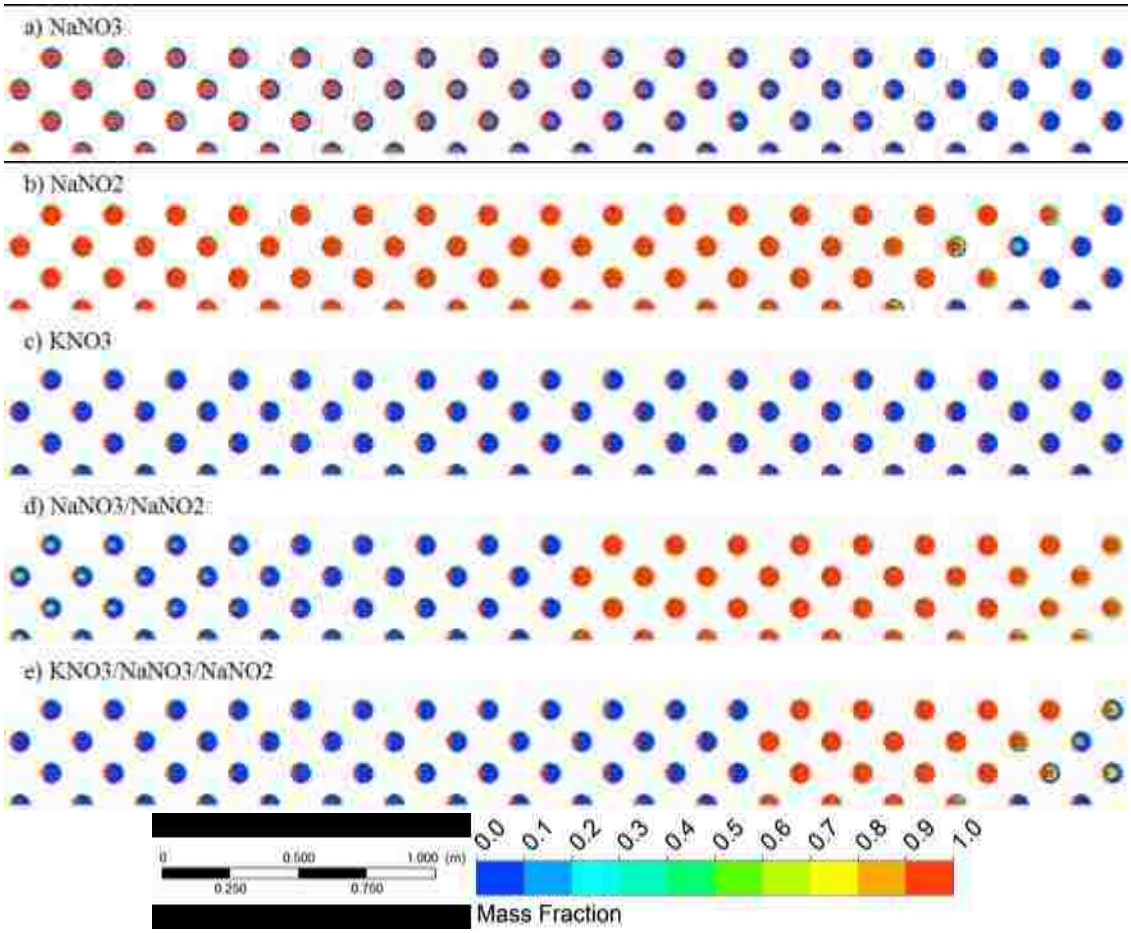

Figure 61. Liquid fraction at 70,000 sec for a) NaNO3 (SteFo=0.098), c) $NaNO_2$ (0.15), d) KNO_3 (2.80), e) $NaNO_3/NaNO_2$ (0.12), f) $KNO_3/NaNO_3/NaNO_2$ (1.00) systems (26,800 sec into discharging)

As discharging draws to a close two-thirds of the capsules in the $NaNO_3$ system are completely solid and the remaining capsules are over halfway solidified, Figure 62a. Only half of the capsules in the $NaNO_2$ system have solidified, Figure 62b. The first six $NaNO_2$ capsules in the 2-PCM system have yet to solidify completely while all of the capsules in the 3-PCM system have finished solidifying, Figure 62d and e respectively. The KNO_3 system has the shortest solidification time of 61,505 sec. The $NaNO_3$ system takes 82,900 whereas the $NaNO_2$ system does not solidify completely over the course of the 12-hour discharging process. With the exception of

the KNO_3 system, the 2- and 3-PCM systems offer an improvement over the single PCM systems and have total solidification times of 81,695 sec and 80,020 sec respectively.

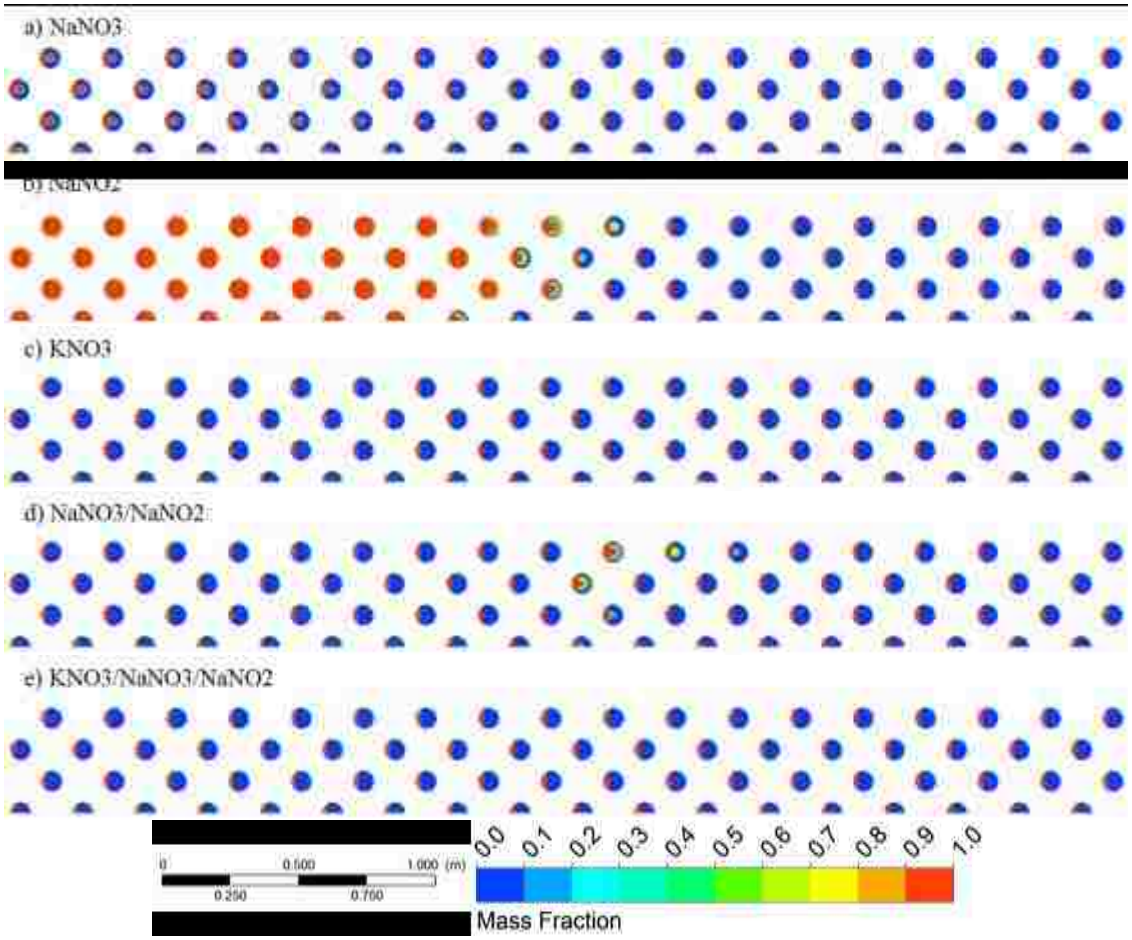

Figure 62. Liquid fraction at 80,000 sec for a) NaNO3 (SteFo=0.13), c) $NaNO_2$ (0.20), d) KNO_3 (3.84), e) $NaNO_3/NaNO_2$ (0.17), f) $KNO_3/NaNO_3/NaNO_2$ (1.37) systems (36,800 sec into discharging)

As with the charging process, a uniform temperature distribution was assumed for the energy calculations and the temperature at the center of the EPCM capsule was used. The evolution of the capsule temperature of the 3-PCM system during discharging evolves in a similar manner as during the charging process, only

decreasing to the melting point instead of increasing. The energy and exergy released from the PCM was calculated using the following equations:

$$Q_{released} = \begin{cases} m_i c_{pi}^{l}\left(T_{char} - T\right) & if \quad T > T_{mi} \\ m_i c_{pi}^{l}\left(T_{char} - T_{mi}\right) + m_i L_i & if \quad T = T_{mi} \\ m_i c_{pi}^{l}\left(T_{char} - T_{mi}\right) + m_i L_i + m_i c_{pi}^{s}\left(T_{mi} - T\right) & if \quad T < T_{mi} \end{cases} \tag{55}$$

$$Ex_{released} = \begin{cases} m_i c_{pi}^{l}\left[\left(T_{char} - T\right) - T_o \, ln\left(\frac{T_{char}}{T}\right)\right] & if \quad T > T_{mi} \\ m_i c_{pi}^{l}\left[\left(T_{char} - T_{mi}\right) - T_o \, ln\left(\frac{T_{char}}{T_{mi}}\right)\right] + m_i L_i\left[1 - \left(\frac{T_o}{T}\right)\right] & if \quad T = T_{mi} \\ m_i c_{pi}^{l}\left[\left(T_{char} - T_{mi}\right) - T_o \, ln\left(\frac{T_{char}}{T_{mi}}\right)\right] + m_i L_i\left[1 - \left(\frac{T_o}{T_{mi}}\right)\right] & if \quad T < T_{mi} \\ \quad + m_i c_{pi}^{s}\left[\left(T_{mi} - T\right) - T_o \, ln\left(\frac{T_{mi}}{T}\right)\right] & \end{cases} \tag{56}$$

where T_{char} is the final temperature of the EPCM capsule at the end of the charging process. The energy released by the individual capsules for the 3-PCM case during the discharging process is shown in Figure 63. As the KNO_3 capsules have the highest melting temperature, they begin to solidify first and do so almost simultaneously. As with the charging process, there is a jump in the energy released when the center of the capsule reaches the melting point followed by a period of constant energy as the solid-liquid interface propagates inward before further energy can be released from the capsules. The row-wise solidification of the $NaNO_2$ capsules is shown by the sequential jumps in energy released from 65,000 to 77,500 sec seen in Figure 63.

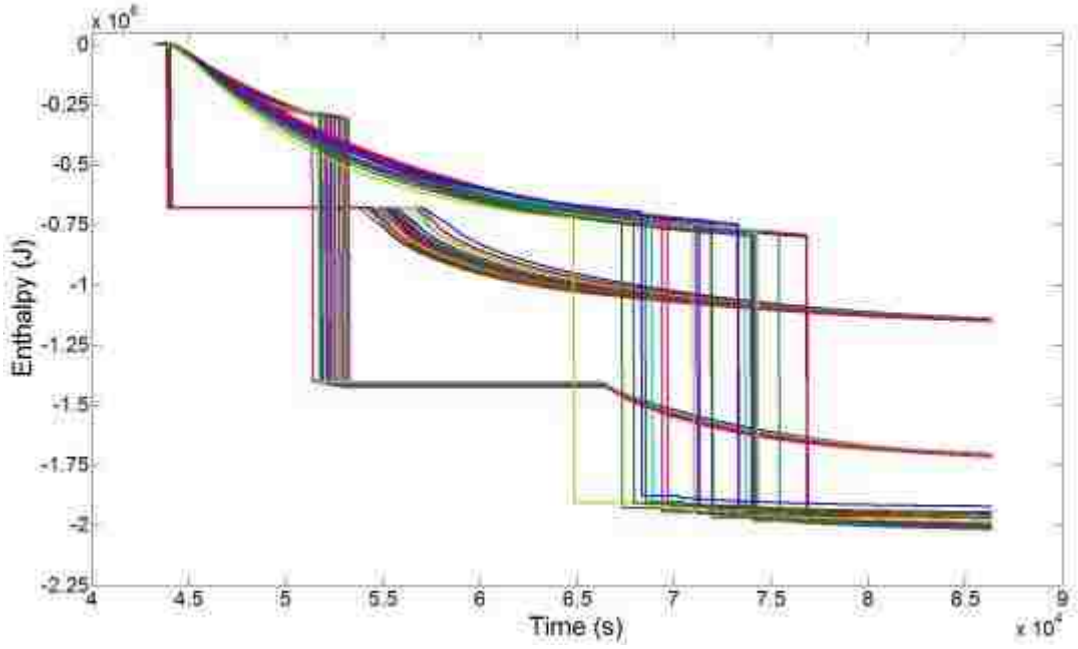

Figure 63. Energy released in each EPCM capsule for the $KNO_3/NaNO_3/NaNO_2$ system

As with the charging process the individual energy released by the EPCM capsules are summed to determine the total energy released by the system. The evolution of the total energy released for the systems considered is shown in Figure 64. Although energy is being released from the PCM, the shape of the curves is similar to the charging process where large increases are seen when a set of capsules begins to solidify and the slope changes depending on the number of capsules that have solidified completely and are now sub-cooling. The most energy was released by the 2-PCM system (128 MJ) followed closely by the $NaNO_2$ system (125 MJ). The KNO_3 system releases the least amount of energy (83.8 MJ); however it had the smallest amount of stored energy. The exergy extracted from the PCM is shown in Figure 65 and as was seen during charging follows the same trend as the energy released.

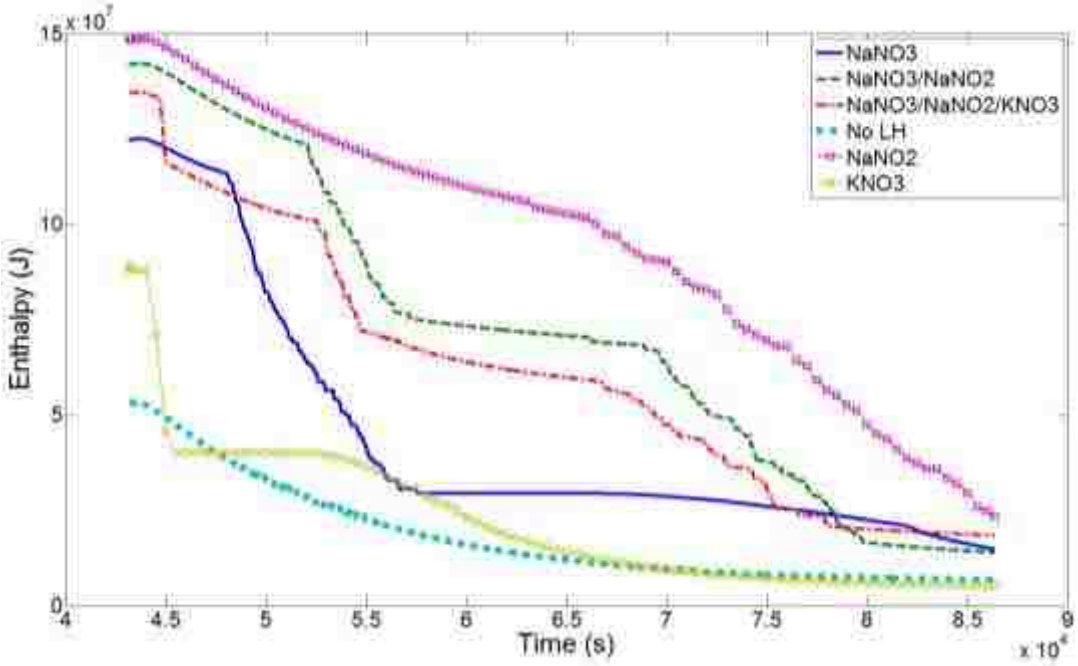

Figure 64. Energy released in the $NaNO_3$ (solid), $NaNO_2$ (square), KNO_3 (circles), $NaNO_3/NaNO_2$ (dashed), $KNO_3/NaNO_3/NaNO_2$ (dash-dot), and sensible heat (dot) systems during the discharging process

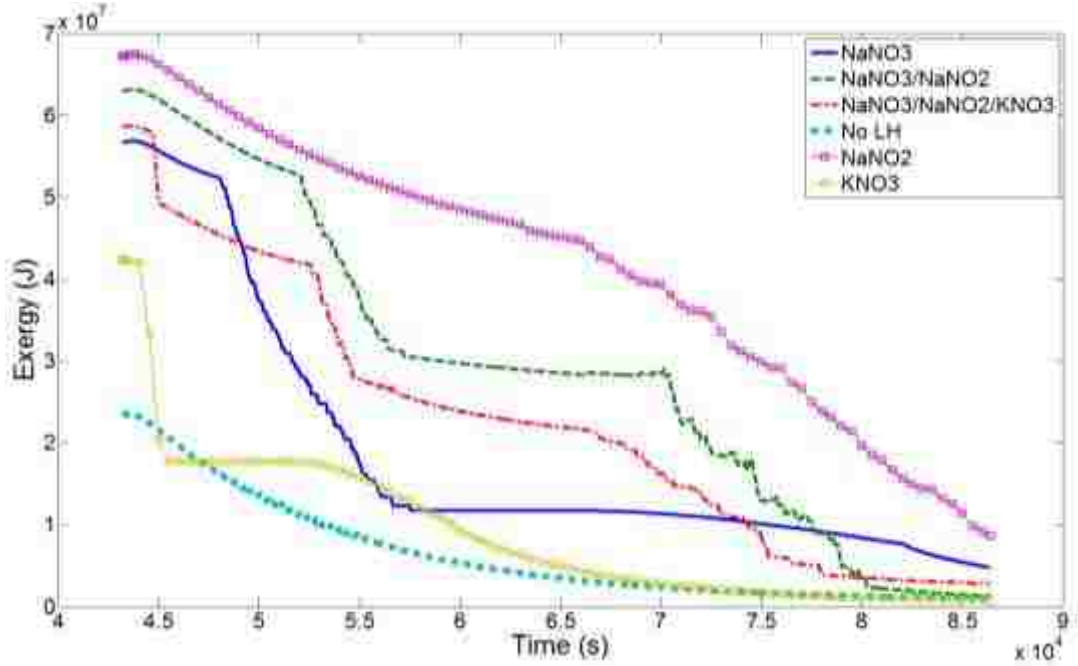

Figure 65. Exergy extracted in the $NaNO_3$ (solid), $NaNO_2$ (square), KNO_3 (circles), $NaNO_3/NaNO_2$ (dashed), $KNO_3/NaNO_3/NaNO_2$ (dash-dot), and sensible heat (dot) systems during the discharging process

For the discharging process, the efficiency is defined as exergy gained by the HTF divided by the initial exergy available within the PCM [41]. The exergy gained by the HTF is given in equation (57).

$$Ex_{HTF} = \dot{m}_{HTF} c_{p,HTF} \left[\left(T_{HTF,in} - T_{HTF} \right) - T_o \, ln\left(\frac{T_{HTF,in}}{T_{HTF}} \right) \right] \times dt \quad \textbf{(57)}$$

$$\eta_{dis} = \frac{Ex_{HTF}}{Ex_{stored}} \quad \textbf{(58)}$$

The efficiency of the systems considered during the discharging process is shown in Figure 66. The $NaNO_3$ system has the highest efficiency (74%) while the $NaNO_2$ system has the lowest (26%). For all of the systems, the efficiency increases during the beginning of the discharging process due to the large temperature increase in the HTF between the inlet and outlet as it extracts energy from the PCM. As the temperature increase in the HTF decreases to the inlet temperature the efficiency of the systems decreases. The 2-PCM system has a slightly larger efficiency than the 3-PCM system.

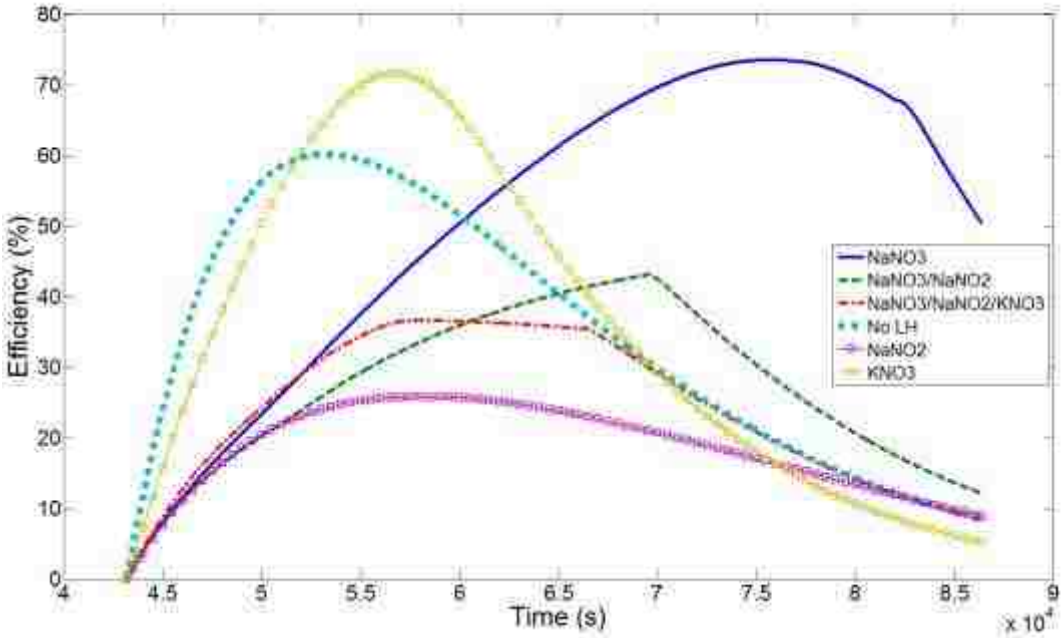

Figure 66. Exergy efficiency of the discharging process

8.3 Overall Cycle Efficiency

The performance of a TES system cannot be determined simply by looking at the charging or discharging process alone, therefore the overall cycle efficiency needs to be determined. The overall energy and exergy efficiencies are defined as:

$$\eta_{Q-overall} = \frac{Q_{released}}{Q_{stored}} \quad \textbf{(59)}$$

$$\eta_{Ex-overall} = \frac{Ex_{released}}{Ex_{stored}} \quad \textbf{(60)}$$

These efficiencies depend on the temperature change of the HTF and thus a smaller difference would lead to an increase in efficiency as well as increase the percent of energy stored via latent heat. However, it should be noted that for the three materials considered here the temperature range can only be minimally decreased due to the melting points of the materials. A key example of the importance of the overall cyclic performance is seen by looking at the $NaNO_2$ system. When you look at the charging process alone, the system stores the most energy at the highest rate. During the discharging process however while it releases the second highest amount of energy, its efficiency was the lowest and the system does not completely solidify. This leads to the $NaNO_2$ system only recovering 88% of the energy and exergy that was stored. The energy stored, exergy stored, energy released, exergy released, charging and discharging Ste, overall charging and discharging efficiencies, and the percent energy stored via latent heat are listed in Table 9. Although the KNO_3 system was the worst performer during the charging process, its good performance during discharging leads to it having the highest overall energy and exergy efficiencies. It is closely followed by the 2- and 3-PCM systems. The multi-PCM systems not only store more energy

than the KNO_3 and $NaNO_3$ single PCM systems but they do so in a more efficient manner. Furthermore, while it is possible to recover all of the energy stored in the sensible heat system, it can only store 40% of the energy the $NaNO_3$ system stores. This highlights the improvement latent heat-based systems offer over pure sensible heat TES systems.

Table 9. Results of the charging and discharging process for the $NaNO_3$, $NaNO_2$, KNO_3, 2-PCM, 3-PCM, and sensible heat systems

	$NaNO_3$	$NaNO_2$	KNO_3	2-PCM	3-PCM	Sensible Heat
Energy Stored (MJ)	116	142	84.4	130	118	47.1
Exergy Stored (MJ)	55.9	66.4	42.0	61.4	56.5	22.8
Ste_{char}	0.30	0.79	0.013	0.55	0.37	---
Energy Released (MJ)	107	125	83.8	128	116	46.5
Exergy Released (MJ)	51.9	58.5	41.7	61.6	55.8	22.5
Ste_{dis}	0.029	0.038	0.73	0.034	0.27	---
$\eta_{Q\text{-overall}}$ (%)	92	88	99	98	98	98
$\eta_{Ex\text{-overall}}$ (%)	93	88	99	100	99	99
%LH	69	60	57	64	60	---

8.4 Conclusions

A two-dimensional analysis of an example EPCM-based TES system was conducted to evaluate the improvement of its performance by employing a multi-PCM system. Six systems were considered: three single PCM systems ($NaNO_3$, $NaNO_2$, and KNO_3), a 2-PCM system ($NaNO_3$ and $NaNO_2$), a 3-PCM system, and a sensible heat only system as a comparison. The performance of the charging and discharging processes are investigated as well as the overall cyclic performance of the systems. The cyclic performance is dependent on the temperature difference of the HTF. Therefore if a smaller operational temperature range is considered there will be an

increase in the efficiency of the system as well as an increase in the fraction of energy stored via latent heat. As expected the latent heat systems are able to store more energy than the sensible heat system. Due to the thermal properties of $NaNO_2$ and the large temperature difference experienced during the charging process, the $NaNO_2$ has the highest efficiency, stores the most energy, and has the highest exergy content at the end of the charging process. The small temperature difference between the melting point of the PCM and the inlet temperature for the KNO_3 system coupled with the low values of latent heat leads to the system having the worst performance of the latent heat systems. With the exception of the $NaNO_2$ system, the multi-PCM systems outperform the single PCM systems by storing more energy at a higher rate and having a higher final exergy content.

Despite being the best system during the charging process, the $NaNO_2$ system has the worst performance during the discharging process as the HTF fails to retrieve all of the stored energy. The prolonged solidification time of the $NaNO_3$ system leads to it having the highest discharging efficiency. The performance of the $NaNO_2$ system during the discharging process highlights the importance of looking at the overall cyclic performance of the system. Since the system fails to solidify fully, only 88% of the energy and exergy stored was able to be recovered and turned into useful work. The $NaNO_3$ system releases 92% of the stored energy while the HTF in the remaining systems are able to extract all of the stored energy. Furthermore, the system cannot be judged on efficiency alone and the total energy and exergy stored is an important factor in determining the best-suited system. For the systems considered, the 2-PCM system does not only store the most energy, but it also released the highest amount.

This was partly due to the extremely small temperature difference between the melting point of KNO_3 and the 611 K inlet temperature. It was also due to the higher energy storage density of $NaNO_2$ compared to KNO_3. The 2-PCM system also has the second highest fraction of energy stored via latent heat behind the $NaNO_3$ system.

These results show that a cascaded multi-PCM has a better energy and exergy performance over that of a single PCM system. While these results indicate a 2-PCM system to be best, as the length of the system is increased the number of PCMs used will have a greater impact. Furthermore, care needs to be taken as to the inlet and melting temperatures of the PCMs as they impact the performance. While the results of this investigation lend insight into key aspects of the performance of EPCM-based latent heat TES systems, additional research is required to determine the optimal operating conditions.

CHAPTER IX: USE OF METALLIC OXIDES AS PCMS FOR TES

While encapsulation of a PCM has many advantages, it poses its own unique obstacles. Great care needs to be taken to ensure that the encapsulation shell and PCM are thermally compatible such that chemical and metallurgical interactions do not occur at the elevated temperatures experienced during thermal cycling of the EPCM capsule. Additionally, the shell must withstand the thermal stresses it will experience as well as allow for the thermal expansion of the PCM upon melting. Given the high temperatures at CSP plants, metal encapsulation shells are preferred, such as stainless and carbon steel or nickel-based alloys [18]. However, when used in conjunction with the currently proposed chloride- and nitrate salt-based PCMs a loss of storage capacity can occur after prolonged exposure to high temperatures due to reactions between the metal shell and molten PCM. Metallic oxides on the other hand are less reactive and corrosive when in contact with materials like stainless steel. Additionally, they offer higher energy storage densities at comparable melting temperatures.

9.1 Determination of a Suitable Metal Oxide for Use as a PCM

Even though having a melting temperature within a desired range is a key factor in the use of a material as a PCM, it is by no means the only one. An ideal material should exhibit further desirable thermo-physical, kinetic, and chemical properties such as a high latent heat of fusion, small volumetric changes, chemical stability, and be in abundance at a low cost [3]. Twelve binary metal oxide systems were considered as potential PCMs. These were the Na_2O-SiO_2, Na_2O-B_2O_3, Na_2O-P_2O_5, CaO-SiO_2, CaO-B_2O_3, CaO-P_2O_5, Al_2O_3-SiO_2, Al_2O_3-B_2O_3, Al_2O_3-P_2O_5, K_2O-SiO_2, K_2O-B_2O_3, and K_2O-P_2O_5 systems. To be considered for use in high temperature

TES applications, a melting temperature in the range of 300 °C to 1,000 °C was imposed which reduced the number of available systems to five; the Na_2O-B_2O_3, Na_2O-P_2O_5, K_2O-SiO_2, K_2O-B_2O_3, and K_2O-P_2O_5 systems. As these materials possess the ability to form amorphous as well as crystalline solids, eutectic materials outside of the glass formation range were considered [87, 88].

For TES applications, a congruently melting material is preferred; therefore the thermodynamic properties of the eight eutectic materials in these systems ($Na_2B_4O_7$, $NaBO_2$, $Na_4B_2O_5$, $K_2B_4O_7$, KBO_2, $Na_4P_2O_7$, KPO_3, and K_2SiO_3) were compared to determine which material would be best suited for TES applications. The melting temperature, latent heat, solid specific heat, and liquid specific heat are listed in Table 10 along with other commonly studied PCMs for comparison. From Table 10 it can be seen that materials from the borate systems have higher latent heat values than those from the phosphate systems. Similarly, sodium oxide materials have higher values than potassium oxide materials. Therefore materials in the Na_2O-B_2O_3 systems are best suited for TES applications.

When these materials are compared to the studied nitrate and chloride salts, the sodium borate materials have comparable melting temperatures while offering a higher energy storage density. For example, the energy storage per unit mass over a 100 °C temperature range centered about the melting temperature for $NaNO_3$ is 324.4 kJ/kg whereas $Na_4B_2O_5$ stores 778.1 kJ/kg. This higher energy storage density allows for a reduction in system size and thus cost. Therefore the materials in the Na_2O-B_2O_3 system are the most attractive for use as a PCM for TES.

Table 10. Physical properties of potential PCMS

	Melting Temperature (°C)	Latent Heat (kJ/kg)	Solid Specific Heat (J/kg K)	Liquid Specific Heat (J/kg K)
$NaNO_3$	308 [89]	162.5 [89]	1,588 [89]	1,650 [89]
$MgCl_2$	714 [78]	454 [78]	798 [90]	974 [78]
NaCl	800 [78]	481 [78]	987 [91]	1200 [78]
Al	660 [75]	397.3 [77]	903 [77]	1177 [77]
Zinc	420 [92]	113 [92]	389 [93]	505 [93]
$Na_2B_4O_7$	742 [94]	403.5 [94]	1174.3 [94]	2213.3 [94]
$NaBO_2$	967 [94]	509.1 [94]	1349.8 [94]	2218.8 [94]
$Na_4B_2O_5$	641 [95]	617.3 [94]	1166.4 [94]	2048.8 [94]
$K_2B_4O_7$	816 [94]	446.4 [94]	----	----
KBO_2	947 [94]	383.4 [94]	----	----
$Na_4P_2O_7$	970 [96]	220.4 [96]	----	----
KPO_3	810 [96]	74.5 [96]	----	----
K_2SiO_3	976 [96]	325.4 [96]	----	----

9.2 Testing of $Na_4B_2O_5$ Capsules

Of the three eutectic materials in the non-glass formable region (38–66.5% *mol.* Na_2O) of the Na_2O-B_2O_3 system, $Na_4B_2O_5$ (66.5% *mol.* Na_2O) has the lowest melting temperature and the highest latent heat, making it an ideal candidate PCM, Figure 67. The energy storage capability of $Na_4B_2O_5$ as a PCM over repeated thermal cycling was evaluated using the immersion calorimeter and experimental methods described in Chapter III.

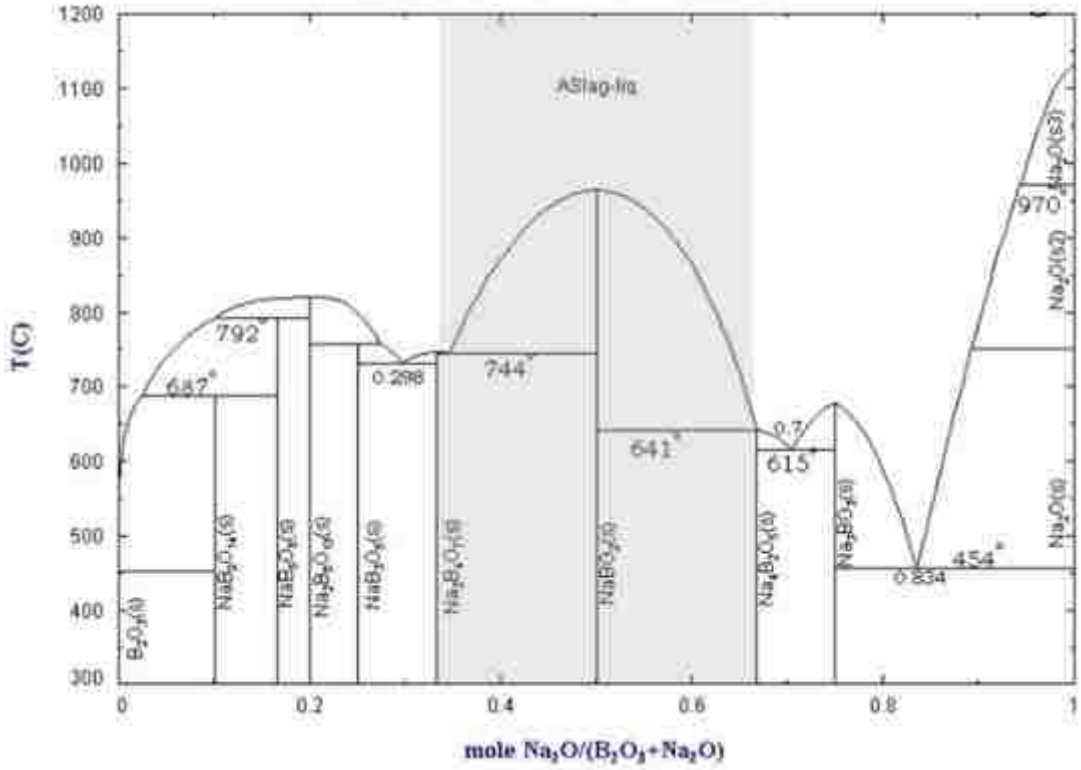

Figure 67. Na_2O-B_2O_3 phase diagram [97]

9.2.1 Design of $Na_4B_2O_5$ EPCM Capsules

Since $Na_4B_2O_5$ has the ability to form an amorphous solid, care must be taken in the size of the calorimetry sample to avoid rapid cooling that could result in glass formation above a critical temporal thermal gradient. An extensive study of the critical cooling rates within the Na_2O-B_2O_3 system was carried out by Ota and Soga [98] and it showed that for $Na_4B_2O_5$ the critical cooling rate is 2 °C/s. It should be noted that while the cooling rate within a CSP plant is likely to be well below this critical cooling rate, cooling rates within the immersion calorimeter experiments may not. Therefore, to reduce the probability of glass formation during experimentation, a two-dimensional analytical calculation was used to determine the optimal capsule size.

Various capsule sizes with a diameter of 25.4 or 50.8 mm and a height of 50.8, 76.2, 101.6 or 127.0 mm were considered. With these capsule dimensions and the thermal conductivity of the material (taken as 0.8 W/m·K) the Biot number (Bi) is much greater than 0.1 and therefore the lumped capacitance method cannot be used. Additionally, since the Fourier number (Fo) is less than 0.2 a first term approximation of the series solution cannot be assumed. Therefore, an *n*-term series solution was used by superimposing the 1-D solutions for a plane wall and an infinite cylinder using the following set of equations:

$$\theta = \sum_{n=1}^{\infty} \frac{4\sin(\lambda_n)}{2\lambda_n + \sin(2\lambda_n)} e^{-\lambda_n^2 Fo} \cos\left(\lambda_n \frac{x}{L}\right) \quad \textbf{(61)}$$

$$\lambda_n \tan(\lambda_n) = Bi \quad \textbf{(62)}$$

$$Bi = \frac{hL}{k} \quad \textbf{(63)}$$

$$Fo = \frac{\alpha t}{L^2} \quad \textbf{(64)}$$

$$\theta = \sum_{n=1}^{\infty} \frac{2}{\lambda_n} \frac{J_1(\lambda_n)}{J_0^2(\lambda_n) + J_1^2(\lambda_n)} e^{-\lambda_n^2 Fo} J_0\left(\lambda_n \frac{r}{r_0}\right) \quad \textbf{(65)}$$

$$\lambda_n \frac{J_1(\lambda_n)}{J_0(\lambda_n)} = Bi \quad \textbf{(66)}$$

$$\mathrm{Bi} = \frac{\mathrm{hr}_0}{\mathrm{k}} \quad \textbf{(67)}$$

$$Fo = \frac{\alpha t}{r_0^{\,2}} \quad \textbf{(68)}$$

Equations (61) to (64) govern transient heat transfer in a plane wall and equations (65) to (68) are for an infinite cylinder. θ is the non-dimensional temperature, x is the distance from the plane wall center line, L is the half thickness of the plane wall, λ_n is the n^{th} solution to the characteristic equations for a plane wall or infinite cylinder, J_0

and J_1 are Bessel functions of the first kind, r is the radial distance from the axis of symmetry, r_0 is the radius of the cylinder, h is the surface heat transfer coefficient, k is the thermal conductivity of the PCM material, α is the thermal diffusivity of the PCM material, and t is time. A schematic of the capsule is given in Figure 68.

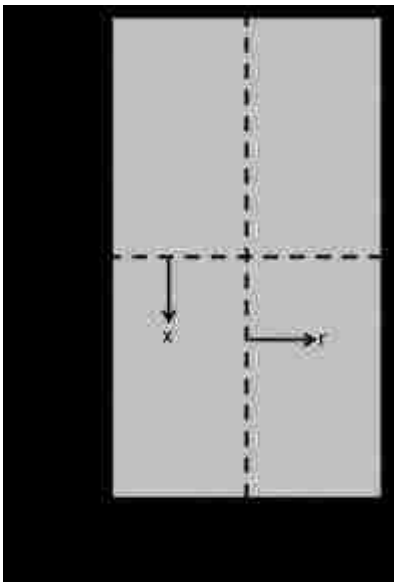

Figure 68. Schematic of EPCM capsule for analytical analysis

The cooling rate for various sample diameters and heights was calculated for an initial sample temperature of 691 °C, 50 degrees above the 641 °C melting temperature of $Na_4B_2O_5$ and the target experimental temperature. Figure 69 shows the results for capsules with a diameter of 25.4 or 50.8 mm with a height of 50.8 or 76.2 mm along with the critical cooling rate using the first 300 roots of the characteristic equations. As both the diameter and height of the capsules increase, the cooling rate at the center of the capsules decreases. The cooling rates within all the capsule sizes considered varied from 1.3 °C/s for the smallest capsules to 0.2 °C/s for the largest and therefore were slower than the 2 °C/s critical cooling rate and therefore the

formation of glass during the experimental testing of samples with these dimensions is unlikely.

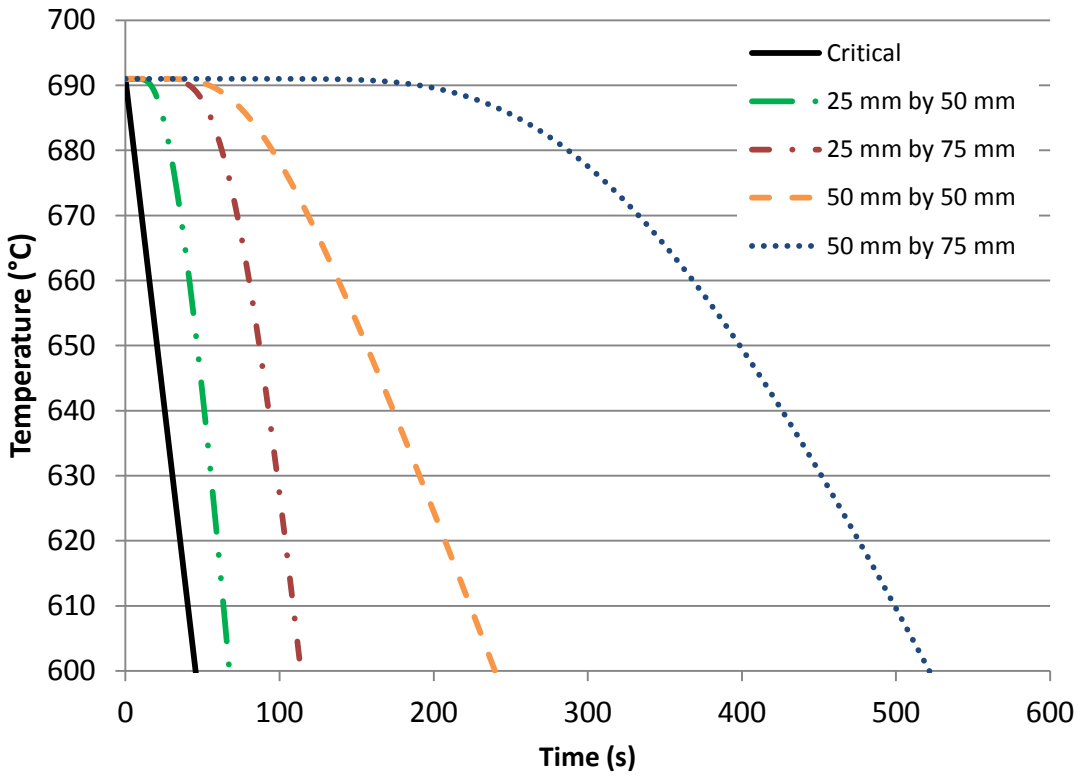

Figure 69. The temperature at the center of the EPCM capsule for a 25.4 mm by 50.8 mm (diameter by height), 25.4 mm by 76.2 mm, 50.8 mm by 50.8 mm, and 50.8 mm by 76.2 mm capsule size along with the critical cooling rate for $Na_4B_2O_5$

While the cooling rate analysis indicates the use of a capsule with the largest diameter and height possible, limitations on the maximum dimensions are imposed as not to exceed the maximum allowable temperature increase within the calorimeter system. For the proposed capsule sizes, an energy balance was conducted to determine the maximum temperature increase of the calorimeter. The enthalpy stored in the capsule is determined by using equations (40), (41), and (42). The enthalpy transferred to the calorimeter (Q_{cal}) is set equal to the energy stored in the EPCM sample ($Q_{EPCM,theo}$). Then equation (39) is solved for T_{cal}. Stainless steel 304 was used as the

encapsulation material and the thermal properties used are listed in Table 3. Using the solid and liquid heat capacities listed in Table 10 the maximum calorimeter temperature was calculated and the results are listed in Table 11. Based on a desirable temperature increase within the calorimeter, a sample with a diameter of 50.8 mm and a height of 50.8 mm was chosen.

Table 11. Final temperature of calorimeter for various capsule sizes

Capsule Size	Temperature
25.4 mm by 50.8 mm	33.70 °C
25.4 mm by 76.2 mm	38.04 °C
50.8 mm by 50.8 mm	59.60 °C
50.8 mm by 76.2 mm	76.86 °C

9.2.2 Initial Calorimeter Testing

Two 50.8 mm by 50.8 mm capsules were prepared for calorimetry testing. A 3.175 mm thick end cap was welded onto the bottom of the 50.8 mm cylinder to create a "cup" that the molten PCM was poured into. Approximately 300 g of $Na_4B_2O_5$ was prepared by mixing the appropriate amounts of Na_2CO_3 and H_3BO_3 together and heating the material in a furnace above 1,000 °C in a platinum crucible. The molten material was poured into the pre-fabricated stainless steel "cups", Figure 70, and then placed into a furnace at 100 °C overnight to prevent water absorption as the samples cooled. It should be noted that the molten oxide appears pink in Figure 70 due to the hot stainless steel capsules as the melt was transparent. Once the material had solidified, the capsules were purged with Argon and the top end cap was welded in place and the hanging wire attached. The samples were weighed both prior and after the filling process to determine mass of both the capsule and PCM; these values are listed in Table 12 for both samples.

Table 12. Specifications of $Na_4B_2O_5$ EPCM samples

	Mass of PCM (g)	Mass of Shell (g)
Sample 1	128.39	194.61
Sample 2	128.23	194.17

Figure 70. EPCM sample during the filling process

The electric furnace was heated from room temperature to 700 °C at a rate of 1,000 °C/hr. and then held at 700 °C for 2 hours. After approximately 10,500 sec, the samples were submerged into the calorimeter causing its temperature to increase as seen in Figure 71. For the first three experiments the samples did not quite reach the desired 691 °C sample temperature, therefore for the fourth experiment the furnace temperature was increased to 750 °C to ensure complete melting of the sample. The results of the calorimetry experiments are listed Table 13.

Table 13. Initial results of $Na_4B_2O_5$ calorimetry testing

Sample #	Charged Temperature	Theoretical Equilibrium Temperature	Theoretical Energy Stored	Measured Energy Stored	Discrepancy
1	667.6 °C	54.21 °C	243.9 kJ	212.9 kJ	12.7%
1	688.7 °C	54.67 °C	248.0 kJ	215.0 kJ	13.4%
2	661.2 °C	55.67 °C	236.9 kJ	218.7 kJ	7.7%
2	749.7 °C	57.40 °C	270.28 kJ	230.9 kJ	14.6%

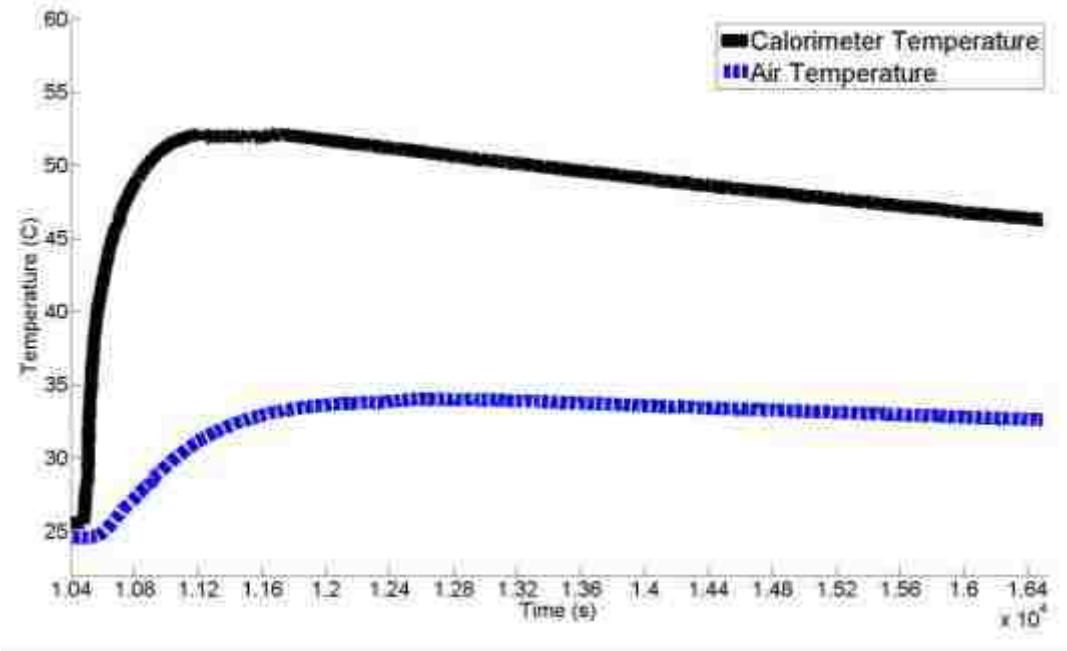

Figure 71. Calorimeter & air temperature during sample 1 cycle 1

The discrepancy between the theoretically stored energy and the measured energy was approximately 10% higher than the anticipated ±2% precision of the system. As the discrepancy was always positive, it indicates that the theoretical energy storage calculation or the underlying assumptions were not fully valid. This can be caused by one or more of the following:

1. Incorrectly reported material properties
2. Glass formation during solidification
3. Contamination during sample preparation
4. Unaccounted phases present
5. Hydration of the sample

To determine the source or sources of the discrepancy the samples were first sectioned and visually examined. Based on this inspection an odd coloring was noticed that

seemed to indicate either a two-phase material or a crystalline material (white) with an amorphous surrounding (gray), as seen in Figure 72. To determine the composition of the material present a scanning electron microscope (SEM) with energy-dispersive X-ray spectroscopy (EDS) capabilities was used and x-ray diffraction (XRD) was performed to determine the crystallinity of the material. Additionally, differential scanning calorimetry (DSC) was conducted to determine the melting temperature of the material.

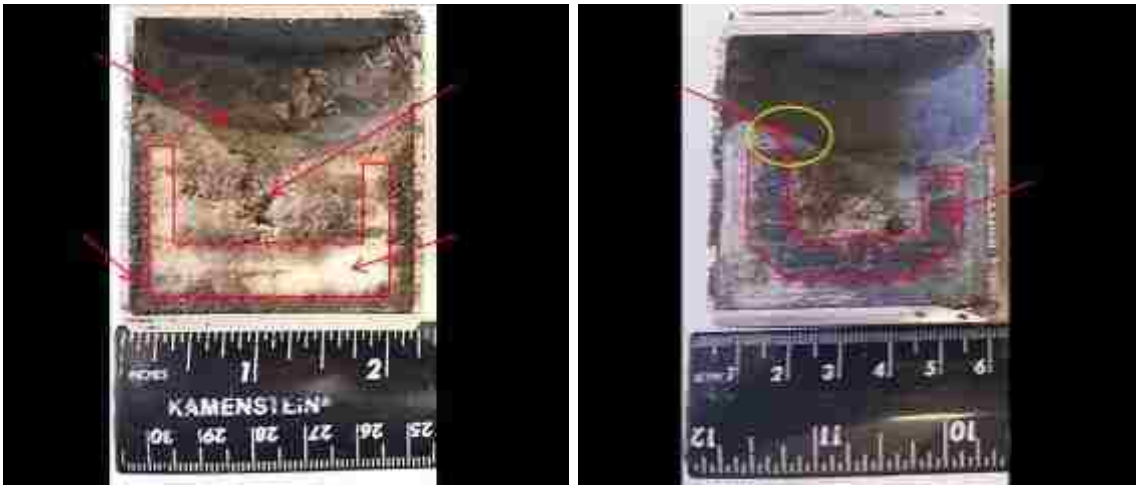

Figure 72. Sectioned $Na_4B_2O_5$ sample 1 (left) and sample 2 (right)

9.2.3 SEM Results

Fifteen locations from four areas (top, middle, edge, and dip) of sample 1 were examined using EDS. The atomic percentage of each element present in the area the beam was focused on was reported. The results showed that only oxygen and sodium were present in the samples hence contamination from another material did not occur. It should be noted that the EDS cannot detect Hydrogen or Boron, therefore the SEM results of sample 1 do not rule out hydration of the material. Trace amounts of iron were detected in the second sample which explains the green discoloration seen in

Figure 72, however the oxygen and sodium ratios did not correspond to those seen in sample 1. The EDS results are listed in Table 14 and Table 15 and photos of the microstructure in the middle and edge regions of both samples are shown in Figure 73.

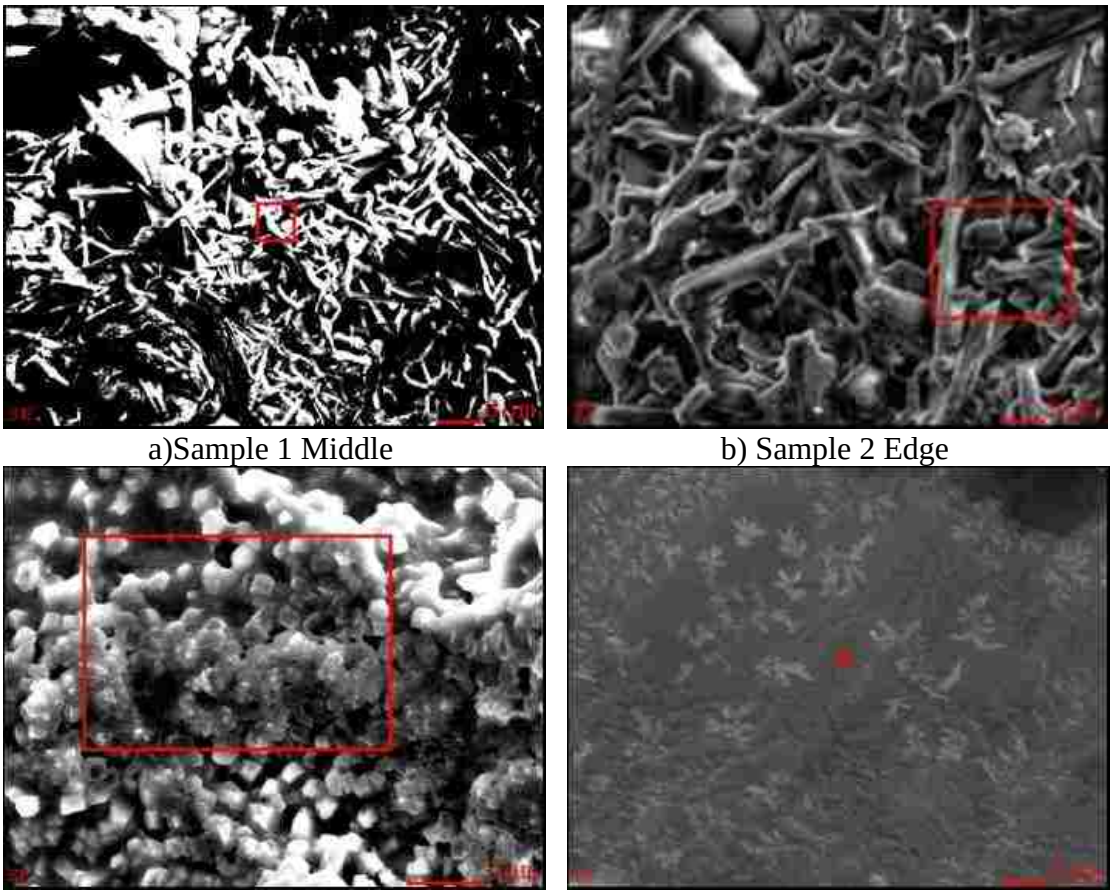

a)Sample 1 Middle b) Sample 2 Edge

c) Sample 2 Middle d) Sample 2 Edge

Figure 73. SEM photos of two locations in both sample 1 and sample 2. Scale bar for a-c are 5 microns while d is 1 micron

Table 14. Sample 1 SEM EDS results

Location	O At%	Na At%	Location	O At%	Na At%
Top	63.0	36.7	Middle	62.0	37.9
	63.0	36.7		62.0	37.9
	64.1	35.9		64.2	35.8
	54.5	45.5		62.0	38.0
	55.5	44.5			
Edge	56.1	43.9	Dip	54.9	45.1
	56.1	43.9		54.1	45.8
	55.3	44.7			
	58.5	41.5			

Table 15. Sample 2 SEM EDS results

Location	O At%	Na At%	Fe At%	Location	O At%	Na At%	Fe At%
Edge	45.3	54.7	0	Edge	44.2	55.7	0.2
Edge	45.0	54.8	0.2	Edge	51.3	48.6	0.1
Edge	47.8	52.0	0.1	Edge	44.0	55.4	0.6
Edge	51.7	48.2	0.1	Edge	39.2	58.8	2.0
Edge	44.8	55.0	0.2	Middle	47.4	52.6	0
Middle	49.3	50.8	0	Middle	47.5	52.5	0

Based on the visual color appearance and assuming an axisymmetric distribution, it was determined that the sample was roughly 59.3% phase 1 (gray) and 40.7% phase 2 (white). With the exception of the top surface, the SEM results for sample 1 in the two regions presented distinct ratios of sodium and oxygen that would indicate the formation of a two-phase material resulting from the partial melting of a non-eutectic initial compound. The average volume-weighted oxygen percentage using the results of Sample 1 was 58.4% which yields a composition that is 62.4% mol. Na2O. This is lower than the 66.6% mol Na_2O of the desired compound due to sodium evaporation during the perpetration of the material. This was calculated using equations (69) to (71) to determine the amount of Na2O required in order to obtain the desired oxygen percentage assuming 1 mol of B_2O_3. It should be noted that this calculation was done assuming that there was no hydration of the storage material during EDS. Furthermore, if the SEM results from sample 2 are included the overall composition change is minimal from 62.4% mol Na_2O to 64.0% mol Na_2O.

$$xNa_2O + B_2O_3 \rightarrow Na_{2x}B_2O_{x+3} \quad \textbf{(69)}$$

$$O\% = \frac{O}{O + Na} = \frac{x+3}{3x+3} \quad \textbf{(70)}$$

$$Na_2O\% = \frac{Na_2O}{Na_2O + B_2O_3} = \frac{x}{x+1} \quad \textbf{(71)}$$

9.2.4 DSC Results

While the SEM results provided insight into the initial makeup of the material and lent credence to the formation of two distinct regions within the material, further evaluation is required. By performing DSC on the different regions of the sample, their thermal properties can be verified with those reported in literature. Additionally, based on the melting temperature reported, the initial composition of the material can be determined. One sample from each section of sample 1 underwent a heating cycle from room temperature to 1,000 °C at a rate of 5 K/min. Prior to the DSC run the material was heated in a 150 °C furnace for approximately 30 min to dehydrate the samples. The two samples had a mass of 20.3 mg and 21.3 mg for the middle and edge locations respectively. A sample from edge the second sample with a mass of 22.4 mg was cycled within the DSC by heating the sample to 1000 °C at a rate of 5 K/min and then cooling it back to 20 °C at a rate of 20 K/min and then reheating it to 1000 °C.

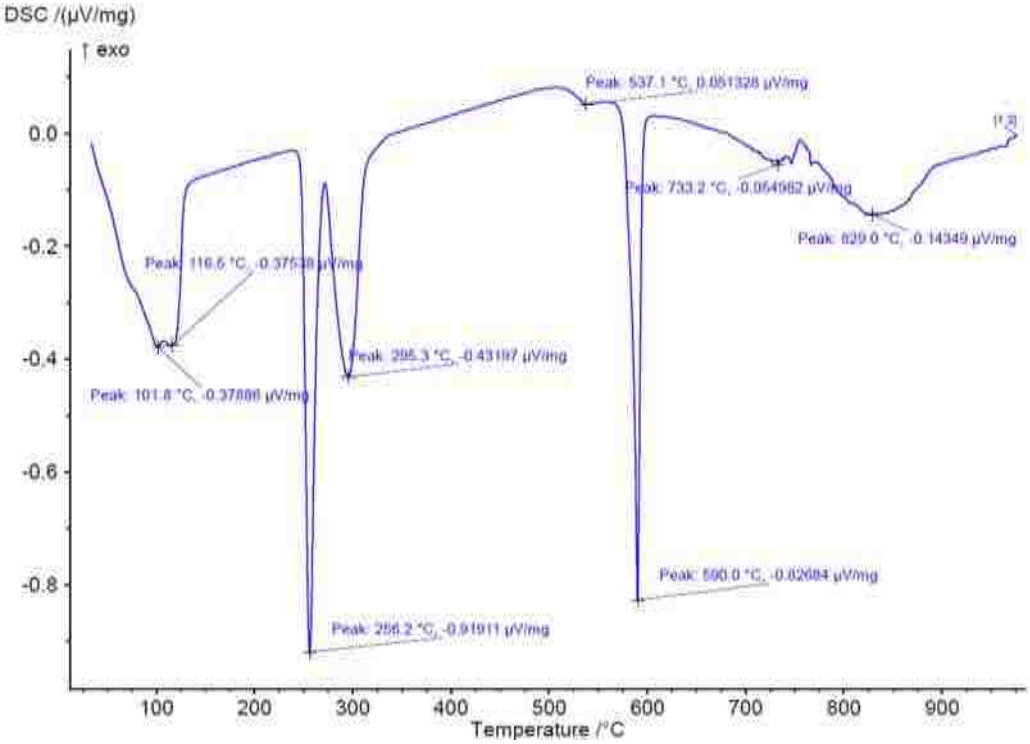

a) Edge of Sample 1

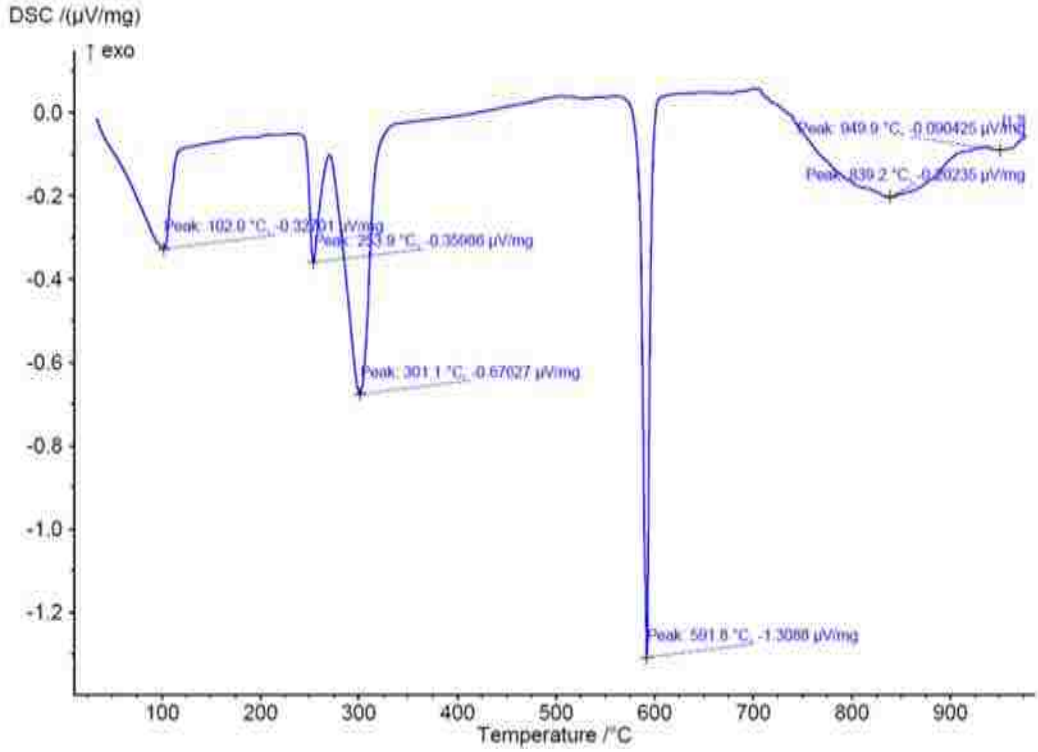

b) Middle of Sample 1

Figure 74. DSC of $Na_4B_2O_5$ Sample 1

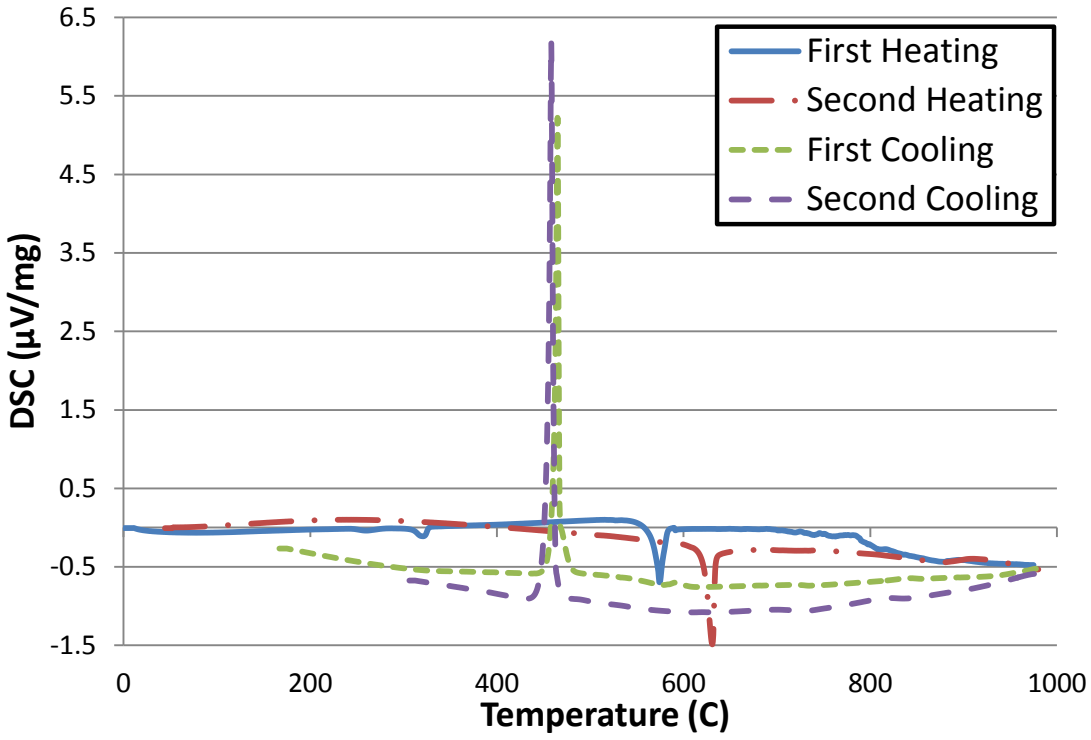

Figure 75. DSC of $Na_4B_2O_5$ Sample 2

The DSC curves for the two locations for sample 1 presented in Figure 74 are extremely similar. The peaks at 102 °C, 256 °C, and 300 °C correspond to the dehydration of $NaBO_2$•Y H_2O [99] as the samples are highly hydroscopic and were exposed to the atmosphere post-sectioning prior to the DSC runs. The peak at 590 °C is the onset of melting of the material. Due to the incongruent melting of the material a large dome over a range of temperatures from 700 °C to 1000 °C is formed centered on the liquidus temperature of the compound. The results of the DSC for sample 1 indicate that the liquidus temperature of the tested material is 830 °C for the edge and 840 °C for the middle based on peak position. The only noticeable difference between the two DSC curves is that the edge material began melting right after the 590 °C peak whereas for the middle a period of additional sensible heating occurred until about 700

°C before melting started. As the edge material had already undergone a phase change previously, it would be more inclined to melt whereas the un-melted center material would require additional energy. The reported liquidus temperature of approximately 835 °C corresponds with the average composition found via the SEM results based on the phase diagram presented in Figure 67. The DSC run for sample 2 was conducted less than 24 hrs. after the samples were sections and therefore only a small peak at approximately 300 °C is seen during the initial heating cycle and it showed the same peak at ~590 °C, Figure 75. However this increased to 630 °C during the second heating cycle. This would indicate that some sort of change is occuring after the initial melting and solidification cycle. Additionally, a small amount of water could have remained wtihin the PCM that results in a lower soldius temperautre and is only fully expelled when the DSC sample is heated above 1,000 °C. Furthermore the solidification temperature was only roughly 460 °. There is limited literature on the melting and solidification of $Na_4B_2O_5$ where there is a reported melting temperature of 641 °C [95, 100].

9.2.5 XRD Results

Neither the DSC nor SEM results could completely rule out the formation of glass within the sample as they only reported on the melting temperature and the oxygen to sodium ratio of the composition. However, XRD can be used to determine whether a material is crystalline or amorphous as well as its composition and unlike EDS it can detect Boron. The XRD pattern for a sample from the middle of sample 1 is seen in Figure 76. The sample was scanned from 10 to 70 degrees at a rate of 2 °/min. The flat background of the pattern indicates that the material is crystalline.

When the XRD results are compared to a database of known materials, it most closely matches that of $NaBO_2 \bullet 2H_2O$, also shown in Figure 76.

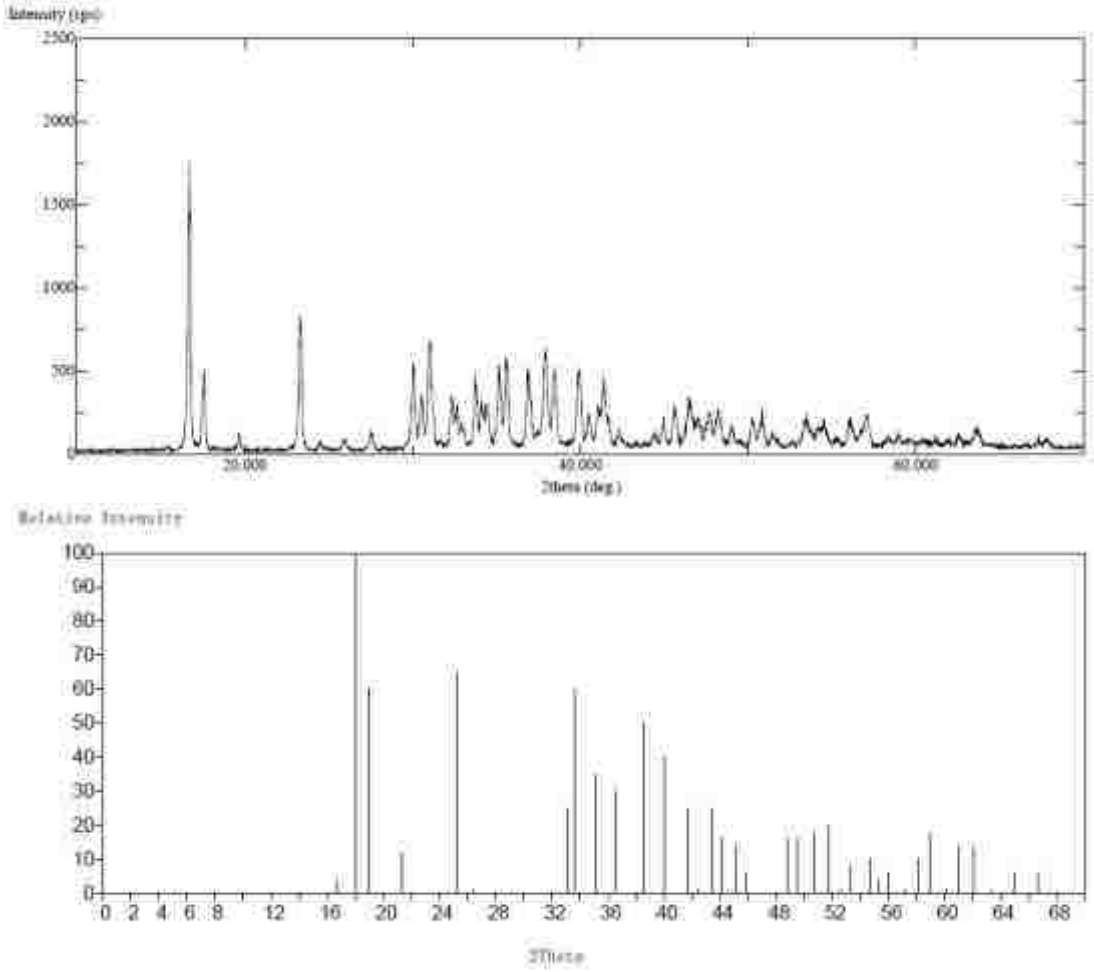

Figure 76. XRD of Middle of Sample 1 (upper) and $NaBO_2 \cdot 2H_2O$ ICDD Card No. 00-006-0122 (lower)

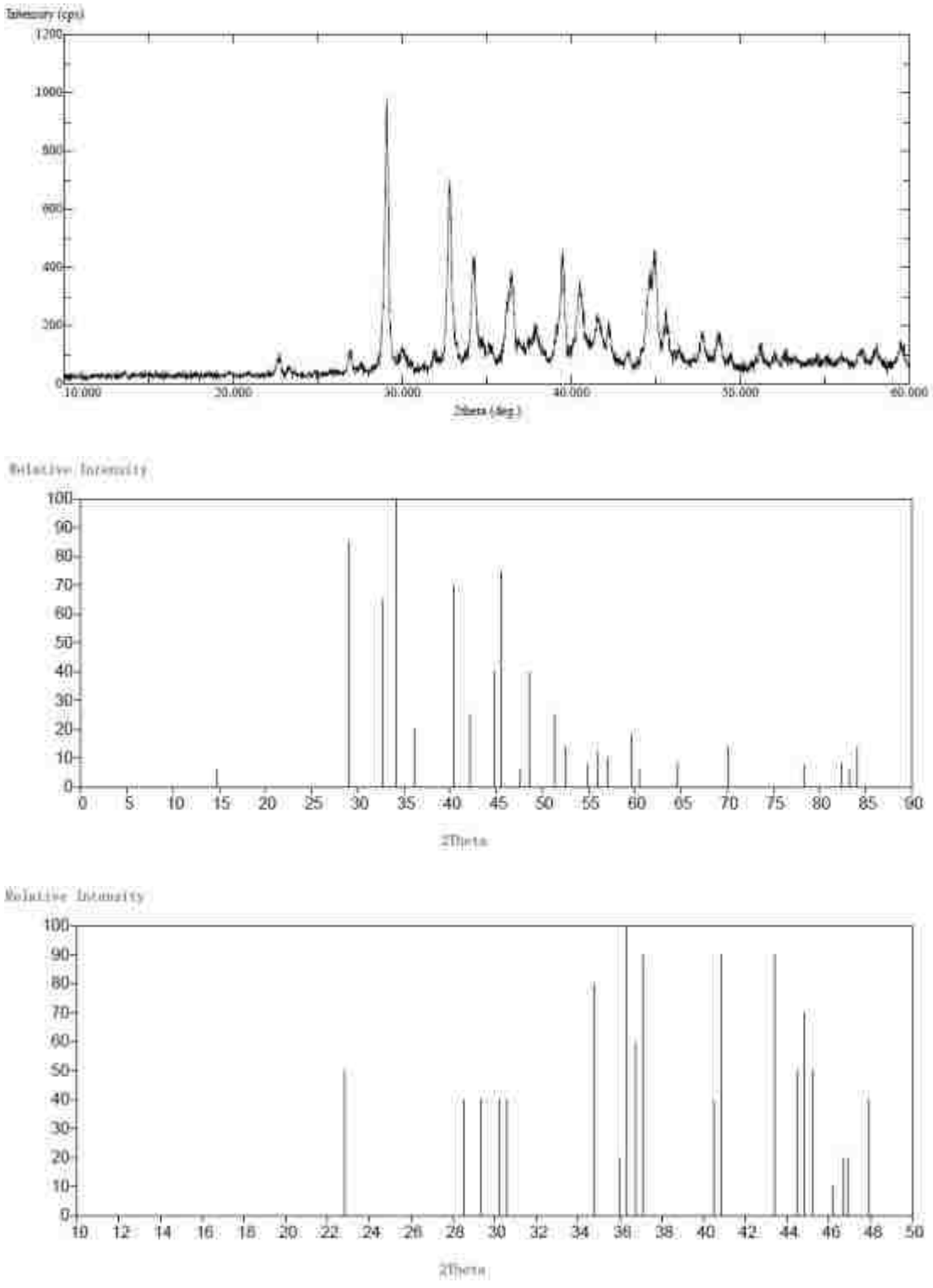

Figure 77. XRD of sample 2 (top), $NaBO_2$ (middle) ICDD Card No. 00-012-0492, and $Na_4B_2O_5$ ICDD Card No. 00-036-0878

XRD was also performed on a sample from the second EPCM sample and the results are shown in Figure 77. These results did not show the high intensity peak at angles below 25° that were seen in sample 1. The pattern showed peaks of both $NaBO_2$ and $Na_4B_2O_5$, which is consistent with the fact that the material composition is between those two limits. This emphasized how the first sample had become hydrated during the time between sectioning and testing. It also lends credence to the calculation of the initial sample composition from the initial SEM results as peaks from both end components are seen in the XRD pattern.

9.2.6 Revised Calorimeter Results

Based on the results of the SEM, DSC, and XRD analyses the calorimetry energy analysis was updated to include a two-phase material resulting from incongruent melting. Using the weighted average of the SEM results, the initial composition of the material was determined to be 62.44% mol. Na_2O. Since the experimental sample temperatures were below the liquidus temperature of the material a tie line was used to determine the percentage of solid and liquid material present based on the final sample temperature. Additionally there was no liquid superheating present during the experiments. The solid specific heat and latent heat of the liquid phase were determined by mass averaging the properties of Na_2O and B_2O_3 based on the previously determined initial composition using equations (72) and (73)

$$c_{p.}^{s} = \frac{x}{1-x} c_{p,Na_2O} + c_{p,B_2O_3} \quad \textbf{(72)}$$

$$L = \frac{x}{1-x} L_{Na_2O} + L_{B_2O_3} \quad \textbf{(73)}$$

While the XRD and DSC results for sample 1 show that the material was hydrated, they were conducted three months after the sample was sectioned whereas the SEM was conducted only a week after the samplers were sectioned. The samples were kept within a hand-pumped vacuum desiccator and the contamination occurred over a prolonged period of time. Furthermore, the oxygen to sodium ratio of the six hydrated forms of $NaBO_2$ is greater than that seen during the EDS analysis. The lowest ratio is for $NaBO_2 \bullet \frac{1}{3}H_2O$ which is 0.7. Therefore, it is unlikely that the material was hydrated during the EDS analysis of sample 1 and the results present a reasonable portrayal of the initial material composition.

The updated results are in Table 16 and Table 17 for both a melting temperature of 641 °C and 592 °C. While the discrepancy of the calorimetry experiments is still higher than the expected ±2%, it is now under 5%. If the solidus temperature reported by the DSC results is used, the discrepancy is within the expected limits for all but sample 2 cycle 1. However, as the furnace during this experiment was set to 700° °C and the thermocouples only reported a temperature of 661 °C so it is likely that the furnace malfunctioned during the experiment and its results should be discarded. While there is still some uncertainly as to the solidus temperature of the initial compound, these results indicate that materials from the Na_2O-B_2O_3 system can be used as PCM for TES applications and still present a better option over the currently used nitrate and chloride based salts.

Table 16. Updated results of $Na_4B_2O_5$ calorimetry testing with T_m= 641 °C

Sample #	Charged Temperature	Theoretical Equilibrium Temperature	Theoretical Energy Stored	Measured Energy Stored	Discrepancy
1	667.6 °C	54.2 °C	224.2 kJ	212.9 kJ	5.0%
1	688.7 °C	54.7 °C	227.1 kJ	218.8 kJ	3.7%
2	661.2 °C	55.7 °C	219.1 kJ	220.2 kJ	-0.50%
2	749.7 °C	57.4 °C	239.2 kJ	232.6 kJ	2.8%

Table 17. Updated results of $Na_4B_2O_5$ calorimetry testing with T_m= 592 °C

Sample #	Charged Temperature	Theoretical Equilibrium Temperature	Theoretical Energy Stored	Measured Energy Stored	Discrepancy
1	667.6 °C	54.2 °C	216.0 kJ	212.9 kJ	1.4%
1	688.7 °C	54.7 °C	219.0 kJ	218.8 kJ	0.05%
2	661.2 °C	55.7 °C	210.9 kJ	220.2 kJ	-4.4%
2	749.7 °C	57.4 °C	231.0 kJ	232.6 kJ	-0.69%

9.3 Conclusions

The eutectic materials in the Na_2O-B_2O_3 system are promising materials for use as PCMs for high temperature TES applications. These materials offer a higher energy storage density at comparable melting temperatures to the commonly used nitrate and chloride salts while being less reactive with the encapsulation materials. While initial testing of the $Na_4B_2O_5$ EPCM capsules did not go as excepted further analysis of the samples indicated that Na_2O evaporated during the formation of the material yielding a non-eutectic compound. This yielded an initial high experimental discrepancy, roughly 10% higher than expected. The causes of these unexpected

results were invested by examining the sample via EDS, DSC, and XRD to determine the composition and crystallinity of the material.

The EDS results of the first sample corroborated the visual inspection that two distinct areas formed within the sample. The center had a composition close to that of a 1:1 ratio of Na_2O to B_2O_3 whereas the edges were closer to the desired 2:1 ratio. DSC showed the liquidus temperature of the material to be approximately 835 °C, which yields a composition in agreement with the EDS results. The possibility of glass formation was examined using XRD. The XRD pattern of the middle indicated that the material was a crystalline form of hydrated $NaBO_2$, most likely $NaBO_2 \cdot 2H_2O$. This is likely the result of improper storage of the samples during the time between the samples being sectioned and the XRD being performed. The second sample was examined less than 24 hours after sectioning and the XRD and DSC results did not show any hydration of the material. However, the DSC data did show a shift in the melting temperature after the first heating cycle.

The experimental energy analysis was modified to accommodate the partial melting of the PCM since the experiments were conducted below the liquidus temperature of the compound with the initial composition. This yielded results closer to the ±2% precision of the calorimetry system depending on the value used as the solidus temperature. The difference in the solidus temperature reported via the DSC and that reported on the phase diagram could be a result of a small fraction of water vapor remaining in the PCM from the initial formation of the PCM. While the results of these initial experiments indicate that sodium borate oxides can be used a PCMs for high temperature TES, further testing is required to evaluate their performance after

prolonged thermal cycling to ensure that they are still a better alternative to the currently used nitrate and chloride salts.

CHAPTER X: SUMMARY AND CONCLUSIONS

Numerical investigations were conducted into the heat transfer that occurs within EPCM capsules to improve the technology of EPCM-based latent heat TES systems. The ability of the enthalpy-porosity and VOF methods to accurately capture the heat transfer that occurs within EPCM capsules was examined by modeling previously conducted calorimetry experiments. Good agreement was obtained with respect to the final shape of the solid PCM within the capsules between the simulations and those seen in a sectioned sample after experimentation. Additionally, the difference between the experimental and predicted equilibrium temperatures was under 1%. The good agreement obtained proves that the numerical methods employed are able to capture the complex heat transfer that occurs within EPCM capsules during a state change and can be used to investigate means of improving their performance.

While the inclusion of an internal void space within an EPCM capsule is required to prevent the capsules from rupturing, its effect on the heat transfer within the capsules has largely been ignored. To investigate the impact of an internal void as well as natural convection within the molten PCM, a three-dimensional model of a spherical EPCM capsule was conducted using the enthalpy-porosity and VOF methods simultaneously. The presence of the void within the capsule acts as an insulator and distorts the isotherms and thus the solid-liquid interface from being circular to "U"-shaped during the conduction-dominated phase of the melting process. Furthermore, as the PCM melts convection becomes the dominant mode of heat transfer both increasing the melting rate and further changing the spatial evolution of the solid-liquid interface. While the melting process is convection-dominated, the solidification

process is conduction-dominated and therefore is limited by the thermal conductivity of the PCM used. As the solid PCM sticks to the capsule surface, the ever-increasing solid layer asymptotically decreases the heat transfer rate leading to significantly longer solidification times compared to melting times. Thus during the design of EPCM-based systems, the discharging process needs to be carefully examined.

The results of the spherical EPCM capsule investigation highlight the impact an internal void space has on the performance of the capsule. To further investigate its impact on the internal heat transfer of EPCM capsules, three limiting initial void distributions were considered: an upper void, a central void, and a random void. As the PCM in the central void distribution is in direct contact with the capsule shell during the initial stages of the melting process, it has the highest initial heat transfer rate and the shortest melting time; 22% faster than the random void distribution and 39% faster than the upper void. The random void distribution is a middle ground between the central and upper void cases; although the PCM is in direct contact with the entire capsule shell it has a lower effective thermal conductivity. Furthermore, the air and PCM phases slowly diffuse as the PCM melts resulting in the formation of an air void at the top of the capsule.

While due to gravitational effects one would expect the air to diffuse to the top of the capsule forming an upper void, the behavior of the void is dependent on the operating conditions of the system and can potentially impact the performance of the TES system for numerous cycles. Ideally, one would like for the void to always be located at near center of the capsule as to mitigate its negative effects on the melting rate. The location of the internal void has a profound effect on the temporal and spatial

evolution of the solid-liquid interface. Thus, to accurately evaluate the performance of EPCM capsules in a TES system the internal void and its effects must be included.

To extend the results from the performance of a single EPCM capsule to that of an entire system, a pilot scale EPCM-based latent heat TES system was numerically evaluated. Metal deflectors were used to promote uniform heat transfer around the capsules. Despite this, the same "U"-shaped solid-liquid interface was seen within the capsules during the initial stages of melting prior to convection becoming the dominate mode of heat transfer due to the void located at the top of the capsules. The solid-liquid interface not only propagates radially inward but due to the increase in heat transfer from the warm test section walls, it also propagates towards the center of the channel. The ten EPCM capsules sequentially experience the same evolution of the melting front resulting in the internal void being compressed from 26% to 19% of the capsule volume over the course of the charging process.

The results of the numerical investigation were compared to the experimental results for the charging process. The agreement between the predicted and measured temperature of the tenth capsule during the solid sensible heating phase was under 3%; however the difference between the predicted and measured temperature started to increase as the capsules within the test section began to melt. Although the simulation predicted an 8% quicker melting time, the rate of temperature increases during the liquid superheating phase matched that of the experiments. Therefore, the shorter melting is a result of using an incorrect value for the latent heat of fusion of $NaNO_3$ that was 8% lower than the actual value. However, the large operational temperature range results in a significant amount of energy being stored via sensible heat; thus the

incorrect latent heat value used had a negligible effect the total energy storage of the system. Of the 22 MJ of energy given up by the HTF over the course of the charging process, 80% was stored in the 10 EPCM capsules. Of the 17.5 MJ of energy stored by the capsules, 14.2 MJ is stored by the 17.7 kg of $NaNO_3$. Furthermore, 20% of the energy stored by the $NaNO_3$ was stored via latent heat. Thus the system is capable of storing a large fraction of the energy supplied by the HTF with a significant contribution from latent heat. Furthermore, if the operational temperature range of the system was reduced, the percentage of latent heat energy stored would vastly increase.

As the purpose of a TES systems is to store useful work and not just simply store energy, a second law analysis must be conducted along with a first law analysis to truly evaluate the performance of the system. Six systems were numerically studied to determine if employing a multi-PCM system is beneficial to the overall performance. In addition to their performance during the charging and discharging process, the overall cycle efficiency of the system was also considered. The overall cycle efficiency is dependent on the temperature change of the HTF and thus a smaller change leads to an increase in efficiency. This also increases the amount of energy that is stored through latent heat. The latent heat-based systems were able to store vastly more energy and exergy than the sensible heat only system at comparable efficiencies. With the exception of the $NaNO_2$ system, the multi-PCM systems offered an improvement over single PCM systems. The notable performance of the $NaNO_2$ system is due to its high energy storage density and the high heat transfer rate resulting from the large temperature difference between the inlet and melting temperatures.

The exceptional performance of the $NaNO_2$ systems is overshadowed by its dismal performance during the discharging process emphasizing the importance of looking at the overall cycle efficiency. The HTF was only able to recover 88% of the energy and exergy that was stored in the capsules. The HTF is able to recover 92% of the energy stored in the $NaNO_3$ systems while all of the energy and exergy was recovered in the remaining systems. In addition to the overall efficiency, it amount of energy stored and the exergy content at the end of charging should be considered when determining the highest performing system. The 2-PCM system has the highest exergy content at the end of the charging process and coupled with its cycle efficiency makes it the best suited system for the chosen operating conditions. While these results indicate that a multi-PCM system is more efficient than a single-PCM system, care must be taken as to the difference between the inlet conditions and the melting points of the PCMs as they highly impact the overall results. Therefore further research is required to determine the optimal operating conditions and PCM properties to yield the most efficient system.

In addition to the numerical investigations conducted, the use of eutectic materials in the Na_2O-B_2O_3 system as PCMs for high temperature applications was experimentally evaluated. These metallic oxides have a higher energy storage density at comparable melting temperatures to the commonly investigated nitrate and chloride salts while being less corrosive. Although the initial calorimetry testing of the $Na_4B_2O_5$ samples did not go as expected further investigation via EDS, DSC, and XRD revealed the initial composition of the material was off from the eutectic point due to sodium evaporation and therefore an incongruently melting material formed.

Since all of the experiments took place below the liquidus temperature of the material, the samples did not undergo a complete phase change leading to the high initial experimental error. The experimental energy analysis was modified to account for the partial melting of the sample and this significantly reduced the discrepancy between the experimental and theoretical energy storage to within the ±2% precision of the system. These results show that the eutectic materials in the Na_2O-B_2O_3 system and other metallic oxides have the potential to revolutionize the technology of EPCM-based latent heat TES. However additional extensive research is required before the materials can be used at operational CSP plants.

The results of the research presented here greatly advance the technology of latent heat-based TES systems. However, additional investigations are required to optimize the operating conditions of EPCM-based TES systems and increase their overall efficiency. Additionally, research into new novel high temperature materials such as metallic oxides is required to not only decrease the overall system size but also increase the lifetime of the systems. This additional research coupled with the results presented will allow for EPCM-based latent heat TES system to be integrated into operational CSP plants and reduce the levelized cost of electricity making grid scale electricity generation via solar thermal power competitive with current fossil fuel based-systems.

REFERENCES

[1] Gil, A., Medrano, M., Martorell, I., Lazaro, A., Dolado, P., Zalba, B., and Cabeza, L. F., 2010, "State of the art on high temperature thermal energy storage for power generation. Part 1—Concepts, materials and modellization," Renewable and Sustainable Energy Reviews, 14(1), pp. 31-55.
[2] Kuravi, S., Trahan, J., Goswami, D. Y., Rahman, M. M., and Stefanakos, E. K., 2013, "Thermal energy storage technologies and systems for concentrating solar power plants," Progress in Energy and Combustion Science, 39(4), pp. 285-319.
[3] Sharma, A., Tyagi, V. V., Chen, C. R., and Buddhi, D., 2009, "Review on thermal energy storage with phase change materials and applications," Renewable and Sustainable energy reviews, 13(2), pp. 318-345.
[4] Kenisarin, M., and Mahkamov, K., 2007, "Solar energy storage using phase change materials," Renewable and Sustainable Energy Reviews, 11(9), pp. 1913-1965.
[5] Farid, M. M., Khudhair, A. M., Razack, S. A. K., and Al-Hallaj, S., 2004, "A review on phase change energy storage: materials and applications," Energy Conversion and Management, 45(9–10), pp. 1597-1615.
[6] Paksoy, H., Mehling, H., and Cabeza, L., 2007, "Phase Change Materials and Their Basic Properties," Thermal Energy Storage for Sustainable Energy Consumption, Springer Netherlands, pp. 257-277.
[7] Lane, G. A., 1983, Solar Heat Storage: Latent Heat Material, Volume I, Background and Scientific Principles, CRC Press, Florida.
[8] Lane, G. A., Lee, M., Collins, J. W., Aubrecht, D. M., Sperling, R. A., Solomon, L., Ha, J.-W., Yi, G.-R., Weitz, D. A., and Manoharan, V. N., 1986, "Solar Heat Storage: Latent Heat Material, Volume II, Technology
Synchronized reinjection and coalescence of droplets in microfluidics," Lab on a Chip, 14(3), pp. 509-513.
[9] Zalba, B., Marín, J. M., Cabeza, L. F., and Mehling, H., 2003, "Review on thermal energy storage with phase change: materials, heat transfer analysis and applications," Applied Thermal Engineering, 23(3), pp. 251-283.
[10] Zheng, Y., Zhao, W., Sabol, J. C., Tuzla, K., Neti, S., Oztekin, A., and Chen, J. C., 2013, "Encapsulated phase change materials for energy storage – Characterization by calorimetry," Solar Energy, 87, pp. 117-126.
[11] Xu, B., Li, P., and Chan, C., 2015, "Application of phase change materials for thermal energy storage in concentrated solar thermal power plants: A review to recent developments," Applied Energy, 160, pp. 286-307.
[12] Hoshi, A., Mills, D. R., Bittar, A., and Saitoh, T. S., 2005, "Screening of high melting point phase change materials (PCM) in solar thermal concentrating technology based on CLFR," Solar Energy, 79(3), pp. 332-339.
[13] Liu, M., Saman, W., and Bruno, F., 2012, "Review on storage materials and thermal performance enhancement techniques for high temperature phase change thermal storage systems," Renewable and Sustainable Energy Reviews, 16(4), pp. 2118-2132.

[14] Jegadheeswaran, S., and Pohekar, S. D., 2009, "Performance enhancement in latent heat thermal storage system: a review," Renewable and Sustainable Energy Reviews, 13(9), pp. 2225-2244.
[15] Colvin, D. P., 1999, "Enhanced thermal management using encapsulated phase change materials: An overview," ASME-PUBLICATIONS-HTD, 363, pp. 199-206.
[16] Chen, J. C. H., and Eichelberger, J. L., 1985, "Encapsulated phase change thermal energy _storage materials," Google Patents.
[17] Blaney, J. J., Neti, S., Misiolek, W. Z., and Oztekin, A., 2013, "Containment capsule stresses for encapsulated phase change materials," Applied Thermal Engineering, 50(1), pp. 555-561.
[18] Jacob, R., and Bruno, F., 2015, "Review on shell materials used in the encapsulation of phase change materials for high temperature thermal energy storage," Renewable and Sustainable Energy Reviews, 48, pp. 79-87.
[19] Zhao, W., Zheng, Y., Sabol, J. C., Tuzla, K., Neti, S., Oztekin, A., and Chen, J. C., 2013, "High temperature calorimetry and use of magnesium chloride for thermal energy storage," Renewable Energy, 50, pp. 988-993.
[20] Solomon, L. D., 2013, "The Use of Sodium Chloride & Aluminum as Phase Change Materials for High Temperature Thermal Energy Storage Characterized by Calorimetry."
[21] Zhao, W., 2013, "Characterization of Encapsulated Phase Change Materials for Thermal Energy Storage," Ph.D, Lehigh University.
[22] Solomon, L., Oztekin, A., and Neti, S., under review
"Thermal Analysis of Phase Change Materials for Energy Storage," Journal of Heat Transfer.
[23] Zheng, Y., Barton, J. L., Tuzla, K., Chen, J. C., Neti, S., Oztekin, A., and Misiolek, W. Z., 2015, "Experimental and computational study of thermal energy storage with encapsulated NaNO3 for high temperature applications," Solar Energy, 115(0), pp. 180-194.
[24] Zheng, Y., 2015, "Thermal Energy Storage with Encapsulated Phase Change Materials for High Temperature Applications," PhD, Lehigh University.
[25] Alam, T. E., Dhau, J. S., Goswami, D. Y., and Stefanakos, E., 2015, "Macroencapsulation and characterization of phase change materials for latent heat thermal energy storage systems," Applied Energy, 154, pp. 92-101.
[26] Voller, V. R., and Prakash, C., 1987, "A fixed grid numerical modeling methodology for convection-diffusion mushy region phase-change problems," International Journal of Heat and Mass Transfer, 30(8), pp. 1709-1718.
[27] Alexiades, V., and Solomon, A. D., 1993, Mathematical Modeling of Melting and Freezing Processes, Hemisphere Publishing Corporation, Washington, D.C.
[28] Brent, A. D., Voller, V. R., and Reid, K. J., 1988, "Enthalpy-Porosity Technique for Modeling Convection-Diffusion Phase Change: Application to the Melting of a Pure Metal," Numerical Heat Transfer, 13(3), pp. 297-318.
[29] Mackenzie, J. A., and Robertson, M. L., 2000, "The Numerical Solution of One-Dimensional Phase Change Problems Using an Adaptive Moving Mesh Method," Journal of Computational Physics, 161(2), pp. 537-557.

[30] Khodadadi, J. M., and Zhang, Y., 2001, "Effects of buoyancy-driven convection on melting within spherical containers," International Journal of Heat and Mass Transfer, 44(8), pp. 1605-1618.
[31] Ismail, K. A. R., 2002, Heat Transfer in Phase Change in Simple and ComplexGeometries.Thermal Energy Storage Systems and Applications, Wiley, Chichester.
[32] Tan, F. L., Hosseinizadeh, S. F., Khodadadi, J. M., and Fan, L., 2009, "Experimental and computational study of constrained melting of phase change materials (PCM) inside a spherical capsule," International Journal of Heat and Mass Transfer, 52(15–16), pp. 3464-3472.
[33] Pinelli, M., and Piva, S., 2003, "Solid/Liquid Phase Change in Presence of Natural Convection: A Thermal Energy Storage Case Study," Journal of Energy Resources Technology, 125(3), pp. 190-198.
[34] Assis, E., Katsman, L., Ziskind, G., and Letan, R., 2007, "Numerical and experimental study of melting in a spherical shell," International Journal of Heat and Mass Transfer, 50(9–10), pp. 1790-1804.
[35] Assis, E., Ziskind, G., and Letan, R., 2008, "Numerical and Experimental Study of Solidification in a Spherical Shell," Journal of Heat Transfer, 131(2), pp. 024502-024502.
[36] Archibold, A. R., Gonzalez-Aguilar, J., Rahman, M. M., Yogi Goswami, D., Romero, M., and Stefanakos, E. K., 2014, "The melting process of storage materials with relatively high phase change temperatures in partially filled spherical shells," Applied Energy, 116(0), pp. 243-252.
[37] Archibold, A. R., Rahman, M. M., Yogi Goswami, D., and Stefanakos, E. K., 2015, "The effects of radiative heat transfer during the melting process of a high temperature phase change material confined in a spherical shell," Applied Energy, 138, pp. 675-684.
[38] Bellan, S., Alam, T. E., González-Aguilar, J., Romero, M., Rahman, M. M., Goswami, D. Y., and Stefanakos, E. K., 2015, "Numerical and experimental studies on heat transfer characteristics of thermal energy storage system packed with molten salt PCM capsules," Applied Thermal Engineering, 90, pp. 970-979.
[39] Zhao, W., Elmozughi, A. F., Oztekin, A., and Neti, S., 2013, "Heat transfer analysis of encapsulated phase change material for thermal energy storage," International Journal of Heat and Mass Transfer, 63(0), pp. 323-335.
[40] Bejan, A., 1978, "Two thermodynamic optima in the design of sensible heat units for energy storage," Journal of Heat Transfer, 100(4), pp. 708-712.
[41] Jegadheeswaran, S., Pohekar, S., and Kousksou, T., 2010, "Exergy based performance evaluation of latent heat thermal storage system: a review," Renewable and Sustainable Energy Reviews, 14(9), pp. 2580-2595.
[42] Rosen, M. A., Pedinelli, N., and Dincer, I., 1999, "Energy and exergy analyses of cold thermal storage systems," International Journal of Energy Research, 23(12), pp. 1029-1038.
[43] Ramayya, A. V., and Ramesh, K., 1998, "Exergy analysis of latent heat storage systems with sensible heating and subcooling of PCM," International journal of energy research, 22(5), pp. 411-426.

[44] Sari, A., and Kaygusuz, K., 2004, "First and second laws analyses of a closed latent heat thermal energy storage system," Chinese Journal of Chemical Engineering, 12(2), pp. 290-293.
[45] Öztürk, H. H., 2005, "Experimental evaluation of energy and exergy efficiency of a seasonal latent heat storage system for greenhouse heating," Energy Conversion and Management, 46(9), pp. 1523-1542.
[46] Koca, A., Oztop, H. F., Koyun, T., and Varol, Y., 2008, "Energy and exergy analysis of a latent heat storage system with phase change material for a solar collector," Renewable Energy, 33(4), pp. 567-574.
[47] Kousksou, T., Rhafiki, T. E., Arid, A., Schall, E., and Zeraouli, Y., 2008, "Power, efficiency and irreversibility of latent energy systems," Journal of Thermophysics and Heat Transfer, 22(2), pp. 234-239.
[48] Erek, A., and Dincer, I., 2009, "A new approach to energy and exergy analyses of latent heat storage unit," Heat Transfer Engineering, 30(6), pp. 506-515.
[49] MacPhee, D., and Dincer, I., 2009, "Thermodynamic analysis of freezing and melting processes in a bed of spherical PCM capsules," Journal of Solar Energy Engineering, 131(3), p. 031017.
[50] El-Dessouky, H., and Al-Juwayhel, F., 1997, "Effectiveness of a thermal energy storage system using phase-change materials," Energy Conversion and Management, 38(6), pp. 601-617.
[51] Singh, D., Zhao, W., Yu, W., France, D. M., and Kim, T., 2015, "Analysis of a graphite foam–NaCl latent heat storage system for supercritical CO2 power cycles for concentrated solar power," Solar Energy, 118, pp. 232-242.
[52] Cui, H., Yuan, X., and Hou, X., 2003, "Thermal performance analysis for a heat receiver using multiple phase change materials," Applied thermal engineering, 23(18), pp. 2353-2361.
[53] Fang, M., and Chen, G., 2007, "Effects of different multiple PCMs on the performance of a latent thermal energy storage system," Applied Thermal Engineering, 27(5), pp. 994-1000.
[54] Seeniraj, R., and Narasimhan, N. L., 2008, "Performance enhancement of a solar dynamic LHTS module having both fins and multiple PCMs," Solar Energy, 82(6), pp. 535-542.
[55] Adine, H. A., and El Qarnia, H., 2009, "Numerical analysis of the thermal behaviour of a shell-and-tube heat storage unit using phase change materials," Applied mathematical modelling, 33(4), pp. 2132-2144.
[56] Peiró, G., Gasia, J., Miró, L., and Cabeza, L. F., 2015, "Experimental evaluation at pilot plant scale of multiple PCMs (cascaded) vs. single PCM configuration for thermal energy storage," Renewable Energy, 83, pp. 729-736.
[57] Watanabe, T., and Kanzawa, A., 1995, "Second law optimization of a latent heat storage system with PCMs having different melting points," Heat Recovery Systems and CHP, 15(7), pp. 641-653.
[58] Gong, Z.-X., and Mujumdar, A. S., 1997, "Thermodynamic optimization of the thermal process in energy storage using multiple phase change materials," Applied Thermal Engineering, 17(11), pp. 1067-1083.

[59] Kousksou, T., Strub, F., Lasvignottes, J. C., Jamil, A., and Bedecarrats, J., 2007, "Second law analysis of latent thermal storage for solar system," Solar energy materials and solar cells, 91(14), pp. 1275-1281.
[60] Domański, R., and Fellah, G., 1996, "Exergy analysis for the evaluation of a thermal storage system employing PCMs with different melting temperatures," Applied thermal engineering, 16(11), pp. 907-919.
[61] Gong, Z.-X., and Mujumdar, A. S., 1996, "Finite element analysis of a multistage latent heat thermal storage system," Numerical Heat Transfer, Part A Applications, 30(7), pp. 669-684.
[62] Li, Y.-Q., He, Y.-L., Wang, Z.-F., Xu, C., and Wang, W., 2012, "Exergy analysis of two phase change materials storage system for solar thermal power with finite-time thermodynamics," Renewable Energy, 39(1), pp. 447-454.
[63] Shabgard, H., Robak, C. W., Bergman, T. L., and Faghri, A., 2012, "Heat transfer and exergy analysis of cascaded latent heat storage with gravity-assisted heat pipes for concentrating solar power applications," Solar Energy, 86(3), pp. 816-830.
[64] Mosaffa, A., Farshi, L. G., Ferreira, C. I., and Rosen, M., 2014, "Energy and exergy evaluation of a multiple-PCM thermal storage unit for free cooling applications," Renewable Energy, 68, pp. 452-458.
[65] Chorin, A. J., 1968, "Numerical solution of the Navier-Stokes equations," Mathematics of computation, 22(104), pp. 745-762.
[66] Rhie, C., and Chow, W., 1983, "Numerical study of the turbulent flow past an airfoil with trailing edge separation," AIAA journal, 21(11), pp. 1525-1532.
[67] Patankar, S., 1980, Numerical heat transfer and fluid flow, CRC press.
[68] Youngs, D. L., 1982, "Time-dependent multi-material flow with large fluid distortion," Numerical methods for fluid dynamics, 24(2), pp. 273-285.
[69] Ubbink, O., 1997, "Numerical prediction of two fluid systems with sharp interfaces," University of London PhD Thesis.
[70] 2010, "ANSYS FLUENT Theory Guide Replease 13.0."
[71] Wilcox, D. C., 1998, Turbulence modeling for CFD, DCW industries La Canada, CA.
[72] Hinze, J., 1975, "Turbulence McGraw-Hill," New York, 218.
[73] Menter, F. R., 1994, "Two-equation eddy-viscosity turbulence models for engineering applications," AIAA journal, 32(8), pp. 1598-1605.
[74] "Dynalene 600 High Temperature Silicone Heat Transfer Fluid," Dynalene, Inc.
[75] Incropera, F. P., and DeWitt, D. P., 2002, Fundamentals of Heat and Mass Transfer, John Wiley & Sons, Inc., New York.
[76] Hatch, J. E., Aluminum, A., and American Society for, M., 1984, "Aluminum properties and physical metallurgy."
[77] McDonald, R. A., 1967, "Enthalpy, heat capacity, and heat of fusion of aluminum from 366.degree. to 1647.degree.K," Journal of Chemical & Engineering Data, 12(1), pp. 115-118.
[78] Janz, G. J., Allen, C. B., Bansal, N. P., Murphy, R. M., and Tomkins, R. P. T., 1979, "Physical properties data compilations relevant to energy storage, 2. Molten salts: Data on single and multi-component salt systems," NASA STI/Recon Technical Report N, 80, p. 10643.

[79] Elmozughi, A. F., Solomon, L., Oztekin, A., and Neti, S., 2014, "Encapsulated phase change material for high temperature thermal energy storage – Heat transfer analysis," International Journal of Heat and Mass Transfer, 78(0), pp. 1135-1144.
[80] Solomon, L., Elmozughi, A. F., Oztekin, A., and Neti, S., 2015, "Effect of internal void placement on the heat transfer performance–Encapsulated phase change material for energy storage," Renewable Energy, 78, pp. 438-447.
[81] Bauer, T., Laing, D., and Tamme, R., 2012, "Characterization of Sodium Nitrate as Phase Change Material," International Journal of Thermophysics, 33(1), pp. 91-104.
[82] Ashjaee, M., Amiri, S., and Habibi, K., 2008, "Slot jet impingement heat transfer from an isothermal circular cylinder," Thermal Issues in Emerging Technologies, 2008. ThETA'08. Second International Conference on, pp. 399-404.
[83] Buyuk, E., 1999, "Heat transfer and flow structures around circular cylinders in cross flow," Journal of Engineering and environmental science, 23, pp. 299-315.
[84] White, L. R., and Davis, H. T., 1967, "Thermal conductivity of molten alkali nitrates," The Journal of Chemical Physics, 47(12), pp. 5433-5439.
[85] Zhang, X., and Fujii, M., 2000, "Simultaneous measurements of the thermal conductivity and thermal diffusivity of molten salts with a transient short-hot-wire method," International journal of thermophysics, 21(1), pp. 71-84.
[86] Janz, G. J., Allen, C. B., Bansal, N., Murphy, R., and Tomkins, R., 1979, "Physical properties data compilations relevant to energy storage. II. Molten salts: data on single and multi-component salt systems," Rensselaer Polytechnic Inst., Troy, NY (USA). Cogswell Lab.
[87] Levin, E. M., Roth, R. S., Robbins, C. R., McMurdie, H. F., and Society, A. C., 1983, Phase diagrams for ceramists, American Ceramic Society.
[88] Harper, C. A., 2001, Handbook of Ceramics, Glasses, and Diamonds, McGraw-Hill.
[89] Zheng, Y., Zhao, W., Sabol, J. C., Tuzla, K., Neti, S., Oztekin, A., and Chen, J. C., 2013, "Encapsulated phase change materials for energy storage – Characterization by calorimetry," Solar Energy, 87(0), pp. 117-126.
[90] Zhao, W., Zheng, Y., Sabol, J. C., Tuzla, K., Neti, S., Oztekin, A., and Chen, J. C., 2013, "High temperature calorimetry and use of magnesium chloride for thermal energy storage," Renewable Energy, 50(0), pp. 988-993.
[91] Chase, M. W., and National Institute of Standards and, T., 1998, NIST-JANAF thermochemical tables, American Chemical Society ; American Institute of Physics for the National Institute of Standards and Technology, [Washington, D.C.]; Woodbury, N.Y.
[92] Awbery, J., and Griffiths, E., 1925, "The latent heat of fusion of some metals," Proceedings of the Physical Society of London, 38(1), p. 378.
[93] Grønvold, F., and Stølen, S., 2002, "Heat capacity of solid zinc from 298.15 to 692.68 K and of liquid zinc from 692.68 to 940 K: thermodynamic function values," Thermochimica acta, 395(1), pp. 127-131.
[94] Kubaschewski, O., Alcock, C. B., and Spencer, P. J., 1993, Materials thermochemistry, Pergamon Press.

[95] Besmann, T. M., and Spear, K. E., 2002, "Thermochemical Modeling of Oxide Glasses," Journal of the American Ceramic Society, 85(12), pp. 2887-2894.
[96] Rossini, F. D., 1952, Selected values of chemical thermodynamic properties, U.S. Govt. Print. Off., Washington.
[97] Bale, C. W., Bélisle, E., Chartrand, P., Decterov, S. A., Eriksson, G., Hack, K., Jung, I. H., Kang, Y. B., Melançon, J., Pelton, A. D., Robelin, C., and Petersen, S., 2009, "*FactSage Thermochemical Software and Databases - Recent Developments*," Calphad, pp. 295-311.
[98] Ota, R., and Soga, N., 1982, "The Critical Cooling Rates and the Liquidus Viscosities for Glass Formation in the B_2O_3-Na_2O System," Journal of the Ceramic Association, Japan, 90(1045), pp. 531-537.
[99] Vilarinho-Franco, T., Teyssier, A., Tenu, R., Pécaut, J., Delmas, J., Heitzmann, M., Capron, P., Counioux, J. J., and Goutaudier, C., 2013, "Solid–liquid equilibria in the ternary system NaBO2–NaOH–H2O thermal behavior of double salts," Fluid Phase Equilibria, 360, pp. 212-221.
[100] Morey, G., and Merwin, H. E., 1936, "Phase equilibrium relationships in the binary system, sodium oxide-boric oxide, with some measurements of the optical properties of the glasses," Journal of the American Chemical Society, 58(11), pp. 2248-2254.

VITA

Laura D. Solomon was born on October 1st, 1989 in Philadelphia, Pennsylvania. She is the daughter of Donald and Sheila Solomon. She attended George Washington High School in the Philadelphia School District and graduated in 2007. She graduated magna cum laude from Temple University with a Bachelor's of Science in Mechanical Engineering in 2011. She then completed her Masters of Science degree in Mechanical Engineering at Lehigh University in 2013 en route to a PhD.